NUMERICAL MODELING AND FABRICATION OF HIGH EFFICIENCY CRYSTALLINE SILICON SOLAR CELLS

A Thesis
Presented to
The Academic Faculty

by

John Samuel Renshaw

In Partial Fulfillment
of the Requirements for the Degree
Doctor of Philosophy in the
School of Physics

Georgia Institute of Technology
August 2013

Copyright © 2013 by John Samuel Renshaw

NUMERICAL MODELING AND FABRICATION OF HIGH EFFICIENCY CRYSTALLINE SILICON SOLAR CELLS

Approved by:

Professor Ajeet Rohatgi,
Committee Chair
School of Electrical and Computer Engineering
Georgia Institute of Technology

Professor Walt DeHeer
School of Physics
Georgia Institute of Technology

Professor Ed Conrad
School of Physics
Georgia Institute of Technology

Professor Phillip First
School of Physics
Georgia Institute of Technology

Professor Bernard Kippelen
School of Electrical and Computer Engineering
Georgia Institute of Technology

Date Approved: 12 June 2013

To Mom and Dad,

For making me believe I can accomplish anything I set my mind to and for the unconditional love and support I have received throughout my life.

To my beautiful wife,

For supporting me through the end of this endeavor and for giving me a wonderful life to look forward to.

ACKNOWLEDGEMENTS

Before I acknowledge my friends, family and colleagues I would like to express my gratitude to God for carrying me through this journey and showing me the way when I was lost.

> The heavens declare the glory of God,
> and the sky above proclaims his handiwork.
> Day to day pours out speech,
> and night to night reveals knowledge.
> There is no speech, nor are there words,
> whose voice is not heard.
> Their voice goes out through all the earth,
> and their words to the end of the world.
> In them he has set a tent for the sun,
> which comes out like a bridegroom leaving his chamber,
> and, like a strong man, runs its course with joy.
> Its rising is from the end of the heavens,
> and its circuit to the end of them,
> and there is nothing hidden from its heat.
> -Psalm 19:1-6 (ESV)

I would like to thank Dr. Rohatgi for the opportunity he has given me and for the freedom to explore the topics that have interested me. I would also like to thank the committee members for their guidance in writing my thesis, and the Georgia Tech Physics department for accepting me into this program when many others turned me away.

I am truly grateful for everyone at the University Center of Excellence for Photovoltaics (UCEP). Every one of you have been a big part of my life since I joined in 2008 and have helped me to make it this far. Specifically I would like to thank Ajay Upadhyaya for insightful conversations and guidance throughout my time at UCEP, Keith Tate for discussions

about modeling and pushing me to question everything; Aba Ebong for sharing his time and vast expertise in solar cell contacts. For help in the lab and stimulating conversations, I would like to thank Brain Rounsaville, Dr. Vijay Yelundur, Dr. Manav Sheoran, Dr Vichai Meemongkolkiat, Dr. Rishi Ramanathan, Dr. Arnab Das, Ricky Chen,Jiun Hong Lai and Moon Hee Kang.

This work was supported by the U.S. Department of Energy, Merck, Dow Chemical and the Silicon Solar Consortium

TABLE OF CONTENTS

DEDICATION . . . . **iii**

ACKNOWLEDGEMENTS . . . . **iv**

LIST OF TABLES . . . . **xi**

LIST OF FIGURES . . . . **xii**

LIST OF ABBREVIATIONS AND SYMBOLS . . . . **xvii**

I INTRODUCTION AND RESEARCH OBJECTIVES **1**

1.1 Market Overview 1

1.2 Motivation for this work 4

1.3 Research Objectives 6

1.3.1 2D and 3D Modeling of Selective Emitter 7

1.3.2 Understanding and optimizing of the laser doping process 7

1.3.3 Fabrication of laser doped selective emitter solar cells 8

1.3.4 Optimization of a screen printed interdigitated back contact solar cell 9

1.3.5 Finding the practical limit of crystalline Si solar cells 10

II DEVICE PHYSICS OF SOLAR CELLS **12**

2.1 Introduction 12

2.2 Solar Cell Operating Principles 12

2.2.1 Energy From the sun 12

2.2.2 Photocurrent in solar cells 14

2.2.3 The dark current 15

2.2.4 The light IV curve and efficiency 15

2.2.5 Parasitic Effects and The Equivalent Circuit of a Solar Cell 16

2.3 P-N junction solar cells 19

2.3.1 Energy bands in semiconductors 19

2.3.2 Densities of state and equilibrium carrier concentration 21

2.3.3 Absorption and carrier generation 23

2.3.4 Carrier recombination 25

2.3.5 Carrier transport in semiconductors 28

2.3.6 The semiconductor equations 30

2.3.7 Electrostatics of a pn-junction 32

2.4 Conclusions 35

III MULTIDIMENSIONAL MODELING OF SILICON SOLAR CELLS 36

3.1 Introduction and Review of Numerical modeling of solar cells 36

3.2 The Finite Element Method 38

3.3 Physical Models used in Device Simulation 40

3.3.1 Carrier Statistics 40

3.3.2 Band Gap Narrowing 42

3.3.3 Schockley Read Hall Recombination 43

3.3.4 Auger Recombination 44

3.3.5 Surface Recombination 45

3.3.6 Carrier Mobility 46

3.4 Application of Ray Tracing Simulations for Calculating Optical Generation for Textured silicon 46

3.4.1 Simulation Details 46

3.4.2 Results 46

3.5 Verification of Models and Establishment of Mesh Through Quantum Efficiency and IV Characteristics of a Test Structure 52

IV QUANTITATIVE UNDERSTANDING OF THE BENEFIT OF SELECTIVE EMITTERS AS A FUNCTION OF IMPROVED SCREEN PRINTING PASTES 57

4.1 Introduction 57

4.2 Using effective barrier height to model contact resistance 58

4.3 Application of the model 60

4.4 Simulation results 61

4.5 Conclusions 62

V A REVIEW OF LASER DOPING IN SI 64

5.1 Introduction 64

5.2 Beginnings of Laser Doping 64

5.3 Laser Doping Mechanism 65

5.4 Laser Induced Defects 69

5.5 Laser Doping in Crystalline Si Solar Cells 70
5.6 Conclusions 77

VI DEVELOPMENT AND OPTIMIZATION OF UV LASER DOPING OF PHOSPHORUS AND BORON IN SI 78

6.1 Introduction 78
6.1.1 Procedures for laser doping 78
6.1.2 Results 79
6.2 Laser doping of textured crystalline Si with spin on B dopants and UV laser 82
6.3 Understanding and Control of Opening widths after laser doping 83
6.4 SEM investigation of laser doped regions 85
6.4.1 Conclusions of the feasibility of plated contact cells by pulsed UV laser radiation and spin on dopants 87
6.5 Development and Optimization of Laser doping textured crystalline Si with P-glass source 87
6.5.1 Laser doping on an industrial type emitter 87
6.5.2 Laser doping on lightly doped emitter 90
6.5.3 Investigation of the effect of selective laser doping on carrier lifetime and the local Voc 93
6.5.4 Understanding the role of the dead layer in laser doping 96
6.5.5 Laser doping and front surface reflectance 97
6.6 Conclusion 98

VII UV LASER DOPED SELECTIVE EMITTER SOLAR CELLS 100

7.1 Introduction 100
7.2 Review of selective emitter technologies 100
7.3 Experiment 106
7.4 Results and Discussion 108
7.5 $POCl_3$ flow effect 113
7.6 Conclusion 114

VIII UV LASER DOPED SELECTIVE EMITTER SOLAR CELLS WITH EMITTER ETCHBACK 116

8.1 Introduction 116
8.2 Laser Process Optimization 116

8.3 Laser Doping with Etch-Back Process 118
8.4 Device Optimization 122
8.5 Conclusion 124

IX DEVICE OPTIMIZATION FOR SCREEN PRINTED INTERDIGITATED BACK CONTACT SOLAR CELLS 126

9.1 Review of numerical modeling of interdigitated back conact solar cells . . . 126
9.2 Introduction 129
9.3 Simulations 130
9.4 Results 132
9.4.1 FSF Profile 132
9.4.2 Emitter Profile 133
9.4.3 BSF Profile 135
9.5 Pitch, Gap Width and Bulk Resistivity 135
9.6 Conclusion 136

X DEVELOPMENT OF A STRATEGY TO APPROACH THE SCHOCKLEY-QUEISSER LIMIT THROUGH NUMERICAL SIMULATIONS . . . 137

10.1 The Shockley-Queisser Limit 137
10.2 Using recent PV technologies to approach the Shockley-Queisser limit . . . 138
10.3 Quantifying the benefit of passivated contacts through numerical simulation 140
10.4 Quantifying the benefit of aluminum oxide surface passivation through numerical simulation 141
10.5 Exploring the practical limit of silicon solar cells 143
10.5.1 Cell Thickness and Resistivity 145
10.5.2 Passivated Emitter Contact 147
10.5.3 Passivated BSF Contact 149
10.5.4 Front and Rear surface passivation by Al_2O_3 149
10.5.5 Lambertian light trapping 152
10.5.6 Roadmap 153

XI CONCLUSIONS AND FUTURE WORK 156

11.1 Accurate modeling of screen printed contacts and the benefit of selective emitter solar cells 157
11.2 Investigation and optimization of ultraviolet laser doping on Si 157

11.3 Application of UV laser doping in crystalline Si solar cells 158

11.4 2D and 3D modeling of back contact solar cells to determine the practical efficiency limit and optimize a screen printed IBC cell 158

11.5 Suggested future work 159

APPENDIX A — INPUT FILES FOR SENTAURUS WORKBENCH FOR SOLAR CELL SIMULATION 161

APPENDIX B — DEVELOPMENT OF LOW-COST PLATED CONTACT SOLAR CELLS USING A SCREEN PRINTED DIELECTRIC ETCHING PASTE 185

REFERENCES 194

VITA 207

LIST OF TABLES

2.1 electrical potential in a 1D pn junction 34

3.1 Auger recombination coefficients 44

3.2 Fit Parameters for Surface Recombination Velocity on P diffused surfaces. . 45

3.3 Parameters used in optical generation calculation 48

3.4 Actual and simulated IV results 56

4.1 Parameters used to fit experimental data using barrier height model 58

4.2 Parameters used in in Sentaurus Device simulations 61

4.3 Comparison of the best device simulations for HE and Se simulations for each effective Schottky barrier height. 62

5.1 Comparison of defects found by DLTS in Ruby and Nd:YAG irradiated Si. . 70

6.1 IV Data from UV laser doping on a typical industrial type solar cell 88

6.2 Average IV results from solar cells with high sheet resistance emitters, with and without laser selective emitter 91

7.1 Review of IV characteristics from various selective emitter technologies. . . 106

7.2 Average and Best IV characteristics, measured under standard test conditions 108

7.3 Active P dose for each profile. Obtained by integrating the ECV data. . . . 109

7.4 IV characteristics for selective emitter cells 111

8.1 Effect of selective emitter pitch on IV characteristics 123

9.1 Modeled Cell Parameters 131

9.2 Profiles Simulated 132

9.3 Values of varied parameters 136

10.1 Initial Modeled Cell Parameters 144

B.1 IV parameters of identically processed cells with screen printed vs plated metallization 189

LIST OF FIGURES

1.1 US energy consumption, history and forecast. Data taken from EIA. 1

1.2 breakdown of US renewable energy by source,from EIA 2

1.3 Module prices from Dec 2001 to Jan 2012, from EIA. 3

1.4 Solar energy consumption by year since 2000. Data from EIA. 3

1.5 Process flow for a "baseline" solar cell 5

1.6 Device structure of a selective emitter solar cell 6

1.7 Device structure of an segmented selective emitter solar cell 9

1.8 Device structure of an IBC solar cell 10

2.1 The AM0,AM1.5G and AM1.5D spectrums. 13

2.2 Global average annual insolation. Data from NASA. 14

2.3 Current generation and collection in a typical Si solar cell. 15

2.4 Light IV, Dark IV and Power vs V curves for an ideal solar cell. 16

2.5 Equivalent circuit of a solar cell. 17

2.6 two diode model of a solar cell. 18

2.7 An example band diagram 20

2.8 Fermi function at 0 and 300 K. 21

2.9 Absorption in an indirect bandgap semiconductor 24

2.10 Diagram of S.R.H., Radiative and Auger recombination 25

2.11 Surface recombination in semiconductors. 28

2.12 a p-n homojunction 33

3.1 (top) The entire domain of interest for simulation. (bottom) The discretized approximation of the domain. 39

3.2 γ_{BGN},γ_{deg} and the pn product for a heavily doped n$^+$ profile. 42

3.3 Comparison of various band gap narrowing models with the Schenk model. 43

3.4 Image of the whole 2D domain used for ray tracing (a) and a zoomed in view near the top textured region (b). 47

3.5 Effect of varying the back surface reflectance on solar cell reflectance. 48

3.6 Simulation results, varying the SiN index and thickness. 50

3.7 (left) The effect of the number of rays on the reflectance curve over the full wavelength range. (right) The effect of the number of rays on the reflectance curve in the escape reflectance regime which is found to be most sensitive to the number of rays used. 51

3.8 Normalized spectral generation versus depth by wavelength. 51

3.9 Structure and mesh of device used for quantum efficiency and IV simulations for this experiment. 52

3.10 Effect of front surface recombination velocity on simulated IQE. 54

3.11 Effect of back surface field on simulated IQE. 55

3.12 Effect of bulk lifetime on simulated IQE. 55

4.1 Experimental data from literature and fits made by varying the effective Schottky barrier height. 59

4.2 The simulation domain used in this work 62

4.3 Efficiency (left) and FF (right) versus peak doping in the field emitter . . . 63

5.1 Solubility of P and B in crystalline Si as a function of temperature and in Si melt 65

5.2 Diffusivity of P in crystalline Si as a function of temperature and in Si melt 66

5.3 Calculations crystalline Si melt depth and duration for $\lambda = 193$ and 308 nm for several laser fluences for a 20 ns pulse. Used with permission. 67

5.4 Calculations crystalline Si melt depth and duration for 20 and 50 ns pulses with $\lambda = 193$ for several laser fluences. Used with permission. 68

5.5 Relationship between melt depth and junction depth for B laser induced diffusion in Si. 69

5.6 proposed laser doping process 69

5.7 Schematic of buried contact solar cell. 71

5.8 Schematic of double sided buried contact solar cell. 72

5.9 Schematic of interdigitated buried contact solar cell. 72

5.10 Schematic of Suntech Pluto cell. 73

5.11 Process differences in LDSE cells and standard screen printed cells 74

5.12 Diagram of LCP apparatus. 75

5.13 Diagram of laser transfer process 76

5.14 Process sequence for add on laser selective emitter solar cells. 76

5.15 Cell structure with intersected laser doped selective emitter. 77

6.1 Cell structure with intersected laser doped selective emitter. 79

6.2 Pulse overlap change with scan speed for an example repetition rate of 180 khz for (a)3000 mm/s,(b)1000 mm/s,(c)500 mm/s,(d)100 mm/s 80

6.3 Sheet resistance vs laser power, scan speed and P dopant source 81

6.4 Passivated rear contact solar cell with locally diffused boron regions on the rear. 82

6.5 Sheet resistance vs laser power, scan speed and boric acid concentration . . 83

6.6 Diagram depicting why the opening width varies with pulse power. 84

6.7 Measured opening width versus pulse power and scan speed. 84

6.8 Cross sectional SEM images of textured laser scribed Si. 86

6.9 Sheet resistance produced from laser doping under different rep. rates and scan speeds on an industrial type emitter. 88

6.10 Process sequence for laser doped selective emitter cells. 89

6.11 Shunt path created from excessive power pulse. 90

6.12 Resulting sheet resistances from various laser doping conditions. 91

6.13 (a)An example TLM pad.(b) non-ideal TLM pad made from dicing solar cell. 92

6.14 TLM measurements on 120 and 150 khz selective emitter solar cells compared to high sheet resistance reference without selective emitter. 93

6.15 Change in effective lifetime after the laser doping step for various laser conditions. 94

6.16 (a) picture of wafer after VocScan measurement, (b) contour plot of Vocscan data for the field and laser doped regions. 95

6.17 Resulting sheet resistance from laser doping on a 90 $\Omega/\square$ emitter with and without the P glass for 120 and 150 khz rep. rates. 96

6.18 Reflectance data from solar cells with a selective emitter created with 120 and 150 khz pulse repetition rates and a standard with no laser doping . . . 98

7.1 Cross section of the Innovalight "Cougar Cell". 101

7.2 Process flow for Centrotherm's S.E. by barrier layer patterning, steps in white are additional compared to the standard industrial process. 102

7.3 Process flow for GP Solar's S.E. by two diffusions and etching paste patterning compared with a standard process, steps in gray represent additional steps compared with a standard process flow for industrial type cells. 103

7.4 Varian's implant S.E. process (a) compared with a standard industrial fabrication sequence (b). Steps in red are removed by the implantation process flow. 104

7.5 Process flow for S.E. solar cells by emitter etch-back method. 104

7.6 Process flow for UNSW's inkjet method for selective emitter with plated contacts. . . . 105

7.7 Process flow for laser doped Si solar cells 107

7.8 ECV doping profiles 108

7.9 Microscopic contact resistivity 110

7.10 LBIC map comparison 111

7.11 Correscan maps of different pitch selective emitters 112

7.12 Sheet resistance after diffusion and after laser doping for different $POCl_3$ flows. The parameters used for laser doping were 180 khz and 3000 mm/s. . . 113

7.13 Normalized IQE in the field (a) and laser doped (b) regions of a test structure 114

8.1 ECV doping profiles 117

8.2 SEM images of laser damage 118

8.3 Effect of etch time 119

8.4 Correscan map of etchback wafers 120

8.5 Vocscan map for various laser settings 121

8.6 Process for laser doped etchback solar cells 122

8.7 IQE comparison of baseline and selective emitter cell 124

9.1 The IBC device architecture. 126

9.2 The PCSC device architecture. 127

9.3 The point IBC-SHJ device architecture. 128

9.4 The simulated effects of the buffer layer thickness (a), doping (b), and bandgap (c) on the IV curve of IBC-SHJ devices. 129

9.5 Modeled unit cell 130

9.6 cell efficiency for different FSF profiles 132

9.7 cell efficiency for different emitter profiles 133

9.8 cell efficiency for the optimized diffusions for a screen printed IBC as a function of pitch, gap and bulk resistivity 134

9.9 cell efficiency for different BSF profiles 135

10.1 Schematic of an IBC showing the device regions optimized in this study. . . 139

10.2 Three concepts for a passivated contact(left)doped poly-Si on top of a lowly doped substrate with a thin oxide in between (center) the HIT concept, amorphous-Si junction with a thin intrinsic layer at the interface (right) diffused p^{++} emitter with a thin interfacial oxide between emitter and contact. 139

10.3 Effect of SRV and peak doping level on J_{0e} for 0.5 (left) and 1.0 (right) micron gaussian phosphorus diffusions 141

10.4 Effect of SRV and peak doping level on J_{0e} for 0.5 (left) and 1.0 (right)micron gaussian boron diffusions 142

10.5 Hole density and band bending induced by high negative charge in Al_2O_3. . 142

10.6 Bottom view of unit cell and mesh used in simulations, blue indicates boron doping and red indicates phosphorus doping. Left half of figure from. 143

10.7 (left) Unit cell simulated showing 2d slice taken to explore shunt behavior (right) zoomed in view of highlighted portion of the unit cell showing the depletion region between the n^+ and p^+ regions 144

10.8 Effect of device thickness and base resistivity on cell parameters. 146

10.9 Effect of SRV of emitter contact. 148

10.10Effect of SRV of BSF contact. 150

10.11A) Figure showing the 3D unit cell and the region from which a 2D slice is taken. B,C and D are contour plots of the hole density within the device for simulations with low BSF doping, low BSF SRV (B) low BSF doping, high BSF SRV (C) and high BSF doping, low BSF SRV (D). 151

10.12Streamlines showing hole current path from the front of the device for A) no induced rear emitter and B) with induced rear emitter. 152

10.13Effect of cell thickness of optimized device with Lambertian light trapping. 154

10.14The path to over 27% through technology innovations and device optimization.155

11.1 Selective emitter solar cell with (left) and without (right) a passivated rear for improved passivation and relfectance. 159

B.1 Plated cell emitter profile vs standard type emitter. 186

B.2 Quasi-steady-state photoconductance decay curve and J_{0e} fit 187

B.3 Cell fabrication process for plated and screen printed cells in this work. . . 188

B.4 Reflectance and normalized internal quantum efficiency of the highest efficiency screen printed solar cells compared with plated contact solar cells. . 189

B.5 Comparison of contact resistance measurements made from TLM pads made on screen printed vs plated contacts. 190

B.6 SEM images of fingers on a finished plated cell 191

B.7 SIMS profile for Ni on a Si wafer that has been through a tube anneal. . . . 192

LIST OF ABBREVIATIONS AND SYMBOLS

a-Si Amorphous Silicon.

BCSC Back Contact Solar Cell.

BSF Back Surface Field.

BSRV Back Surface Recombination Velocity.

C-Si Crystalline Silicon.

EWT Emitter Wrap Through.

FSF Front Surface Field.

FSRV Front Surface Recombination Velocity.

IBC Interdigitated Back Contact.

IBC-SHJ Interdigitated Back Contact with Silicon Heterojunction.

J_{01} In the two diode model, the J_0 of the diode with ideality factor of 1.

J_{02} In the two diode model, the J_0 of the diode with ideality factor > 1.

J_{0b} Base Reverse Saturation Current Density.

J_{0e} Emitter Reverse Saturation Current Density.

J_{sc} Short Circuit Current.

LDSE Laser Doped Selective Emitter.

LID Light Induced Degradation.

MWT Metallization Wrap Through.

n_2 In the two diode model, the ideality factor of the non-ideal diode.

PCSC Point Contact Solar Cell.

PECVD Plasma Enhanced Chemical Vapor Deposition.

PSG Phosphosilicate Glass.

PV Photovoltaics.

SD Sentaurus Device.

SRV Surface Recombination Velocity.

V_{oc} Open Circuit Voltage.

CHAPTER I

INTRODUCTION AND RESEARCH OBJECTIVES

1.1 Market Overview

Growing power needs and knowledge of eventual fossil fuel shortages along with growing evidence of global warming have created an ever increasing need for clean renewable energy sources. Among these energy sources are wind, nuclear, hydroelectric, biomass, geothermal, solar thermal and photovoltaics (PV). Hydroelectric, wind and geothermal energy sources have been adopted into the grid but are limited to regions where these resources are available. Nuclear energy has been developed for many years, however, it has not become a dominant source of power in the U.S. most likely because of fears of disaster similar to those at Chernobyl, three mile island and also most recently in Tokyo, Japan. Another factor is the lack of a good way to dispose of radioactive waste. Biomass is also an attractive energy source, however, more work needs to be done to harvest this source in more efficient ways that do not diminish the food supply. Solar energy does not face the drawback of limited availability like fossil fuels nor does it face the challenge of regional availability like hydroelectric, wind or geothermal. Figure 1.1 shows that despite the availability of

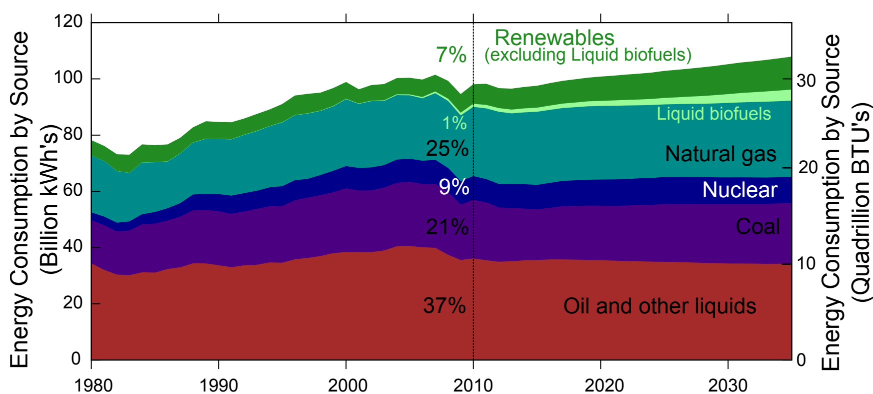

Figure 1.1: US energy consumption, history and forecast. Data taken from EIA [1].

renewable energy sources, in 2010 over 80% of power in the U.S. was generated by oil, coal or natural gas while renewables generated only about 8% [1]. Our power needs have been

steadily increasing over the last thirty years and this trend is not likely to stop any time soon. To meet this growing need, renewable energy sources must be developed to become more economical and widely available if they are going to contribute more than the meager 8% they provided in 2010.

The spectrum of renewable energy sources consumed in 2010 along with non-renewable sources is shown in figure 1.2. Even though the sun is truly the only unlimited resource

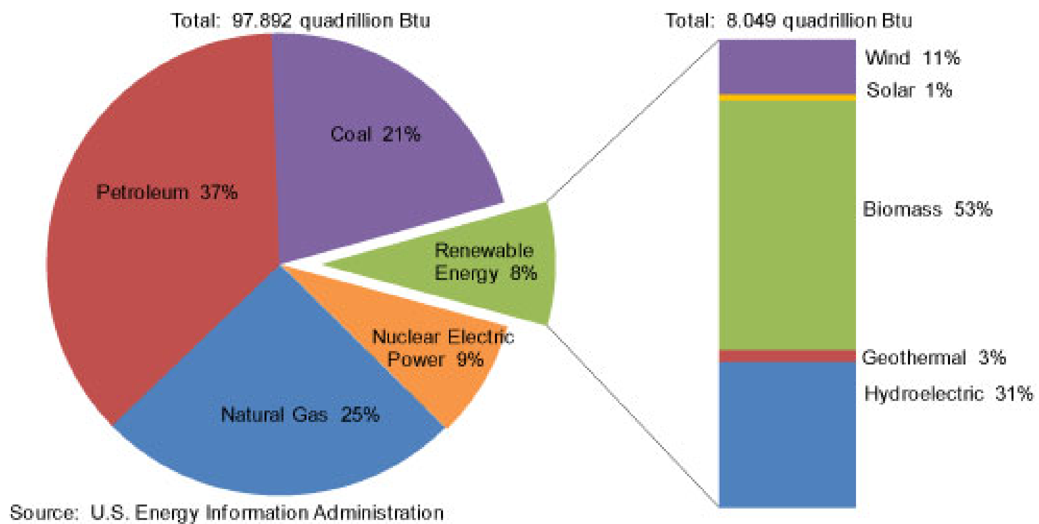

Figure 1.2: breakdown of US renewable energy by source,from EIA [2].

that we have, solar energy only comprised about 1% of all renewable energy sources in 2010 and PV has even less than that. The cost of Photovoltaic energy is currently too high for widespread adoption and power companies often make it difficult to transition to photovoltaics through lobbying at state legislature levels. However, the cost of photovoltaic cells and modules (shown in figure 1.3) has been decreasing overall in the last decade due to innovation, economy of scale, competition and subsidies. While solar energy only makes up a small portion of our energy supply, PV has been growing radipdly in recent years despite the recession. Data from the United States Energy Information Administration (EIA) in figure 1.4 show that the amount of solar energy consumed increased 67% from 65,421 billion Btu in 2000 to 109,404 billion Btu in 2010. The potential for photovoltaics is huge and it would be a grave disservice to humanity not to pursue this virtually limitless resource.

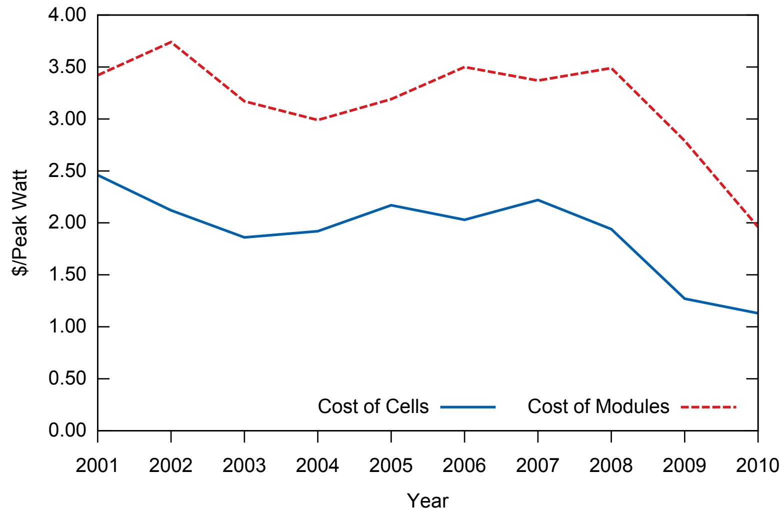

Figure 1.3: Module prices from Dec 2001 to Jan 2012, from EIA [3].

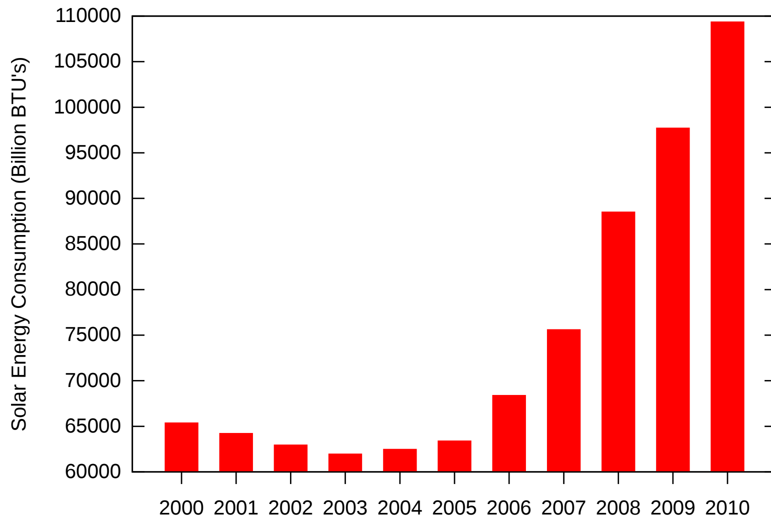

Figure 1.4: Solar energy consumption by year since 2000. Data from EIA [4].

Standard industrial monocrystalline silicon solar cells with homogeneous emitters are created from silicon wafers in 6 steps. First, p-type wafers are textured in a heated solution containing potassium hydroxide and isopropyl alcohol. This solution preferentially etches the <100> crystal plane at a much faster rate than the <111> plane. After this process, the surface of the wafer is covered with pyramids with the faces of the pyramids being the <111> plane. This surface is much less reflective than a planar surface since the reflected light off of one pyramid can be collected in an adjacent pyramid. This process is one of the major reasons that <100> silicon is used for solar cells over other crystal orientations. Following texturing, wafers are cleaned and put into a tube furnace heated between 800 and 900 °C. Then nitrogen gas is flown through a $POCl_3$ bubbler into the tube along with oxygen to form a n^+ layer on the surface of the wafers and a phosphorus rich glass above that. After the phosphorus glass is removed, the wafers are coated with a hydrogenated silicon nitride film about 780 nm thick to reduce reflection and passivate the surface. Metalization is achieved through screen printing silver paste on the front of the wafer in a grid pattern and aluminum paste on the rear side of the wafer . Finally, the wafers are fired in a belt furnace at temperatures between 700 and 900 °C. During firing three main things happen: first, glass frit in the silver paste etches through the silicon nitride and contact is formed between the silver paste and the substrate. Secondly, a eutectic is formed between Al and Si which results in an aluminum doped p^+ layer beneath the aluminum contact after cooling. Finally, hydrogen in the silicon nitride film diffuses into the wafer and can passivate defects which can increase the carrier lifetime especially in multicrystalline materials. This process very similar to the manufacture of most silicon solar cells today and the motivation of this research is to build and improve upon this process so high efficiency cells can be produced at low cost. A schematic diagram of this process flow can is shown in figure 1.5.

1.2 Motivation for this work

The motivation of this research is to further reduce the cost of photovoltaic energy from crystalline silicon solar cells in order to become more competitive with energy from traditional energy sources. One way to reduce the cost of photovoltaic energy is to increase the

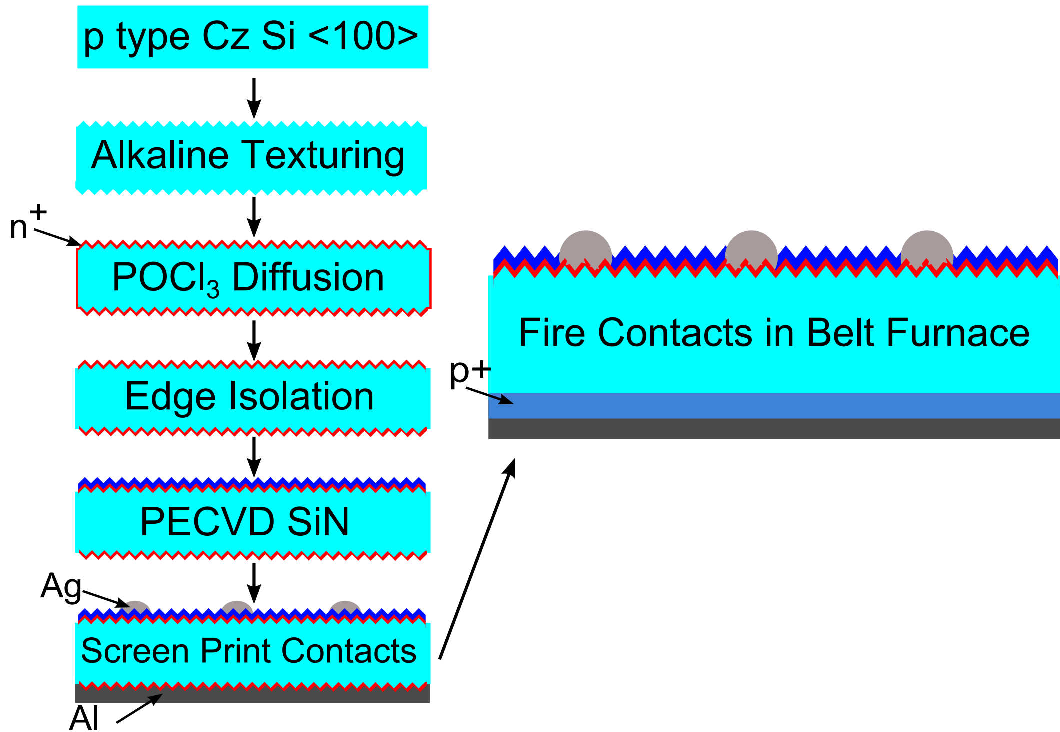

Figure 1.5: Process flow for a "baseline" solar cell

cell and module efficiency without increasing the cost of manufacturing or input materials. This is a challenging task, many technologies exist which can increase solar cell efficiency but they often require more manufacturing steps or equipment which can result in a net increase in \$/Watt compared to a standard industrial type crystalline silicon solar cell.

This research focuses on increasing solar cell efficiency through the use of a selective emitter created by laser doping, which has the advantage of only adding one processing step compared with the standard industrial process. In addition, laser processing has a low cost of ownership since the only costs are the initial purchase of the laser system, it's maintenance and the electricity that it consumes. Laser doping has been a hot research topic recently in photovoltaics, but most of the work has focused on laser doping with a green laser, not much work has been done with a UV laser. UV light has a shorter wavelength than green light and is absorbed more strongly than green light. Therefore, the resulting doping profiles from UV laser doping will be more shallow and have a lower total laser doped volume. Such shallower profile could minimize the amount of auger recombination in the laser doped region and be advantageous over a green laser for screen printed contacts

where a deeper emitter is not necessary.

1.3 Research Objectives

The ultimate goal of this research is to lower the cost of electricity generated from crystalline silicon solar cells through raising the solar cell efficiency by means of a ultraviolet laser doped selective emitter. The selective emitter device design (figure 1.6) allows for the diffusion profile beneath the silver grid lines to be optimized for low-ohmic contacts while the diffusion profile between the grid lines is optimized to minimize recombination which results in higher short circuit current (Jsc) and open circuit voltage (Voc). Laser doping is a single step in

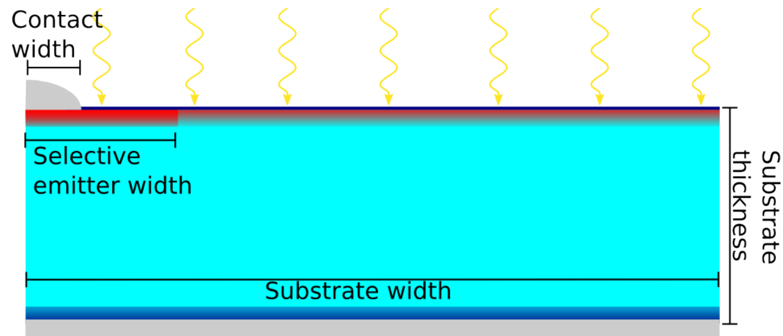

Figure 1.6: Device structure of a selective emitter solar cell

addition to the standard manufacturing process and the objective of this research is to show that it can increase the absolute solar cell efficiency by 0.5% to 19%. This combination provides a great cost to benefit ratio and could lower the $/Watt cost of energy from crystalline silicon solar cells. This work is divided into 5 tasks. In the first task, the benefit of a selective emitter device over a homogeneous emitter device is demonstrated through 2D device modeling in the finite element analysis semiconductor simulation software, Sentaurus Device. The second task focuses on exploration and optimization of laser and dopant parameters to minimize defects created through thermal cycling and for low resistance contacts. The third task combines tasks 1 and 2 to manufacture of the first commercial size high efficiency crystalline silicon solar cells with a UV laser doped selective emitter. The fourth task explores the use of an emitter etch-back to further increase solar cell performance. Finally, the fifth task focuses on the optimization of a high efficiency solar cell device architecture called the interdigitated back contact solar cell, again through 2D

and 3D modeling in Sentaurus Device.

1.3.1 Task 1: Demonstrate the benefit of selective emitter through 2D modeling

In crystalline silicon solar cell device design there is a trade-off that must be considered when choosing an emitter doping level. Lowering the doping concentration can decrease the depth of the dead layer that is at the surface of the cell caused by auger recombination and increase the Jsc and Voc, however this also increases the contact resistance and lowers the fill factor (FF). While increasing the doping has the opposite effect of increasing the FF and reducing the Jsc and Voc. Therefore, in widely used homogeneous emitter solar cells a compromise must be made to enable decent contacts while trying to minimize recombination in the emitter. The selective emitter solar cell does not suffer from this trade-off. In this device design the doping profile beneath the front contact is different from the doping profile between the front contacts. This device architecture is explored in this task using a semiconductor simulation software called Sentaurus Device which uses the finite element method to solve the semiconductor equations for a user input device design, grid and illumination/generation profile in each element of the grid to accurately model a unit cell of a solar cell. In this software surface, Auger and Schockley-Read-Hall recombination are accounted for as well as band gap narrowing via the Schenk model derived from quantum mechanical principles to accurately model the device using Fermi statistics. Through this highly accurate modeling software, this task shows quantitatatively the potential benefit that a selective emitter solar cell has over a homogeneous emitter solar cell.

1.3.2 Task 2: Understanding and Optimizing of the laser doping process

This task involves investigating the parameters that influence ultraviolet laser doping in silicon. Parameters explored include laser power,repetition rate scan speed and dopant source on textured silicon wafers. Laser doping in silicon is not new, however in recent years it has been researched as a possible method to increase solar cell efficiency. Most work to date has been primarily done using a green laser. In this task the use of an ultraviolet laser for doping is optimized. We find the UV laser is not well suited for incorporating spun on

dopant sources into the wafer, it is however efficient at driving in dopants in Phosphorus glass left over from $POCL_3$ diffusion. As the laser repeatedly heats the silicon, defects are introduced which can be detected through a chemical defect etch and also through the response of the solar cell in highly defective regions. In this task process conditions are investigated to minimize defects by preventing the silicon from being heated to its melting point. Dopant profiles resulting from this process are explored to determine the effect of the laser parameters on the laser doped profiles. Choosing the correct profile can minimize the contact resistance and maximize the solar cell fill factor and efficiency. When the silicon is not melted completely the surface concentration is higher then samples where the silicon is melted completely, therefore complete melting of the silicon should be avoided. In addition to minimizing defects and having a preferable doping profile, use of low pulse powers to prevent melting of silicon leaves the pyramidal texture intact and do not diminish the reflectance of the wafer in the laser doped regions unlike higher pulse powers which remove the pyramidal texture. This task establishes appropriate laser parameters to create laser doped regions that have minimal defects, high doping levels and good reflectance characteristics.

1.3.3 Task 3: Manufacture of high efficiency solar cells with selective emitters by ultraviolet laser doping

The results of tasks 1 and 3 are combined in this task for the realization of high efficiency crystalline silicon solar cells with a UV laser doped selective emitter (LDSE). High performance emitters with low surface concentration are developed that can exhibit low resistance contacts only after laser doping. As a result, efficiency gains of about 0.5% absolute are seen over a homogeneous emitter solar cell. To minimize the effect of laser defects while still capitalizing on their low resistance contacts, a novel concept of the segmented selective emitter is introduced (figure 1.7). In this device design the selective emitter only covers a fraction of the front grid lines and as a result the Jsc loss is minimal while the contact is still very good. This work results an efficiency enhancement over homogeneous emitter solar cells with only one additional step. For optimized laser doping parameters efficiencies

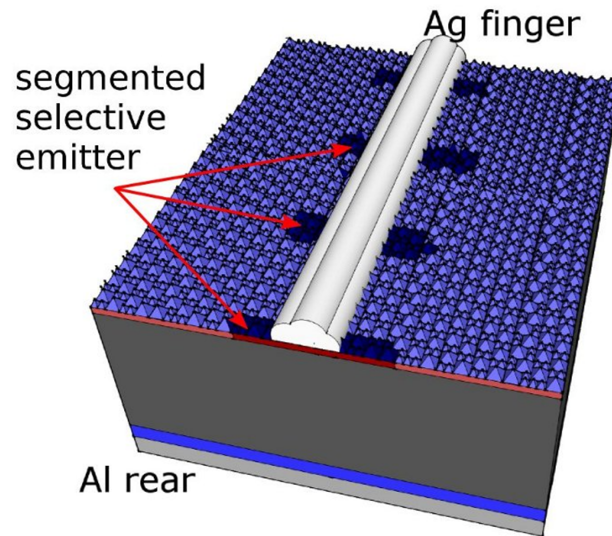

Figure 1.7: Device structure of an segmented selective emitter solar cell

above 19.1% can be achieved. Additionally, it is shown that UV laser doping is compatable with an emitter etch back process. In the etch-back process a highly doped emitter is formed by $POCl_3$ diffusion, which is then doped more heavily in selective regions via laser doping. After laser doping the wafer is then subjected to a very slow etch which removes the first 10 to 50 nanometers of the surface of the wafer. This process benefits from having an extremely heavily doped selective emitter and at the same time having a very low recombination emitter in the field regions formed by the etch-back. The characterization of the effect of this etch-back process in the field emitter and selective emitter regions is carried out in this task and then applied in the manufacture of solar cells that exhibit an efficiency of 19%.

1.3.4 Task 4: Optimization of a screen printed interdigitated back contact solar cell

The interdigitated back contact (IBC) solar cell (figure 1.8) is unique in that the n-type and p-type contacts are both located on the rear side of the cell. In this device design, the p and n doped regions alternate across the rear side of the wafer. The benefit of having no front side contacts is that there is no metal shading so that the current can be maximized. Another benefit is that the contacts can be made much thicker with higher conductivity compared

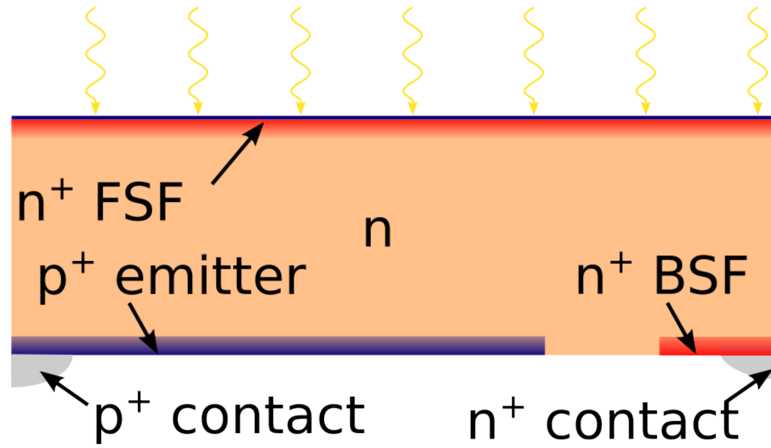

Figure 1.8: Device structure of an IBC solar cell

with cells that have front side contacts. This can help the fill factor and give higher cell performance. Because the contacts are located at the rear of the device, performance of the IBC cell is highly dependent on the minority carrier lifetime. For this reason n-type silicon is often used in manufacture of these devices because of the much lower capture cross section of holes compared with electrons for most defects. This task investigates the potential for a low cost screen printed IBC cell. To model such a cell, geometries of doped regions are kept large enough that they could be aligned to for metalization using todays screen printing technologies. Similarly, emitter and BSF doping levels are kept consistent with what is necessary for low contact resistance screen printed contacts. In these simulations, the doping level and dimensions of the emitter, back surface field (BSF) and front surface field (FSF) for high and low resistivity materials are optimized and show that this low cost IBC device design can also achieve efficiencies above 22%. This task demonstrates quantitatively the potential for several different high efficiency device designs that can be manufactured with lower cost technologies.

1.3.5 Task 5: Finding the practical limit of crystalline Si solar cells

In this task, an attempt to find find the practical efficiency limit of crystalline silicon solar cells is made. In order for a limit efficiency cell to be made all of the recombination mechanisms must be minimized. It is proposed that the appropriate device for this task is the point contact solar cell, which is a variation of the IBC cell only with point contacts

instead of line contacts. In order to approach the practical limit, a device is proposed which takes advantage of two new PV technologies, namely passivated contacts and the highly negatively charged dielectric aluminum oxide. The advantage of implementing these new technologies is quantified through numerical modeling. This device, when optimized is shown to be capable of reaching above 27% which is roughly 2% absolute lower than the Schockley-Queisser theoretical limit.

CHAPTER II

DEVICE PHYSICS OF SOLAR CELLS

2.1 Introduction

This chapter aims to give a review of the device physics of solar cells. Jenny Nelson gives a thorough review of this topic in her book *The Physics of Solar Cells* [5] and this review is organized in a similar layout and for the most part uses the same forms of the equations to highlight topics relevant to this thesis. In section 2.2 the solar resource is discussed followed by photocurrent, dark current, parasitic resistances and the two diode model of the solar cell. Together these topics give a basic understanding of how solar cells operate. Section 2.3 further explains the operation of P-N junction solar cells through a review of carrier generation and recombination, carrier diffusion, the transport equations and finally putting them all together for the complete picture of P-N junction solar cell operation.

2.2 Solar Cell Operating Principles

2.2.1 Energy From the sun

The sun is the most crucial resource we have on our planet, in one way or another most energy sources we have came from the sun. Plants can convert sunlight into energy stored in sugars, animals can then eat plants for the energy stored in those sugars and finally other animals can eat the plant eating animals for energy. Aside from energy from food, fossil fuels that power most of our daily energy needs come from decayed plant matter which survived on sunlight.

Our sun is essentially a very large hot ball of hydrogen gas powered by nuclear fusion reactions at the center. The spectrum of energy emitted by the sun is well approximated by assuming that it is a perfect black body and obeys Planck's radiation law. The spectrum emitted from the sun is characteristic of a 6000 K black body even though the core of the sun is approximated to reach temperatures of 20,000,000 K. This is because most of the light emitted from the sun's core is absorbed by Hydrogen ions near the sun's surface

which are then heated to roughly 6000 K [6]. The spectrum of available energy from the sun at the outer edge of the earth's atmosphere is referred to as the air mass zero, AM0, spectrum. This spectrum has an integrated power density of 1366.1 W/m^2. The two spectrums that are relevant here on the earth's surface are referred to as the AM1.5G and the AM1.5D spectrum. The AM1.5G spectrum includes direct and diffuse radiation and has an integrated power density of 1000 W/m^2, this spectrum is relevant for flat panel photovoltaics while the AM1.5D spectrum consists of only direct radiation from the sun and is applicable to concentrator photovoltaics. It has an integrated power density of 900 W/m^2 [7]. All three of these spectra may be seen in figure 2.1.

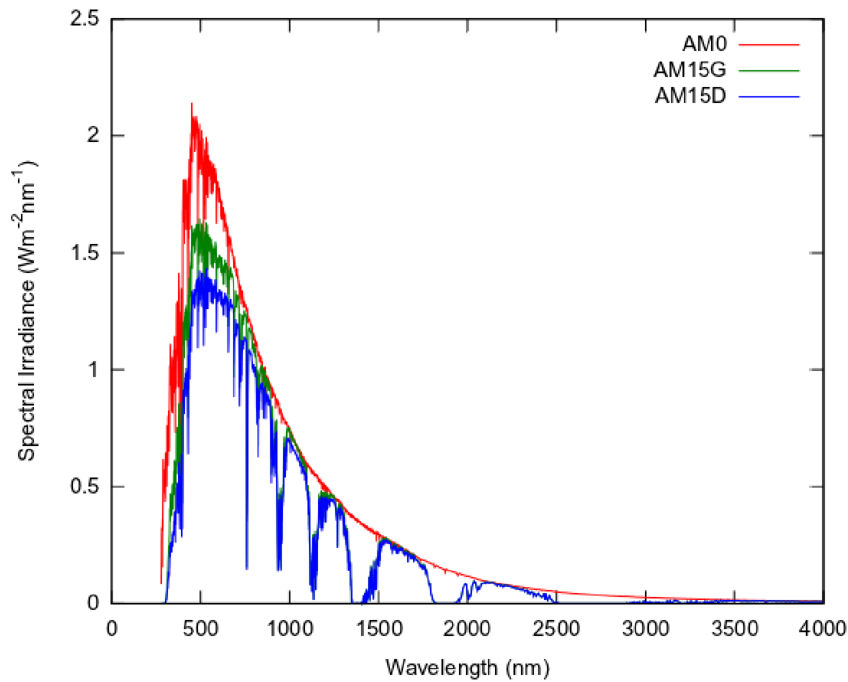

Figure 2.1: The AM0,AM1.5G and AM1.5D spectrums [8].

The sun is truly an amazing power source. According to NASA's atmospheric science data center, the sun transmits an average annual power of over 730,000 trillion kilowatt hours [9] to the earth's surface, while in 2009 the total global net energy consumption was only 17.3 tkWh [10], a mere .002% of the power incident on the earth's surface. Figure 2.2 shows the average annual global insolation (kWh/m^2/yr) in different parts of the world. It is a convenient coincidence that the U.S. and China, the worlds two largest power consumers

are both rich in solar insolation in regions of their territory. In fact five countries (U.S., China, India, Brazil, Australia) that consume over 48% of the worlds energy are blessed with high solar insolation [11]. Therefore, photovoltaics has the potential to provide energy where demand is the highest.

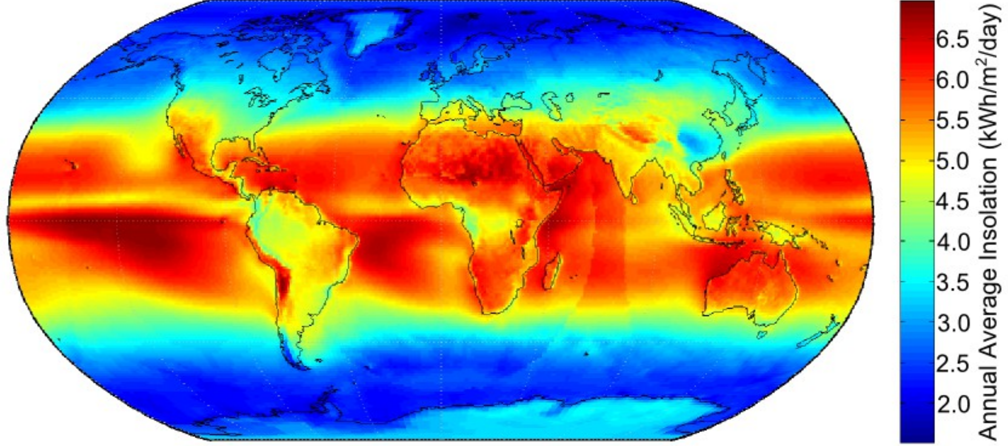

Figure 2.2: Global average annual insolation. Data from NASA [9].

2.2.2 Photocurrent in solar cells

When a solar cell is illuminated under the short circuit condition a photocurrent is generated which is proportional to the incident spectrum and the cell's external quantum efficiency (EQE). EQE(E) is the probability that a photon with energy E will be absorbed by the solar cell and excite one valence electron into the conduction band that is then collected before it recombines in the device. The J_{sc} is related to the incident spectrum and the EQE by relation 2.1.

$$J_{sc} = q \int b_s(E) EQE(E)\, dE \tag{2.1}$$

Where $b_s(E)$ is the incident spectrum between E and E+dE and q is the charge of an electron. Figure 2.3 shows photocurrent generation and collection in a typical Si p-n junction solar cell.

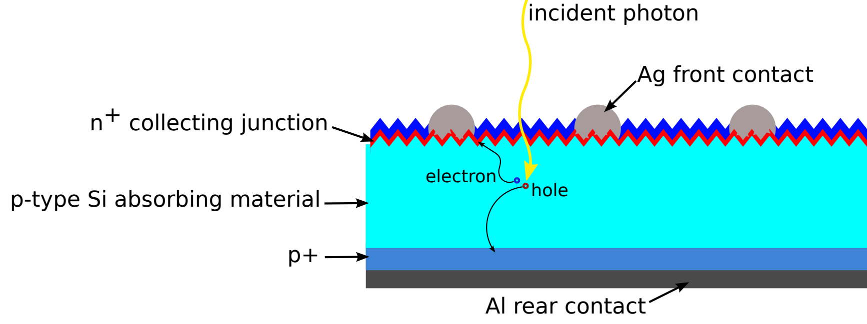

Figure 2.3: Current generation and collection in a typical Si solar cell.

2.2.3 The dark current

When a forward bias is applied across a solar cell, a potential difference develops between the front and rear contacts. This potential difference creates a current, usually called the dark current (J_{dark}), which is in the opposite direction of the photocurrent. Since a solar cell is essentially a large diode, it is rectifying and the dark current can be described by equation 2.2, where J_0 is a constant that is proportional to the total reombination in the device, V is the potential across the device, k_B is the Boltzmann constant and T is the temperature.

$$J_{dark} = J_0(e^{\frac{qV}{k_B T}} - 1) \tag{2.2}$$

The total current can then be approximated as the sum of the dark current and the photocurrent.

$$J_{Tot} = J_{sc} - J_{dark} \tag{2.3}$$

By definition, under open circuit condition the total current in the device is zero, therefore, we can define the open circuit voltage as the voltage at which J_{dark} and J_{sc} are equal. An expression for V_{oc} can be derived from equation 2.3 by substituting 0 for J_{Tot}, V_{oc} for V, and solving for V_{oc} which can be expressed as.

$$V_{oc} = \frac{k_B T}{q} \ln\left(\frac{J_{sc}}{J_0} - 1\right) \tag{2.4}$$

2.2.4 The light IV curve and efficiency

Figure 2.4 shows the light and dark JV curves for an ideal solar cell plotted using equations 2.2 and 2.3. At each point along the JV curve the power density is given by the simple

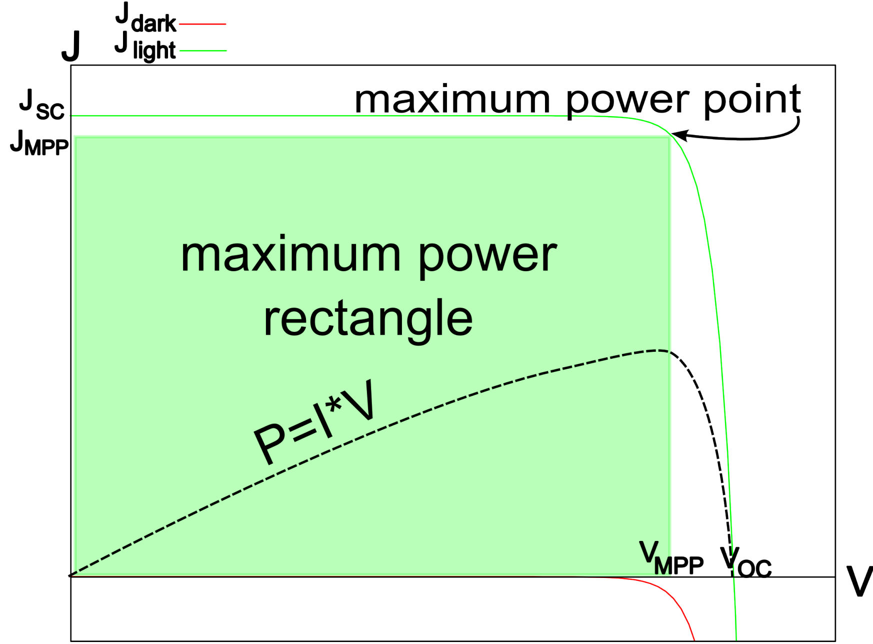

Figure 2.4: Light IV, Dark IV and Power vs V curves for an ideal solar cell.

relation seen in equation 2.6.

$$P = JV \tag{2.5}$$

The voltage at which the power is maximized is called the maximum power point and is often abbreviated by V_{MPP} and the current density at the maximum power point is abbreviated by J_{MPP}. The maximum power point is important to know because the solar cell efficiency, η, is given by the following relation.

$$\eta = \frac{P_{MPP}}{P_{in}} = \frac{J_{sc}V_{oc}FF}{P_{in}} \tag{2.6}$$

where the P_{in} is the incident power of the light shining on the cell and FF is the fill factor which is a measure of the squareness of the JV curve and is defined in equation 2.7.

$$FF = \frac{J_{MPP}V_{MPP}}{J_{sc}V_{oc}} \tag{2.7}$$

The product of the FF,J_{sc} and V_{oc} determines solar cell efficiency and are therefore the most important solar cell parameters. Solar cells are measured under standard test conditions which are the AM1.5G spectrum at 1000 w/m^2 at 25° C.

2.2.5 Parasitic Effects and The Equivalent Circuit of a Solar Cell

A solar cell can be modeled by the circuit shown in figure 2.5. R_s and R_{sh} are the series

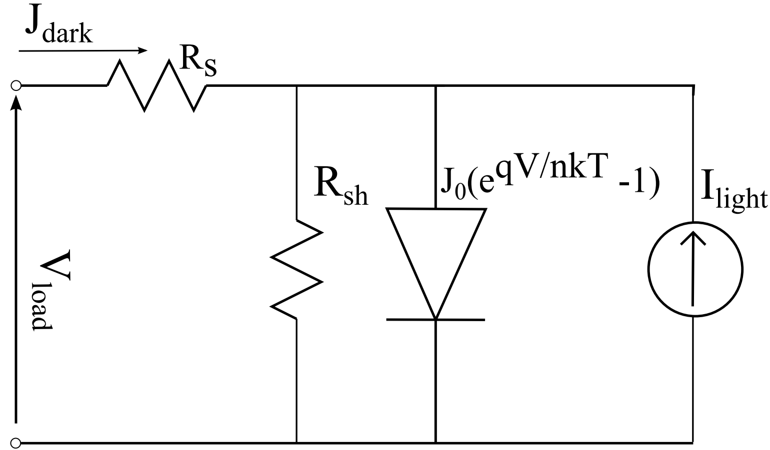

Figure 2.5: Equivalent circuit of a solar cell.

and shunt resistances, respectively, both are parasitic resistances that can reduce the fill factor of a solar cell. In describing the effects of these different pieces of the circuit on solar cell performance I will use the notation of Green in *SOLAR CELLS* [6]. The diode in the figure has reverse saturation current density J_0 and ideality factor of n. The diode allows the dark current to pass when under light-induced forward bias condition in the opposite direction of the photocurrent. Finally, the current source shown in figure 2.5 represents the photocurrent. In the rest of this section the physical cause of the elements shown in the circuit diagram and the effect they have on solar cell performance will be discussed.

Recombination in the depletion region of the junction can lead to non ideal behavior of the diode [12] and lower the fill factor. This effect is quantized in equation 2.8 which defines FF_0, the maximum possible fill factor with no series and shunt resistance.

$$FF_0 = \frac{v_{oc} - ln(v_{oc} + 0.72)}{v_{oc} + 1} \tag{2.8}$$

The v_{oc} is defined as the normalized V_{oc} and is given in equation 2.9

$$v_{oc} = \frac{V_{oc}}{\frac{nk_bT}{q}} \tag{2.9}$$

where n is called the diode ideality factor which is a measure of how ideally the diode performs.

The series resistance, R_s, is comprised of the combined resistance of carriers traveling through the back contact, substrate, emitter, contact interface, grid lines and busbars. A

high series resistance will lower the fill factor of a solar cell according to equation 2.10.

$$FF = FF_0(1 - r_s) \tag{2.10}$$

where r_s is the normalized resistance defined by equation 2.11 and R_{ch} is the characteristic resistance defined by V_{oc}/I_{sc}

$$r_s = R_s/R_{ch} \tag{2.11}$$

Similar to r_s, r_{sh} is defined as R_{sh}/R_{ch} and the expression relating the shunt resistance to the fill factor of a solar cell is given in equation 2.12.

$$FF = FF_0\left(1 - \frac{v_{oc} + 0.7}{v_{oc}}\frac{FF_0}{r_{sh}}\right) \tag{2.12}$$

To consider the series and shunt resistances' effect on the fill factor simultaneously, the FF from equation 2.10 can be substituted in for FF_0 in equation 2.12.

An alternative equivalent circuit of a solar cell is the so called two diode model and is very similar to the one diode model shown in figure 2.5 except that there are now two diodes instead of one. In this model the first diode will have an ideality factor of one and reverse saturation current density J_{01}, this represents the portion of the solar cell that behaves like an ideal diode. The second diode with ideality factor n_2 and reverse saturation current density J_{02} represents non-ideal diode behavior in the solar cell. The two diode model is frequently used in fitting dark-IV curves. A diagram of the two diode model can be seen in figure 2.6. Using the two diode model the total current density in the solar cell shown in

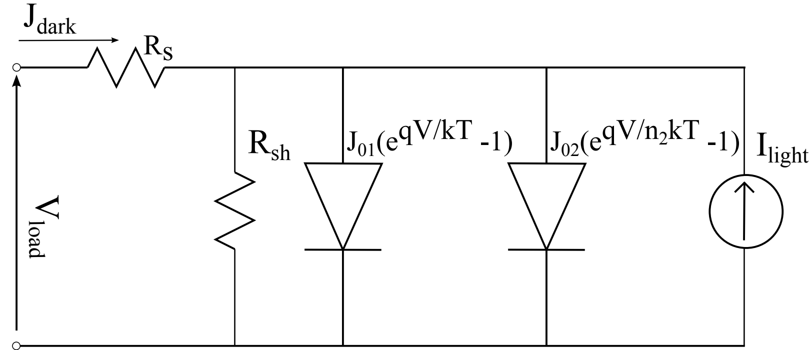

Figure 2.6: two diode model of a solar cell.

equation 2.3 can be modified to include R_s, R_{sh} and the second diode. This expression is

shown in equation 2.13

$$J_{Tot} = J_{sc} - J_{01}(e^{\frac{q(V+JR_s)}{k_BT}} - 1) - J_{02}(e^{\frac{q(V+JR_s)}{n_2k_BT}} - 1) - \frac{V + JR_s}{k_BT} \quad (2.13)$$

2.3 P-N junction solar cells

When light of sufficient energy is absorbed by a semiconductor solar cell a valence electron is given enough energy to escape the coulomb potential binding it. The electron is then free to move around the bulk of the semiconductor and the atom that contained the electron now has a net positive charge. An electron from a nearby atom can transfer to the atom with a net positive charge, in this way an positive charge can move around the bulk of a semiconductor in a similar manner as an electron. This moving positive charge is referred to as a hole. In a solar cell the goal is to separate and collect the electrons and holes at separate electrodes and provide the current to an external circuit. This section is a review of energy bands in semiconductors, mechanisms for carrier generation and recombination and carrier transport in semiconductors. There are many good books which review basic semiconductor physics for solar cells, this review follows the notation of *Handbook of Photovoltaic Science and Engineering* [13].

2.3.1 Energy bands in semiconductors

To understand the motion of an electron in a semiconductor we can treat the semiconductor as a three dimensional box with a periodic potential which is defined by the Coulomb potential of the atoms in the lattice. The behavior of the electron is described by it's wavefunction,Ψ, which can be found by solving the time-independent Scrödinger equation (2.14) [14].

$$-\frac{\hbar^2}{2m}\nabla^2\Psi(x,y,z) + V(x,y,z)\Psi(x,y,z) = E\Psi(x,y,z) \quad (2.14)$$

Where $\hbar$ is Planck's constant divided by 2π, m is the electron mass and V is the periodic potential of the atoms in the lattice. The solution to this differential equation will give the allowed energy levels. The Pauli exclusion principle causes these energy levels to split due to their close proximity in the lattice and gives rise to allowed energy bands. A fictitious example band diagram is shown in figure 2.7. The x axis of the figure is the wavevector, k,

which determines the electrons momentum when multiplied by $\hbar$. The blue and red regions show the conducting electrons and holes in the conduction and valence band respectively. When the maximum energy in the valence band is at the same wavevector as the minimum

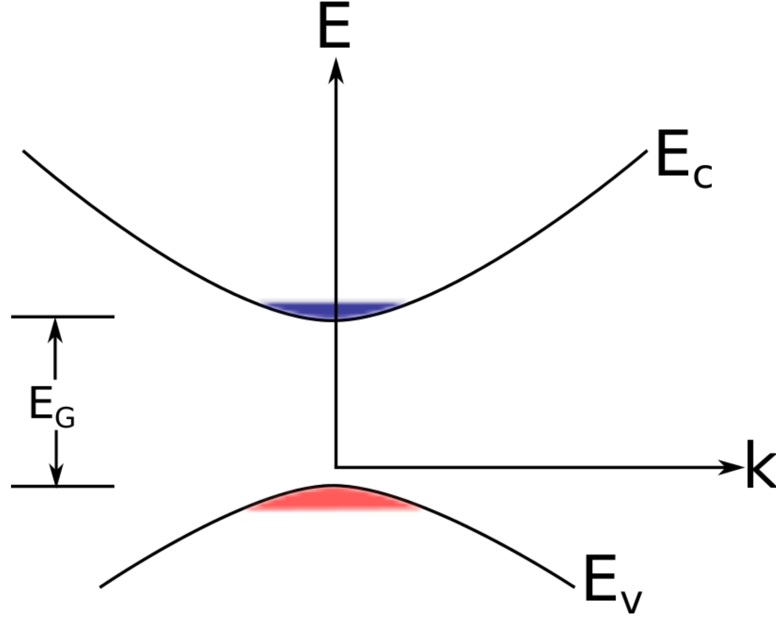

Figure 2.7: An example band diagram, not all allowed energy levels are shown. Bands with energies below the valence band energy are assumed to be full of electrons and bands above the conduction band are assumed to full of holes. The pink and blue regions represent conducting holes and electrons in the in the valence and conduction band respectively.

energy in the conduction band as shown in figure 2.7 the semiconductor is said to have a direct bandgap, when they lie at different wavevectors it is called an indirect bandgap. It is a interesting result that the motion of an electron in a periodic potential is similar to that of an electron in free space and obeys Newton's second law of motion with an effective mass ,m*, rather than the free electron mass.

$$F = m^* a \tag{2.15}$$

The effective mass defined by equation 2.16 is dependent on the shape of the band diagram and is not homogeneous for all wavevectors. Therefore, electrons and holes at different wavevectors respond differently to external fields.

$$m^* \equiv \left(\frac{d^2E}{dp^2}\right)^{-1} = \left(\frac{1}{\hbar^2}\frac{d^2E}{dk^2}\right)^{-1} \tag{2.16}$$

2.3.2 Densities of state and equilibrium carrier concentration

Using the effective masses of electrons and holes we can solve the time-independent Schrodinger equation to determine the density of states in each band. By using the effective mass we effectively take into account the periodic potential of the lattice atoms, therefore we just need to solve the Schrodinger equation for a particle in a box. The densities of states for the conduction and valence band are found to be

$$g_C(E) = \frac{m_n^* \sqrt{2m_n^*(E - E_C)}}{\pi^2 \hbar^3} cm^{-3} eV{-1} \tag{2.17}$$

and

$$g_P(E) = \frac{m_p^* \sqrt{2m_p^*(E_V - E)}}{\pi^2 \hbar^3} cm^{-3} eV{-1} \tag{2.18}$$

In a semiconductor, the probability of a state with energy E being occupied is given by the Fermi function,

$$f(E) = \frac{1}{1 + e^{(E-E_F)/kT}}, \tag{2.19}$$

where E_F is the Fermi energy, T is the temperature in Kelvin and k is the Boltzmann constant. $f(E)$ is shown in figure 2.8 for T=0 and 300 K. At absolute zero all the energy

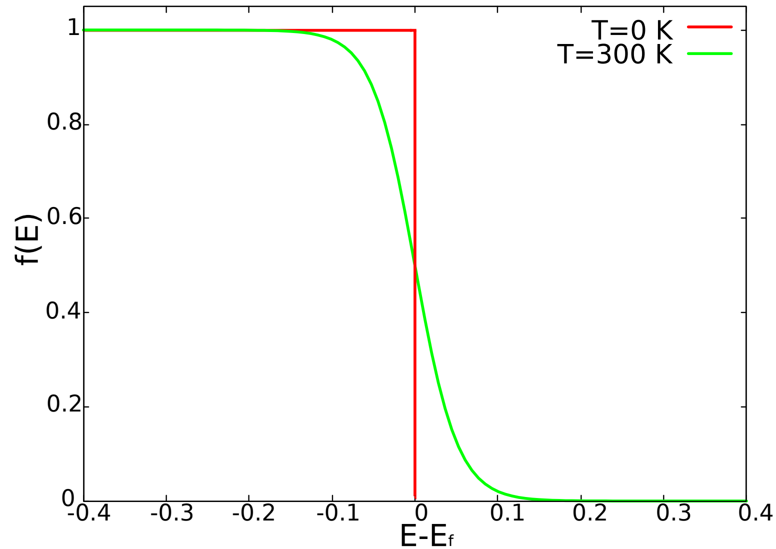

Figure 2.8: Fermi function at 0 and 300 K.

levels below the Fermi energy are occupied and all the levels above the Fermi energy are not. For temperatures above absolute zero, some carriers have enough energy to occupy

states above the Fermi energy, leaving some empty states beneath the Fermi energy. As the temperature increases the step-like shape of the Fermi function begins to round out. The equilibrium carrier concentration is then calculated by integrating the product of the density of states and the probability that state is occupied. Therefore, for electrons the equilibrium carrier concentration n_0 is given by

$$n_0 = \int_{E_C}^{\infty} g_C(E) f(E)\, dE = \frac{2N_C}{\sqrt{\pi}} F_{1/2}((E_F - E_C)/kT). \tag{2.20}$$

Similarly, for holes the equilibrium carrier concentration is given by

$$p_0 = \int_{E_C}^{\infty} g_C(E)(1 - f(E))\, dE = \frac{2N_V}{\sqrt{\pi}} F_{1/2}((E_V - E_F)/kT), \tag{2.21}$$

where $F_{1/2}$ is the Fermi integral of order 1/2, N_C is the effective density of states of the conduction band and N_V is the effective density of states of the valence band. The expressions for N_C and N_V are shown in 2.22 and 2.23.

$$N_C = 2(\frac{2\pi m_n^* kT}{h^2})^{3/2} \tag{2.22}$$

$$N_V = 2(\frac{2\pi m_p^* kT}{h^2})^{3/2} \tag{2.23}$$

when the Fermi energy is not close to either band edge the expressions for n_0 and p_0 can be approximated as

$$n_0 = N_C e^{(E_F - E_C)/kT} \tag{2.24}$$

and

$$p_0 = N_C e^{(E_V - E_F)/kT}. \tag{2.25}$$

In this circumstance the semiconductor is said to be non-degenerate and the product of the equilibrium electron and hole concentrations is constant with location in the semiconductor and is given by 2.26.

$$n_0 p_0 = n_i^2 = \sqrt{N_C N_V} e^{(E_V - E_C)/2kT} = \sqrt{N_C N_V} e^{-E_G/2kT} \tag{2.26}$$

If a semiconductor has no dopants it is called intrinsic and the number of electrons are holes are equal,$n_0 = p_0 = n_i$. An intrinsic semiconductors Fermi energy can be written as

$$E_i = \frac{E_V + E_C}{2} + \frac{kT}{2} ln\left(\frac{N_V}{N_C}\right). \tag{2.27}$$

The addition of dopants to a semiconductor can increase the number of electrons and holes available in the conduction and valence band. The most commonly used dopants in Si solar cells are boron and phosphorus, boron has one less electron than Si and therefore gives an acceptor state within the band gap when it takes a substitutional site in Si, where as phosphorus has an one electron more than Si and gives a donor state. The number of ionized donors and acceptors are given by

$$N_D^+ = \frac{N_D}{1 + g_D e^{(E_F - E_D)/kT}} = \frac{N_D}{1 + e^{(E_F - E_D')/kT}} \tag{2.28}$$

and

$$N_A^- = \frac{N_A}{1 + g_A e^{(E_A - E_F)/kT}} = \frac{N_D}{1 + e^{(E_A' - E_F)/kT}} \tag{2.29}$$

where g_D and g_A are degeneracy factors for the donor and acceptor sites. It is often assumed that all dopants are ionized, in this special case we can rewrite the Fermi energy as

$$E_F = E_i + kT \ln \frac{N_D}{n_i} \tag{2.30}$$

for n type semiconductors and

$$E_F = E_i - kT \ln \frac{N_A}{n_i} \tag{2.31}$$

in p type semiconductors. When semiconductors are very heavily doped the band gap can actually be narrowed which then in turn increases the equilibrium carrier density. The most accurate model for modeling band-gap narrowing in Si devices was presented by Schenk [15], The Schenk model takes into account band gap narrowing due to doping concentrations as well as excess carrrier concentrations due to optical generation or injection via applied bias.

2.3.3 Absorption and carrier generation

Absorption of light to free charge carriers is the most fundamental aspect of solar cells, without this mechanism no photovoltaic devices could exist. When a semiconductor's surface is illuminated with light of a given wavelength, the intensity of light within a distance x of the semiconductor surface is given by expression 2.32 [6].

$$I(x) = I_0 e^{-\alpha x} \tag{2.32}$$

I_0 is the intensity of light on the surface of the semiconductor and α is the wavelength dependent absorption coefficient. The absorption coefficient is proportional to the sum of all the all the possible electronic state transitions times the densities of states of the beginning and ending states. Absorption results in the creation of an electron hole pair. Because light has very little momentum and momentum must be conserved it is much harder to absorb light for indirect bandgap semiconductors compared to direct bandgap semiconductors for light with energy close to the band gap energy. For absorption of photons with energy close to the bandgap energy in a indirect bandgap semiconductor, a phonon with the correct momentum must be emitted or absorbed to conserve momentum between the initial and final states. An example of absorption in an indirect bandgap semiconductor like silicon is

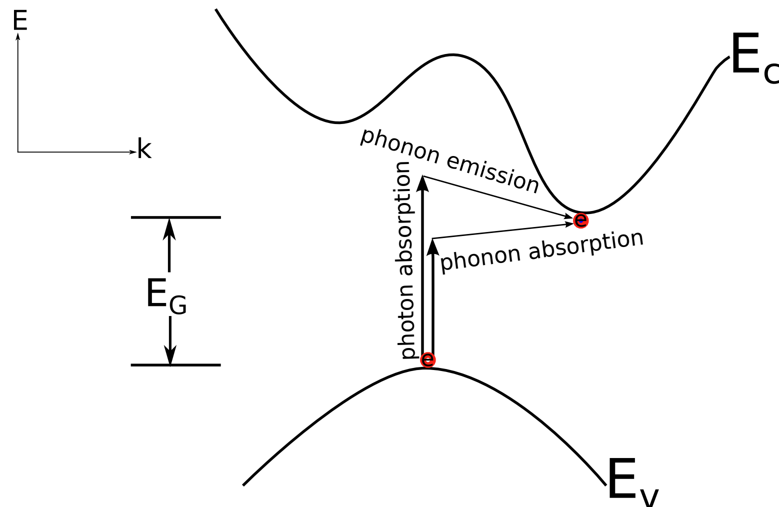

Figure 2.9: Absorption in an indirect bandgap semiconductor. Many transitions require simultaneous absorption of photons and phonon absorption or emission

shown in figure 2.9. It should be noted that absorption in indirect bandgap materials can take place without a phonon, however the photon energy must sufficient to excite an electron from a given wavevector in the valence band to the same wavevector in the conduction band.

The electron and hole generation rate caused by absorption of light as a function of depth into a solar cell is given by equation 2.33 [13].

$$G(x) = (1 - s) \int_{\lambda} (1 - r(\lambda)) f(\lambda) \alpha(\lambda) e^{-\alpha x} \mathrm{d}\lambda \tag{2.33}$$

Where s is factor to account for shading from the grid lines, r(λ) is the reflectance of the

solar cell, f(λ) is the incident photon flux and $\alpha(\lambda)$ is the wavelength dependent absorption coefficient.

2.3.4 Carrier recombination

After electrons and holes are generated within a semiconductor they can recombine with one another through several different mechanisms : through defects in the bandgap (commonly referred to as Schockley-Read-Hall recombination or SRH), Auger recombination and radiative recombination. These processes of recombination are shown in figure 2.10. For a

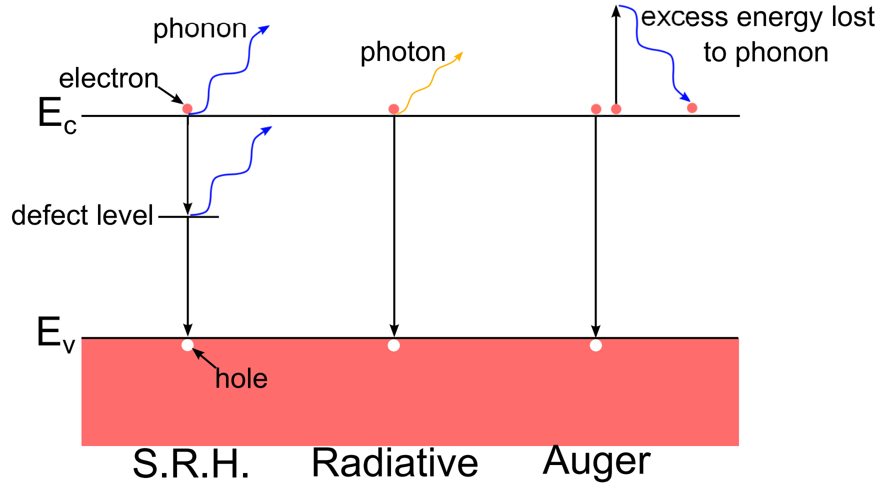

Figure 2.10: Diagram of S.R.H., Radiative and Auger recombination

defect level in the gap located at energy E_T, the Shockley-Read-Hall recombination can be expressed as

$$R_{SRH} = \frac{pn - n_i^2}{\tau_{SRH,n}(p + n_i e^{E_i - E_T/kT}) + \tau_{SRH,p}(n + n_i e^{E_T - E_i/kT})} \tag{2.34}$$

where $\tau_{SRH,n}$ and $\tau_{SRH,p}$ are the carrier lifetimes, $E_i$and n_i are the fermi energy and equilibrium carrier concentration in an intrinsic semiconductor respectively. The SRH lifetime can be expressed as

$$\tau_{SRH} = \frac{1}{\sigma v_{th} N_T} \tag{2.35}$$

where σ is the capture cross section of the trap, v_{th} is the thermal velocity of the carriers and N_T is density of traps. Therefore, large capture cross sections, high thermal velocities and large trap densities all decrease the carrier lifetime in semiconductors through SRH

recombination. It has been shown that SRH recombination could be dependent on the substrate doping level [16], in device simulations this is taken into account using the Scharfetter relation [17]

$$\tau_{SRH,dop} = \tau_{min} + \frac{\tau_{max} - \tau_{min}}{1 + \left(\frac{N_A + N_D}{N_{ref}}\right)^{\gamma}} \tag{2.36}$$

where γ and N_{ref} are fit parameters, τ_{max} and τ_{min} are the best and worst case carrier lifetimes and N_A and N_D are the bulk acceptor and donor levels.

Radiative recombination is essentially the inverse of absorption, it occurs when electrons in the conduction band recombine with holes in the valence band and emit a photon with an energy equal to the difference in energy of the starting and final states. This form of recombination is very important in direct bandgap semiconductors but not as important in indirect semiconductors since a phonon must also me absorbed or emitted for an electron to make the transition. This is one reason that we do not have lasers with silicon as the gain medium, because it has an indirect bandgap and it is difficult to make it emit radiation. The recombination rate for radiative recombination is give in equation 2.37

$$R_{\lambda} = B(pn - n_i^2) \tag{2.37}$$

where B is a material dependent constant. For n type semiconductors under low-level injection ($p_0 \leq p \ll n_0$) equation 2.37 can be approximated by expression 2.38.

$$R_{\lambda} \approx \frac{p - p_0}{\tau_{\lambda,p}} \tag{2.38}$$

The effective lifetime due to radiative recombination, $\tau_{\lambda,p}$, is given by equation 2.39

$$\tau_{\lambda,p} = \frac{1}{n_0 B} \tag{2.39}$$

Auger recombination can be thought of as the inverse process of impact ionization. In Auger recombination, an energy equal to the difference in the initial and final energy states is passed on to an electron or hole which becomes excited in the conduction or valence band respectively. The excited electron or hole then decays through phonon emission. Auger recombination is an important mechanism that dominates in highly doped regions of silicon

solar cells, it's net recombination rate can be expressed as

$$R_{Auger} = (C_n n + C_p p)(pn - n_i^2) \tag{2.40}$$

where C_n and C_p are the temperature dependent coefficients. We can simplify the Auger recombination expression if we assume low injection conditions and that C_n and C_p are of similar magnitude. In terms of an effective lifetime from Auger recombination (shown in equation 2.41)

$$\tau_{Auger,p} = \frac{1}{C_n n_0^2} \tag{2.41}$$

we can write the simplified expression for Auger recombination in an n-type semiconductor as follows.

$$R_{Auger} \approx \frac{p - p_0}{\tau_{Auger,p}} \tag{2.42}$$

A similar expression can be derived for p-type semiconductors.

The net recombination rate from these three recombination mechanisms is found simply by summing the rates of the individual processes

$$R_{Total} = R_{SRH} + R_{\lambda} + R_{Auger} \tag{2.43}$$

and the effective lifetime is similarly given in 2.44.

$$\frac{1}{\tau_{Total}} = \frac{1}{\tau_{SRH}} + \frac{1}{\tau_{\lambda}} + \frac{1}{\tau_{Auger}} \tag{2.44}$$

In addition to recombination centers in the bulk, electron and hole pairs can recombine at interfaces between two materials or at two grain boundaries of one material. Dangling bonds at the interfaces create allowed energy levels in the band gap for this special case of SRH hall recombination. The net expression for surface SRH recombination through all the surface defect states is given by [17]

$$R_{surf,SRH} = \frac{pn - n_i^2}{(n + n_1)/s_p + (p + p_1)/s_n} \tag{2.45}$$

where

$$n_1 = n_{i,eff} e^{\frac{E_{trap}}{kT}} \tag{2.46}$$

and

$$p_1 = n_{i,eff} e^{\frac{-E_{trap}}{kT}} \tag{2.47}$$

s_n and s_p are the doping dependent surface recombination velocities for electrons and holes, respectively. A schematic showing the recombination mechanism for surface SRH recombination can be seen in 2.11.

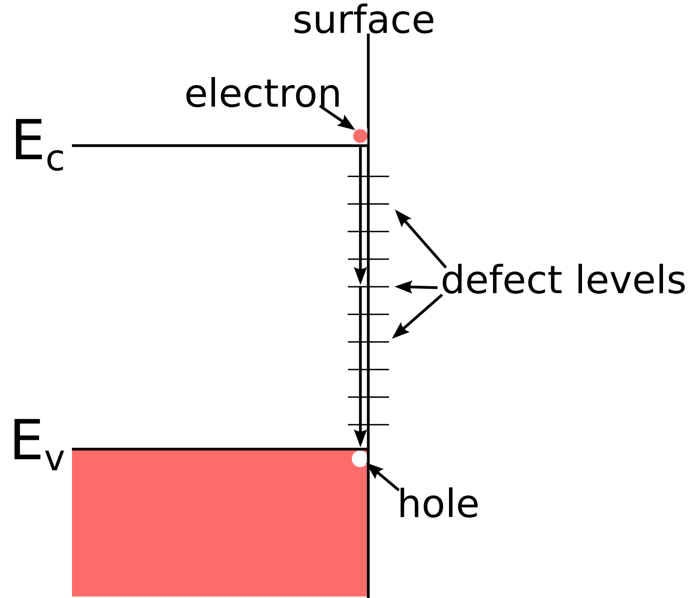

Figure 2.11: Surface recombination in semiconductors.

2.3.5 Carrier transport in semiconductors

The literature review in section 2.3 we established that electrons and holes behave similarly to free particles with effective mass m^*. It logically follows then that these electrons and holes should obey the classical laws of drift and diffusion. Drift is how carriers move in the presence of an electric field, electrons will drift in the opposite direction of the field due to their negative charge and holes will drift in the direction of the electric field. As the electrons and holes drift they are scattered off of lattice atoms, dopant atoms, lattice defects and other electrons and holes [13]. The net result is that on a macroscopic scale electrons and holes appear to move with a constant velocity called the drift velocity, v_d, in response to an electric field. The drift velocity is proportional to the applied electric field

but is scaled by μ, the carrier mobility.

$$|\vec{v_d}| = |\mu\vec{E}| = |\mu\nabla\phi| \tag{2.48}$$

The carrier mobility is in generally not dependent on the electric field strength within the regimes of operation of solar cells. Lattice scattering from phonons and ionized impurities are the largest scattering mechanisms, their effect on the carrier mobility can be approximated as

$$\mu_L = C_L T^{-3/2} \tag{2.49}$$

and

$$\mu_I = \frac{C_I T^{3/2}}{N_D^+ + N_A^-} \tag{2.50}$$

respectively. These two expressions for carrier mobility can be summed using Matthiessen's rule to find the net mobility.

$$\frac{1}{\mu} = \frac{1}{\mu_L} + \frac{1}{\mu_I} \tag{2.51}$$

When modeling silicon solar cells Klaassens unified mobility model is often used because it more precisely takes into account phonon scattering, impurity scattering as well as carrier-carrier scattering [18]. The current density due to carrier drift in an electric field can be expressed as

$$\vec{J}_p^{drift} = qpv_d = q\mu_p p\vec{E} = -q\mu_p p\nabla\phi \tag{2.52}$$

for holes, and

$$\vec{J}_n^{drift} = qnv_d = q\mu_n n\vec{E} = -q\mu_n n\nabla\phi \tag{2.53}$$

Through random thermal motion electrons and holes tend to move from regions of high carrier concentration to low through a process called diffusion. When no other forces are present the carriers will distribute themselves evenly through the substrate. This diffusion current is proportional to the gradient of the carrier densities and can be written as

$$\vec{J}_p^{diff} = qD_p\nabla p \tag{2.54}$$

for holes and as

$$\vec{J}_n^{diff} = qD_n\nabla n \tag{2.55}$$

for electrons, where D_n and D_p are the electron and hole diffusivity. In thermal equilibrium the net current must be zero, therefore in thermal equilibrium the drift and diffusion currents must be equal. This leads to the Einstein relationship which is valid in non-degenerate materials and can be expressed as

$$\frac{D}{\mu} = \frac{kT}{q} \tag{2.56}$$

Putting this all together we can write the total electron and hole current as

$$\vec{J}_n = -qD_n\nabla n + q\mu_n n\nabla\phi \tag{2.57}$$

and

$$\vec{J}_p = -qD_p\nabla p - q\mu_p p\nabla\phi \tag{2.58}$$

, then the total current in the device is expressed as

$$\vec{J}_{Tot} = \vec{J}_p + \vec{J}_n + \vec{J}_{disp.} \tag{2.59}$$

where $\vec{J}_{disp.}$ is the displacement current which is usually neglected in solar cells due to their dc operation.

2.3.6 The semiconductor equations

To find the equations that govern the behavior of semiconductor devices we need only to consider that charge must be conserved and that the poisson equation describes the electrical potential in the device. We can write the Poisson equation as follows

$$\nabla \cdot \varepsilon\vec{E} = q(p - n + N) \tag{2.60}$$

where N is the density of fixed charges in the substrate. We can write an expression for conservation of electrons and holes as

$$\nabla \cdot J_p = q(G - R_p - \frac{dp}{dt}) \tag{2.61}$$

$$\nabla \cdot J_n = q(R_n - G + \frac{dn}{dt}) \tag{2.62}$$

where G is the optical generation rate of electron-hole pairs and R_n and R_p are the electron and hole recombination rates. To accurately describe the current in a semiconductor device

we need to modify equations 2.57 and 2.58 to include ϕ_n and ϕ_p which are called the band parameters that take into account spatial variations in the band gap and electron affinity.

$$\vec{J}_n = -qD_n \nabla n + q\mu_n n \nabla(\phi + \phi_n) \tag{2.63}$$

$$\vec{J}_p = -qD_p \nabla p - q\mu_p p \nabla(\phi - \phi_p) \tag{2.64}$$

Equations 2.60,2.61 and 2.62 can be solved to determine the current voltage characteristics of a semiconductor device.

For a uniformly doped semiconductor the bandgap and permittivity are not position dependent as well as the carrier mobility and diffusion coefficients. In the steady state condition (solar cells operate in steady state), the semiconductor equations simplify to equations 2.65, 2.66 and 2.67.

$$\frac{d\vec{E}}{dx} = \frac{q}{\varepsilon}(p - n + N_D - N_A) \tag{2.65}$$

$$q\mu_p \frac{d(p\vec{E})}{dx} - qD_p \frac{d^2 p}{dx^2} = q(G - R) \tag{2.66}$$

$$q\mu_n \frac{d(n\vec{E})}{dx} + qD_n \frac{d^2 n}{dx^2} = q(R - G) \tag{2.67}$$

Under low level injection ($\Delta n = \Delta p \ll N$) in the regions far from the junction ($d\vec{E}/dx \approx 0$) the minority carrier recombination rate can be simplified to

$$R = \frac{\Delta n_P}{\tau_n} \tag{2.68}$$

and

$$R = \frac{\Delta p_N}{\tau_p} \tag{2.69}$$

for electrons in a p type semiconductor and holes in an n type semiconductor respectively, where Δn_P and Δp_N are the excess carrier concentrations. We can combine equations 2.68, 2.69 , 2.66 and 2.67 to write the minority carrier diffusion equations.

$$D_p \frac{d^2 \Delta p_N}{dx^2} - \frac{\Delta p_N}{\tau_p} = -G(x) \tag{2.70}$$

$$D_n \frac{d^2 \Delta n_P}{dx^2} - \frac{\Delta n_P}{\tau_n} = -G(x) \tag{2.71}$$

2.3.7 Electrostatics of a pn-junction

A pn-junction is formed when a p type semiconductor is brought into contact with an n type semiconductor. Since the density of electrons is much higher in the n type side than in the p type side, electrons will diffuse into the p type side of the semiconductor device until equilibrium is reached and the fermi energy is independent of position. Similarly, holes will diffuse into the n type side of the device. This diffusion leaves some of the dopant atoms ionized near the pn junction. These ionized dopants create a potential across the junction called the built in potential, V_{BI},and an electric field responsible for the rectifying behavior of pn-junctions. The electric field will sweep electrons across the junction from the p type side to the n type side, and holes from the n type side to the p type side. Further, the electric field prevents free carriers from staying in the region of the ionized dopants near the junction. Therefore, this region is called the depletion region or the space charge region. The rest of the device is approximately net neutral in equilibrium due to the diffusion of electrons and holes and is frequently called the quasi-neutral region. An example of a pn-homojunction (called a homojunction because both sides of the junction are made of the same semiconductor), it's charge density, electric field and band diagram are shown in figure 2.12 We can write Poisson's equation for this situation simply as

$$\nabla^2\phi = \frac{q}{\varepsilon}(n_0 - p_0 + N_A^- - N_D^+) \tag{2.72}$$

where n_0 and p_0 are the equilibrium electron and hole concentrations, N_A^- and N_D^+ are the concentrations of ionized acceptors and donors and ε is the permittivity of the semiconductor. If we assume that within the space charge region there are no free carriers and that within the rest of the device the net charge is zero (this is called the depletion approximation) then we can rewrite equation 2.72 for each region of the device shown in figure 2.12 as

$$\nabla^2\phi = -\frac{q}{\varepsilon}N_D^+ \tag{2.73}$$

for $-x_n < x < 0$,

$$\nabla^2\phi = \frac{q}{\varepsilon}N_A^- \tag{2.74}$$

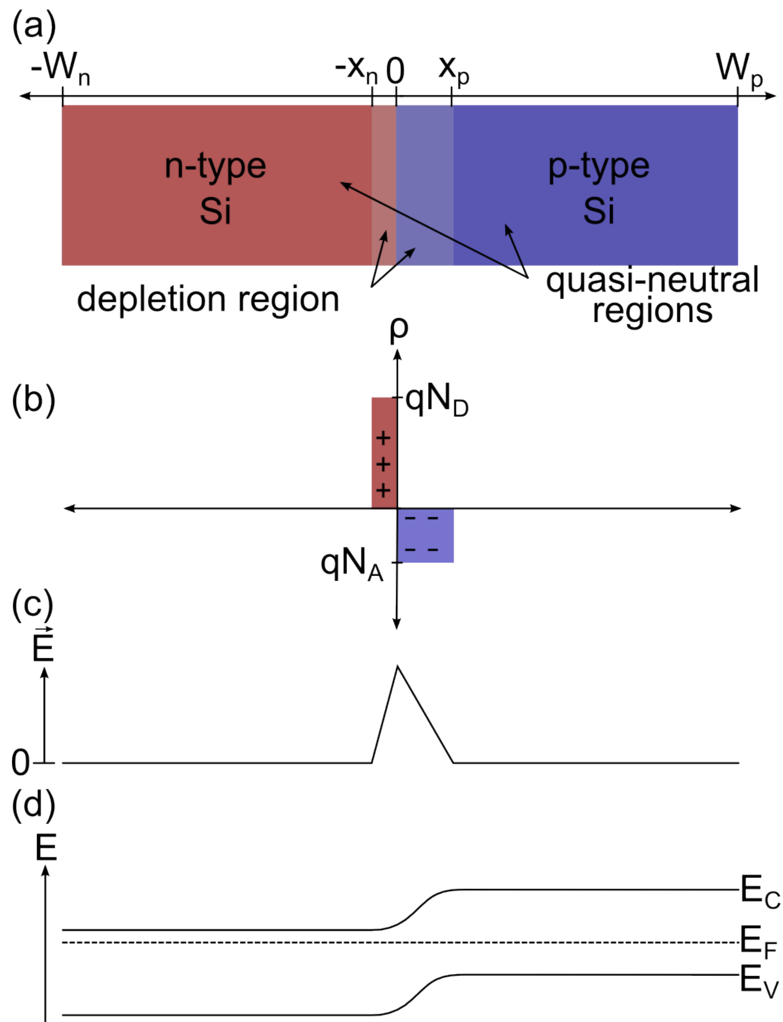

Figure 2.12: Diagram showing (a) a p-n junction with depletion and quasi-neutral regions, (b) the corresponding charge densities, (c) the electric field in the homojunction and (d) the band diagram

for $0 > x > x_p$, and

$$\nabla^2 \phi = 0 \tag{2.75}$$

for $x < x_n$and $x > x_p$. If we define the electric potential to be zero at $x = x_p$ and V_{BI} at $x = -x_n$, the electric potential is given the terms in table 2. From the continuity of the

Table 2.1: electrical potential in a 1D pn junction

$$\phi(x) = \begin{array}{cc} V_{BI} & x \leq -x_n \\ V_{BI} - \frac{qN_D}{2\varepsilon}(x + x_N)^2 & -x_n < x < 0 \\ \frac{qN_A}{2\varepsilon}(x - x_P)^2 & 0 > x > x_p \\ 0 & x \geq x_p \end{array}$$

electric potential and table 2.3.7 it can be shown that the total charge on either side of the depletion region is the same, therefore the depletion region extends further into the more lightly doped side of the device. The depletion width for the equilibrium (zero bias) case is given by

$$W_D = \frac{2\varepsilon}{q}\sqrt{\frac{N_A + N_D}{N_A N_D} V_{BI}} \tag{2.76}$$

and

$$W_D = \frac{2\varepsilon}{q}\sqrt{\frac{N_A + N_D}{N_A N_D} (V_{BI} - V_{App})} \tag{2.77}$$

with an applied bias.

The actual value for V_{BI} can be found by setting the drift and diffusion currents equal to each other since the net current under thermal equilibrium is zero. If we substitute $\vec{E}$ for $\nabla\phi$, this is written as

$$q\mu_p p_0 \vec{E} = qD_p \nabla p \tag{2.78}$$

for holes. Then using the Einstein relationship, $\vec{E}$ can be written as

$$\vec{E} = \frac{kT}{qp_0}\frac{dp_0}{dx}. \tag{2.79}$$

Upon integration we find the V_{BI} is given by equation 2.80.

$$V_{BI} = \frac{kt}{q} ln\left[\frac{N_D N_A}{n_i^2}\right] \tag{2.80}$$

2.4 Conclusions

This chapter has described the basics needed to understand solar cell operation as well as the parameters that are important in describing solar cell performance. A solar cell is merely a pn-junction which is made up of a small region devoid of free carriers called the depletion region and two regions that are net neutral but do contain free carriers. The more heavily doped of these two regions is called the emitter and the more lightly doped of the two is called the base. Solar cell behavior can usually be described by a two diode model in which one diode represents the ideal behavior of the device while the other takes into account non-ideal behavior. The series and shunt resistances are parasitic and reduce the solar cell fill factor and thus the efficiency. The dominant forms of recombination in silicon solar cells are Auger recombination in heavily doped silicon and SRH recombination for lightly doped silicon.

CHAPTER III

MULTIDIMENSIONAL MODELING OF SILICON SOLAR CELLS

3.1 Introduction and Review of Numerical modeling of solar cells

Multidimensional simulation of silicon solar cells provides a way to optimize device geometries and doping levels more quickly than by experimentation. Additionally, simulation experiments do not require material cost as fabrication experiments would. These simulations can also be used to analyze electrical and optical loss mechanisms quickly and reveal information that would be impossible or very difficult to obtain experimentally. Multidimensional models are necessary to accurately model solar cells because lateral and vertical currents in the device can not both be accounted for in a 1D model. In most cases a 2D simulation domain is sufficient because of device symmetry, however some device architectures require a 3D domain. The general strategy when simulating solar cells is to find the smallest repeating unit cell of the device. Minimizing the size of the structure which will decrease the total number of nodes and the simulation time.

Numerical modeling of Si solar cells dates back to 1967 when Gwyn *et al* at Sandia National Labs modeled the effect of radiation on solar cell performance for space applications [19]. This finite differences model was extended by Fossum to simulate a conventional 11.8% efficient solar cell (a standard efficiency at the time). This model identified efficiency limiting areas in the solar cell and demonstrated a feasible path to over 20% through cell design enhancements [20]. By the early 1980's two-dimensional simulation was possible. Gray *et al* at Purdue developed a model they called SCAP2D and used it to explore two dimensional effects in solar cells at high light intensities [21]. By the mid 1980's personal computers had become powerful enough that they could solve the semiconductor equations, using a software developed at Iowa State University called PC1D [22]. Unlike most other previous programs which use the finite difference method to solve the coupled semiconductor equations, PC1D uses the finite element method (FEM). PC1D has become widely

adopted in the photovoltaics industry , but is limited to one dimensional simulations and uses Boltzmann statistics along with dated models describing band gap narrowing and mobility. Today, PC1D is still the most widely used simulation tool in the photovoltaics community despite it's shortcomings. For multidimensional simulations today the simulation software Sentaurus [17] is the most widely used in solar cell simulations, however, COMSOL Multiphysics has also been adapted to model solar cells [23, 24]

Numerical models have been used to explore a variety of different solar cell designs. Loss mechanisms in industrial type solar cells limit the cell performance have been quantized using a numerical model with a distributed grid model [25]. These simulations involve two steps, one which calculates the IV curve of a unit cell and another which uses that IV curve as a voltage controlled current source which can then be connected in series by resistors to construct a full solar cell, rather than just modeling the unit cell. The results of these simulations place the maximum attainable efficiency of Full Al BSF cells around 19%. This same two step simulation approach has led to world record efficiency solar cells through the minimization of series resistance in passivated emitter rear locally diffused (PERL) solar cells [26]. Further, emitter wrap through (EWT), thin film IBC and heterojunction solar cells been investigated using Sentaurus [27, 28, 29]

In this work a schottky-barrier model is applied to Ag screen printed contacts to accurately predict contact resistance. Additionally, an optimization of IBC cells to approach the Schockley-Queisser limit is presented. Further, modeling of a new cell structure, an IBC with a selective emitter, is introduced. We explore the effect of the substrate doping, bulk lifetime and surface recombination and determine that efficiencies of 22.7% can be achieved with this device design. Two dimensional simulations are used to optimize the efficiency of a screen printed IBC cells through variations in the front surface field, back surface field emitter, bulk resistivity as well as the contact geometry. These simulations combine 3D ray tracing to create an optical generation profile which is then used in a 2D device simulation. Separating the optical and electrical simulations reduces computation times by only having to compute the time intensive ray tracing step once.

3.2 The Finite Element Method

As previously mentioned, the most commonly used software to simulate semiconductor devices including solar cells is Sentaurus. Sentaurus solves the semiconductor equations (equations 2.65,2.66,2.67 using current densities 2.63,2.64) using the FEM which has the advantage of being able to handle nonuniform meshes and geometry easily over other methods such as the finite difference method [30]. The FEM has been employed in many diverse problem area besides semiconductor devices such as stress analysis, fluid flow analysis, thermal analysis and fluid flow analysis to name a few [31]. This section provides a broad overview of the FEM.

Generally applying the FEM to any problem involves four steps [32].

- The domain is discretized into subregions or elements
- The governing equations for each element must be derived
- All of the elements must be assembled in the solution region
- The system of equations are solved.

The goal of the first step is to divide the domain into elements that are much smaller and cover the whole domain without overlapping . The geometry of the elements is usually triangular or quadrilateral.Figure 3.1 is an example of a discretized domain using a triangular mesh to connect the nodes within the domain.

An interpolation function, V_i, which approximates the unknown function to be solved for is defined within each element. Together the elements comprise the solution for the entire domain. Equation 3.1 is a first order interpolation function for a triangular mesh element using electric potential, V, as an example.

$$V_i(x, y) = a + bx + cy \tag{3.1}$$

Where a, b and c are constants to be solved for. V_i must vanish outside of element i but is generally non-zero within it. The electric potential for the whole domain is then

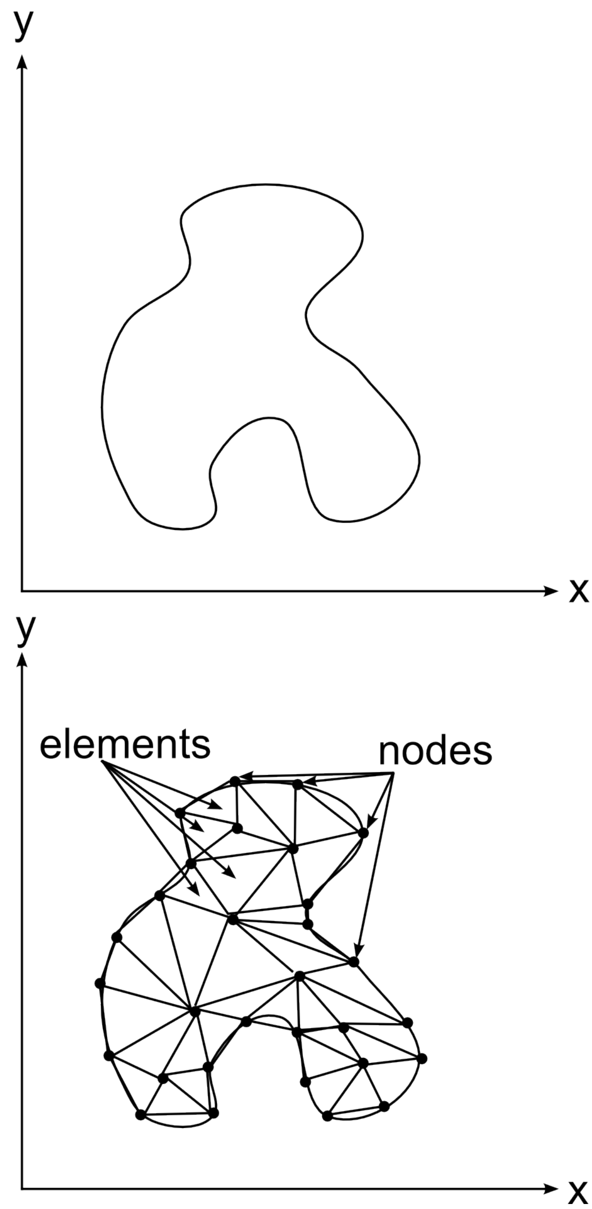

Figure 3.1: (top) The entire domain of interest for simulation. (bottom) The discretized approximation of the domain.

approximated as equation3.2.

$$V(x,y) \backsimeq \sum_{i=1}^{N} V_i(x,y) \tag{3.2}$$

For a semiconductor device this process must be completed to solve for the electric potential and the electron and hole quasi-fermi levels (the electron and hole quasi-fermi levels determine the electron and hole density, respectively). The determination of the parameters a, b and c is then the main key to finding the approximate solution over the whole domain. Once the parameters for each element are known, the solution for the whole domain can be assembled. Solving the equations usually uses the Bank/Rose method [30] with an iterative 'plug-in' method. In this method the electric potential is solved using the Poisson equation in all N elements first [33]. That electric potential is then plugged into the electron continuity equation to find the electron quasi-fermi level. Finally the calculated electric potential and electron quasi-fermi level are plugged into the hole continuity equation to find the hole quasi-fermi level. This process is repeated until the desired level of convergence is achieved.

3.3 Physical Models used in Device Simulation

The accuracy of the simulation results are only as accurate as the physical models used in the device simulation. Therefore, choosing the correct physical models is paramount for obtaining accurate results. A quite thorough review on this topic is given by Altermatt in [34]. Important models for accurate simulation of solar cells are carrier statistics (Fermi-Dirac vs Boltzmann), SRH recombination, Auger recombination, surface recombination, intrinsic carrier concentration and band gap narrowing. This section gives a review of implementations of physical models for device simulations. For a review of the physics of these models see chapter 2.

3.3.1 Carrier Statistics

For doping densities above 10^{19} Fermi-Dirac statistics must be used because the carrier density is high enough for the Pauli exclusion principle to take effect, this effect is referred to as Pauli blocking [35]. Usually the heavily doped n^+ emitter is in the regime where Fermi-Dirac statistics are necessary. In this regime we calculate the electron density, n,

using

$$n = N_c F_{1/2}(\frac{E_{fn} - E_c^0 + \Delta E_c}{kT}), \tag{3.3}$$

where N_c is the conduction band effective density of states, $F_{1/2}$ is the Fermi integral of order 1/2, E_c^0 is the intrinsic conduction band edge , ΔE_c is the shift in the conduction band edge due to band gap narrowing, k is the Boltzmann constant and T is the absolute temperature. The hole density in the emitter is much lower and can therefore be approximated accurately using Boltzmann statistics.

$$p = N_v exp(\frac{E_{fp} - E_v^0 + \Delta E_v}{kT}) \tag{3.4}$$

The symbols in equation 3.4 have the equivalent meaning as their counterparts in equation 3.3. Combining equations 3.4 and 3.3 the pn product is easily obtained.

$$pn = N_c N_v F_{1/2}(\frac{E_{fn} - E_c^0 + \Delta E_c}{kT}) exp(\frac{E_{fp} - E_v^0 + \Delta E_v}{kT}), \tag{3.5}$$

With some algebra, equation 3.5 can be rearranged in a more meaningful form.

$$\begin{aligned} pn &= n_i^2 \frac{F_{1/2}(\frac{E_{fn}-E_c^0}{kT})}{exp(\frac{E_c^0-E_{fn}}{kT})} \frac{F_{1/2}(\frac{E_{fn}-E_c^0+\Delta E_c}{kT})}{F_{1/2}(\frac{E_{fn}-E_c^0}{kT})} exp(\frac{\Delta E_v}{kT}) exp(\frac{E_{fn} - E_{fp}}{kT}) && (3.6) \\ &= n_i^2 \times exp(\frac{\Delta E_v}{kT}) \times exp(\frac{E_{fn} - E_{fp}}{kT}) \times \gamma_{deg} \times \gamma_{BGN} && (3.7) \end{aligned}$$

The increase in carriers due to band gap narrowing is taken into account by the γ_{BGN} term and the degeneracy factor γ_{deg} calculates how much the pn product deviates from an ideal gas. For lowly doped regions γ_{BGN} and γ_{deg} become 1 and Boltzmann statistics accurately predict the pn product. Figure 3.2 shows the error in the pn product introduced by using Boltzmann statistics in highly doped P emitters as well as the effect of γ_{BGN} and γ_{deg}. The recombination rates of SRH recombination, Auger recombination, radiative recombination and surface recombination (see section 2.3.4 for more details on the recombination models) all depend on the pn product. Especially Auger recombination which has a quadratic dependence on the carrier density. It is therefore critical to use Fermi-Dirac statistics when modeling heavily doped Si regions. Using Boltzmann statistics, it is possible to match the total recombination in a heavily doped region if the surface recombination is held as a free parameter. This process however, does not match the relative contributions of the total

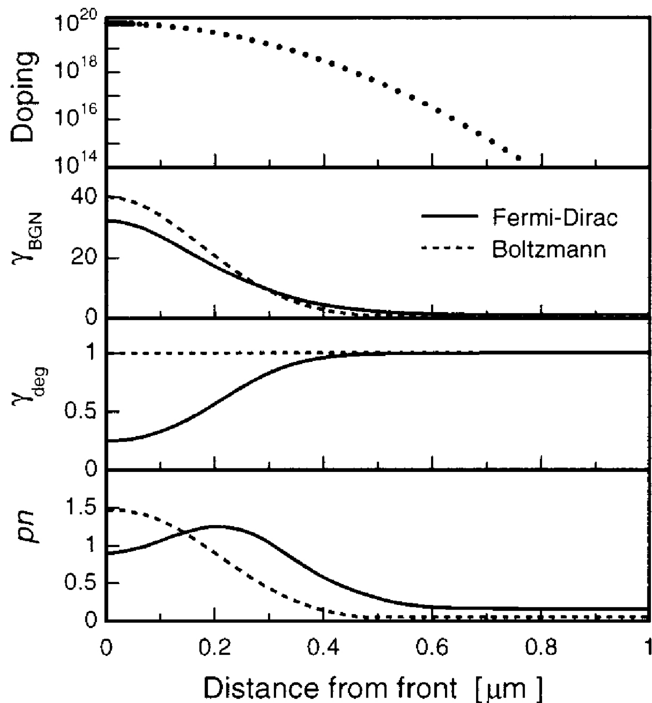

Figure 3.2: γ_{BGN},γ_{deg} and the pn product for a heavily doped n^+ profile. Taken from [35].

recombination from each type of recombination and thus the information extracted from this process is not meaningful.

3.3.2 Band Gap Narrowing

The importance of the carrier densities and their dependence on band gap narrowing was demonstrated in section 3.3.1. Having an accurate model to determine the band gap narrowing is obviously a necessary step to determine the correct carrier densities. The model of Schenk was derived from a non-self consistent finite temperature full random-phase approximation formalism [15]. The Schenk model calculates the conduction and valence band energies separately rather from quantum mechanical principles as opposed to deriving band gap narrowing from transport measurements on highly doped Si [36]. Additionally, the Schenk model distinguishes between free carrier or plasma-induced and dopant induced band gap narrowing, which is especially important in solar cells with many injected carriers from optical absorption. The band gap narrowing for this model is the sum of two parts, an exchange correlation part which is temperature and plasma density dependent and an ionic

part which is dependent on the activated doping concentration, the plasma density and the temperature. Figure 3.3 compares the Schenk model with other band gap narrowing models based on Boltzmann statistics. The Slotboom [37] and Del Alamo [38] models are based

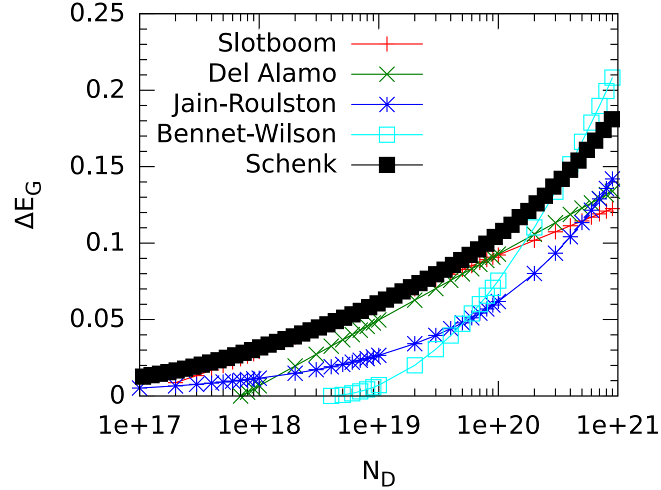

Figure 3.3: Comparison of various band gap narrowing models with the Schenk model.

on apparent band gap narrowing data from electrical measurements and are incompatible with Fermi statistics because the degeneracy factor is not distinguished from from band gap narrowing.

3.3.3 Schockley Read Hall Recombination

Recombination in the forbidden gap through defect levels is well described by SRH theory described in section 2.3.4. Defect levels created by boron and oxygen limit SRH lifetime in in Cz grown Si after illumination, this effect is known as light induced degradation or LID. This defect has been shown to be created by substitutional boron and interstitial oxygen dimer which form BO_2 [39]. Boron and oxygen concentrations have been shown to predict stable carrier lifetimes after illumination by Bothe *et al* [40] by the parametrization

$$\tau_{SRH} = 7.675 \times 10^{45} [B_s]^{-0.824} [O_i]^{-1.748} \tag{3.8}$$

where B_s is the substitutional boron concentration and O_i is the interstitial oxygen concentration. After $POCl_3$ diffusion the lifetime increases by a factor of 2-3.5 as a result of decreased oxygen dimer concentration with thermal cycling [41]. Equation 3.8 can be taken

Table 3.1: Auger recombination coefficients

	n	p	
A	2.8×10^{-31}	7.91×10^{-32}	cm^6/s
B	0	-1.29×10^{-32}	cm^6/s
C	0	3.231×10^{-32}	cm^6/s
H	8	8	
N_0	2.5×10^{17}	2.5×10^{17}	cm^{-3}

as an upper bound for lifetimes in multicrystalline materials, however other crystallographic defects keep the lifetime well below this limit.

3.3.4 Auger Recombination

The auger recombination rate (equation 2.40) is determined by the electron and hole densities along with the temperature dependent coefficients C_n and C_p shown in equations 3.9 and 3.10.

$$C_n(T) = \left(A_{A,n} + B_{A,n}\left(\frac{T}{T_0}\right) + C_{A,n}\left(\frac{T}{T_0}\right)^2\right)\left[1 + H_n e^{-n/N_{0,n}}\right] \tag{3.9}$$

$$C_p(T) = \left(A_{A,p} + B_{A,p}\left(\frac{T}{T_0}\right) + C_{A,p}\left(\frac{T}{T_0}\right)^2\right)\left[1 + H_p e^{-p/N_{0,p}}\right] \tag{3.10}$$

In equations 3.9 and 3.10 T_0 is 300K and the term $1 + H_n \exp -n/N_{0,n}$ is to take into account exciton decay at high carrier densities. Dziewior and Schmid measured C_n and C_p at 77K, 300K and 400K [42], a parameterization of their results are seen in table 3.3.4 [34]. Auger recombination is still an area where further understanding is required. Dziewior and Schmid's Auger coefficients were determined at high carrier densities where the electrons and holes can be considered to be in an ideal gas because of the screening. As a result their Auger coefficients are independent of dopant density. However, at lower carrier densities such as around 10^{18} cm^{-3} the screening effect is diminished and electrons and holes are attracted to one another resulting in higher Auger coefficients. The are a few parameterizations of this effect [43, 44], but none have been implemented into device simulation software.

Table 3.2: Fit Parameters for Surface Recombination Velocity on P diffused surfaces. Fit parameters by Altermatt [35].

	P_{planar}	$P_{textured}$
S_1	500	2800
N_1	1×10^{19}	1×10^{19}
γ_1	0.6	0.6
S_2	60	300
N_2	1×10^{19}	1×10^{19}
γ_2	3	3

3.3.5 Surface Recombination

Surface recombination is determined by carrier densities and the surface recombination velocity, SRV (see equation 2.45). The surface recombination velocity is doping dependent and is calculated in Sentaurus Device using equation 3.11

$$S = S_0\left(1 + S_{ref}\left(\frac{N_{dop}}{N_{ref}}\right)^{\gamma}\right) \tag{3.11}$$

where S_0, S_{ref}, N_{ref} and γ are user defined parameters and N_{dop} is the surface doping concentration. However, Altermatt *et al* found that existing data for SRV vs N_{dop} for P diffused surfaces passivated by various dielectrics is better fit by the double exponential expression [35]

$$S = S_1\left(\frac{N_{dop}}{N_1}\right)^{\gamma_1} + S_2\left(\frac{N_{dop}}{N_2}\right)^{\gamma_2}. \tag{3.12}$$

All the the parameters in equation 3.12 other than N_{dop} are dependent on the surface (textured vs planar), the passivating dielectric and the doping species. The functional form of equation 3.12 can be achieved in Sentaurus Device by setting S_{ref} equal to zero in equation 3.11, and creating a script to calculate 3.12 and setting it as S_0. The parameters to fit equation 3.12 for planar and textured phosphorus diffused surfaces is shown in table 3.3.5. For B diffused surfaces the same model can be used but the charge of the dielectric layer must be included [45, 46].

3.3.6 Carrier Mobility

For modeling carrier mobility in crystalline silicon solar cells Klaassen's mobility model is most often used because it a physics-based model that describes majority and minority carrier mobility and includes impurity screen by charge carriers, temperature dependence, electron-hole scattering as well as clustering of impurities[18]. The Klaassen model fits existing data in boron doped silicon very well but there are some uncertainties in the very high doping range of phosphorus doped silicon due to clustering of phosphorus precipitates which is not included in the model [34]. There are also uncertainties of the carrier mobility low doping range of phosphorus doped silicon due to differences in reported mobility values.

3.4 Application of Ray Tracing Simulations for Calculating Optical Generation for Textured silicon

3.4.1 Simulation Details

To accurately model the performance of a solar cell the generation profile of carriers within the substrate must be known. In this thesis a 2D approximation of pyramidal texture is used in sentaurus device [47] to perform a ray tracing simulation. The effect of the silicon nitride anti-reflection coating is taken into effect using the transfer matrix method while the rest of the simulation is carried out using ray tracing. The domain for the simulations is shown in figure 3.4.1. The side walls of the domain are 100% reflective while the bottom surface uses the Phong [48] rough surface scattering model to emulate the reflectance of the silicon/screen printed aluminum interface. In the simulation, raytracing of each specified wavelength is carried out and then the generation is weighted by the insolation in the AM15G spectrum. The parameters used in the simulations are shown in table 3.4.1. The strategy used to find an accurate generation profile is to optimize the ray tracing simulation parameters so that the simulated reflectance curve matches the experimentally measured one.

3.4.2 Results

The effect of the rear surface reflectance in the Phong model on the total reflectance curve is shown in figure 3.5. Before 950 nm the simulated reflectance curves are identical because the

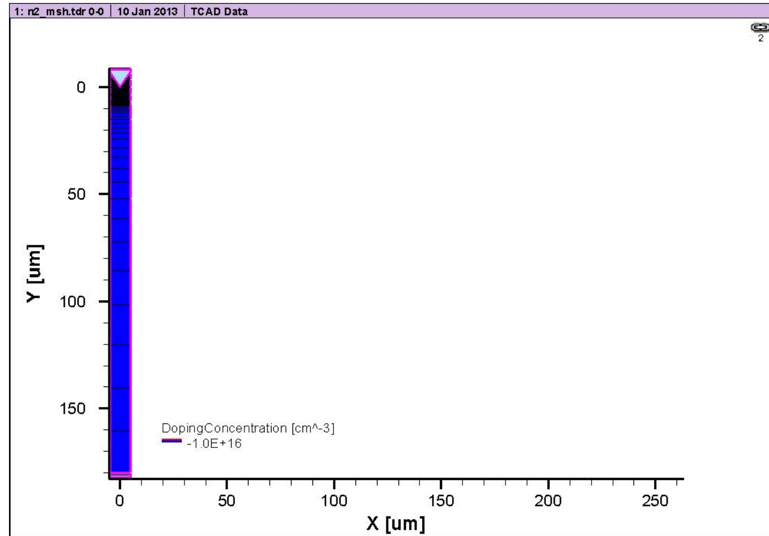

(a)

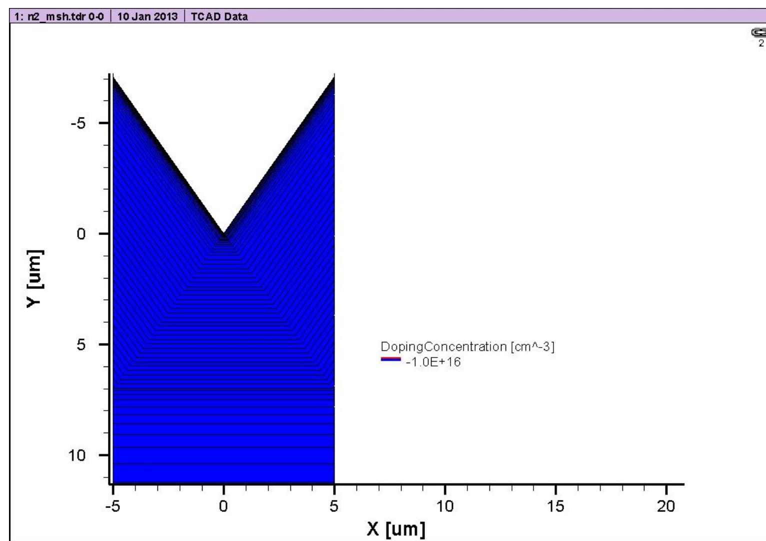

(b)

Figure 3.4: Image of the whole 2D domain used for ray tracing (a) and a zoomed in view near the top textured region (b).

Table 3.3: Parameters used in optical generation calculation

Number of rays per wavelength	20000
Phong reflection coefficient	varied 0.4-0.75
Wavelength range	300-1200nm
Wavelength step size	10nm
Silicon nitride n-k	n=2.15 Duttagupta *et al.* [49]
Silicon nitride thickness	750 Å
Silicon n-k	Green *et al.* [50]
Substrate Thickness	180 μm

reflectance of the top surface is identical and the silicon absorption coefficient is too great for a ray to traverse through the substrate reflect off the rear surface and escape through the front surface. However at longer wavelengths, this effect is common and is known as escape reflectance. As the back surface reflectance increases the escape reflectance increases and a back surface reflectance of 0.55 matches well with the experimentally measured curve in the long wavelength regime.

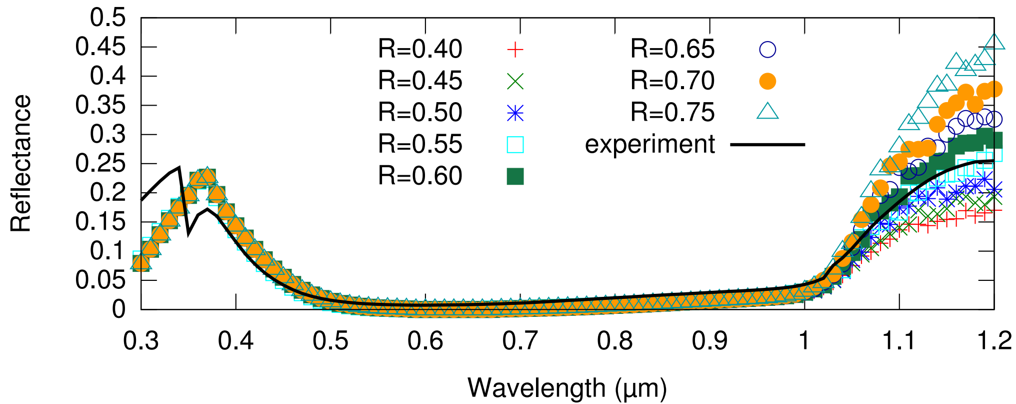

Figure 3.5: Effect of varying the back surface reflectance on solar cell reflectance.

The previous simulations determined that the correct back surface reflectance to match a textured, SiN coated wafer with a full Al BSF is R=0.55. The next goal is to match the rest of the reflectance curve which is determined by the reflectance properties of the front of the wafer. In these simulations the back surface reflectance was fixed at 0.55 but the SiN thickness was varied from 700 to 800 nm and the index of the SiN was varied from 1.92 to 2.15 using tabulated n-k values from Duttagupta *et al* [49]. The results of

the simulations are shown in figure 3.6. It can be seen from figure 3.6 that increasing this SiN index shifts the minimum in the reflectance curve towards longer wavelengths as we would expect from theory. Further, increasing the SiN thickness also shifts the minimum towards longer wavelength. We find the index and thickness that most closely match the experimentally determined reflectance are a thickness of 76 nm and an index of 2.03.

Thus far the ray tracing simulations have been optimized to match the front and rear surface reflectance by varying the SiN index and thickness and the reflectance coefficient of the phong model respectively. However, the simulated escape reflectance data looks noisy. In these simulations an attempt to smooth out the escape relfectance portion of the relfectance curve is carried our by increasing the number of rays used in the ray tracing simulations. The number of rays per wavelength used is varied from 20000 to 1000000 keeping all other parameters equal to the previously determined ones that give the closest match to the experimental curve. The results of the simulations are shown in 3.7. The escape reflectance becomes more smooth with additional rays, however, the total amount of absorbed current density is basically unchanged with only a variation of 0.005 mA/cm^2 which is only 0.01% of a typical device short circuit current density of 37.5 mA/cm^2.

Even after optimizing the SiN index and thickness as well as the rear surface reflectance and number of rays there is still a considerable difference between the simulated and actual reflectance curves, mostly between 50 and 100 nm. This difference is attributed to the error in the reflectance measurement which is about 1% absolute at best if the tool has just been calibrated. The measured minimum reflectance is only 0.0074 while it should be zero at the minimum due to destructive interference. The total current density absorbed for the simulation with 1,000,000 rays was found to be 40.01 mA/cm^2. In addition to the total current density absorbed, the absorption profile for each wavelength is also important when trying to simulate the spectral response of a device. The absorption profiles for wavelengths between 300 and 1200 nm that were calculated in the 1,000,000 ray simulation are shown in 3.8. This absorption profile can now be loaded into device simulations, so that the device simulations do not need to include a ray tracing calculation.

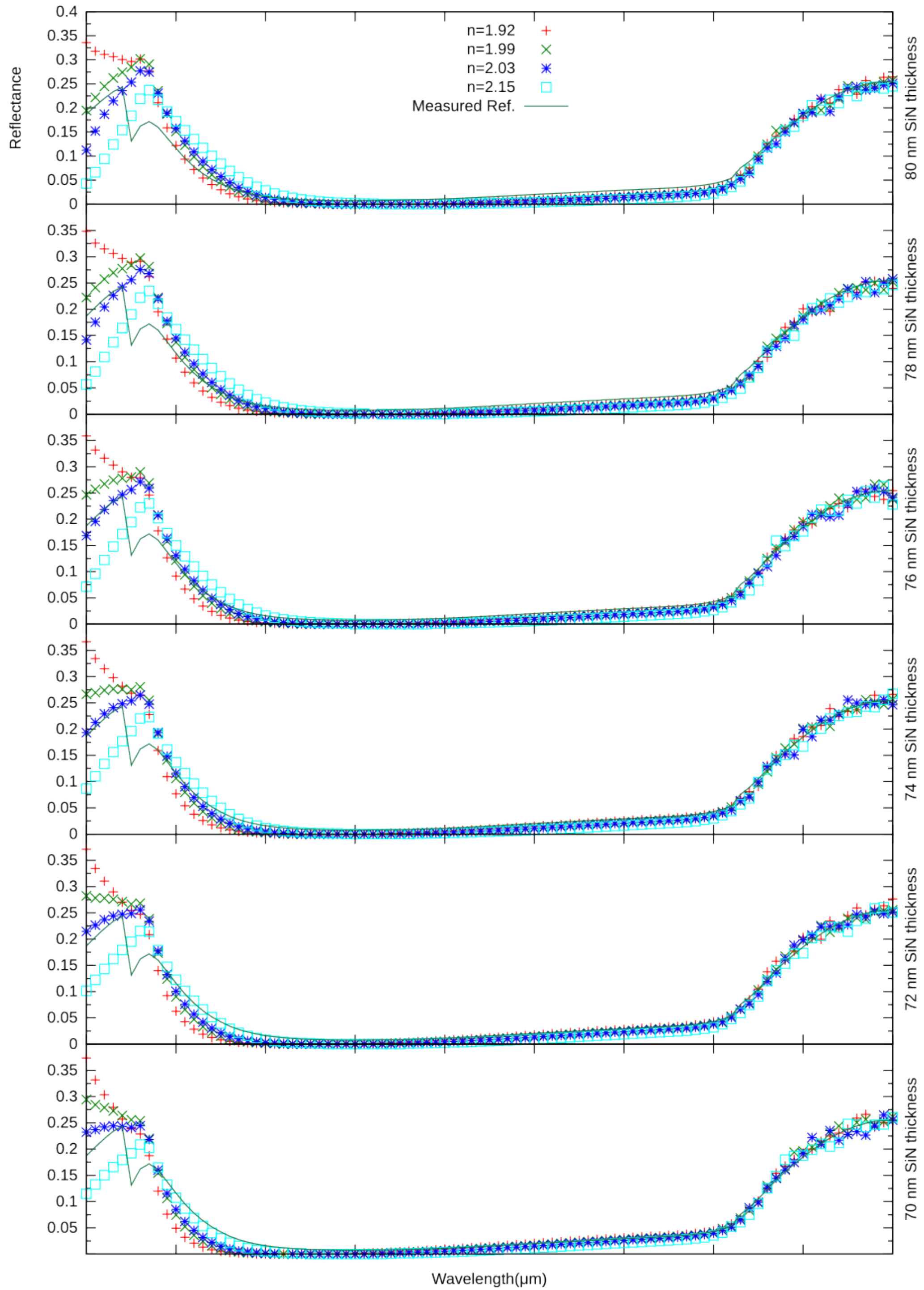

Figure 3.6: Simulation results, varying the SiN index and thickness.

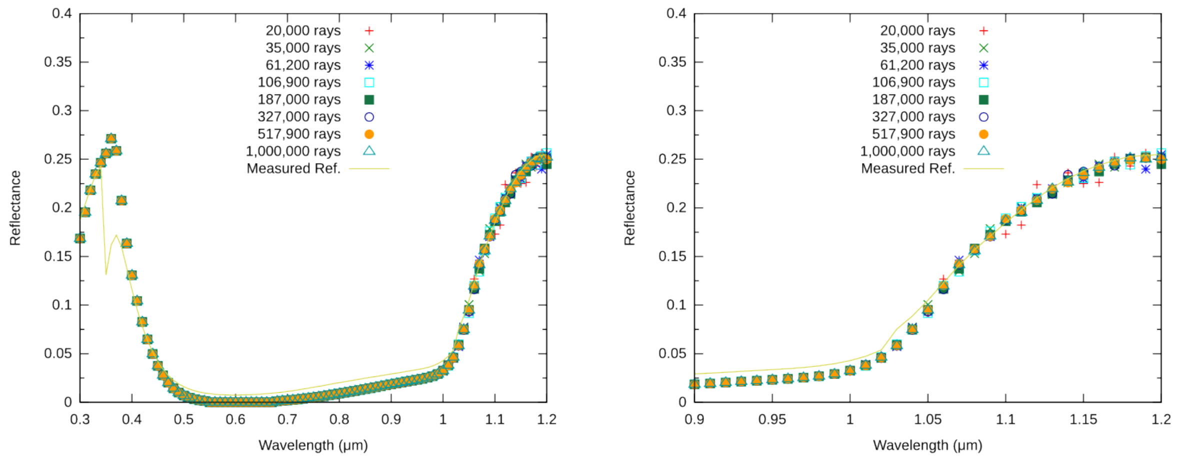

Figure 3.7: (left) The effect of the number of rays on the reflectance curve over the full wavelength range. (right) The effect of the number of rays on the reflectance curve in the escape reflectance regime which is found to be most sensitive to the number of rays used.

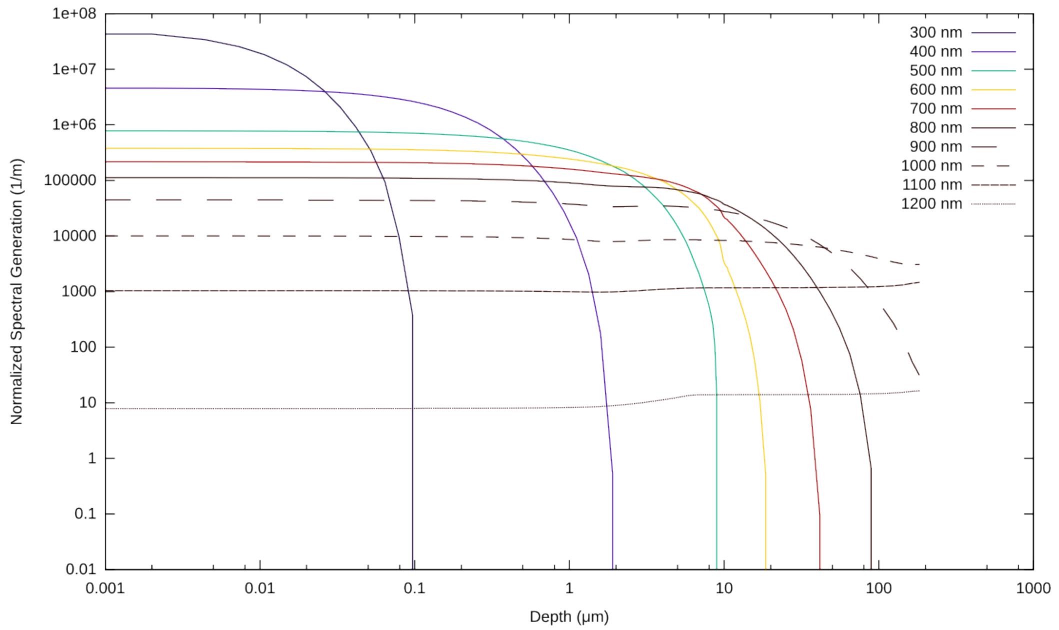

Figure 3.8: Normalized spectral generation versus depth by wavelength.

3.5 Verification of Models and Establishment of Mesh Through Quantum Efficiency and IV Characteristics of a Test Structure

Quantum efficiency simulations provide an opportunity to explore how different recombination models are performing and how it compares with an actual device. Figure 3.8 shows that as the wavelength increases the absorption depth also increases due to the decreasing extinction coefficient of Si. Therefore, the quantum efficiency at different wavelengths provides insight into recombination behavior within different regions of the device. For these simulations a small test structure with 1D symmetry was generated (uniform contact across top surface). The mesh near the front surface is very fine to give good resolution because of the high carrier density and auger/surface recombination. The mesh near the rear surface is also much finer than the bulk of the device. Figure 3.9 shows the structure and mesh used for these simulations. During the device simulation the generation profile for the given

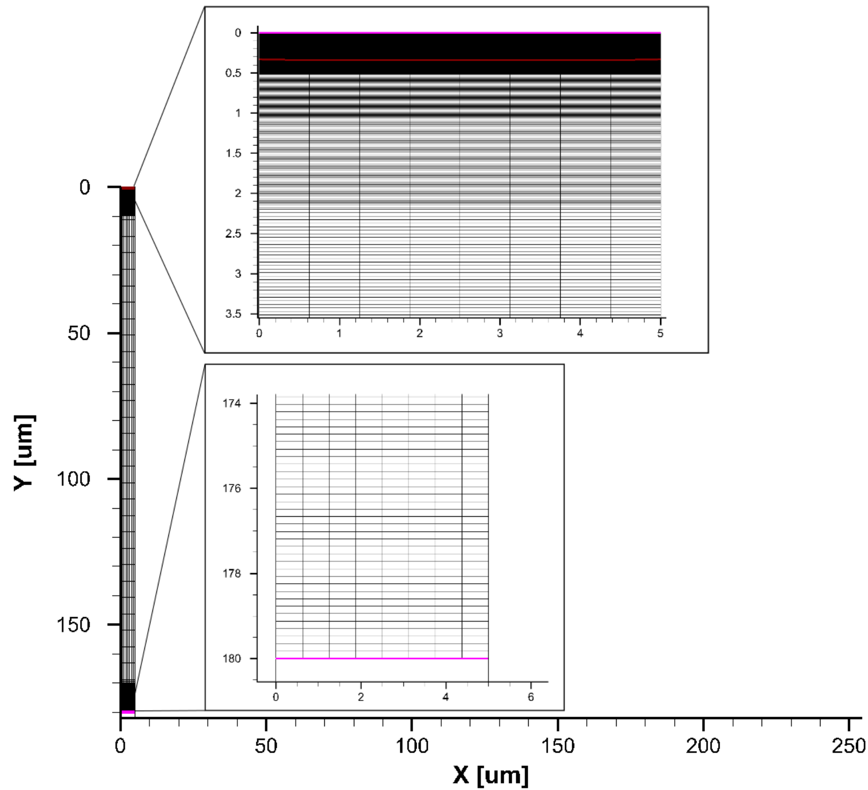

Figure 3.9: Structure and mesh of device used for quantum efficiency and IV simulations for this experiment.

wavelength is loaded and the mesh is regenerated with the new generation profile using a

script from Synopsys [47]. Using this new structure the device is simulated at the short circuit condition. The current from this simulation is called the spectral response. The external quantum efficiency, EQE, is then derived from the spectral response using 3.13

$$EQE = \frac{SR}{qI_{sig}} \frac{\lambda}{hc} \tag{3.13}$$

where q is the charge of an electron, I_{sig} is the signal intensity of light used, h is Plank's constant and c is the speed of light. The EQE gives the fraction of photons of a given energy incident on the device that create carriers which get collected. The internal quantum efficiency, IQE, is the fraction of absorbed photons which create carriers that get collected. To convert from EQE to IQE (which is more frequently discussed) the fraction of light that is reflected away or absorbed in the SiN antireflection coating must be divided out. The expression to convert from EQE to IQE is shown in equation 3.14,

$$IQE = \frac{EQE}{1 - (R + A_{SiN})}. \tag{3.14}$$

where R is the reflectance and A_{SiN} is the light absorbed in the silicon nitride layer.

Simulations were carried out using the generation profile from ray tracing simulations previously discussed and the described in this chapter. The results are then compared with an actual industrial type solar cell. The emitter profile was taken from a similarly processed wafer sent for spreading resistance profiling and the BSF was assumed to have a constant profile shape with a peak doping of $3*10^{18}$ with a thickness of 4 μm and a typical Cz Si lifetime of 300 μs was used. For these simulations the front surface recombination velocity, FSRV, was varied between 1000 and 70,000 cm/s. The results of the simulations are shown in comparison to the experimentally measured IQE in figure 3.10. As expected, varying the FSRV only affects the short wavelength IQE with increasing FSRV lowering the IQE. It is found that a simulated FSRV of 40,000 cm/s matches the experimental data best.

Next the effect of the BSF thickness is explored through simulations, it was varied between 0.1 and 12 μm keeping all other parameters the same as the previous simulation, retaining the closest matching value of 40,000 cm/s for the FSRV. The results can be seen in figure 3.11, an increasing BSF thickness causes sufficient band bending to shield electrons in the bulk from the highly recombinative rear surface. For a constant BSF doping of $3*10^{18}$,

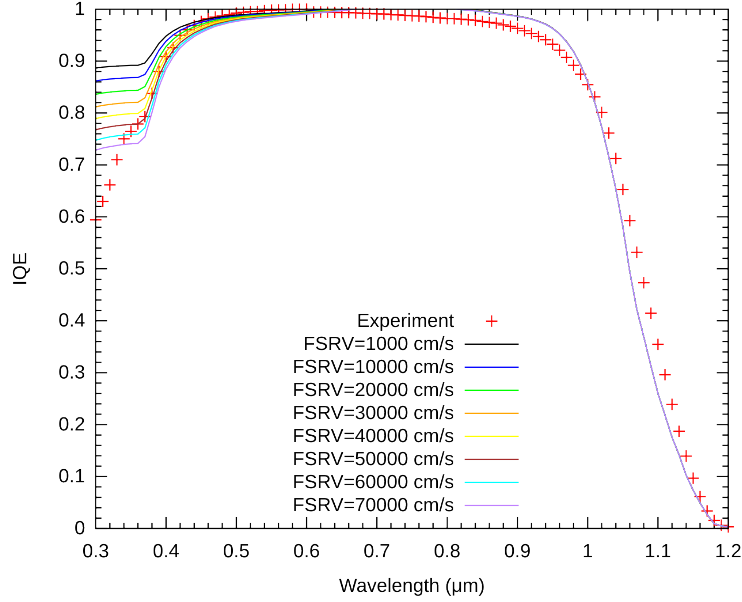

Figure 3.10: Effect of front surface recombination velocity on simulated IQE.

increasing the BSF beyond a 4 μm depth does not further improve the IQE. The effect of the bulk lifetime on the IQE (figure 3.12) looks similar to the effect of varying the BSF thickness. For short lifetimes, carriers generated near the rear surface recombine before they can get collected. Similarly, in a device with a poor BSF carriers generated near the rear of the device are likely to recombine at the rear surface before they can diffuse to the front surface even if the carrier lifetime is high. In summary, the simulations show that for a typical industrial type solar cell manufactured at UCEP it can be well described using the physical models: Schenk band gap narrowing model, Dziewiors Auger parameters and Fermi-Dirac statistics in conjunction with an FSRV of 40,000 cm/s, BSF thickness of 4 μm and SRH lifetime of 300 μs. To further illustrate the accuracy of these models and parameters, an IV sweep simulation is performed on the same device using all of the same optimized parameters and compared to the IV parameters of the same actual device discussed above. In the IV simulation 6% was derated from the incident spectrum to account for shading losses in the fingers and busbars and a series resistance of 0.6 Ω-cm^2 was added to include the contact, finger and bus resistances. The IV comparison from the actual and simulated industrial type cell can be seen in table 3.5. Each of the parameters are within 1% of the actual device and the overall efficiency is only 0.4% different. Synopsys tools employing the

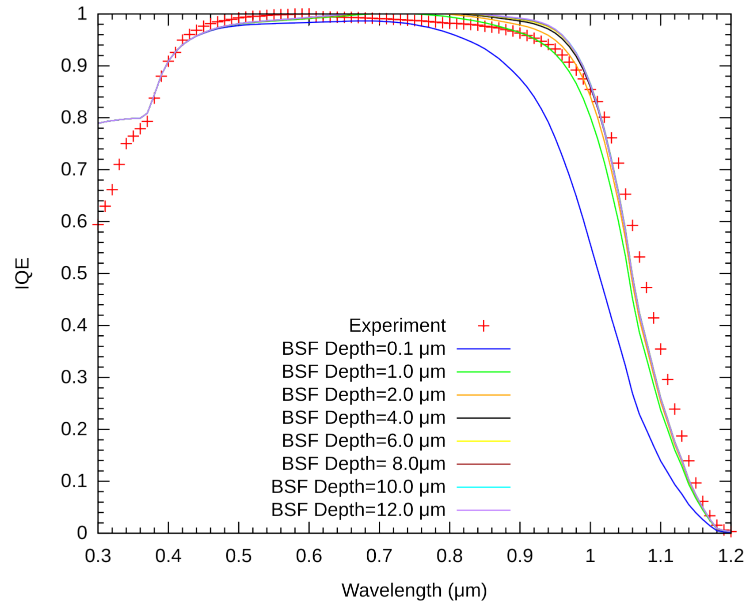

Figure 3.11: Effect of back surface field on simulated IQE.

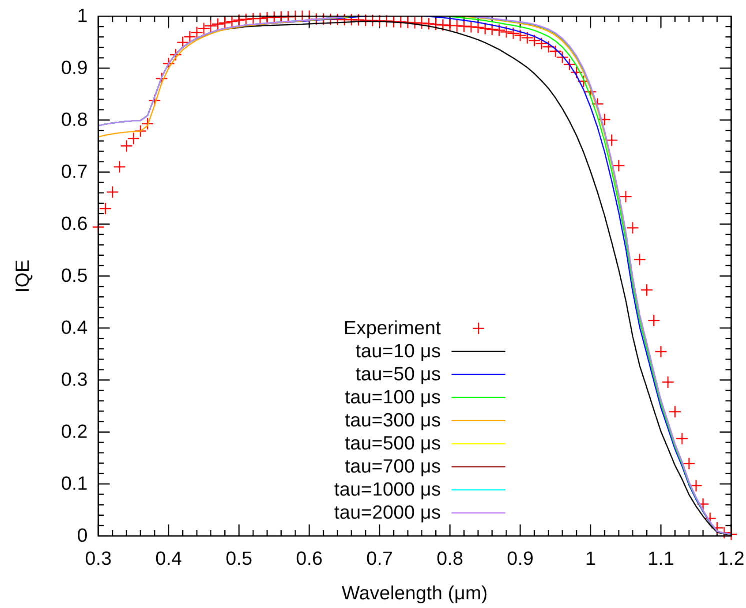

Figure 3.12: Effect of bulk lifetime on simulated IQE.

Table 3.4: Actual and simulated IV results

	Voc (V)	Jsc (mA/cm^2)	F.F.	Eff.
Simulation	0.6259	36.90	80.12	18.50
Actual	0.6323	36.94	79.51	18.57

most current physical models and correctly chosen mesh sizes can accurately model solar cell IQE and IV characteristics. This having been established, much of the rest of this thesis will involve characterizing more advanced devices which are less easily fabricated or to optimize solar cell design through simulation rather than iterations of experiments.

CHAPTER IV

QUANTITATIVE UNDERSTANDING OF THE BENEFIT OF SELECTIVE EMITTERS AS A FUNCTION OF IMPROVED SCREEN PRINTING PASTES

4.1 Introduction

Increasing solar cell efficiency is crucial to lowering the cost of photovoltaic electricity generated from crystalline silicon solar cells [51]. One method that is commonly used to increase solar cell efficiency is the formation of a selective emitter. This technology has been shown to increase the solar cell efficiency by up to 0.5-0.95% absolute [52, 53]. Selective emitters can lead to high short circuit current, J_{sc}, open circuit voltage, V_{oc}, and fill factor, FF simultaneously, on the same device. The need for selective emitters for high efficiency arises due to the inability of screen printed pastes to contact lowly doped ($N_d \leq 10^{20} cm^{-3}$) phosphorus emitters. However, recently significant progress has been made in silver screen printing pastes so that emitters with surface concentration as low as $1x10^{20}/cm^3$ can now be contacted [54]. With this improvement in paste technology, we must reexamine the benefit of selective emitters.

The selective emitter concept has been modeled extensively. Models have been used to explore the effect of the field emitter doping profile [55], the selective emitter doping profile [56] and the proportions of those two regions [23]. A more thorough review of selective emitter models can be found in the work by Greulich et al [57]. To the best of our knowledge no other work has tried to relate the efficiency benefit of selective emitters (SE) compared with homogeneous emitters (HE) using the doping level dependence of Ag/Si contact resistance.

In this work we propose a simple method to approximate the relationship between screen printed silver paste contact resistance, ρ_c, and the peak doping in the emitter. This model employs what we are calling an "effective Schottky barrier height". In this approximation

we assume that different Ag pastes behave as if they form different Schottky barrier heights when contacting Si. The model is shown to fit experimental data with reasonable accuracy. With this approximation we explore the efficiency benefit of SE solar cells over HE solar cells for a range of effective barrier heights. The results of these simulations show that selective emitter design should be tailored to current paste technology and that as Ag paste quality improves the advantage of a SE over a HE is diminished.

4.2 Using effective barrier height to model contact resistance

When a metal and semiconductor are brought together the Schottky formulation states that a potential barrier will arise between the two materials equal to the difference between the metal workfunction and the semiconductor electron affinity [58]. This barrier impedes the flow of electrons from the semiconductor to the metal. This impedance can be expressed by equation 4.1 [17, 59]

$$\rho_c = \rho_\infty \frac{300K}{T_0} \exp\left(\frac{q\Phi_{b,eff}}{E_0}\right) \tag{4.1}$$

where

$$E_0 = E_{00} \coth\left(\frac{E_{00}}{kT_0}\right) \tag{4.2}$$

and E_{00}, the characteristic energy, is given by

$$E_{00} = \frac{q\hbar}{4\pi}\sqrt{\frac{|N_{D,0} - N_{A,0}|}{\epsilon_s m_t}}. \tag{4.3}$$

The effective Schottky barrier height is given by $\Phi_{b,eff}$, ρ_∞ is the resistance for infinite doping,ϵ_s is the semiconductor permittivity, m_t is the tunneling mass and T_0 is the lattice temperature. The parameters used to fit this equation to the experimental data are mostly the defaults from *Sentaurus Device User Guide* and are shown in table 4.1

Table 4.1: Parameters used to fit experimental data using barrier height model

T_0	300 K
ϵ_s	11.9xϵ_0
m_t	0.19xm_e
R_∞	$2.4x10^{-9}$ $\Omega - cm^2$
Φ_B	1.8-4.2 eV

Screen printed contacts are formed by printing a Ag paste consisting of Ag powder, glass frit and organic binder onto a random pyramid textured Si wafer with a SiN antireflection coating and firing in a belt furnace. When fired, usually between 700 and 800 °C, the binder is evaporated away and the frit melts and consumes the antireflection coating beneath the grid lines. During this process Ag is incorporated into the glass melt as well as well as some of the Si from the surface of the wafer [60]. A fraction of the Ag precipitates in the glass near the Si surface and some forms crystallites etching into the Si surface . The mechanism of contact is still not completely understood, however, it is beleived that contact is made through direct contact of the Ag crystallites to the Ag grid line ,possibly at the tips of the pyramidal texture [61], and through tunneling via precipitates in the glass layer at the interface[62]. Different paste formulations and firing conditions give rise to different amounts of precipitates, crystallites and glass layer thicknesses as well as glass compositions. We propose the despite the variety of mechanisms contributing to the contact properties of screen printed Ag paste that it's behavior can be described as Schottky-like.

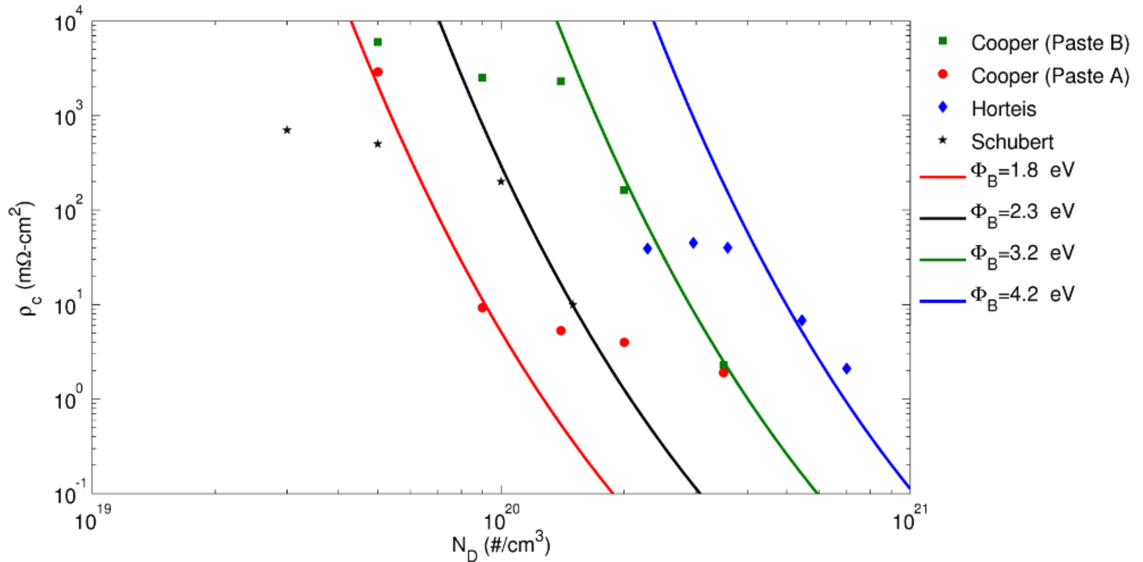

Figure 4.1: Experimental data from literature and fits made by varying the effective Schottky barrier height [54, 63, 64]

The method we propose to obtain a specific contact resistivity, ρ_c, for a given paste/firing condition is to fabricate solar cells with varying emitter surface concentration (5x10^{19}-5x10^{20}), measure ρ_c, and then fit the Nd vs. ρ_c data using equation 4.1 by varying $\Phi_{b,eff}$.

Figure 4.1 shows that existing data on Nd vs. ρ_c can be fit by assuming a Schottky type contact and by changing the barrier height. The authors are not suggesting that different Ag pastes or firing conditions necessarily give rise to different Schottky barrier heights, only that this assumption models their behavior well enough to justify the approximation. We aimed to fit each data set in theρ_c range between 10 and 1000 mΩ-cm^2 because below this range the contact resistance should not be a limiting factor in device performance and above that level the high contact resistance is extremely performance limiting and is not in a region of interest. Our aim was to have a good fit in the transition level when the contact resistance starts to go from acceptable to poor. The model fits Cooper's [54] data well in the region of interest and it also fits Schubert's [64] data well down to about 1e20 cm^{-3}. Horteis data is the poorest fit of the available data, but is still acceptable down to a doping level of around 3e20 cm^{-3}. Using this information it is possible to vary the contact resistance with the emitter doping in simulations to allow for a further level of device optimization based on current paste technologies. We will demonstrate the applicability of this model by examining the benefit that selective emitters provide over homogeneous emitters based on effective barrier heights of SP pastes.

4.3 Application of the model

The contact resistance model mentioned in the previous section is applied to simulations of SE and HE solar cells using Synopsys TCAD tools. In these simulations we vary the emitter field peak doping as well as the effective barrier height for a range of emitters and effective barrier heights. The parameters used for these simulations are detailed in table 4.2, a thorough review of the current models for Si solar cells can be found in Altermatt's work [34]. The diagram of the simulation domain can be found in figure 4.2

Table 4.2: Parameters used in in Sentaurus Device simulations

Parameter	Value
Free Carrier Statistics	Fremi-Dirac
Intrinsic carrier density	9.65x10^9 cm^{-3}
Mobility	Klaassen's mobility model [18]
Auger	Dziewior and Schmid [42]
Band gap narrowing	Table utilizing Schenk's BGN [15]
Surface SRH	Default Sentaurus parameters
Bulk lifetime	350μs
Substrate Thickness	180μm
Substrate width	1047.5μm
Selective emitter width	245μm
Contact width	45μm
Field peak doping	varied
Field junction depth (Gaussian)	0.35μm
Selective peak doping	2.32x10^{20} cm^{-3}
Selective junction depth (Gaussian)	0.35μm
External Rs for grid loss	0.4 Ω-cm^2

4.4 Simulation results

In our Synopsys TCAD simulations we varied the emitter peak doping from 5e19 to 3e20 cm^{-3} and the effective Schottky barrier height from 1 to 3 eV for two groups of simulations. One group had a HE while the other group has a SE, other than one group having a selective emitter the two sets of simulations were identical. The results of these simulations give us an idea of what efficiency benefit a selective emitter provides for a paste whose contact resistance follows Schottky type behavior of a given barrier height. In addition, we propose that this method can be used to optimize selective emitter design considering current paste limitations. The results of the simulations can be found in figure 4.3.

As the effective barrier height decreases, our simulations predict that the HE solar cell efficiency rises and approaches that of SE. This is because the contact resistance of the HE design is decreasing with barrier height while the SE already has very small contact

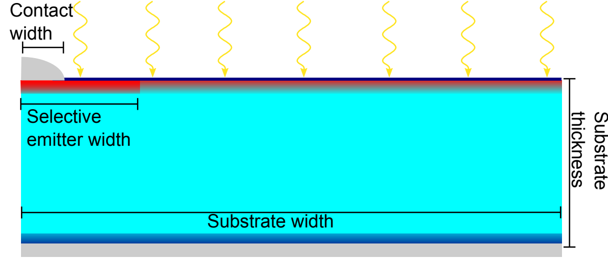

Figure 4.2: The simulation domain used in this work

Table 4.3: Comparison of the best device simulations for HE and Se simulations for each effective Schottky barrier height.

Simulations Summary

$\Phi_{B,eff}$		Jsc (mA/cm^2)	Voc(V)	FF (%)	Eff (%)
1 eV	Selective	37.34	0.637	79.8	18.97
	Homogeneous	37.41	0.639	79.2	18.94
1.5 eV	Selective	37.34	0.637	79.8	18.97
	Homogeneous	37.36	0.637	79.5	18.92
2.0 eV	Selective	37.34	0.637	79.7	18.96
	Homogeneous	37.31	0.635	79.3	18.78
2.5 eV	Selective	37.34	0.637	79.6	18.92
	Homogeneous	37.03	0.625	79.8	18.49
3.0 eV	Selective	37.34	0.637	77.7	18.39
	Homogeneous	36.79	0.620	79.7	18.17

resistance even for large barrier heights, so it does not benefit from a further reduction in ρ_c. Table 4.3 shows the cell parameters of the best HE and SE device simulations for each barrier height. The Benefit of implementing a SE cell design decreases from a maximum benefit 0.43 % at a barrier height of 2.5 eV to virtually no benefit at 1.0 eV.

4.5 Conclusions

We have demonstrated that the use of an effective barrier height model to approximate contact behavior of screen printed Ag pastes on crystalline silicon solar cells is justified. Further, using this approximation we explore the efficiency benefit a selective emitter provides for different effective barrier heights. For the screen printed pastes available during most of this thesis work, a selective emitter can provide roughly 0.5% efficiency advantage

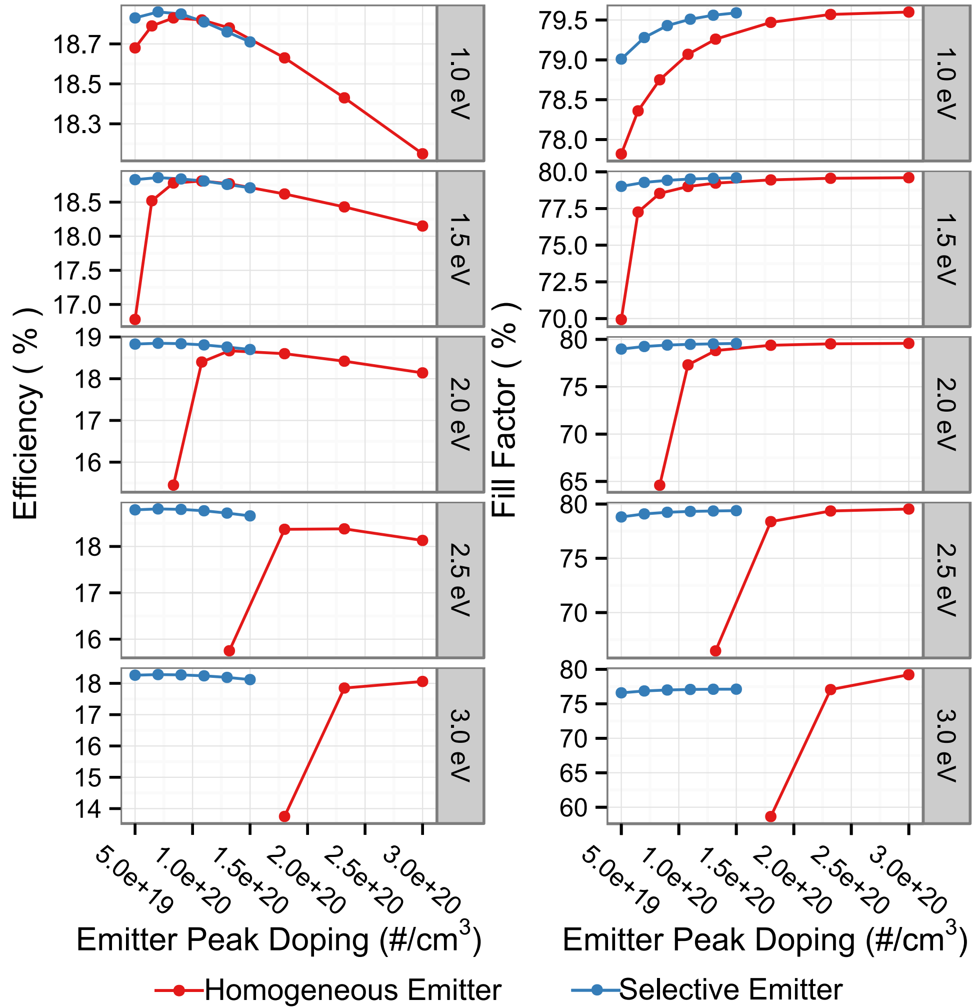

Figure 4.3: Efficiency (left) and FF (right) versus peak doping in the field emitter

over a homogeneous emitter. However as screen printing pastes improve and the effective barrier height approaches 1.0 eV the efficiency benefit of a selective emitter has essentially vanished. For this reason simulations showing the path towards higher efficiency devices will be developed and shown in later chapters.

CHAPTER V

A REVIEW OF LASER DOPING IN SI

5.1 Introduction

Laser doping is an attractive process for semiconductor processing because it allows selective regions to be doped by locally heating them in conjunction with a dopant source. This is advantageous from a thermal budget point of view and also is much simpler than a typical photolithography process. For solar cells, laser doping provides a simple way to heavily dope selective regions beneath grid lines to reduce the contact resistance and allows the field region to be lightly doped to minimize recombination without sacrificing good contact properties. In this chapter a review of laser doping in silicon is given. First, the beginnings of laser doping is discussed followed by a review of the mechanism of laser doping and defects created by laser doping of Si. Finally, a review of solar cell structures that have used laser processing/doping is given to put into context the work carried out in this thesis.

5.2 Beginnings of Laser Doping

The first time a PN junction was created via laser doping was in 1968 when IBM (Fairfield and Schwuttke) used a paint on phosphorus source and a ruby laser (λ = 6943Å) to P dope a polished boron doped Si wafer to create diodes using several different pulse powers [65]. However, it wasn't until a series of Soviet papers were written in 1974-1976 that great interest was generated in the laser doping process [66]. Shtyrkov et al showed that the amorphous region created by ion implantion in Si and GaAs can be recrystallized using a Q-switched Nd:YAG and that the implanted dopants can be activated by the laser pulse [67]. Similarly, Kachurin and Klimenko showed that a continuous wave, CW, laser doping or "laser annealing" can produce similar results to pulsed laser doping [68][69]. Pulsed laser radiation generally melts the irradiated region of the Si. The molten Si then recrystallizes through liquid phase epitaxy at speeds up to 15 m/s [70] and dopant atoms are incorporated into the lattice. In contrast, continuous wave lasers are generally used to heat but not melt

Si and thus solid phase epitaxy occurs when annealing implanted Si. Obviously, with a high enough power CW laser, sufficient heating could occur to melt the Si as well. Melting Si can be advantageous when highly doped regions are desibrable. This is due to the higher solubility of dopants in Si melt compared to crystalline silicon. An example of this is shown for P and B, two of the most common dopants used in Si solar cells, in figure 5.1 where their solid solubilities are plotted versus temperature and the solubilities in melt are included as a reference [71, 72]. Melting of Si during the laser doping process also creates a much

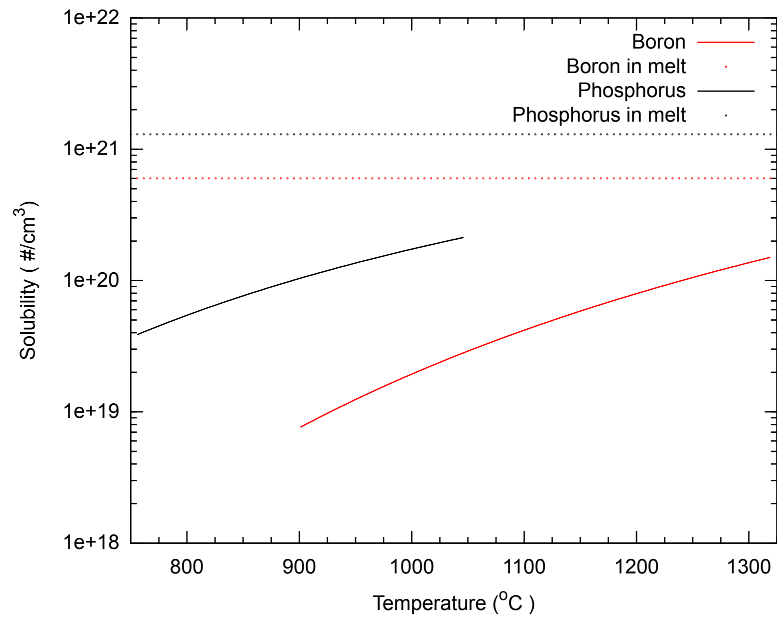

Figure 5.1: Solubility of P and B in crystalline Si as a function of temperature and in Si melt

deeper junction because of the much higher diffusivity of dopants in molten Si compared with crystalline Si, as shown for the case of P in figure 5.2.

5.3 Laser Doping Mechanism

In laser doping, the laser pulses perform two simultaneous actions that lead to doping. Heating the substrate and dissasociating dopant molecules in the the gas phase (if a gaseous dopant source is used) and at the surface of the substrate. This mechanism was explained by Deutsch et al at Lincoln Labs in a clever experiment where two lasers of different wavelengths (193 nm and 351 nm) were used to dope Si substrates using a BCl_3 gas dopant source [73]. They determined that BCl_3 has 10% absorbance at 193nm and no absorbance at 351 nm.

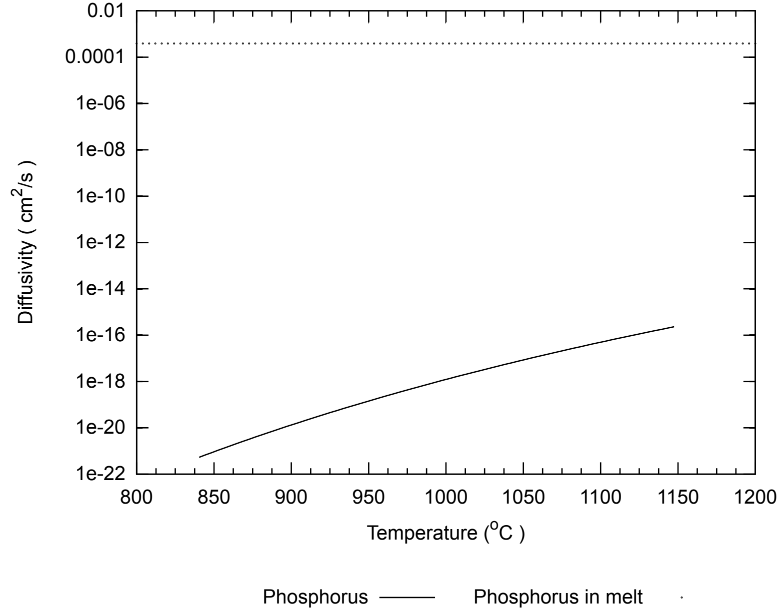

Figure 5.2: Diffusivity of P in crystalline Si as a function of temperature and in Si melt

Therefore, when laser doping is carried out with a 193 nm ArF laser with a BCl_3 source the possibility exists for B atoms to be liberated in gas phase and get adsorbed at the surface to contribute to the doping as well as B atoms dissasociation at the surface. For laser doping with the 351 nm XeF only B atoms disassociated at the surface can contribute to the doping since BCl_3 has no absorbance at that wavelength. They found that the laser doped samples with the 193nm ArF laser had 2-3 times lower sheet resistance than those doped with the 351nm XeF laser using the same pulse powers with each laser. Therefore, gas phase and surface disassociation play an important role in the laser doping process. Slaoui et al, performed a similar experiment using an excimer laser and a PF5 gaseous dopant source [74]. They found that PF5 shows no absorption at the excimer lasers wavelength (193 nm). However, when doping was carried out in a chamber with successively higher PF5 pressures, the sheet resistance kept decreasing, implying that adsorption of dopant containing molecules onto the heated Si surface plays an important role in supplying dopant to the surface even when the dopant source is transparent to the radiation.

The melt depth and duration of melting are dependent on material parameters such as the density, melting temperature, latent heat heat of melting, thermal conductivity and specific heat for crystalline and liquid Si. Obviously, how the material interacts with the

laser (reflectance (T) and absorption (T))used is also important. Unamuno and Fogarassy used the finite differences method to model the melting of Si under laser radiation and found reasonable agreement with experiment [75]. Their model accurately predicts the melt depth and duration. Figure 5.3 shows the results of their simulations of how pulse power and wavelength affects the melt depth as a function of time. Not surprisingly, higher

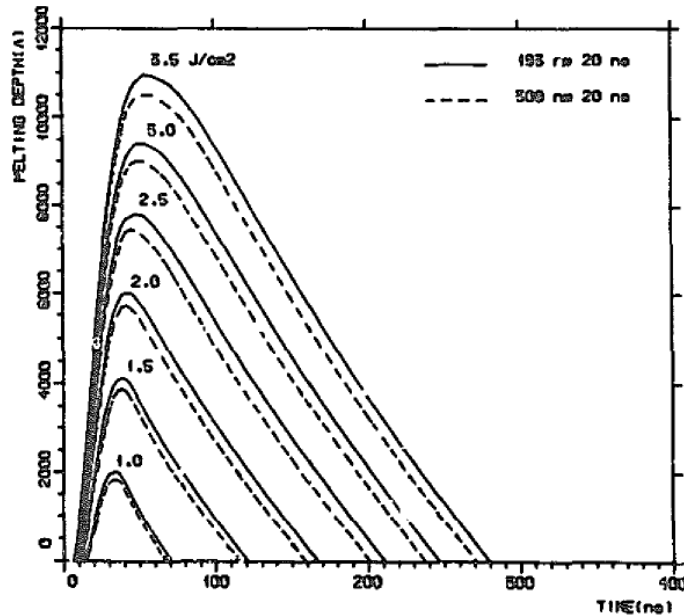

Figure 5.3: Calculations crystalline Si melt depth and duration for $\lambda = 193$ and 308 nm for several laser fluences for a 20 ns pulse. Used with permission [75]

pulse powers deliver more energy and heat and thus more melting, the 193 nm wavelength radiation produces a slightly deeper junction depth for each pulse power compared with the 308 nm wavelength. This is due to the stronger absorption of 193 nm light compared with 308 nm. The effect of pulse duration on the melt depth and melt duration was also explored and can be seen in figure 5.4. The simulations reveal that longer pulses lead to longer melt times and smaller melt depths

Since the diffusivity of dopant in liquid Si is so high, one might expect that the junction depth would be the same as the melt depth. However,some simulations have predicted that the boron junction depth for a certain range of laser pulse energies should actually be less than the melt depth [76]. They explain that the junction depth does not have to

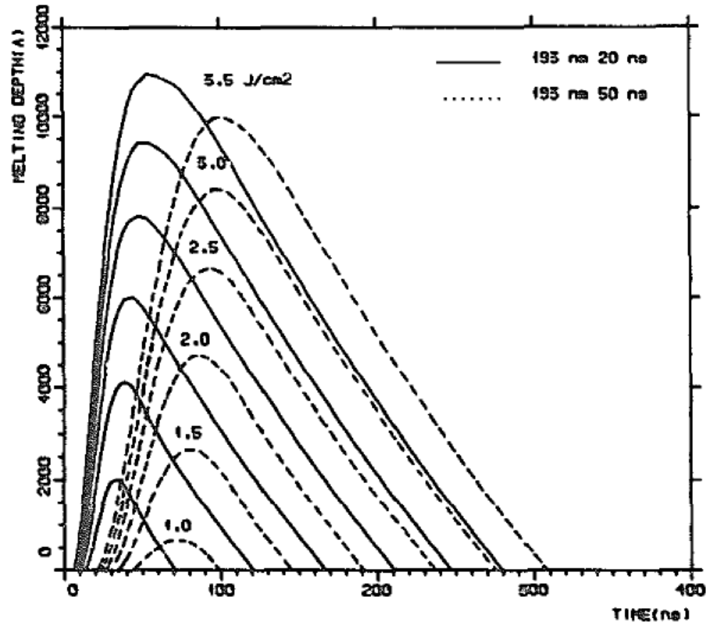

Figure 5.4: Calculations crystalline Si melt depth and duration for 20 and 50 ns pulses with $\lambda = 193$ for several laser fluences. Used with permission [75]

coincide with the melt depth if the melt front velocity (the speed at which molten Si is recrystallizing) is much greater than than the diffusion of dopant atoms. Figure 5.5 shows the laser fluences in which it is predicted that the junction depth may or may not coincide with the melt depth for a 30ns pulse. The pulse energy, repetition rate and laser raster speed together determine the amount of melting on a given region of Si as well the number of times an area will be melted and how much dopant is incorporated into the surface.

Up until now, only laser doping with a gaseous dopant source is discussed, which is an effective method but it requires a vacuum chamber and mass flow controllers in conjunction with the laser system and is thus a rather cumbersome method especially for the application in solar cell where only one device per wafer is made. The alternative to a gaseous dopant source is a spin on liquid source or evaporated solid source. Zhang et al proposed using a boron doped spin-on-glass (SOG) and found that it works quite well [77]. They were able to create diffusion profiles with peaks near the solubility limit. Similarly, P laser doping using P509 SOG from Filmtronics has been used as a laser doping source [78]. A diagram depicting the proposed laser doping process for a spin on liquid source dopant is shown in

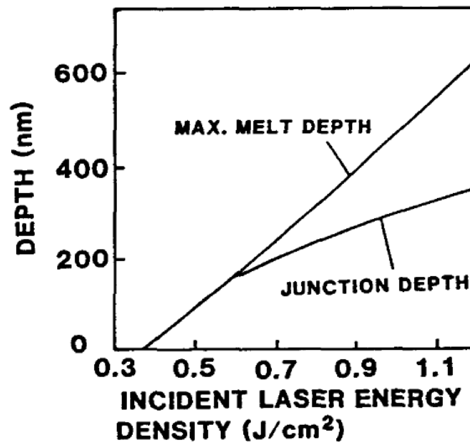

Figure 5.5: Relationship between melt depth and junction depth for B laser induced diffusion in Si figure from [76] with permission.

figure 5.6.

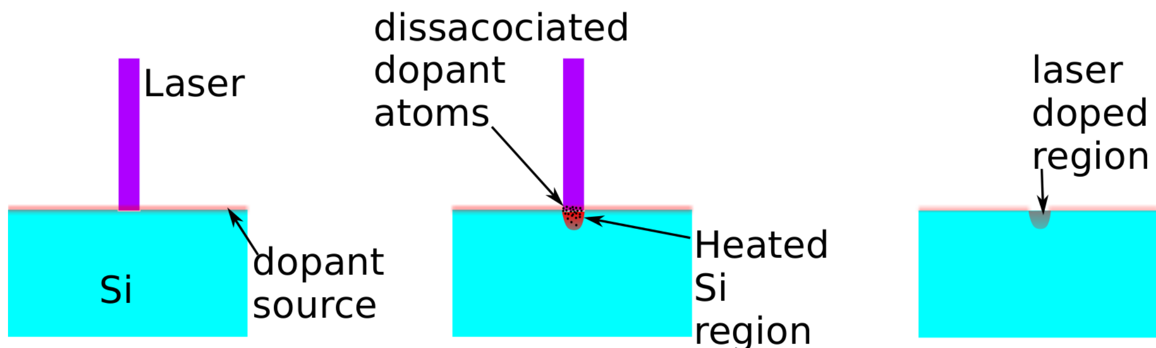

Figure 5.6: Proposed laser doping process. from left to right, first the laser pulse strikes the surface of the wafer and dopant,some of which is vaporized. As the surface is heated adsorbed dopant atoms dissasociate and begin to diffuse into the substrate. Gaseous dopant atoms can also be disassociated and then land on the surface and contribute to laser doping. After the surface cools the laser irradiated region now incorporates some of the dopant atoms from the spin on source.

5.4 Laser Induced Defects

The first reports of laser induced defects in semiconductors was in 1965 when Birnbaum *et al* 1965 explored the effect of ruby laser irradiation on polished Si, Ge, GaAs, GaSb, InSb and InAs [79]. They observed parallel cracks on the surface of the wafer after irradiation. The cause of these cracks was later determined to be thermal shock and it was also found

Table 5.1: Comparison of defects found by DLTS in Ruby and Nd:YAG irradiated Si [82]

Laser Type	Deep Level E1	Deep Level E2	Deep Level E3
		Nd:YAG	
E_c (eV)	E_c-0.32	E_c-0.45	E_c-0.53
σ_n (cm^{-2})	$8*10^{16}$	$2*10^{16}$	$6*10^{16}$
		Ruby	
E_c (eV)	E_c-0.32	E_c-0.43	E_c-0.58
σ_n (cm^{-2})	$4.4*10^{16}$	$1.4*10^{16}$	$5*10^{15}$

that surface treatments on the wafers play an important role in defect formation, for example polished surfaces are much more susceptible to laser damage [80]. Even when no laser damage is visible, bulk lifetime degradation in Czochralski and float-zone Si has been observed after irradiation by ruby laser. The electrically active defects created by laser radiation can be detected by DLTS [81] and are largely similar for damage from similar wavelength lasers as can be seen in table 5.4 [82]. The same defect levels are seen in ArF radiation as in the Nd:Yag and ruby laser case as well as two additional defects at 0.18 and 0.25 eV which have very low concentration. In this discussion only electron traps are highlighted because in solar cell applications throughout this thesis, laser doping is carried out on n type Si. However, laser doping does give rise to hole traps as well. Defects have been reported without visible damage, it is largely believed that most defects are created during epitaxial regrowth of the molten Si.

5.5 Laser Doping in Crystalline Si Solar Cells

Laser doping in silicon solar cells goes as far back as 1980 when solar cells were created by laser doping a boron emitter using a gaseous source on a n type substrate [83], achieving an efficiency on 9.6%. In these solar cells the entire emitter was formed by laser doping, in most current devices that use laser doping the laser doped region is only beneath the contacts. This type of cell design is called a selective emitter. The benefit of a selective emitter is the ability to simultaneously optimize the device for optimum contact properties by tailoring the selective diffusion beneath the gridlines and minimizing emitter recombination by lowering the doping in the field emitter. The benefits of selective emitters are further discussed in

chapter 7. The precursor to most modern laser doped solar cells is the laser grooved solar cell developed by Wenham in his PhD work at UNSW [84]. In this cell design, seen in figure 5.7, laser grooves are formed after P diffusion and oxidation. Then a heavier diffusion is performed to form a n^{++} region in the laser opened grooves while the rest of the emitter is masked by the thermal oxide. The heavily diffused regions are then plated with Ni/Cu, conveniently the thermal oxide acts as a plating mask to keep the plated metal off of the field emitter. However when surface damage or organic contamination is present the thermal oxide can not entirely protect the region between the contacts from being plated [85], this phenomenon is called background plating. A similar device design is the double sided buried

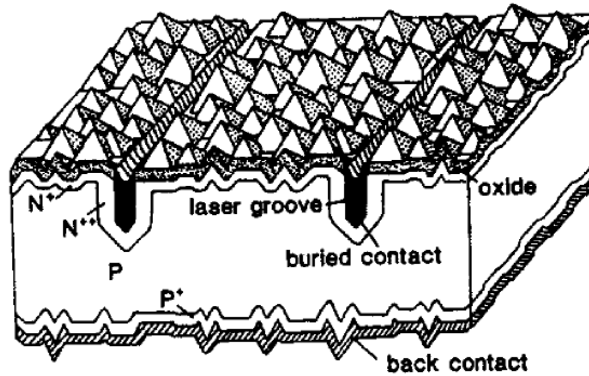

Figure 5.7: Schematic of buried contact solar cell [86]

contact DSBC solar cell. Which is similar to the buried contact solar cell except that the rear side of the device is also laser scribed and then boron diffused and plated at the time as the n^{++} contact. The advantage of this design in over the standard buried contact design is that now most of the rear side of the device is passivated, lowering the Jo of the device. Another benefit of this design is that the device can be bi-facial, which means that the device can be illuminated from both sides. A diagram of a DSBC cell is shown in 5.8. A slight modification of the DSBC cell design is the interdigitated back contact IBBC cell design. This device is the same as the DSBC device except that it contains the n^{++} and p^{++} contacts on the rear side so that none of the device is shaded by the metal contacts. The IBBC device design can be found in figure 5.9.

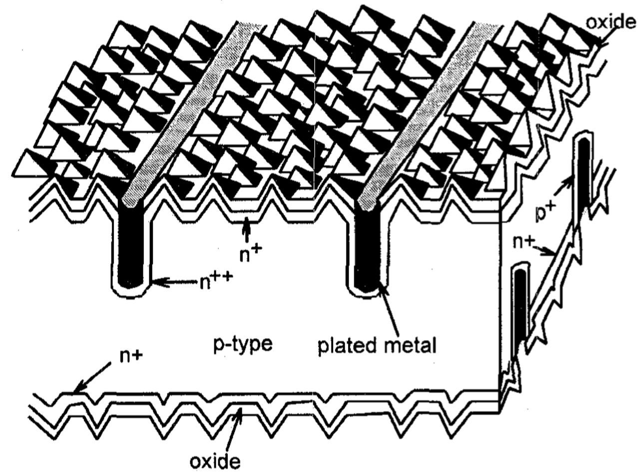

Figure 5.8: Schematic of double sided buried contact solar cell [87]

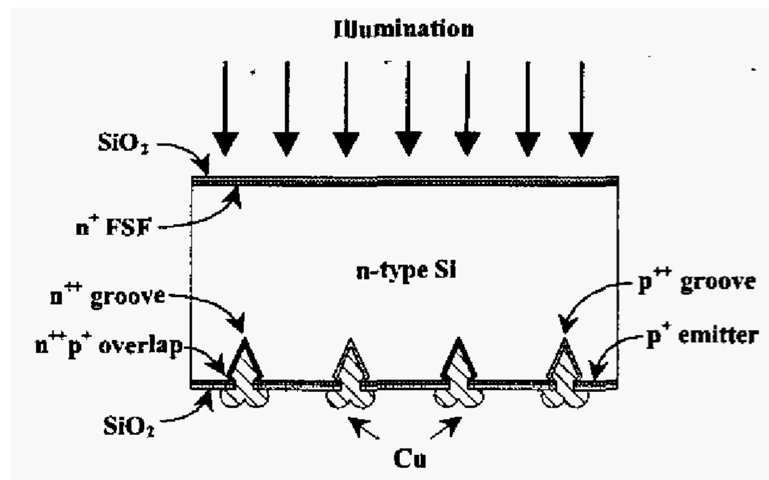

Figure 5.9: Schematic of interdigitated buried contact solar cell [88]

The previous buried contact cell structures discussed employed laser processing but were not truly laser doped. The laser was only used to create channels which were then diffused in a tube furnace. The next structure discussed in this section was also developed at UNSW and employs true laser doping [89] , it is a logical follow up to the buried contact solar cell. The so called laser doped selective emitter cell, LDSE, can be seen in figure 5.10. This

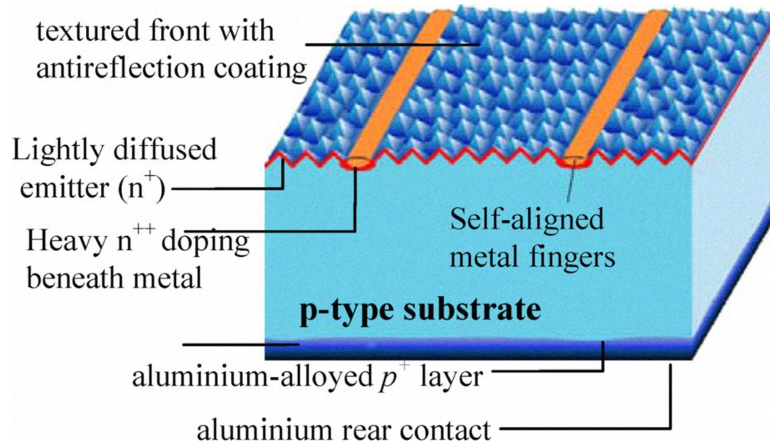

Figure 5.10: Schematic of Suntech Pluto cell [90]

device design only differs slightly from the standard screen printed solar cell production sequence so that existing production lines can be converted to this process [90]. The laser grooved and laser doped solar cells have the advantage of narrow finger widths, which lead to reduced front surface shading and higher J_{sc}. The narrower finger widths are possible because the width of the finger is largely determined by the opening the laser makes. While screen printed contacts finger width are dependent on the properties of the Ag paste and of the screen and printer used. The processing all the way up through SiN deposition is the same as in a standard screen printed solar cell. However, after SiN deposition the LDSE process flow is completely different to incorporate the laser doping and plating steps. The production sequence for a LDSE cell can be seen in figure 5.11.

A similar approach is laser chemical processing or LCP. The LCP method couples a laser beam into a liquid jet of dopant through a nozzle with is rastered over the wafer. The beam is limited to the spot size of the liquid jet due to total internal reflection [91]. The main difference between this method and the laser doping method developed UNSW is that LCP does not require a dopant spin on step. LCP has been tested with 532 and 1064nm

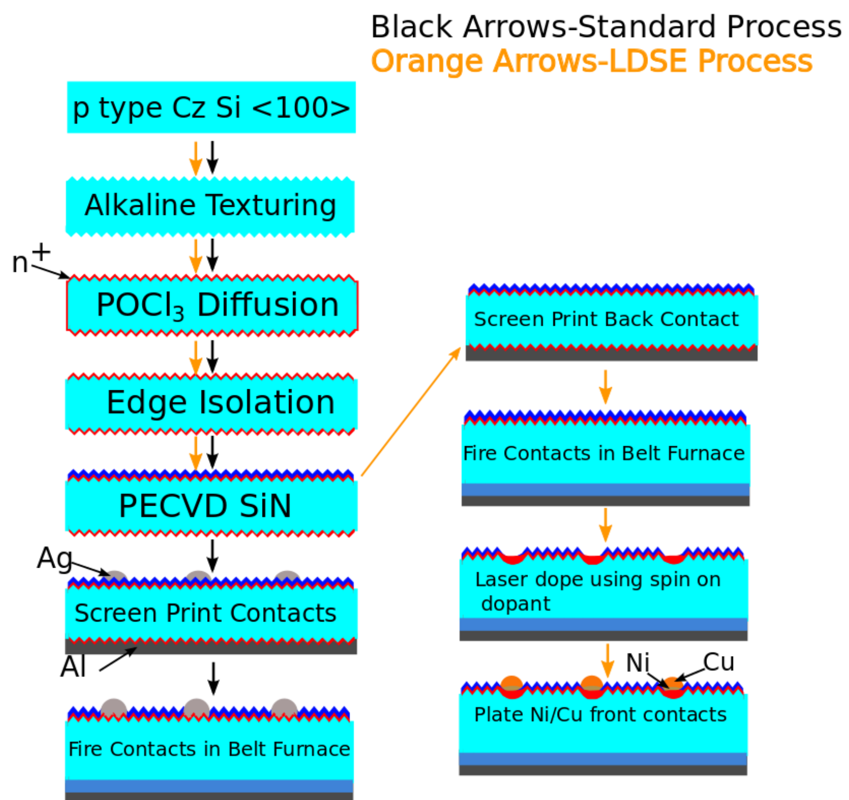

Figure 5.11: Process differences in LDSE cells and standard screen printed cells

lasers, with better performance coming from the 532nm laser [91]. The work on LCP has resulted in an industrial tool available at Rena corporation.

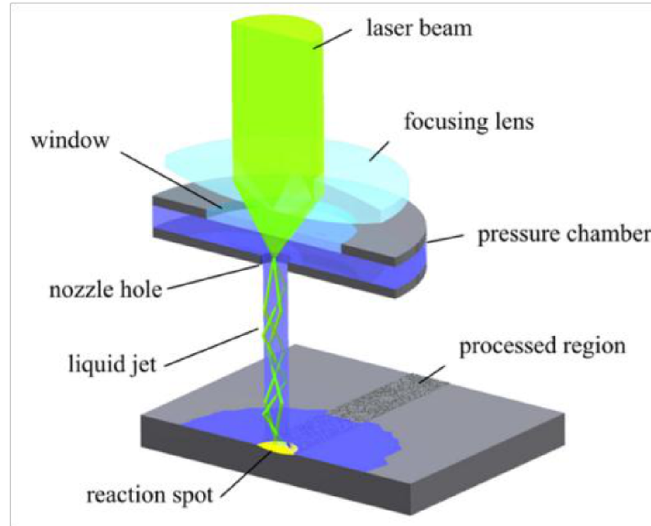

Figure 5.12: Diagram of LCP apparatus [92]

Yet another method for laser doping in crystalline Si solar cells is the laser transfer method. In this technique a dopant such as antimony or phosphorus is applied to a transparent substrate which is then held above a wafer with the dopant side down [93][94]. As the laser rastered over the glass slide dopant is transferred to the wafer and incorporated into the molten silicon created by the same pulsed that liberated it from the transparent substrate. This process is shown schematically in figure 5.13. One benefit of this process is that it does not require any wet processing. A schematic of the process is shown in 5.13

Laser doping with plating is an attractive option for high efficiency solar cells, but it has not caught on much in industry partly due to costs of disposal of plating bath waste and various other problems with the plating process. Perhaps, the simplest way to create a laser doped selective emitter is to use the P in the SiO_2:P_2O_5 that is left over from the emitter diffusion as the P source [52]. This method only requires a single additional step compared with a standard screen printed solar cell. This is demonstrated in figure 5.14 Additionally, adding on a laser process step is rather cheap since the only cost is to purchase the laser and maintain it. This process has produced 0.5% efficiency enhancement over standard screen

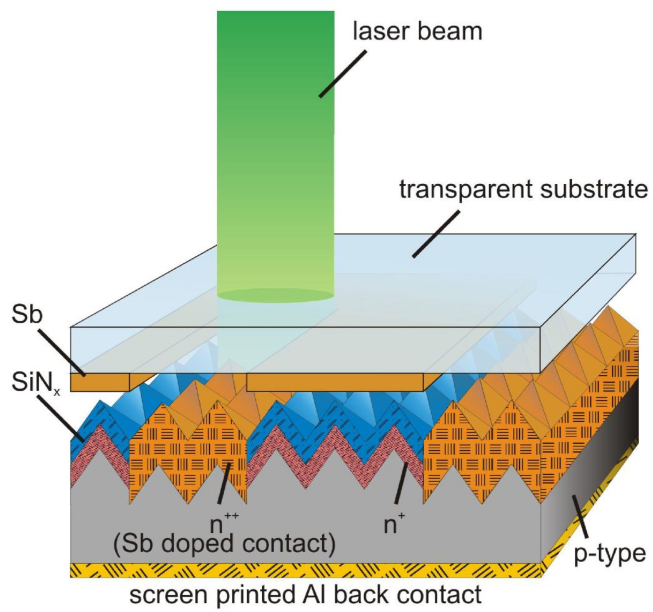

Figure 5.13: Diagram of laser transfer process [92]

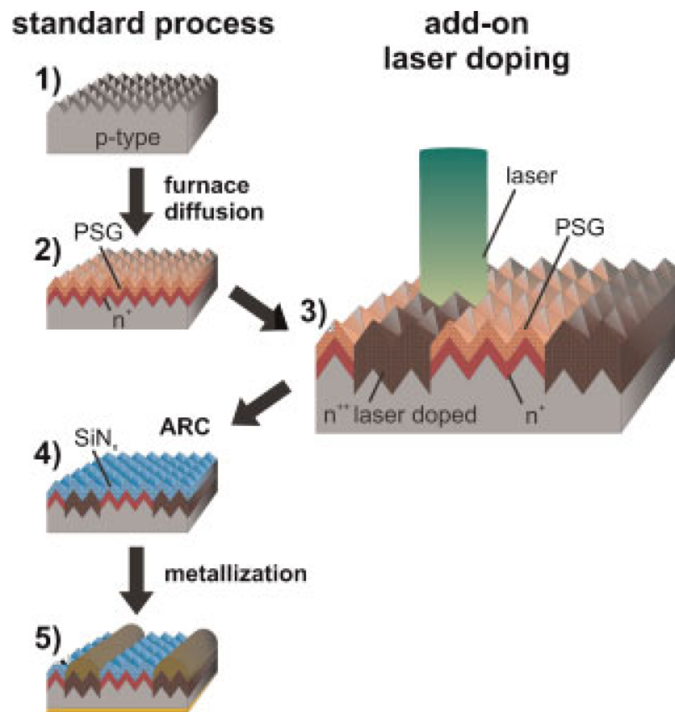

Figure 5.14: Process sequence for add on laser selective emitter solar cells. Figure used with permission from [52]

printed solar cells. The main challenge in fabricating these types of devices is aligning the screen printed front metallization to the laser doped regions and optimizing the laser doped regions. Zhu *et al* proposed using an intersected laser doping pattern to avoid having to align the screen printed fingers and laser doped regions [95]. This is achieved by printing the Ag grid lines perpendicular to the selective emitter pattern. A diagram of this cell structure is seen in 5.15. While this method solves the problem of alignment, it is rather

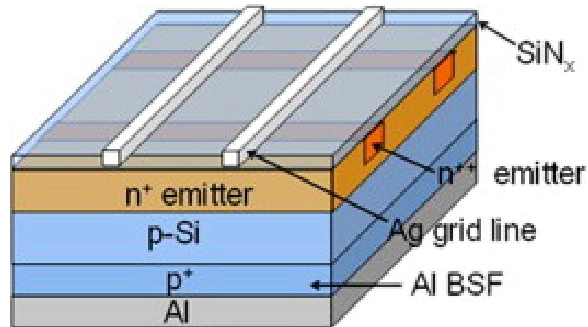

Figure 5.15: Cell structure with intersected laser doped selective emitter [95].

inelegant, the laser doped regions which have higher doping levels have a lower quantum efficiency [96]. Therefore, the area that is laser doped and is not beneath the grid lines should be minimized. It should be noted that for both of these approaches with P-glass laser doping a 532 nm wavelength laser was used.

5.6 Conclusions

Laser doping in silicon is a simple and effective way to create highly doped regions in semiconductors. This process has been shown to be capable to assist in the manufacture of high efficiency solar cells. While most of the early work done on laser doping was carried in the UV wavelength range, most work done on Si solar cells has been done with 532nm frequency doubled Nd:YAG lasers. The focus on the green lasers is most likely due to the fact that many laser doped solar cells have Ni and Cu plated contacts and Ni is a fast diffuser in Si [97]. Green laser radiation has a longer absorption length than UV radiation [6] and therefore creates a deeper junction when used for laser doping. However, since screen printed contacts do not have Ni a deeper junction is not required. Therefore, in this work UV laser is explored for doping in Si solar cells in conjunction with screen printed contacts.

CHAPTER VI

DEVELOPMENT AND OPTIMIZATION OF UV LASER DOPING OF PHOSPHORUS AND BORON IN SI

6.1 Introduction

In this chapter the efficacy and potential of UV laser doping in C-Si is explored. First, the use of P and B spin on dopants as a source is investigated. The doping levels achieved for different concentrations of these dopants are measured by sheet resistance. The widths of the openings produced from different laser frequencies and scan speeds are determined along with the damage created from laser doping by SEM imaging. Further, the use of a P rich glass is explored as a dopant source. This method only requires one additional step compared to a standard industrial process. It is shown that selective emitters by UV laser can reduce the solar cell contact resistance and, therefore, series resistance to increase the fill factor on high sheet resistance emitters. Finally, the role of the dead layer in the laser doping process is investigated and the effect of laser doping on the reflectance is quantized. Through these steps, a laser doping process is developed which will be used in the fabrication of high efficiency solar cells in later chapters.

6.1.1 Procedures for laser doping

156 mm psuedo square, textured, p-type, Cz grown Si wafers were cleaned with hydrofluoric acid, HF, and hydrochloric acid to remove any native oxide and metal contaminants, respectively. Following the clean the wafers were diffused in a tube furnace with a $POCl_3$ source to create a 100 $\Omega/\Box$ n^+ layer on the surface of the wafer. The P rich glass was then removed from the surface of the wafer by an HF dip and different P dopant solutions were spun onto the surface of the wafer. The dopants chosen were an aqueous 85% solution phosphoric acid (H_3PO_4) and a solution of 228 g/L of phophorous acid (H_3PO_3) in methanol. A Coherent AVIA diode-pumped, solid-state, Q-switched laser fequency tripled to 354.7 nm was used to carry out the laser doping. In this experiment the pulse power scan speed and dopant

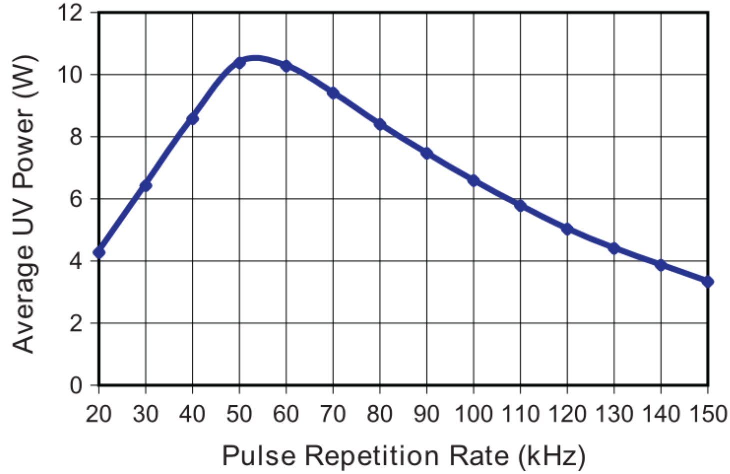

Figure 6.1: Cell structure with intersected laser doped selective emitter [98]

source were varied. To vary the power with this laser the pulse repetition rate was changed, the relationship between the repetition rate and the power output is seen in figure 6.1. For each condition, a box shape of about 1cm x 2cm was laser doped by overlapping pulses to create a continuously doped sheet. The amount of overlap of each pulse varies with the pulse rate and with the scan speed, an example of how the pulse overlap can change with scan speed is seen in figure 6.2. After laser doping, the dopant was rinsed off of the wafers in a DI dump-rinser and dried. The sheet resistance of each laser doped box was then measured to determine the doping effectiveness of each laser condition. Sheet resistance is defined as

$$\rho/t \tag{6.1}$$

where ρ is resistivity and t is thickness, in general a low sheet resistance implies a heavily doped layer. However, A lightly doped deeply diffused layer could also have a low sheet resistance.

6.1.2 Results

The results of the experiment can be seen in figure 6.3. It is clear that higher pulse energies and slower scan speeds create a more highly doped layer. Phosphoric and phosphorous acid are both suitable P dopants and produce similar sheet resistance layers after laser doping.

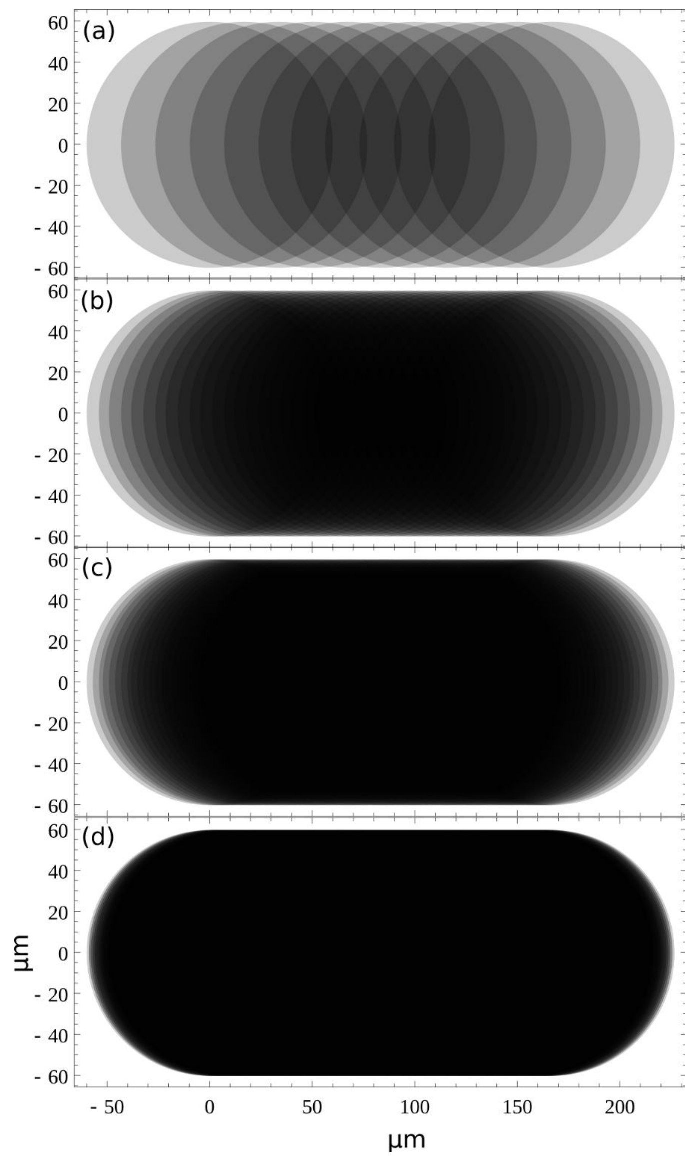

Figure 6.2: Pulse overlap change with scan speed for an example repetition rate of 180 khz for (a)3000 mm/s,(b)1000 mm/s,(c)500 mm/s,(d)100 mm/s

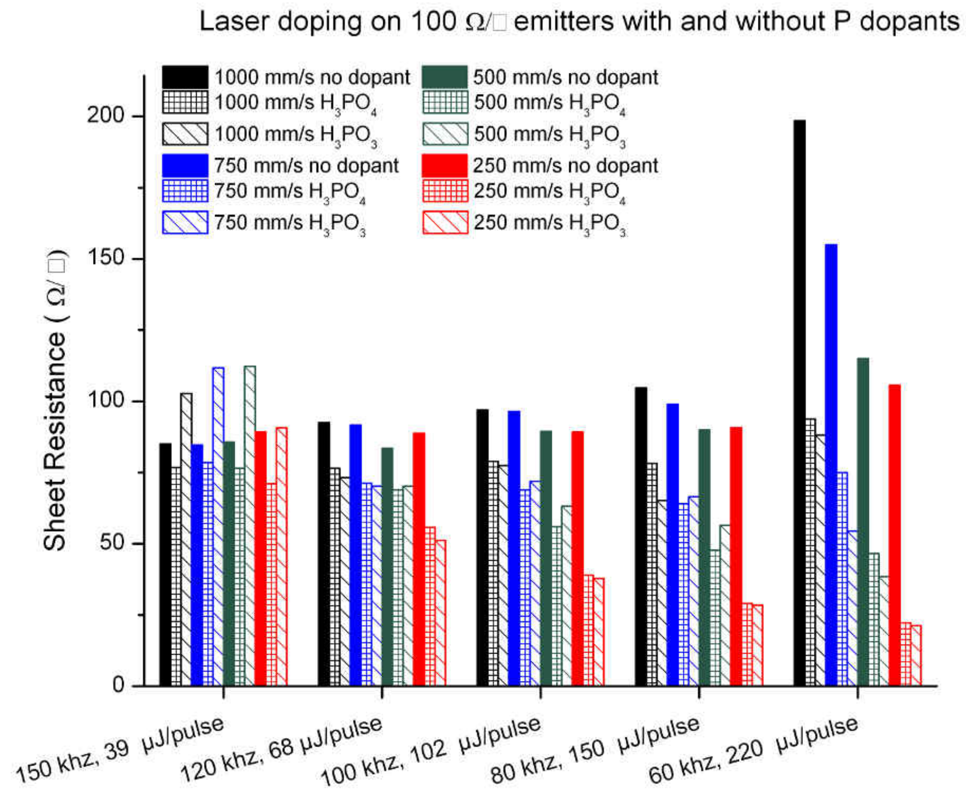

Figure 6.3: Sheet resistance vs laser power, scan speed and P dopant source

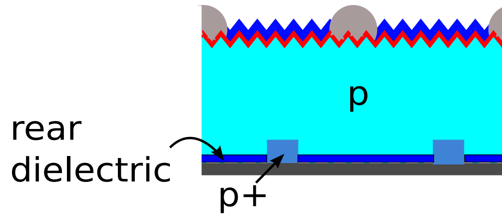

Figure 6.4: Passivated rear contact solar cell with locally diffused boron regions on the rear.

There is also a trend for the reference regions with no dopant added to have a decreasing sheet resistance with slower scan speeds within each pulse power. This is likely due to a redistribution of dopants in the 100 Ω/□ tube diffusion prior to laser processing, with the post laser annealed profile being slightly deeper than the pre-annealed profile. The 60 khz reptition rate produces the most heavily doped layers of all the repetition rates explored. However, without any spin on dopant present the sheet resistance skyrockets after laser irradiation. This indicates that this laser condition as actually so powerful that it is able to remove part of the diffused layer and is probably creating damage to the substrate. In conclusion, higher pulse energies are more effective at producing highly diffused regions but may create damage to the surface of the emitter.

6.2 Laser doping of textured crystalline Si with spin on B dopants and UV laser

While phosphorous laser doping can be used to create a selective emitter in p-type solar cells, boron laser doping could also be used in fabrication of advanced solar cells with a dielectric passivated rear side and locally doped contacts, cell structure shown in figure 6.4. Boron laser doping could also be used to create a selective emitter on n type solar cells with a Boron emitter to fabricate high efficiency n-base cells. Similar to the previous experiment, textured p-type Cz wafers were employed to test the efficacy of UV laser doping of Boron on textured Si. Two boric acid concentrations solutions were used, one with 228 g/L boric acid in methanol and one with 114 g/L boric acid in methanol. The solutions were spun onto the wafers after an HF dip. Laser doping was carried out using the same UV laser system previously discussed. The resulting sheet resistances from B UV laser doping are

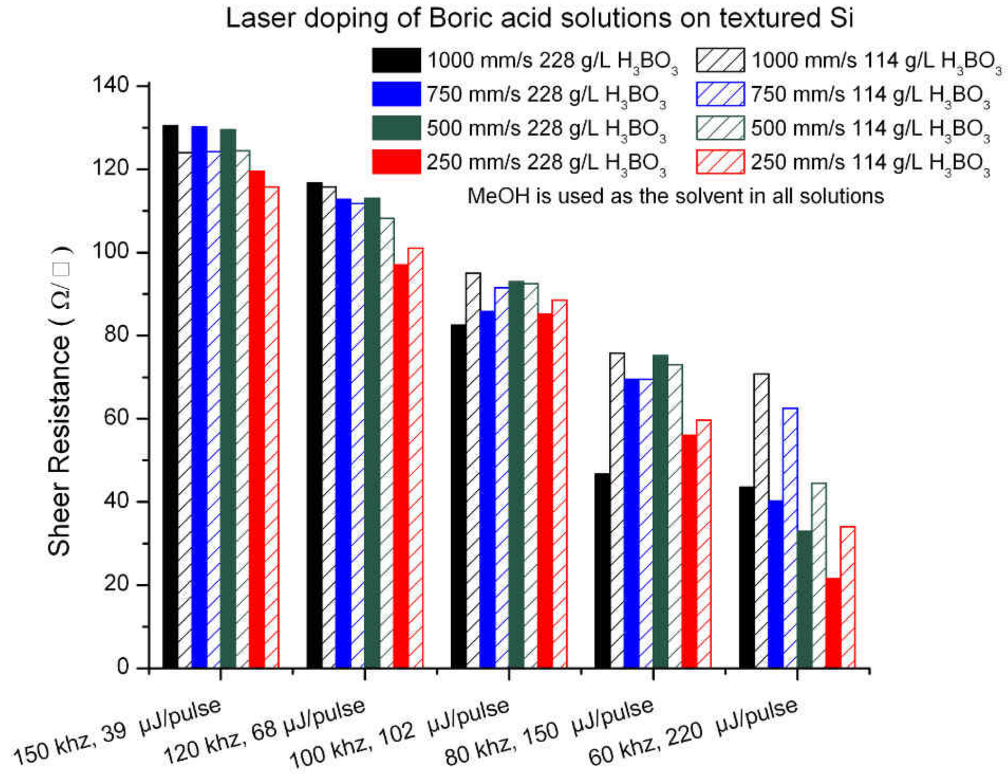

Figure 6.5: Sheet resistance vs laser power, scan speed and boric acid concentration

seen in 6.5. Similar to P dopants, the B laser doped regions that received the highest pulse energy have the lowest sheet resistance. At 150 khz the sheet resistance is around 130 $\Omega/\square$ which is essentially just the sheet resistance of the entire wafer. Since P type wafers were used for this test, the resistance of the laser doped region and the bulk of the wafers are measured in parallel. Therefore the measured values are lower than the actual sheet resistance values. There is no consistent trend as to why the higher concentration boric acid solution gives lower sheet resistance values for pulse energies below 150 μJ/pulse. However at 220 μ J/pulse the higher concentration boric acid solution consistently gives a lower sheet resistance.

6.3 Understanding and Control of Opening widths after laser doping

Laser doping with spin on dopants has been shown to be compatible with high efficiency industrial plated contact solar cells [99]. In a solar cell with laser doped and plated contacts the determining factors in the width of the grid lines is the opening in the SiN anti-reflection

coating and the width of the plated deposit. It is therefore important to characterize how the width of the opening varies with different laser parameters. Because the laser has a Gaussian shape, as the laser pulse power changes different fractions of the pulse contain enough energy to melt Si and remove the SiN layer above it. This concept is explained in figure 6.6. The measured finger widths shown in figure 6.7 were measured by optical

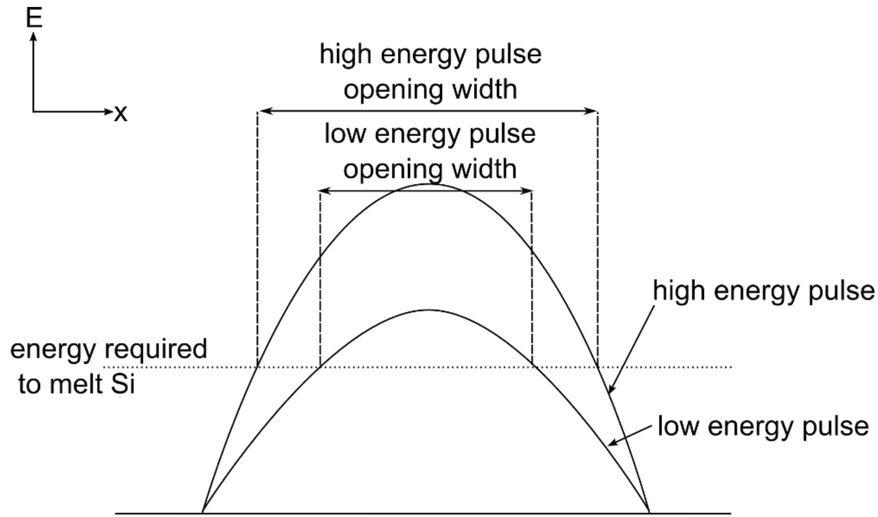

Figure 6.6: Diagram depicting why the opening width varies with pulse power.

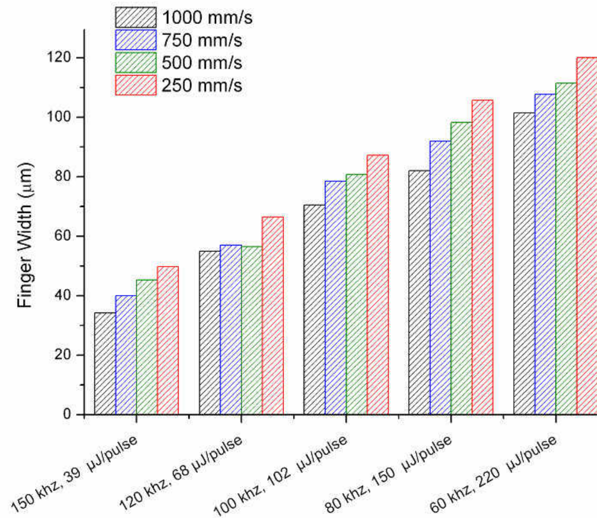

Figure 6.7: Measured opening width versus pulse power and scan speed.

microscope after laser doping on textured Si wafers with PECVD SiN on the front side that

received the laser doping. As expected higher pulse energies give larger finger widths and slower scan speeds also increase the finger widths compares with fast scan speeds.

6.4 SEM investigation of laser doped regions

Textured Si samples were scribed in a line pattern using the same UV laser as in the previous work with pulse repitition rates of 60,80,100,120 and 150 khz all at a scan speed of 250 mm/s. After laser scribing, the wafers were cleaved and cross-sections of the laser scribed regions were explored in a Zeiss Ultra60 FE-SEM. The SEM images can be seen in figure 6.8. The 60 and 80 khz repetition rates clearly are too powerful and create extensive damage to the surface of the wafer. This is consistent with the observed increase in sheet resistance for these repetition rates in figure 6.3 when no external dopant is present. The laser pulses literally blow away the existing emitter layer. The damage created in this regime is not suited for a high performance laser doped device despite its ability to create highly doped regions. At the 100 khz repetition rate, the laser operation does not appear to be stable. At irregular intervals deep holes are left in the surface of the wafer. This effect is assumed to be due to a "missing pulse" where the laser misses a pulse and therefore the population inversion achieved in the laser cavity is much higher for the next pulse and next pulse is significantly more powerful than the other pulses. This pulse is extremely powerful and creates a conical shaped hole over 30 μm deep. This phenomenon was only seen in the 100 khz rep. rate. Therefore, this condition is avoided in all other work because the holes caused by the missing pulse are most likely not laser doped and would therefore present a shunt path between the n^{++} selective emitter and the p type base. The 120 khz rep. rate produces a smooth surface without much visible damage and without craters from missing pulses. It appears that this condition which produces a pulse energy of roughly 70 μJ/pulse contains enough energy to melt the Si pyramids and leave a smooth surface but not so much energy that Si is removed from the surface. At 150 khz (40 μJ/pulse) the Si pyramids begin to melt but not completely. Thus, only the 120 and 150 khz rep. rates for UV laser doping gave an acceptable surface for Si device fabrication.

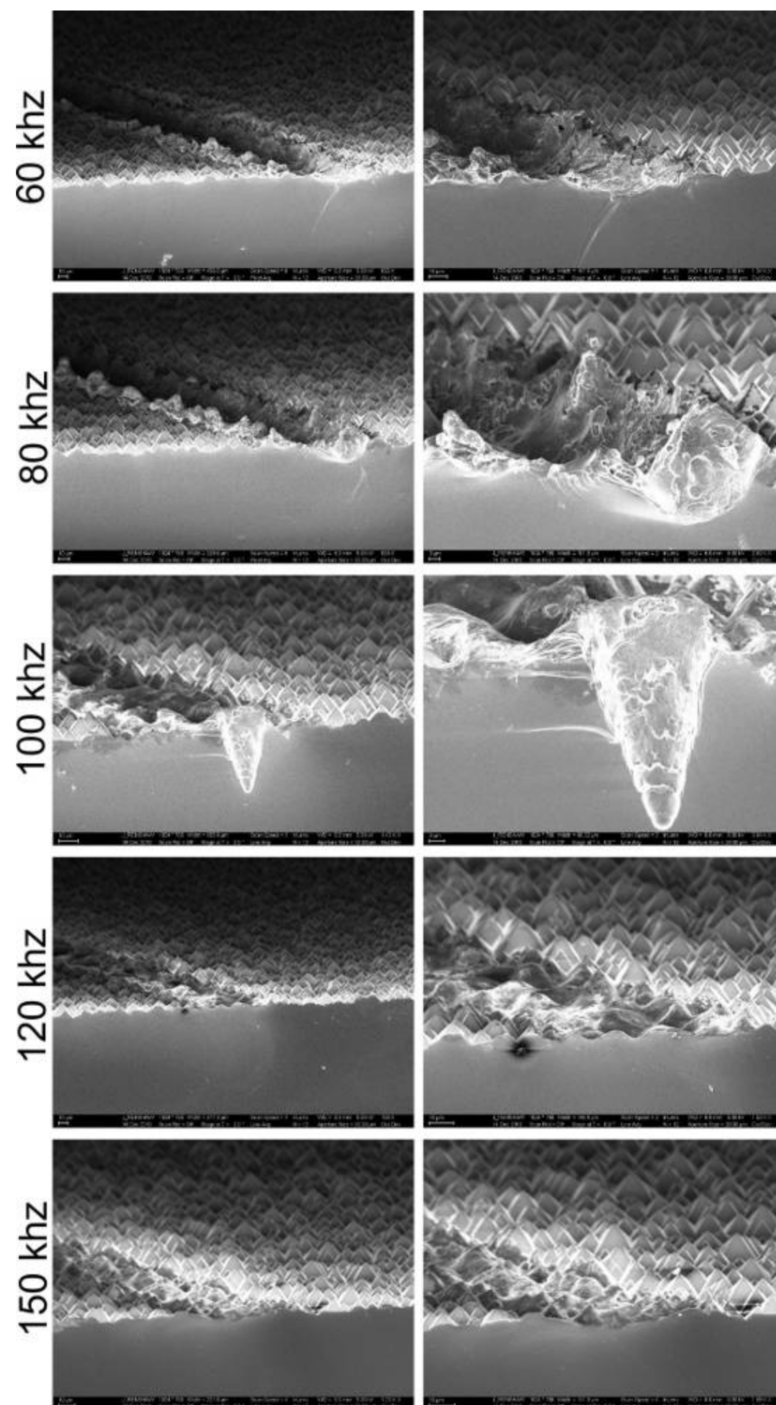

Figure 6.8: Cross sectional SEM images of textured laser scribed Si.

6.4.1 Conclusions of the feasibility of plated contact cells by pulsed UV laser radiation and spin on dopants

In conclusion, a UV laser system is not well suited for creating selective emitters with a spin on dopant for plated contact cells. The 60 and 80 khz rep. rates produce acceptable doping levels but they create too much damage and the line width of over 100 μm is unacceptable. It should be noted the the line width could be reduced by changing the optics of the laser system. At the 100 khz rep. rate the laser is unstable and creates deep holes in the wafers and unsuited for device fabrication. The 120 and 150 khz rep. rates create an acceptable surface for device fabrication and give narrow opening widths but fail to give a high doping level which is the aim of a selective emitter device.

6.5 Development and Optimization of Laser doping textured crystalline Si with P-glass source

After concluding that a pulsed UV laser system is not well suited for the manufacture of high efficiency solar cells by means of a spin on dopant, the feasibility of using the P-glass(that is a product of $POCl_3$ diffusion) was explored. This process is more elegant than spin on dopant method in that does not require the purchase of an additional P source because the P-glass that is a natural byproduct of standard P-diffusion used for lightly doped field region. Additionally, spin on dopants are generally used in conjunction with plated contacts which have not been widely adopted in industry because of the challenges associated with background plating and nickel shunting. Using the P-glass as the dopant source only adds one additional low-cost processing step and is compatible with industry standard screen printed contacts.

6.5.1 Laser doping on an industrial type emitter

In this experiment 156 mm textured P type Si wafers were cleaned in HF and HCl and then diffused in a tube furnace with a $POCl_3$ source. The diffusion resulted in a roughly $63\Omega/\Box$ diffused layer and a P rich SiO_2 glass on the surface. Boxes were then laser doped using the same tools and methods described in the previous sections and the sheet resistance was meausred. The results of the experiment are seen in figure 6.9 Wafers from the same

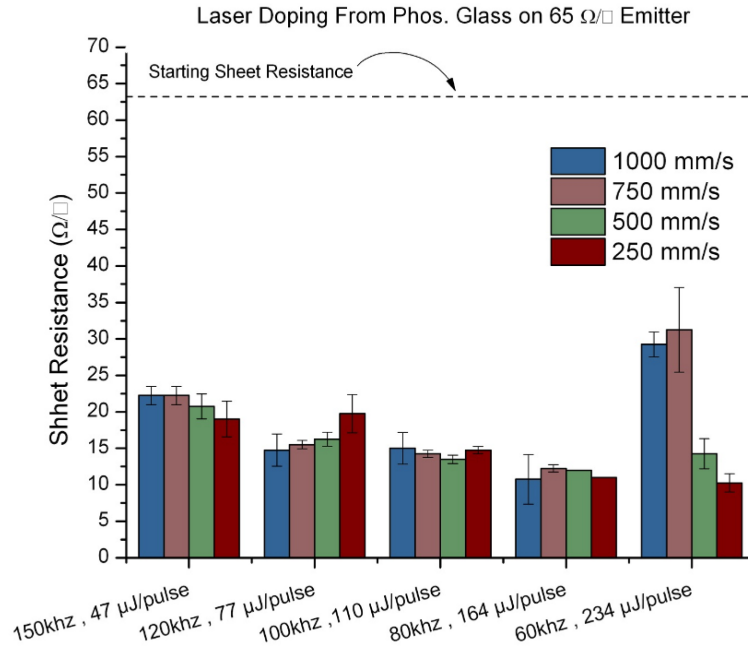

Figure 6.9: Sheet resistance produced from laser doping under different rep. rates and scan speeds on an industrial type emitter.

	Jsc(mA/cm^2)	Voc (V)	FF (%)	Eff. (%)	Rs (Ω-cm^2)	Rsh(Ω-cm^2)
60 Khz	26.6	0.596	58.7	9.3	4.02	130.05
80 Khz	29.5	0.615	60.3	11.0	3.69	143.43
120 Khz	33.1	0.624	78.6	16.2	0.65	4357.77
150 Khz	33.4	0.624	78.7	16.4	0.58	2863.52
No Laser	35.5	0.625	78.5	17.4	0.64	4880.38

Table 6.1: IV Data from UV laser doping on a typical industrial type solar cell

experiment were laser doped in a pattern identical to the front Ag-grid pattern for the front Ag paste. The laser doped regions were roughly 500 μm wide to allow for sufficient room for alignment during the Ag screen printing step. After laser doping the wafers were cleaned in HF and edge isolated. Following edge isolation the SiN anti-reflection coating was deposited by low frequency PECVD. Finally, Ag paste was screen printed on the front and Al paste was screen printed on the rear of the wafer and the wafer was fired in a belt furnace with a peak temperature around 750°C. Process shown in figure 6.10. The finished device results are shown in table 6.1. The 60 and 80 khz laser doped solar cells gave very low cell efficiency (¡12%) due to shunt resistance values, suggesting that the Ag paste may

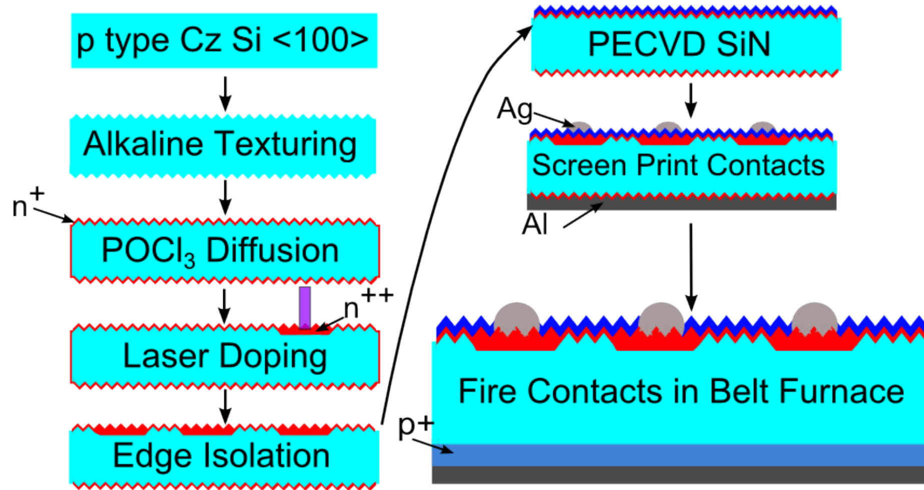

Figure 6.10: Process sequence for laser doped selective emitter cells.

have shorted the n^{++} selective emitter to the p type base. This is not surprising given the amount of damage that was seen from these conditions in figure 6.8. This shunt is most likely caused by the laser thinning or removing the emitter layer in various regions, exposing the base. The proposed shunt path is shown in figure 6.11. Devices made with a 120 and 150 khz laser doped selective emitter showed no signs of shunting and had similar Voc and FF to the reference cell with no selective emitter. However, these selective emitter devices had poor Jsc compared with the reference because of poor response in the laser doped regions. As a result, cell efficiency was lower for the 150 khz laser doped cells in spite of slight improvement in improved fill factor and series resistance over the reference cells with no laser doping. Since the wafers were printed with the same Ag paste using the same screen, we assumed that the slight reduction in the series resistance is due to reduced contact resistance and not due to finger conductivity. The resistance due to carrier travel through the emitter sheet should also reduce the series resistance, however, the series resistance for the 120 khz laser doped sample is the same as the reference so this effect does not seem to be large. This further justifies the assumption that the 150 khz samples have reduced contact resistance. Further proof of reduced contact resistance is given in later chapters. This result demonstrates that UV laser doping can be used to improve contact properties in textured Si solar cells.

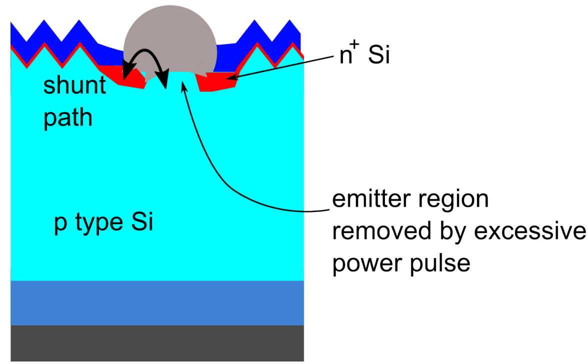

Figure 6.11: Shunt path created from excessive power pulse.

6.5.2 Laser doping on lightly doped emitter

In section 6.5.2, it was demonstrated that laser doped selective emitters can reduce series resistance on a solar cell with a highly doped (60 Ω/□) industrial type emitter. However, these emitters have good contact properties even without a selective emitter. In this section, the previous experiment will be repeated on lightly doped emitters that have poor contact properties without a selective emitter. Similar wafers as used in the previous experiment were cleaned and then diffused in a tube furnace to obtain to 90 Ω/□. Several samples were set aside to have a test pattern laser doped so that the sheet resistance could be measured while others were laser doped selectively by driving in the P-glass in the pattern of the front grid lines. The remaining wafers received no laser doping and served as a reference. All of the wafers that did not receive the test pattern were then edge isolated, AR coated, screen printed and fired. The sheet resistance measurements on the test wafers are summarized in figure 6.12. Figure 6.12 reveals that laser doping on the high sheet resistance emitter has different behavior than on an industrial emitter. As the pulse power decreases the sheet resistance increases much more than on the industrial-type emitter. For example, at the 250 mm/s scan speed the sheet resistance is 20 Ω/□ at the 60 khz rep. rate and increases to 45 Ω/□ at the 150 khz rep. rate. For the baseline emitter the difference between these two conditions was only 7 Ω/□. The difference in doping levels between the industrial and high-sheet resistance emitter after laser doping is likely due difference in initial doping levels as well as the quantity of P in the glass layer. The high sheet resistance emitter examined here has a much lower $POCl_3$ flow rate than the industrial type emitter and as a result

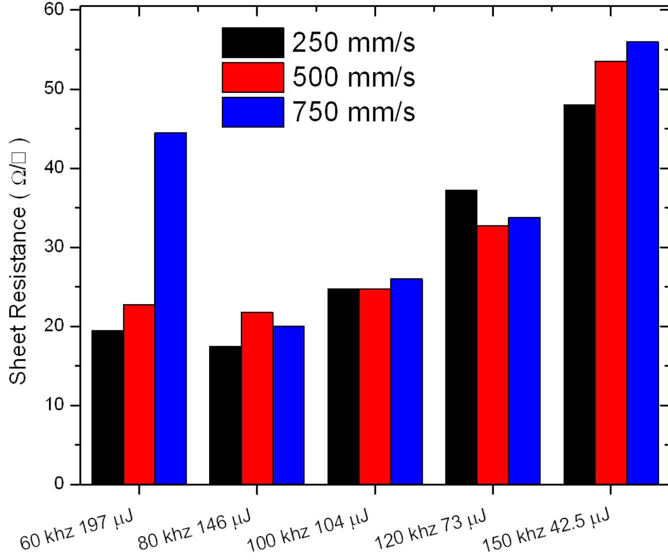

Figure 6.12: Resulting sheet resistances from various laser doping conditions.

Table 6.2: Average IV results from solar cells with high sheet resistance emitters, with and without laser selective emitter

	Voc (V)	Jsc (mA/cm^2)	FF(%)	Eff (%)	Rseries (Ω-cm^2)	Rshunt (Ω-cm^2)
120 khz 43μJ	0.635	36.1	75	17.2	1.40	11842
150 khz 25μJ	0.636	36.2	74	17.1	1.67	18030
Reference	0.633	36.3	66	15.1	3.65	10385

there should be less P in the glass.

The IV results from wafers fabricated into selective emitter solar cells with 90 Ω/□ field region are shown on table 6.2. On these lowly doped emitters the laser doped samples performed much better than the reference without a selective emitter. The performance difference is mostly seen in the FF which is roughly 10% higher (absolute) in the selective emitter samples. The level of defects generated due to the laser doping was not enough to lower the Voc of the selective emitter cells using either 120 or 150 khz rep. rates. In fact, both selective emitter conditions have an improved Voc compared with the reference, possibly due to the the increased doping level beneath the contacts, shielding carriers from the high recombination Si/Ag paste interface. The average Jsc of the selective emitter cells

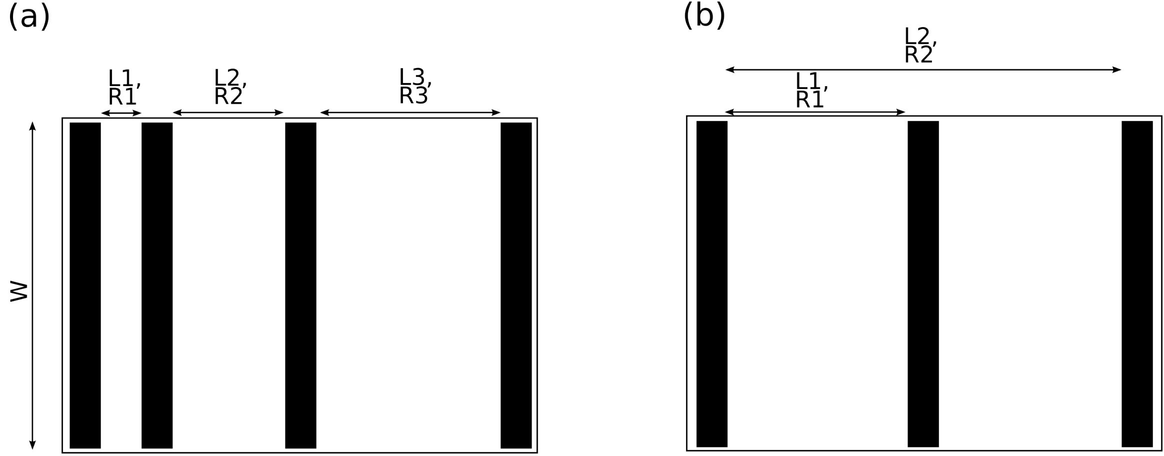

Figure 6.13: (a)An example TLM pad.(b) non-ideal TLM pad made from dicing solar cell.

is lower than the reference cells. This is due to a combination of lower spectral response [96] and change in the reflectance properties in the selective emitter region. The loss in performance due to change in reflectance is investigated in section 6.5.5. Also note that the series resistance in the selective emitter cells is less than half of the series resistance achieved on the same emitter without a selective emitter, indicating the benefit of selective emitter formation over the homogeneous emitter reference cells. The contact resistance was measured on these samples using the transmission line method or TLM [100]. In the TLM method contacts are formed at increasing length intervals as shown in figure 6.13 and then the resistance between each contact pad is measured. The contact resistance, R_c, and sheet resistance, R_{sheet}, can then be extracted by a linear fit using equation 6.2.

$$[htb]R_{total} = R_{sheet}\frac{L}{W} + 2R_c \tag{6.2}$$

The TLM strips were created from these cells by dicing out a 1mm strip, perpendicular to the direction of the grid lines. Since the grid lines are all spaced at the same interval, measurements had to be made across contact pads that had one or more contact pads between them to get increasing values of L/W. This introduces error because the derivation of equation 6.2 assumes a layer of uniform resistance . The results of the TLM measurement, however, still give a good indication of the contact resistance.The TLM measurements shown in figure figure 6.14 reveals significantly lower contact resistance on the 120 and 150 khz laser doped samples compared with the reference with respective contact resistance values

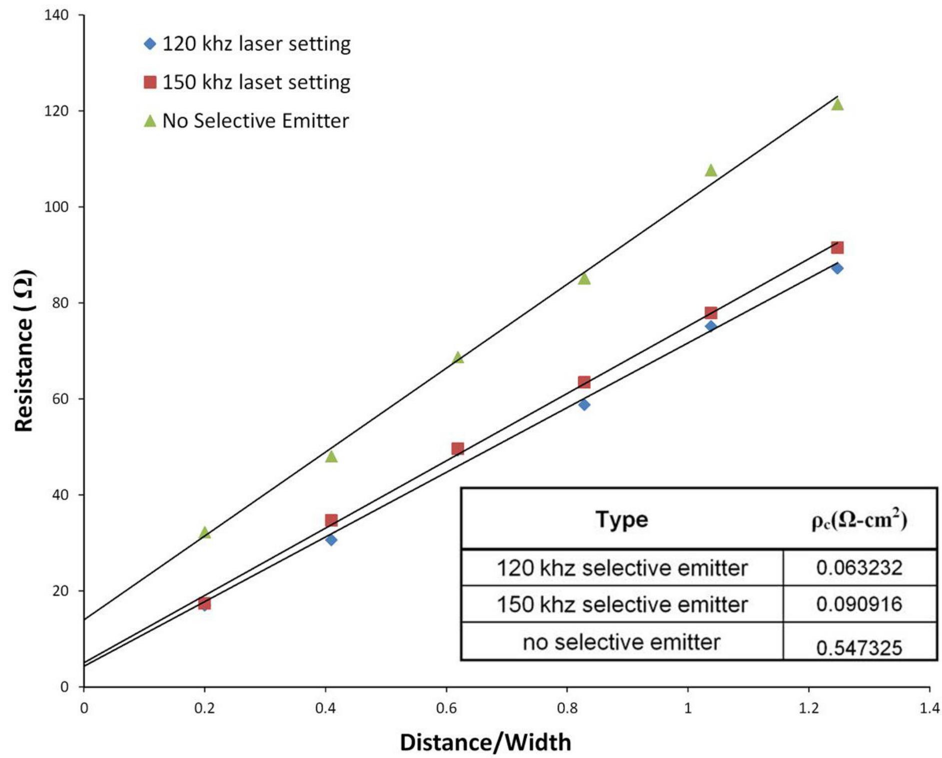

Figure 6.14: TLM measurements on 120 and 150 khz selective emitter solar cells compared to high sheet resistance reference without selective emitter.

of 63, 90 and 547 mΩ-cm^2. In conclusion, UV laser doping reduces contact resistance on C-Si solar cells, the resulting in an order of magnitude drop drop in contact resistance for the 120 khz condition.

6.5.3 Investigation of the effect of selective laser doping on carrier lifetime and the local Voc

Six inch textured Cz wafers were cleaned, P diffused and laser doped using 60, 90, 120 and 150 khz rep. rates all at 250 mm/s in a pattern that coincides with the front grid pattern for a solar cell to ensure the same area fraction of laser doping as would be characteristic of an actual device. After laser doping the lifetime was measured using the quasi-steady state photoconductance method [101]. The measurement works by injecting carriers into the wafer via a flash from a lamp that varies slowly in time compared with lifetime of the carriers in the wafer. The excess conductivity due to the injected carriers is measured with an inductively coupled coil. The effective lifetime contains information about the lifetime

of the carriers in the bulk as well as at the surface according to to equation 6.3.

$$\frac{1}{\tau_{eff}} = \frac{1}{\tau_{bulk}} + \frac{1}{\tau_{surf}} \tag{6.3}$$

Since the wafers are all adjacent wafers from the same ingot and received the same texturing and $POCl_3$ diffusion it is reasonable to assume that the starting bulk lifetime of the wafers is the same. Further, since laser doping only locally heats the substrate it is a reasonable assumption that any observed change in lifetime should be attributed to changes in the lifetime of carriers near the surface of laser doped regions. The QSSPCD measurements were carried out before and after the laser doping step, the change in lifetime is plotted in figure 6.15. Appreciable change in lifetime was observed after laser doping. The change in

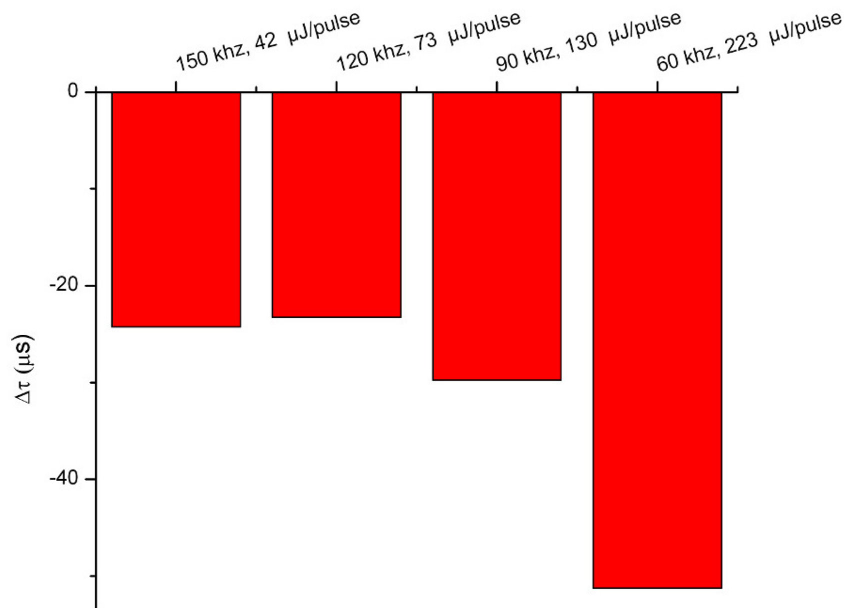

Figure 6.15: Change in effective lifetime after the laser doping step for various laser conditions.

lifetime was greatest for the 60 khz rep. rate which has been previously shown to create excessive damage. The 150 and 120 khz conditions showed the smallest drop in τ_{eff} of only about 25 μs compared to 50 μs at 60 khz. The drop in lifetime is due to a combination of increased auger recombination in the laser doped layer, defects created from the laser doping process and loss of surface passivation on top of the laser doped regions.

Further insight into how laser damage affects device performance is gained through using

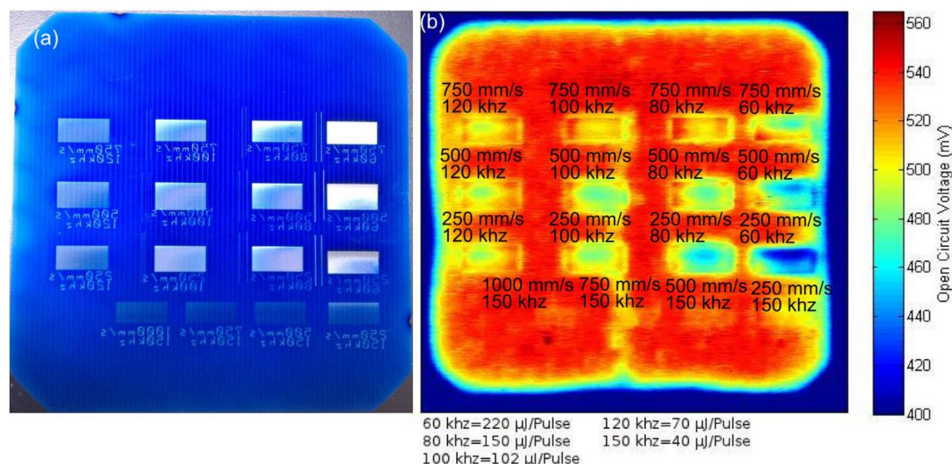

Figure 6.16: (a) picture of wafer after VocScan measurement, (b) contour plot of Vocscan data for the field and laser doped regions.

the Vocscan tool called Correscan. A Vocscan measurement requires a finished solar cell without the front grid lines. The Vocscan works by shining a light on a small area of the wafer (roughly 3mm) and probing the voltage in the middle of that point with a stiff metal wire with the device at open circuit. The light and wire simultaneously scan across the wafer at your desired speed and resolution, mapping the Voc across the wafer. This test is useful for probing the uniformity of passivation quality and recombination in the emitter. In this an area with poor Voc indicates significant damage to the surface.

Wafers were prepared for correscan by the following steps: Clean in HF and HCl, $POCl_3$ diffusion, laser doping with various rep. rates and scan speeds in boxes across the surface of the wafer,PECVD SiN for passivation, Al paste printing and firing for rear side contact. The Vocscan outputs a text file of x,y, Voltage values which are then plotted in matlab. A contour plot of the results can be seen in figure 6.16. As expected, the 60 khz rep. rate with roughly (220 μJ/pulse) exhibits the lowest Voc of all the conditions investigated. For each rep. rate, as the scan speed increases the local Voc increases, this is clear evidence that extra laser pulses hitting the same spot repeatedly increases the damage and limits performance. As expected, the lower power pulses cause less damage to the surface and have higher local Voc. For 1000 mm/s scan speed and 150 khz rep rate. the laser doped region is almost indistinguishable from the background, indicating very little damage. In

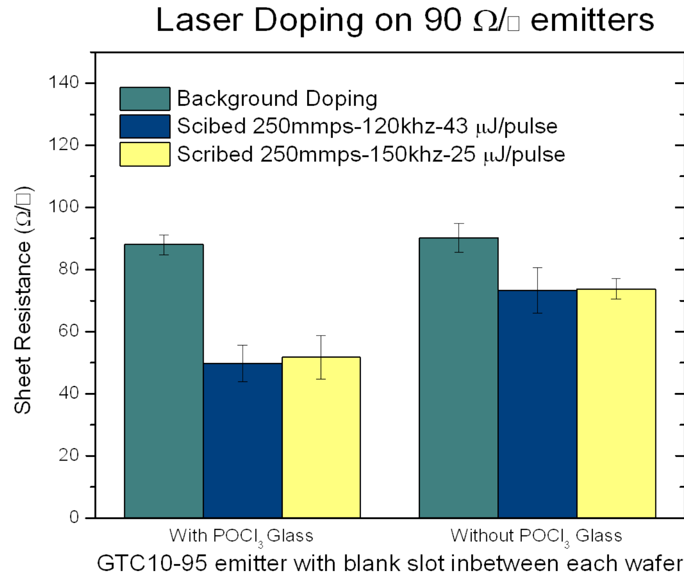

Figure 6.17: Resulting sheet resistance from laser doping on a 90 Ω/□ emitter with and without the P glass for 120 and 150 khz rep. rates.

summary, low rep. rates and high scan speed minimizes the damage to the emitter region and should be chosen if possible for best performance.

6.5.4 Understanding the role of the dead layer in laser doping

$POCl_3$ diffusions for Si solar cells often have a "dead layer" near the highly doped surface which is attributed to excess inactive interstitial P atoms [54]. It is possible then that these excess P atoms could act as an additional dopant source during laser irradiation if these atoms are driven in and activated. To determine the role of the dead layer in the laser doping process, a batch textured Si wafers were $POCl_3$ diffused. Following diffusion half of the wafers had the P-glass removed with a HF dip until they were hydrophobic, each set of wafers were then laser doped using only the 120 and 150 khz rep. rates because they have proven to be the least damaging. The samples with no P-glass only have the dead layer as a source for additional doping. The resulting sheet resistances from these two groups is shown in figure 6.17. Without P-glass the sheet resistance is reduced compared with the non laser doped regions, but only by roughly 15 Ω/□ , whereas the sample with P-glass' sheet resistance is reduced by roughly 50 Ω/□. This experiment conclusively shows that the

P-glass is the main dopant source and not the emitter dead layer, however it does appear that the dead layer can contribute to some doping.

6.5.5 Laser doping and front surface reflectance

When creating a selective emitter for a screen printed solar cell, the width of the selective emitter should be larger than the grid lines so that they can be aligned during the screen printing step. We have found that 500 μm wide is about the minimum width that we can give the selective emitter and still align to it. This is roughly 400 μm wider than a Ag grid lines. The extra width of the selective emitter constitutes 20% of the available collective area between grid lines for a grid line spacing of 2.1 mm and a finger width of 100μm. Therefore, the reflectance of the laser doped selective emitter should be optimized as well as the electrical properties if possible.

The reflectance of three finished solar cells was measured, two with UV laser selective emitter (one with 120khz rep. rate and one 150khz) and one standard without. The measurement was made using a system from Optronik. The tools basically consists of a light souce, a filter wheel with roughly 10nm spectral width, an integrating sphere and 2 photodetectors. A Si photodetector is used for wavelengths between 250 and 1000 nm and a Ge detector for 1000 to 1250nm. The results of the measurements are plotted in 6.18. The reference cell without a selective emitter has the lowest reflectance of the three samples. This is most likely due to the pyramidal texturing not being removed by laser doping. A useful way to quantize a reflectance measurement is by calculating the average weighted reflectance, AWR, which is essentially the photocurrent reflected divided by the total available photocurrent. An expression to calculate AWR is found in equation 6.4.

$$AWR = \frac{\int_{\lambda 1}^{\lambda 2} R(\lambda)S(\lambda)d\lambda}{\int_{\lambda 1}^{\lambda 2} S(\lambda)d\lambda} \tag{6.4}$$

In Eq. 6.4 $R(\lambda)$ is the reflectance and a function of wavelength and $S(\lambda)$ is the AM15G spectrum. The AWR data is consistent with the images in figure 6.8 showing that the 120 khz, 70 μJ/pulse condition melts away the surface texture, resulting in a smooth surface where as the 150 khz, 40 μJ/pulse condition rounds out the pyramids but the surface is not completely smooth. The rougher texture of the 150 khz rep .rate laser doped regions

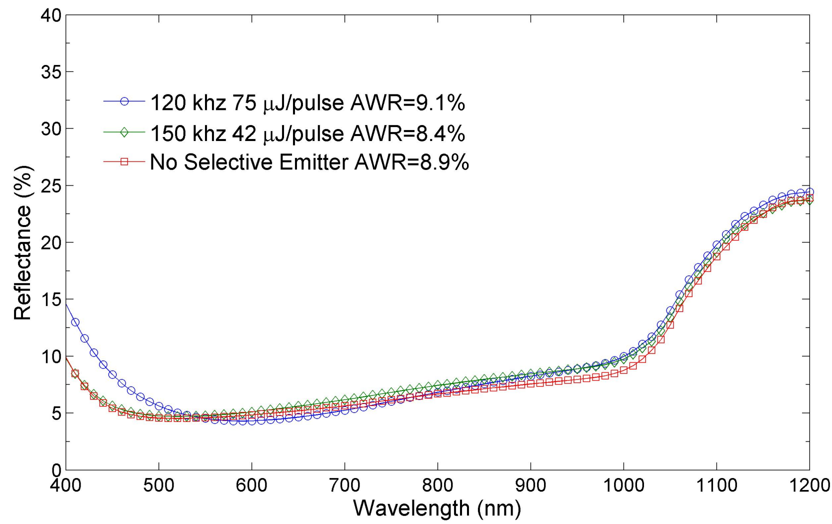

Figure 6.18: Reflectance data from solar cells with a selective emitter created with 120 and 150 khz pulse repetition rates and a standard with no laser doping .

has a 0.2% lower AWR compared with 120 khz but is still 0.5% higher than the reference. These AWR's result in 42.6, 42.7 and 42.9 mA/cm^2 of photocurrent available for the 120 khz selective emitter cell, 150 khz selective emitter cell and reference cell respectively. In summary, the 150 khz rep. rate shows less altering the surface relative to 120 khz and, therefore, it has superior reflectance properies.

6.6 Conclusion

This chapter deals with the fundamental understanding and formation of selective emitters using UV laser doping in conjunction with various dopant sources. The potential and technology for forming selective emitters by UV laser is demonstrated. It is shown that P-glass doping for selective emitter formation is effective at producing highly doped regions, but using spin-on dopants with a pulsed UV laser system is not very compatible with the manufacture of high efficiency devices. For the spin on dopants there is a trade off between the doping level and the amount of damage created. To generate highly doped regions using the spin on dopant, high pulse powers must be used which also create damage which kills the device performance. It is shown that with lower power UV laser radiation high doping levels are achieved with a P-glass source while simultaneously minimizing damage

to the surface. The resulting selective emitter layers show nearly an order of magnitude lower contact resistance compared with a reference without a selective emitter on high sheet resistance emitters.

CHAPTER VII

UV LASER DOPED SELECTIVE EMITTER SOLAR CELLS

7.1 Introduction

A selective emitter is a highly diffused region beneath the grid lines in a solar cell. Selective emitter devices can be optimized to have low contact resistance by adjusting the selective emitter doping and to simultaneously minimize recombination in the emitter through tailoring the field emitter between the grid lines. This removes the compromise between good contact and good emitter recombinatoin porperties that must be made in solar cells with a homogeneous emitter and allows simultaneously high FF, Jsc and Voc. The selective emitter concept has been used to create record efficiency solar cells such as the PERL (passivated emitter rear locally diffused)cell [102].

Many technologies exist for creating selective emitters in crystalline Si solar cells. A review of these methods is given in section 7.2. This chapter introduces the segmented selective emitter concept to screen printed solar cells. By segmenting the selective emitter the fraction of the emitter with heavy doping is reduced and therefore the recombination in the emitter is reduced. The benefit of the segmented selective emitter is seen by an increase in the short circuit current compared to a continuous selective emitter. The increase in Jsc of segmented selective emitter cells is shown to be attributed to the response of the regions around the grid lines by laser beam induced current (LBIC) measurements. Additionally, segmented selective emitter devices can have similar contact resistance to continuous selective emitter devices as demonstrated by the correscan method.

7.2 Review of selective emitter technologies

Selective emitters have been reported to increase absolute efficiency by up to 0.95% [53]. For a selective emitter technology to be industrially viable it should increase cell efficiency through the addition of a minimal number of steps (prefereably one) whose cost is small enough so that the price in $/W is reduced compared to devices without a selective emitter.

In this section a review of selective emitter technologies will be given followed by a summary of their performance.

Innovalight has developed a doped silicon ink which is screen printed onto the front surface of the wafer before $POCl_3$ diffusion in the pattern of the front grid lines. The diffusion recipe is tailored so that the sheet resistance in the field region is roughly 100 $\Omega/\Box$ while the region beneath the doped silicon ink is less than 50 $\Omega/\Box$. Following diffusion the fabrication process is identical to a standard industrial solar cell. The silicon ink is visible to the naked eye so the screen printed grid lines can easily be aligned. Figure 7.2 shows a cross section of the Innovalight "Cougar Cell". Centrotherm has demonstrated selective

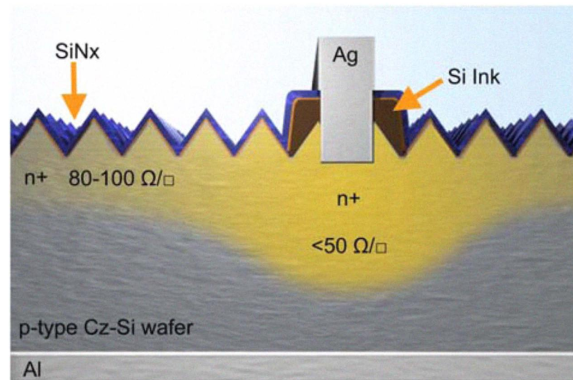

Figure 7.1: Cross section of the Innovalight "Cougar Cell" [53].

emitter formation through the use of a diffusion barrier layer. This process, seen in figure 7.2 utilizes a diffusion barrier which partially blocks diffusion between the grid lines. The diffusion barrier is applied after wafer texturing. Laser ablation removes the barrier layer in the regions that will become the highly doped selective emitter layer while the barrier is left intact everywhere else. After barrier layer patterning, the laser damage is removed and the emitter and selective emitter are formed simultaneously during $POCl_3$ diffusion. Following diffusion the cell processing is identical to a typical industrial Si solar cell. This process introduces several extra steps and therefore may no be feasible for industrial application.

A similar selective emitter approach has been demonstrated by GP solar. Their process, Figure 7.2, uses an etching paste and two diffusion steps to acheive a selective emitter. First, a light diffusion creates a 100 $\Omega/\Box$ emitter. Following diffusion an etching paste is screen

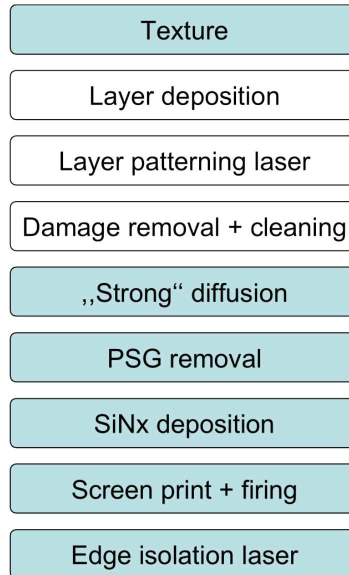

Figure 7.2: Process flow for Centrotherm's S.E. by barrier layer patterning, steps in white are additional compared to the standard industrial process [103].

printed onto the wafer which removes the oxide from diffusion in the regions where the grid lines will be. After the etching paste is cleaned off a second heavier diffusion is performed at 50 $\Omega/\square$. This process requires three additional steps compared to the standard process with one of them being a high temperature step. These additional steps are prohibitive to this process going into manufacturing.

Varian (now owned by Applied Materials) has developed an P ion implantation technique which achieves a selective emitter through two implantation steps and one anneal step [105]. One implantation step creates the blanket emitter across the whole front side of the wafer while the other uses a mask so that only the regions where the selective emitter will be receives an extra P dose. One benefit of this process is that it creates a single sided diffusion which alleviates the need for an edge isolation step. Additionally, during the anneal step, a thermal oxide is grown on the surface of the wafer which provides superior passivation to SiN alone [106]. This oxide also reduces the thickness of SiN necessary to complete the AR coating which increases throughput on the PECVD SiN step. This process is compared with a typical process sequence in figure 7.2

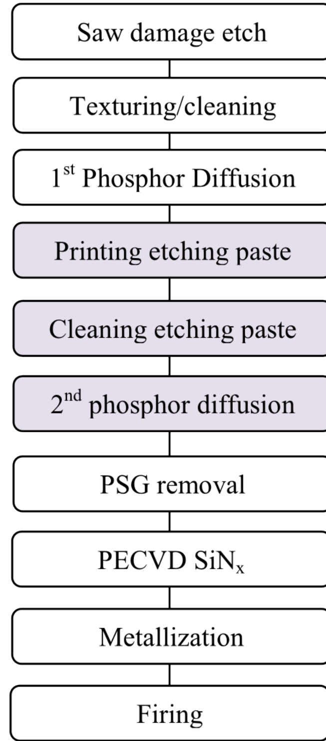

Figure 7.3: Process flow for GP Solar's S.E. by two diffusions and etching paste patterning compared with a standard process, steps in gray represent additional steps compared with a standard process flow for industrial type cells [104].

The emitter etch-back is another method for creating S.E. developed by the university of Konstanz [107]. This process employs a chemical etch to remove the highly doped surface of the wafer in the field emitter regions. The etching solution usually comprises of a mixture of $HF/HNO_3/H_2O$ but alkaline etching solutions have also been investigated. The selective emitter regions are protected by a screen printed etch barrier which must be removed following the etch-back. While this process adds three additional processing steps, see figure 7.2, all of them are with tools already existing in manufacturing and as a results Schmid has commercialized this process and it is available today.

Finally, another method for selective emitter formation on screen printed Si solar cells is by laser doping using the P-glass that is a byproduct of $POCl_3$ diffusion. This method has been reviewed in chapter 5 so it will not be reviewed in detail here. However, it is worth noting that this method only contains a single additional step compared to a

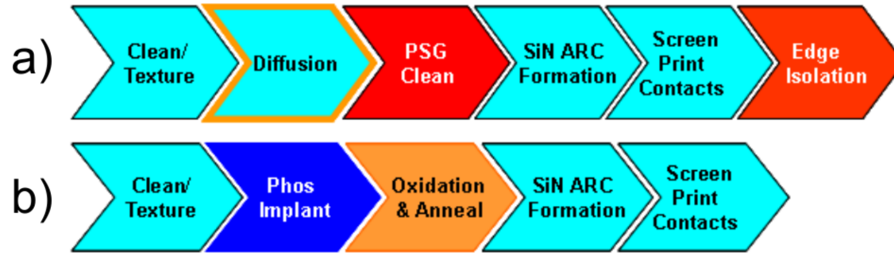

Figure 7.4: Varian's implant S.E. process (a) compared with a standard industrial fabrication sequence (b). Steps in red are removed by the implantation process flow [105].

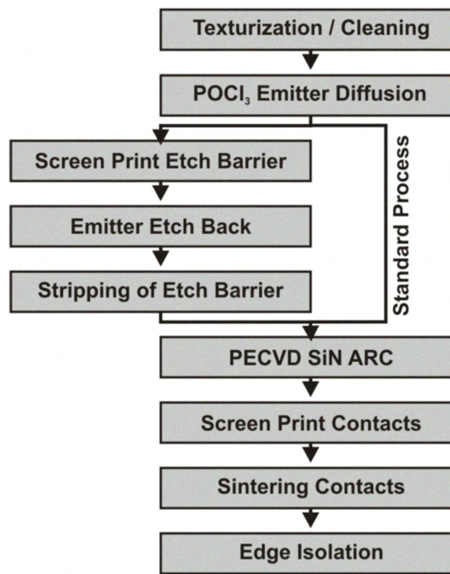

Figure 7.5: Process flow for S.E. solar cells by emitter etch-back method [107].

typical industrial step. In addition, it does not require any additional consumables per wafer like some of the other S.E. processes (e.g. silicon ink or etch resist). The only cost associated with including a laser doping processing step it the cost of the laser system and it's maintenance.

Thus far in this chapter a review of S.E. technologies that incorporate screen printed contacts has been given. However with the rising cost of Ag, plated contacts are an appealing alternative. Plated contacts are self aligned and usually employ a Ni barrier layer and Cu as the main grid line component while making use of low resistance Ni silicide contact

interfaces. These advantages have led to the development of several technologies with plated contacts.

UNSW has developed an process using a spin on resist which is patterned by selective inkjet deposition of diethlyine glycol [108]. Fabrication of these cells, figure 7.2 require a thermal oxidation step, an inkjet step, a HF dip, a resist removal step and a second diffusion in addition to that standard process flow making it an unlikely contender for industrial application.

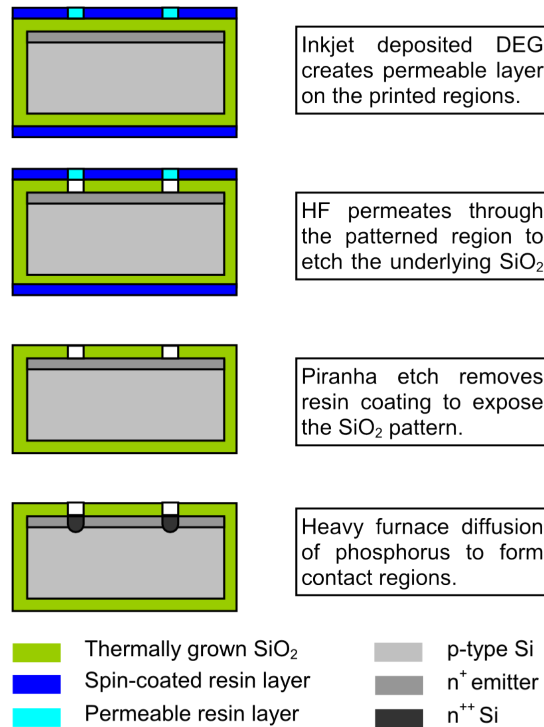

Figure 7.6: Process flow for UNSW's inkjet method for selective emitter with plated contacts [108].

The other common methods for creating plated contacts devices use laser processing and have been described already in chapter 5, these include laser doping with a spin on dopant such as phosphoric acid, or laser chemical processing which employs laser beam coupled inside a liquid stream of dopant or laser transfer doping. All of these methods have identical processing to an industrial type cell up until the SiN AR coating step. Following PECVD SiN they each receive their perspective laser doping methods and the rear Al is screen

printed an fired and then the front contacts are plated using a combination of Ni and Cu plating. The challenges that must be met with plated contacts are overcoming background plating, achieving good contact adhesion and overcoming the high cost of disposal of used plating solutions.

A review of the IV characteristics that each of the described methods has produced is shown in table 7.1.

Table 7.1: Review of IV characteristics from various selective emitter technologies [53, 95, 103, 52, 99, 104, 108, 91, 93, 109, 107]

S.E. method	V_{oc}(mV)	J_{sc}(mA/cm^2)	F.F. (%)	Efficiency (%)
	Screen Printed Contacts			
Silicon Ink	637	37.6	78.9	18.9
Intersected Laser Doping	618	36.2	79.3	17.7
Oxide Mask (Laser)	633	36.9	78.1	18.2
Oxide Mask (Etch Paste)	638	37.1	79.5	18.8
Ion Implantation	641	37.2	37.5	18.7
Emitter Etch-Back	634	36.0	79.4	18.1
Laser Doping (P-glass)	629	37.1	77.2	18.0
	Plated Contacts			
Laser Doping (spin-on)	638	38.4	78.8	19.3
Inkjet Resist	607	33.6	80.0	16.4
LCP	631	38.1	77.5	18.6
Laser Transfer	603	39.5	73.4	17.5

7.3 Experiment

The laser employed for this research is a pulsed, frequency tripled Coherent Avia laser with a wavelength of 355 nm. A scan head is used to raster the beam across the wafer surface in the desired pattern, the scan speed across the wafer is 3000 mm/s and the laser spot has an 50 μm diameter and is gaussian in shape. In this work we used commercial grade 2 Ω-cm, 239 cm^2, Czochralski (CZ) grown Si, P type wafers. The fabrication procedure for LDSE cells is shown in figure 7.3. This process only varies slightly from a standard industrial solar type cell process flow, the only additional step is laser doping. The first step in the LDSE process is to remove the saw damage and texture the surface with pyramids to reduce

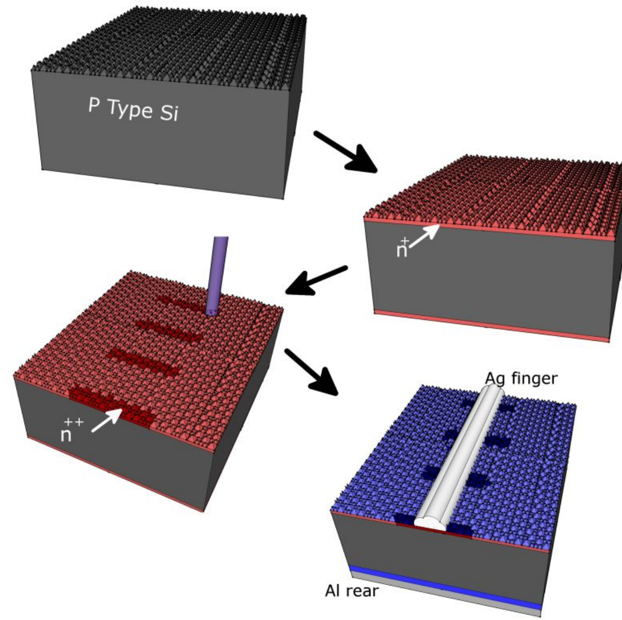

Figure 7.7: Process flow for LDSE solar cells. Step 1: Damage Etch and texture wafer surface Step 2:POCl_3 diffusion to create the n$^+$ emitter Step 3:Laser doping in selective regions to create the n^{++} regions Step 4:Finish the solar cell by chemical edge isolation, PSG removal, PECVD SiN for the antireflection coating,screen printing and firing contacts

reflectance. This is followed by diffusion in a tube furnace using $POCl_3$ as a P source. After diffusion the Si surface is now n^+ with a PSG coating. After diffusion laser doping beneath the grid lines drives in P dopants from the PSG glass in 500 μm long strips that are spaced about 100 μm center to center and have the width of the laser spot size. The resulting doping profiles from POCl_3 diffusion and laser doping for various laser conditions can be seen in figure 7.3. Following laser doping the wafers go through chemical edge isolation and PSG removal in HF. A commercial PECVD SiN tool is then used to form the antireflection coating on the wafers before Ag and Al paste are screen printed on the front and rear of the cell respectively. Finally the wafers are fired in a belt furnace to form the contacts and create the p$^+$ back surface field. Table 7.2 summarizes the IV parameters of the best and average cells from a run of 12 wafers.

Table 7.2: Average and Best IV characteristics, measured under standard test conditions

	V_{oc}(mV)	J_{sc}(mA/cm^2)	F.F. (%)	Efficiency (%)
Average	632	36.9	79.1	18.4
Best	633	36.9	79.4	18.6

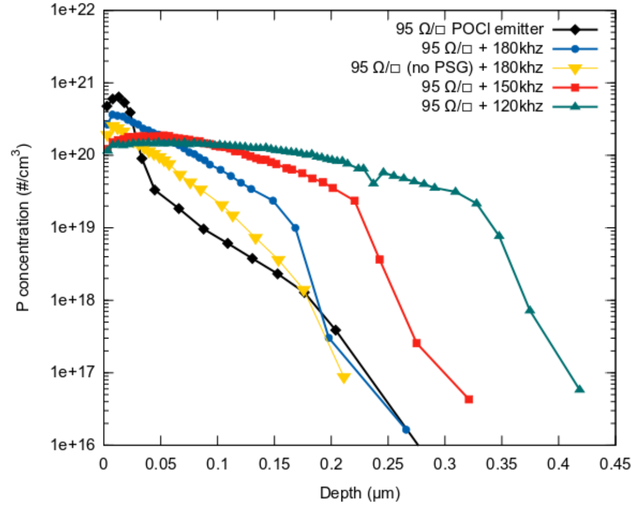

Figure 7.8: ECV Doping profiles for: the $POCl_3$ emitter before laser doping, laser doping profiles for various laser powers using PSG a dopant source and the result of laser irradiation with no P source

7.4 Results and Discussion

As previously mentioned this process differs from others presented in literature because the laser used in this research employs a UV laser where as most others have used a green laser and this process uses a segmented selective emitter. The doping profiles generated from the UV laser seen in figure 7.3 are quite different from those obtained by laser doping with a green laser [52]. The deepest junction formed is only 0.4 μm deep where as junction depths of 0.8-1 μm can be formed using a green laser. This result is not surprising since the absorption coefficient for 355 nm uv light in Si is over two orders of magnitude larger than for 532 nm green light [110]. The shallower junction depth provided by UV laser doping could be advantageous because the shallower volume of high doping where Auger recombination is high. The total active P dose for each profile was calculated by integration

and is shown in table 7.3

Table 7.3: Active P dose for each profile. Obtained by integrating the ECV data.

Profile	Dose (10^{15} atoms/cm^2)
90 Ω/□ $POCl_3$ emitter	1.54
180 khz, 33 μJ/pulse laser doping	2.13
180 khz, 33 μJ/pulse laser doping (PSG removed)	1.09
150 khz, 50 μJ/pulse laser doping	2.52
120 khz, 86 μJ/pulse laser doping	3.23

It is interesting to note that the total P dose increases between 38% and 109% of the starting $POCl_3$ dose depending on the laser power used but when the PSG is removed before laser doping, the total P dose goes down. This shows that the PSG is the source of the extra P dose incorporated into the profile and not inactive dopants near the surface. The fact that the dose goes down after laser doping without the PSG could be explained if some of the P atoms end up in interstitial sites after laser doping. The peak doping is higher in samples doped with the 180 khz rep. rate compared with samples doped with the 150 khz and 120 khz rep. rate, this is because the power associated with the 180 khz rep. rate is insufficient to melt the Si, where as at 150 khz the pyramids start to melt and at 120 khz they are completely gone and the surface is flat. Once the Si is melted P can diffuse quickly and redistribute the high doping level at the surface due to the high diffusivity of P in Si melt [111]. For this reason we chose the 180 khz rep. rate in our process.

Even though the surface concentration for the laser doped selective emitter is lower than the $POCl_3$ emitter we see a lower contact resistance on the laser doped samples indicated by the average cell series resistance that is three times lower on samples that are laser doped compared with reference cells made on the same emitter with no laser doping (0.6 vs 2.0 Ω-cm^2). This is because screen printed Ag contacts make contact to Si through Ag crystallites that etch into Si on average 0.13 μm [60]. At this depth the $POCl_3$ emitter doping level is approximately 3.8x10^{18}/cm^3 where as the 180 khz rep. rate doped profile has a P concentration of about 4x10^{19}/cm^3. This concept is demonstrated in figure 7.9, which

shows the microscopic contact resistivity between the silver crystallites and the substrate for these different doping profiles as a function of depth. The microscopic contact resistivity was obtained using the Wentzel-Kramers-Brillouin [112] approximation in the thermionic field emission regime, a Schottky barrier height of 0.78 eV was used in the calculations. Where the dashed line drawn at ρ_c=10^{-3}mΩ -cm^2 intersects each doping profile represents the maximum depth at which good contact between the Ag crystallite and the emitter can be formed [52]. For the $POCl_3$ emitter profile most of the Ag crystallite would be making contact to lowly doped Si, however for the laser doped samples the entire Ag crystallite would make good contact to the Si, explaining the better contact in laser doped samples. It should be noted that this contact resistance does not represent the actual contact resistance of the whole Ag finger to the emitter but rather an approximation of the contact resistance of the Ag crystallites to the emitter formed during contact firing. The effect of the pitch of

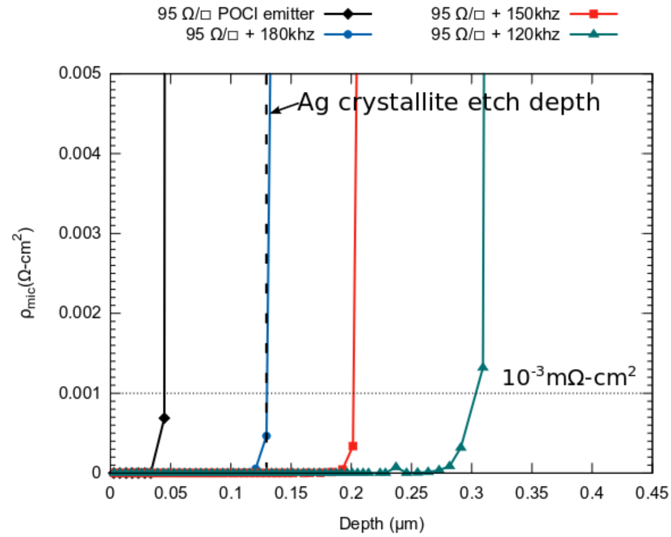

Figure 7.9: Microscopic contact resistivity using the Wentzel-Kramers-Brillouin approximation for the thermionic field emission regime

the selective emitter is demonstrated in table 7.4. The benefit of the segmented selective emitter is seen in the short circuit current (J_{sc}) which increases as the pitch between the selective emitter regions increases. This effect does not appear to be due to a change in the reflectance of the wafers, the laser power used in the experiment does not alter the pyramidal texturing of the wafers. The authors believe the current is most likely lower in

Table 7.4: Average and Best IV characteristics for varying selective emitter pitch, measured under standard test conditions. The selective emitter region is 500μm wide and about 50μm thick, the longer side is the one perpendicular to the finger, 180 khz, 33 μJ/pulse laser setting was used on these wafers

Pitch	V_{oc}(mV)	J_{sc}(mA/cm^2)	F.F. (%)	Efficiency (%)
No Selective Emitter	629	37.3	72.4	17.0
50μm (overlapping)	629	36.7	79.5	18.4
100μm	629	37.0	79.7	18.5
200μm	629	37.1	79.0	18.5

samples with smaller pitch to due to traps created from laser induced defects, this effect is currently under investigation.

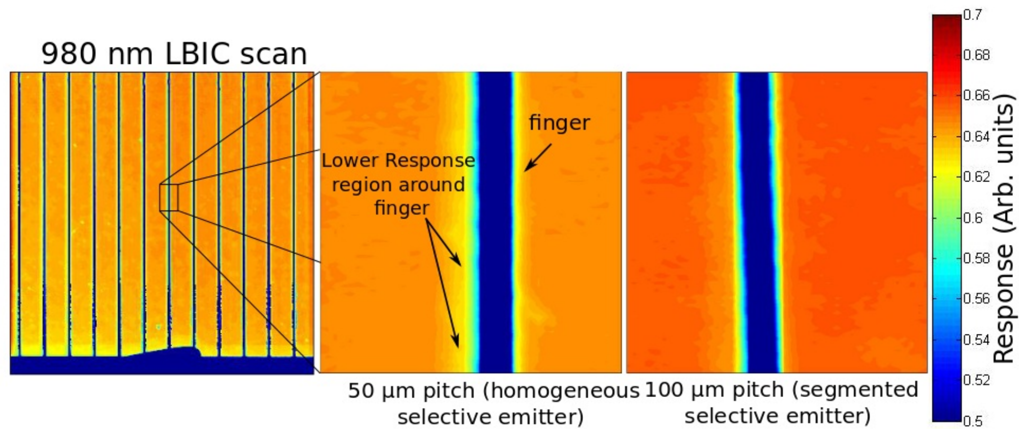

Figure 7.10: LBIC map showing the response at 980 nm for a representative finger on solar cells with 50 and 100 μm selective emitter pitch

The lower response region around the contacts due to Auger recombination and laser induced defects can be seen in laser beam induced current (LBIC) maps, shown in figure 7.10. For samples with a 50μm selective emitter pitch, a fairly wide region of lower response can be seen around the finger. As the pitch increases to 100 the area of the lower response region decreases. It can be seen from the correscan plots in figure 7.11 that the line contact resistance of samples with 50 to 100 μm pitch are very low and have roughly the same contact resistance. This is impressive since the selective emitter coverage is roughly half for

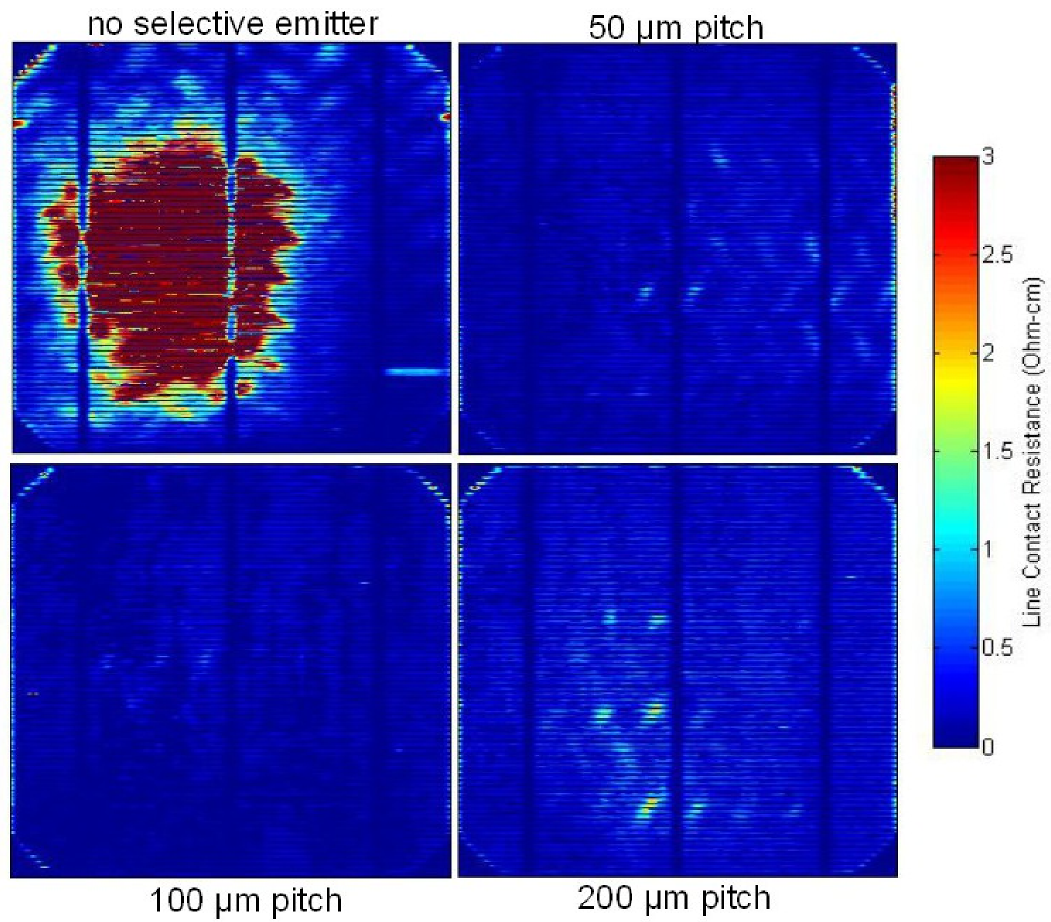

Figure 7.11: correscan of cells with no selective emitter and with selective emitter pitch of 50,100 and 200μm.

the 100 μm pitch compared to the 50 μm pitch. For samples with a 200 μm pitch selective emitter, line contact resistance is still good; however, there are a few localized regions with higher line contact resistance. These regions are most likely the cause of the slightly lower fill factor for samples with a 200 μm pitch selective emitter seen in table 8.1. Without the selective emitter the contact resistance is highly non-uniform and is not sufficient for high fill factors. Segmented selective emitters allow for improvement in response around the grid line compared to a homogeneous selective emitter without any sacrifice in the contact resistance.

7.5 $POCl_3$ flow effect

The dependence of the sheet resistance in the field and laser doped regions on the $POCl_3$ flow during diffusion is shown in figure 7.12. Reducing the $POCl_3$ flow increases the sheet resistance of the field regions as well as the laser doped regions. The segmented selective

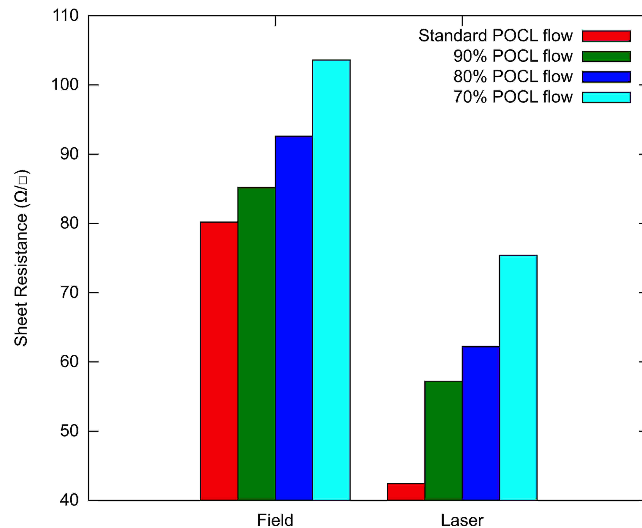

Figure 7.12: Sheet resistance after diffusion and after laser doping for different $POCl_3$ flows. The parameters used for laser doping were 180 khz and 3000 mm/s.

emitter design is robust and can achieve over 19% on all three four emitters shown in figure 7.12. With the decreasing $POCl_3$ flow the Jsc and Voc increase however the FF begins to drop off at 70% of the original flow as can be seen in table 7.5. Test structures were created with a large laser doped square so that quantum efficiency measurements could be made to

$POCl_3$ flow		Voc (V)	Jsc(mA/cm^2)	FF (%)	Eff (%)
Standard	Best	0.637	37.46	80.0	19.08
	Average	0.636	37.32	80.0	18.99
90%	Best	0.638	37.44	79.8	19.05
	Average	0.638	37.35	79.8	19.00
80%	Best	0.639	37.46	79.7	19.07
	Average	0.639	37.45	79.6	19.04
70%	Best	0.641	37.62	79.2	19.12
	Average	0.641	37.61	78.7	18.98

compare the laser doped regions with the field regions. Figure 7.13 shows the normalized internal quantum efficiency (NIQE) in the laser doped and field regions.

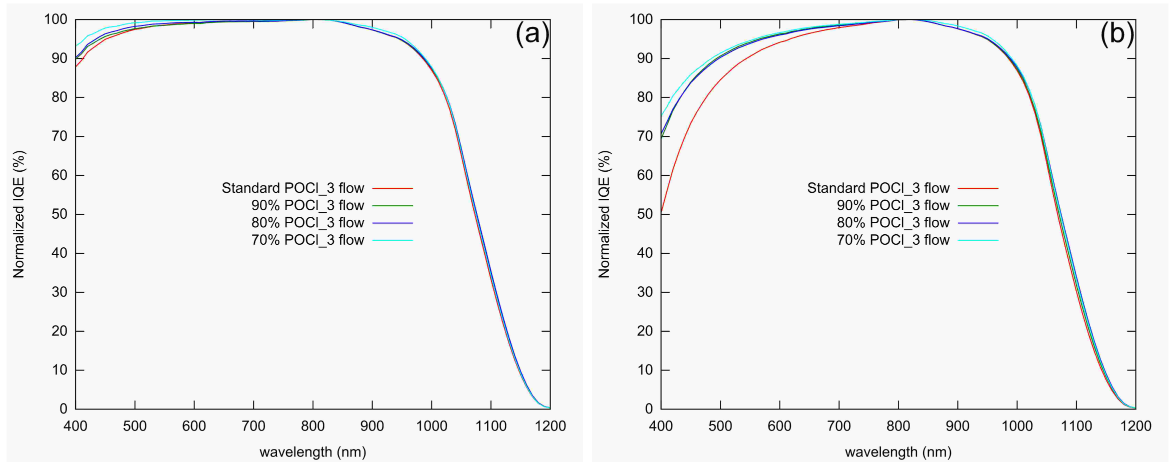

Figure 7.13: Normalized IQE in the field (a) and laser doped (b) regions of a test structure

Decreasing the $POCl_3$ flow creates a modest increase in the short wavelength NIQE in the field regions but produces a more pronounced increase in the laser doped regions. Thus, in selective emitter devices current can be maximized by using a segmented selective emitter to minimize selective emitter coverage and by tailoring the diffusion so that the difference in short wavelength IQE of the field and selective regions is reduced.

7.6 Conclusion

In conclusion, we have demonstrated that an ultraviolet laser can be used to create a selective emitter in the fabrication of high efficiency crystalline Si solar cells. The selective emitter profiles created are suitable for low-ohmic contacts and that the dopant source is

the PSG not the inactive dopants in the electrically dead layer at the surface. We find that device performance is best when the selective emitter is segmented and not continuous due to an increase in the J_{sc}. Segmented selective emitters have low contact resistance even though only a fraction of the finger is contacting the selective emitter. We also show that segmented selective emitter solar cells can have a more uniform response than a non-segmented selective emitter solar cell.

CHAPTER VIII

UV LASER DOPED SELECTIVE EMITTER SOLAR CELLS WITH EMITTER ETCHBACK

8.1 Introduction

Removing the very highly doped surface of $POCl_3$ diffused Si wafers via a chemical etch has been shown to reduce the J_0 of the diffused regions [107]. In the chapter 7 a solar cell with an emitter etch-back was reviewed, in the process by the university of Konstanz a screen printed etch resist is used to define selective emitter regions. In this chapter I show that a similar approach can be used to further enhance the performance of the segmented selective emitter devices introduced in chapter 7. Laser doped Si profiles have a much different profile than furnace diffused Si as seen in fig 9.2. Laser doped profiles tend to maintain a higher doping level deeper into the substrate than a furnace diffused profile, meaning that if the surface of laser doped Si is etched, the resulting sheet resistance and surface concentration are not drastically different from before the etch. It is demonstrated in this work that high efficiency solar cells with a segmented selective emitter can be fabricated using laser doping and an etch-back without the need for a screen printed mask. Correscan measurements show that as etching depth increases the contacts resistance in the furnace diffused regions increases quickly while the laser doped regions maintain an acceptable contact resistance. Vocscan measurements reveal that the etch-back improves the local Voc in the laser doped and furnace diffused regions. This process increases the efficiency to 19% compared to 18.6% achieved without the etch-back step.

8.2 Laser Process Optimization

Monocrystalline p-type ⟨100⟩ silicon wafers (Czochroaski (Cz) 2Ω-cm) were textured in an alkaline solution after a damage removal step. Following texturing, the wafers were cleaned by the RCA method and phosphorous diffused in a tube by a phosphorousoxychloride ($POCl_3$) source. The diffusion produces an n^+ P emitter with PSG on the surface of the

wafer. The PSG is then used as a solid-state P source for laser doping. The laser used for this process is a pulsed, frequency tripled (355 nm wavelength) Coherent Avia laser with a scan head to raster the spot across the wafer. The laser spot size is roughly 50 μm and the laser cross sectional power density is Gaussian in shape. Doping profiles generated by this process on 45 and 95 $\Omega/\square$ emitters can be seen in figure 8.1. The doping profiles formed by the 180 khz laser repetition rate keep the same junction depth as the initial profiles but the high P concentration kink in the emitter near the surface in driven in further giving a high doping level deeper into the substrate, while the 150 and 120 khz repetition rates extend the junction depth and completely remove the kink in the profile resulting in a more flat doping profile with depth. These trends can be explained by the increased melting of silicon with decreasing repetition rate, because the laser power is inversely related to the repetition rate. As more silicon is melted, the profile decays more slowly with depth into the substrate.

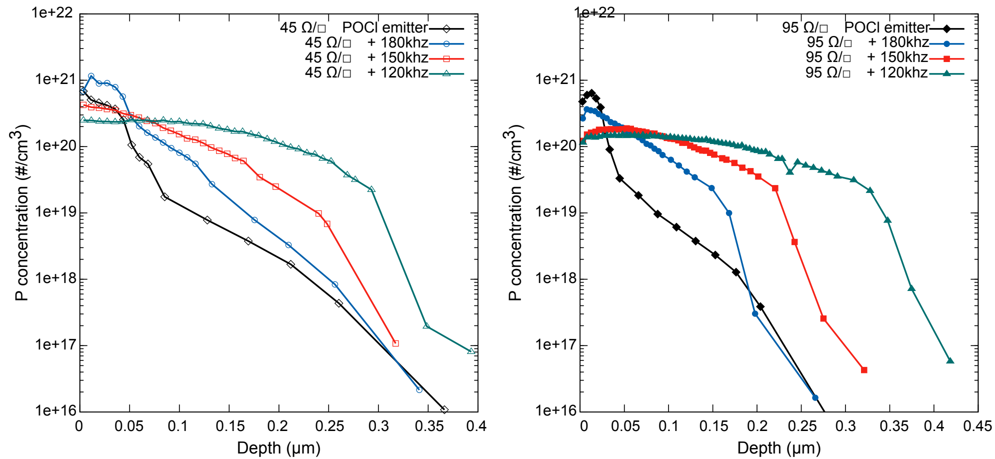

Figure 8.1: Doping profiles measured by ECV for the 45 $\Omega/\square$ $POCl_3$ diffusion, and the selective diffusions after laser doping at 180khz-30μJ/pulse, 150khz-47μJ/pulse and 120 khz-81μJ/pulse (left) and for the corresponding profiles on the 95 $\Omega/\square$ $POCl_3$ diffusion (right).All laser doped regions were scanned by the laser at 3000mm/s

To investigate the amount of damage induced by laser doping, several samples with laser doped regions created by different laser parameters were etched using the Yang etch to expose any resulting defects [113]. Identically processed samples with and without laser doping were then imaged by scanning electron microscopy; the resulting images can be seen

in figure 8.2. The areas where the silicon melted due to laser exposure have more defects areas that did not melt, however, even the areas that did not melt had more defects than the reference sample with no laser doping.

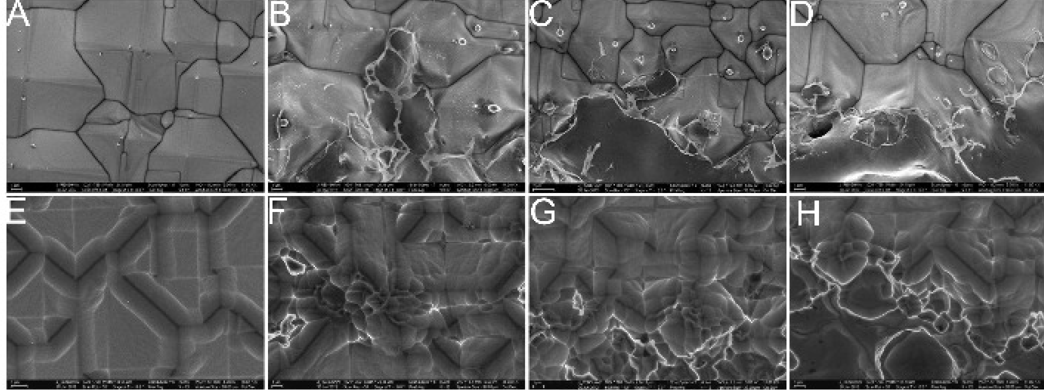

Figure 8.2: SEM images of the surface of laser doped Si wafers before (A-D) and after (E-H) the defect etch. A and E are reference points with no laser doping, B and F received the 180 khz laser condition, C and G received the 150 khz laser condition,D and H received the 120 khz laser condition

8.3 Laser Doping with Etch-Back Process

Because laser doped regions maintain a high doping level deeper in the the substrate when compared with regions that were not laser doped, laser doped selective emitter solar cells could benefit from an etch-back process. By removing the surface layer an etch-back process can reduce the Auger recombination in heavily doped kink in the field diffusion, lowering the reverse saturation current in the emitter (J_{0e}) while maintaining a high doping level in the laser irradiated regions. To explore the potential for this type of device, test structures were created on wafers that received a 45 $\Omega/\square$ P diffusion and laser doping in different regions to determine the sheet resistance as a function of etching time in the laser doped regions and in the non laser doped regions. In addition, high lifetime samples were prepared with the same diffusion and etching conditions but no laser doping. These samples were passivated on both sides with SiN and fired without any metal. Following firing, J_{0e} was extracted from the quasi-steady-state photoconductance decay method using relation 8.1

[114].

$$\frac{1}{\tau_{eff}} = \frac{1}{\tau_{bulk}} + 2J_{0e}\frac{n}{qn_i^2 w} + C_A n^2 \tag{8.1}$$

Where w is the wafer thickness, τ_{bulk} is the Schockley-Read-Hall recombination lifetime and C_A is the ambipolar bulk auger coefficient. Plotting $1/\tau_{eff} - C_A n^2$ versus n gives a straight line whose slope is proportional to J_{0e}. The etching solution used in this experiment contained Nitric, Acetic and Hydrofluoric acids. Figure 8.3 demonstrates that the sheet resistance of laser doped regions increases much more slowly with etch time compared to the non laser doped regions. For instance, after 90 seconds of etching the non laser

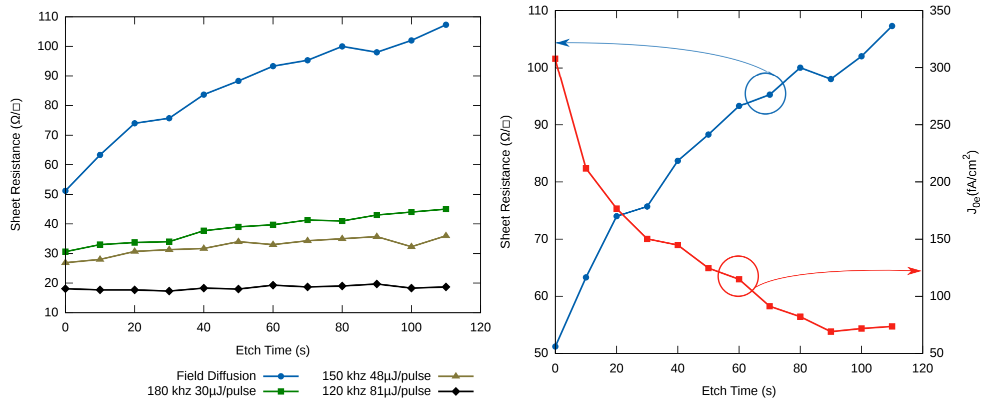

Figure 8.3: Sheet resistance vs. etch time for laser doped and non-laser doped regions for a 50 Ω/□ $POCl_3$ n diffusion recipe (left) and the measured J_{0e} in the field regions vs etch time (right)

doped region has a sheet resistance of 98 Ω/□ with a very low J_{0e} of 69 fA/cm^2 while all the different laser doped regions have sheet resistances below 50 Ω/□. How the contact resistance is affected by the etching process was explored using similarly processed wafers as mentioned above. Textured p type wafers underwent a 50 Ω/□ $POCl_3$ diffusion and received laser doping with 120,150 and 180 khz repetition rates in different regions of the wafer and underwent etching for various times. After etching, the wafers were coated with PECVD SiN and printed with Ag metallization for the front and Al for the rear followed by firing in a belt furnace by TP Solar ®. The line contact resistance of the test devices was then measured using the Correscan tool. The correscan tool provides a way to generate a contact resistance map across the surface of a solar cell. Using it on samples prepared with different etch times gives us insight into the how the contact resistance changes with etching

time. Figure 8.4 shows that the contact resistance in the laser doped regions from all three laser repetition rates explored is good even after 110 seconds etching time and the field diffusion is over 100 $\Omega/\square$. While the line contact resistances for all the laser doped regions are good, we find that the 180 khz irradiated region has the lowest contact resistance most likely because this setting melts the silicon less than the 120 and 150 khz settings. Less melting prevents dopants near the surface from being driven much deeper into the wafer, this trend can be seen in figure 8.1.

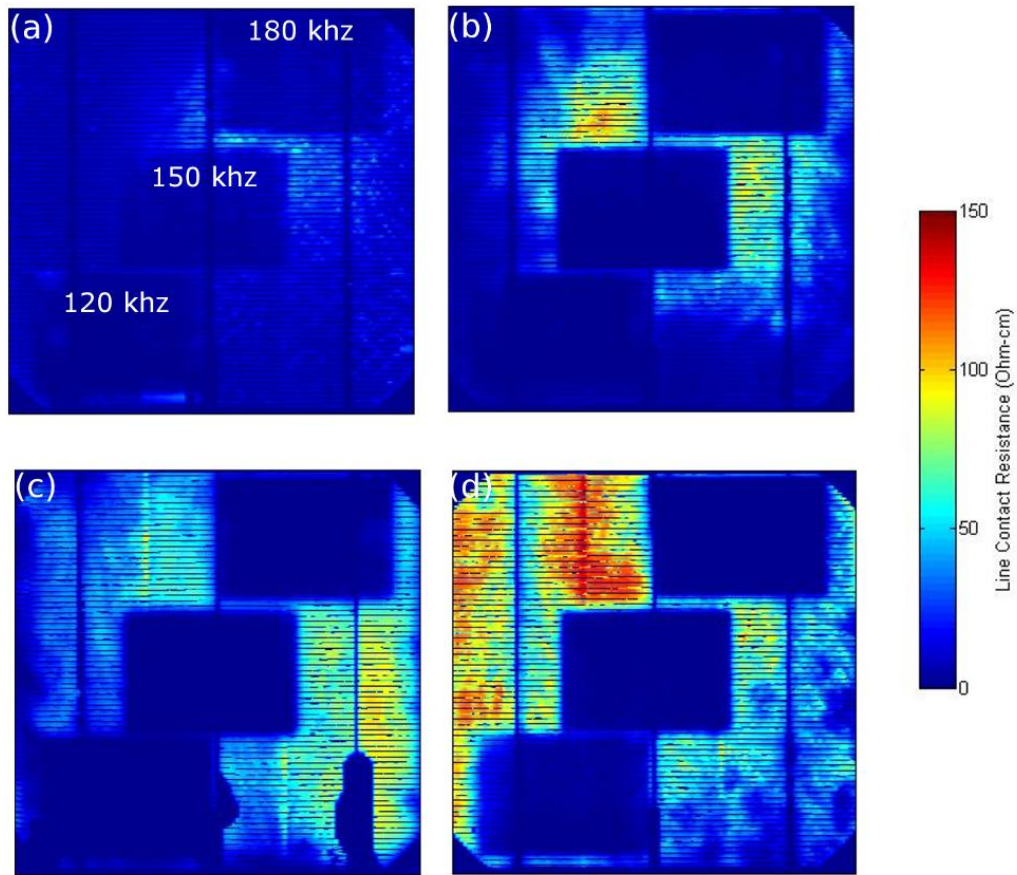

Figure 8.4: Correscan maps of laser doped and etched wafers after 10 (a), 30(b),70(c) and 110 (d) seconds in etching solution. The laser frequencies used to scribe the boxes labeled in part (a) apply to parts (b),(c) and (d) as well.

The recombination in the laser doped regions was explored using the Vocscan tool.

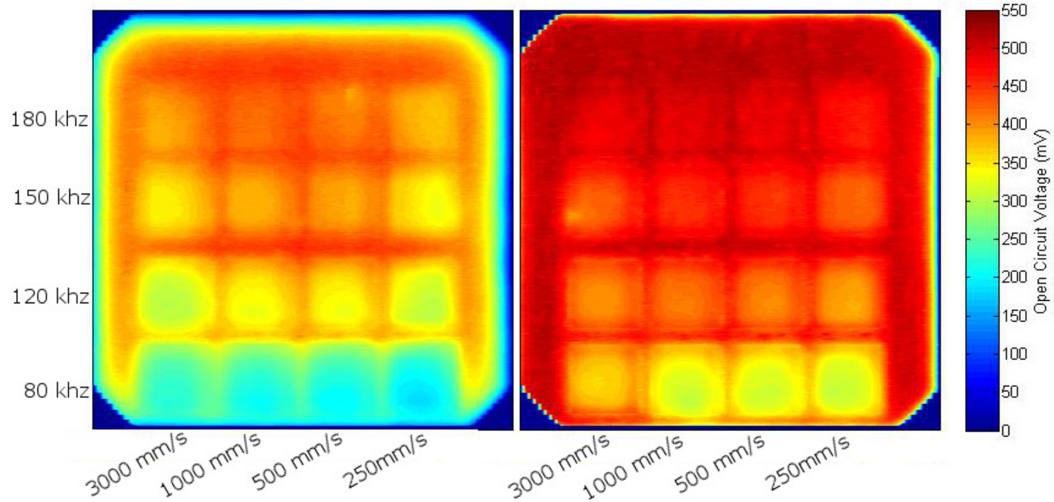

Figure 8.5: Vocscan map showing the effect of laser damage on the local Voc of an as diffused (45 Ω/□) + laser doped(left) device and after a device that received an etch-back for 80 seconds in a solution of Nitric, Acetic and Hydrofluoric acids (right).

This was achieved by preparing test devices on wafers diffused with the same 45 Ω/□ $POCl_3$ diffusion recipe and laser doped with a variety of laser repetition rates and scan speeds on the same wafer. Following laser doping, the devices received PECVD SiN and Al printing and firing. The Vocscan tool makes a map of the open circuit voltage of a wafer achieved by scanning a light and metal probe across the wafer at open circuit condition. It should be noted that the light used in this apparatus is less than one sun and therefore the voltages measured are lower than observed under standard test conditions. This test does, however, provide a good method to compare the effect of laser doping from region to region. The Vocscan maps for laser doped test devices are shown in figure 8.5. The devices were identically prepared except the device on the right received a chemical etch-back for 80 seconds in a solution containing Nitric, Acetic and Hydrofluoric acids . The Vocscan data shows that slower scan speeds and higher pulse powers (low rep. rates) create more recombination sites at the surface of the wafer which lead to a lower local voltage around the laser damaged region. The higher recombination resulting from high pulse energy or slow speed could be from recrystallization defects when the Si is melted. Low pulse energy and fast scan speed minimize the thermal budget on the surface thereby decreasing the

probability of defect formation. From our tests we conclude that UV laser doping should be carried out at low pulse energies (< 40 μJ/pulse) and high scan speeds (500 mm/s or greater). For a well optimized laser doped region we see that the local Voc is only around 10mV lower than the field for both the etched and non etched samples. It is interesting to note that the local V_{oc} increases with the etch-back time for the optimized settings to almost the same extent as the field diffusion even on the etch-back sample where the sheet resistance in the laser doped regions is about 50 $\Omega/\Box$ less than the field. In summary, we find that damage in UV laser doped silicon can be minimized by choosing a high repetition rate and low pulse power along with a high scan speed, and that laser doped regions can maintain low contact resistance even after long etch times.

8.4 Device Optimization

Laser doped selective emitter (LDSE) solar cells were created using the optimized laser and etching parameters described previously. For this experiment we used 2 Ω-cm p type Cz wafers to create a LDSE cell with a segmented selective emitter. The abbreviated process flow can be seen in figure 8.6. Four groups of wafers were processed identically using the

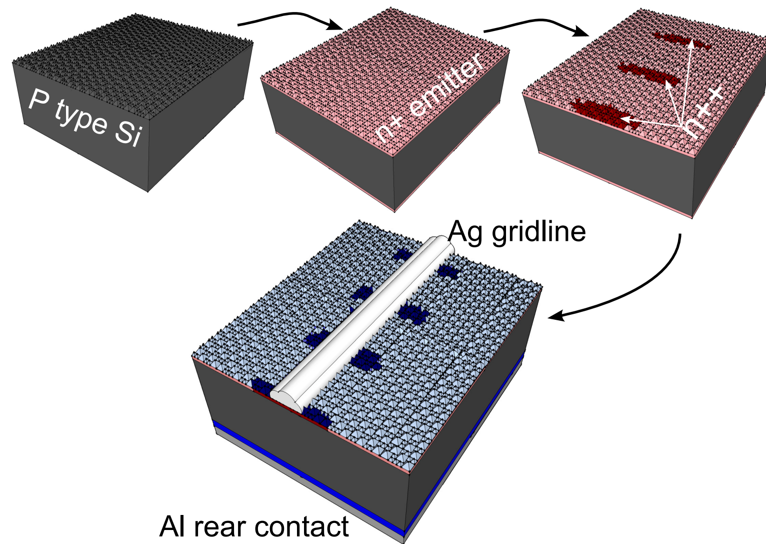

Figure 8.6: Process flow for LDSE solar cells. Step 1: Damage etch and texture wafer surface Step 2:$POCl_3$ diffusion to create the n^+ emitter Step 3:Laser doping in selective regions to create the n^{++} regions Step 4:Chemical edge isolation, etch-back and PECVD SiN (not shown to minimize figure size) Step 5: Screen printing and firing

same 45 Ω/□ $POCl_3$ diffusion used in the previous experiments described in this work. After diffusion, three groups received segmented laser doping, each with a different segment pitch. Using a laser repetition rate of 180khz and scan speed of 3000 mm/s, doping was applied with segment pitch varied from from 50 μm (complete overlap) to 200 μm. Following laser doping the samples were chemically etched for 90 sec using the solution described above. A fourth group of wafers were used as a control with no laser doping along with a group of cells that received a industrial type 65 Ω/□ $POCl_3$ emitter and no laser doping. All of the wafers were chemically edge isolated before applying PECVD SiN for the anti-reflection coating. Metallization was achieved by screen printing Ag front and Al rear contacts followed by firing. The effect of the segmented selective emitter pitch is seen in table 8.1. By using

Table 8.1: Average light IV characteristics for varying selective emitter pitch. The selective emitter region is 500 μm wide and about 50 μm thick, with the longer side perpendicular to the gridline. The laser rep. rate was 180 khz for a power of 33 μJ/pulse and cells were measured under STC using a Fraunhofer calibrated secondary standard.

Pitch		V_{oc}(mV)	J_{sc}(mA/cm^2)	F.F. (%)	Efficiency (%)
50μm (non segmented)	Best	643	37.1	79.0	18.8
	Average	642	37.1	78.3	18.6
100μm	Best	644	37.4	79.0	19.0
	Average	643	37.3	78.4	18.8
200μm	Best	641	37.3	78.2	18.7
	Average	642	37.3	77.5	18.6
Industrial Type Emitter	Best	631	37.0	80.0	18.7
	Average	631	37.0	79.8	18.6
No Selective Emitter	Average	634	33.0	32.5	6.8

a segmented selective emitter we were able to minimize the lower response, laser damaged region and increase the average J_{sc} by 0.2 mA/cm^2 compared with a non-segmented select emitter (50 μm pitch) while maintaining the fill factor (FF) at 79%. It is interesting to note that the cell Voc remains virtually constant throughout the four groups of cells despite the increasing selective emitter coverage (decreasing pitch). The trend of the FF is as expected: with decreasing selective emitter pitch the FF increases because more of the finger is in contact with the highly doped region. The normalized internal quantum efficiency (IQE)

is plotted in the short wavelength range in figure 8.7. The blue-response of the etch-back emitter is clearly superior to that of the industrial type emitter, though the J_{sc} is roughly the same because the etch-back cells have higher shading because the front grid has 9 more fingers than the industrial type cell. The response of the segmented selective emitter vs homogeneous selective emitter is more similar than would be expected because of the difference in J_{sc} measured from the light IV curve. The authors believe this discrepancy could be due to non-uniformity of the etching process. By increasing the short circuit

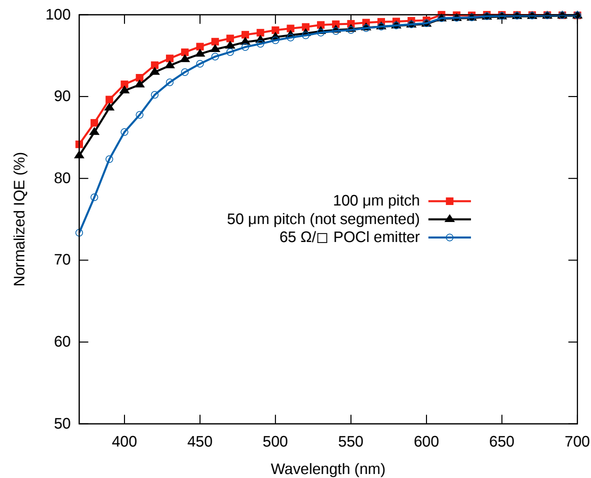

Figure 8.7: Short wavelength IQE for a segmented selective emitter cell, a non-segmented selective emitter cell and an industrial type cell

current, a 0.2% absolute efficiency boost is achieved when compared with non-segmented laser doped selective emitter cells and 0.3% over an industrial type emitter solar cell.

8.5 Conclusion

Here, we present a novel method of selective emitter formation via UV laser doping. We have shown by SEM investigations that UV laser doping of Si creates defects near the surface.These defects lead to a lower local surface voltage compared with the field diffusion. We have found that laser pulse power less than 40μJ/pulse and scan speed greater than 500 mm/s are optimum for minimizing damage while doping sufficiently for low resistance contact. Even with optimized laser parameters, the laser doped regions have lower response than the field so we introduce a novel segmented selective emitter cell design which takes

advantage of the low resistance ohmic contacts of a selective emitter while minimizing defect and Auger recombination. Further we combine this method with an emitter etch-back process to achieve very low J_{0e} while maintaining low resistance ohmic contacts. UV laser doped selective emitters are shown to provide low-ohmic contacts on emitters that are otherwise not contactable. We demonstrate that a segmented selective emitter design can give a 0.2% absolute efficiency gain over a non segmented selective emitter and 0.3% over a industrial type emitter solar cell.

CHAPTER IX

DEVICE OPTIMIZATION FOR SCREEN PRINTED INTERDIGITATED BACK CONTACT SOLAR CELLS

9.1 Review of numerical modeling of interdigitated back conact solar cells

The interdigitated back contact (IBC) solar cell was introduced in 1977 by Lammert and Schwartz [115]. The device design places alternating p^+ and n^+ diffused regions on the rear side of the device. A schematic of the IBC structure is shown in figure 9.1. Completely

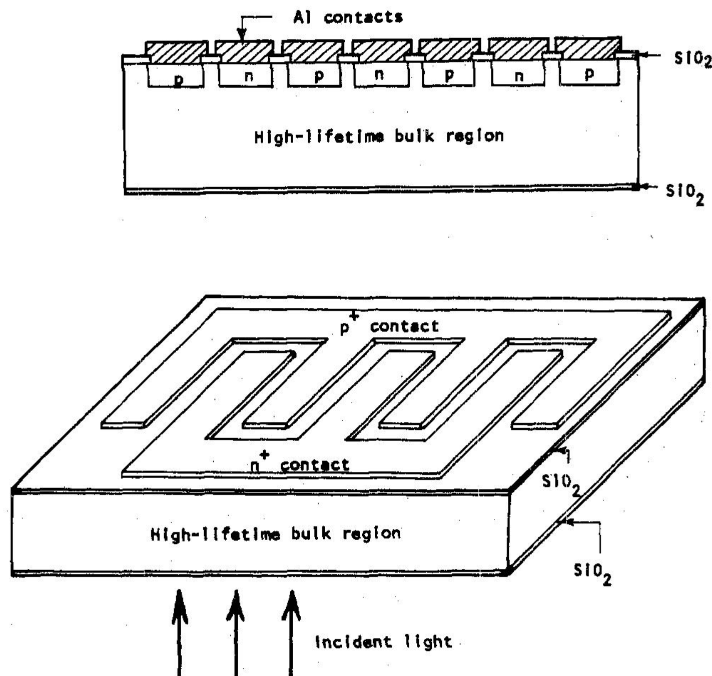

Figure 9.1: The IBC device architecture. Taken from [115].

rear contacted solar cells have several advantages over traditional cell architectures with contacts on the front and rear of the device. The most obvious benefit is that there is no shading on the front of the device due to metallization. Additionally, with a rear contacted cell the contacts can be made large to minimize series resistance without paying a penalty

in shading losses as in a front contact device. Further, contact spacing can be made small without increasing shading. Small contact spacing allows for the use of high-sheet resistance lightly diffused emitters which have a lower emitter reverse saturation current (J_{0e}).

When the IBC was introduced it was proposed for use as a concentrator cell, however today it is in manufacturing for 1 sun use by Sunpower Corp. Not many details were given in Lammert and Schwartz initial paper on the device architecture on how they modeled the device other than that they used Boltzmann statistics, the mobilities were constant, the junctions were treated as ideal, space charge quasi-neutrality holds in the bulk region and no photons were reflected from the front surface. Their initial analysis predicted a 1-sun efficiency of 20% was possible and that 24% was possible at 300 suns.

In 1986 a variant of the IBC design called the point contact solar cell (PCSC) was introduced [116]. The PCSC differs only from the IBC in that the emitter and base regions are only contacted in points rather than the full area of the diffused regions. The PCSC cell design is seen in figure 9.2. The advantage of the PCSC over the IBC is that the fraction of

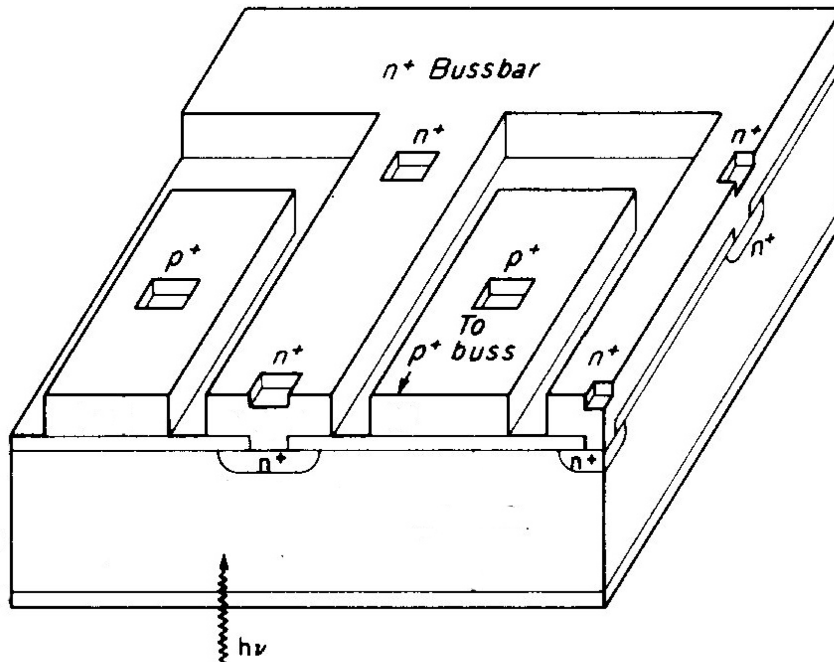

Figure 9.2: The PCSC device architecture. Taken from [116].

the rear Si surface that has the highly recombinative metal/Si interface is greatly reduced.

This reduction in metal/Si interface area results in an improvement in the cell V_{oc}. Three dimensional modeling of the PCSC was carried out using an approach in which the total recombination current is found rather than carrier densities and fluxes. This method solves the semiconductor equations by a variational approach. The results of their numerical analysis is that the PCSC can reach a one sun efficiency around 25% and an efficiency of around 28% at 500 suns, a relative improvement of about 4% absolute for an optimized cell design with small contact pitch.

More detailed simulations were carried out on IBC cells and point IBC with the aid of a three dimensional semiconductor simulation software CADDETH on a supercomputer [117].These simulations varied pitch, emitter area, collector area, contact area, surface recombination velocity and bulk life time were varied for a contact device thickness of 50 μm. They report the contact area should be minimized with the smallest possible feature sizes and that the device performance is highly dependent on the surface recombination velocity.

Another attempt to improve the IBC cell to replace the n^+ and p^+ diffused regions with doped amorphous Si (a-Si) layers [118]. This is the so-called interdigitated back contact silicon heterojunction (IBC-SHJ) solar cell which is shown in figure 9.3. The advantage of an

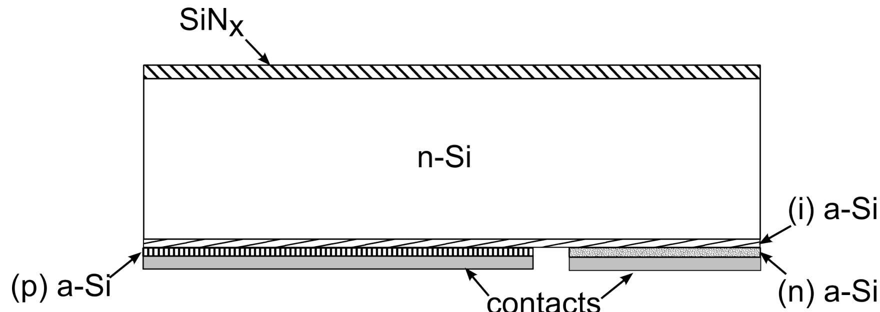

Figure 9.3: The point IBC-SHJ device architecture.

a-Si heterojunction is that it can reflect majority carriers away from the C-Si/a-Si interface because of a-Si's wider bandgap [119] leading to a very low recombination interface with favorable electronic properties. To achieve these very low recombination heterojunction interfaces a thin intrinsic a-Si is used between the doped a-Si and C-Si layer, otherwise the reverse current is very large [120]. A unique feature of IBC-SHJ cell is that if the intrinsic layer is not grown properly the IV curve exhibits an s-shape with a very low fill

factor. This phenomenon has been modeled using sentaurus device [121]. The authors found that this effect is related to the intrinsic layer thickness, doping, and band gap. Figure 9.4 demonstrates the effect of these parameters on the IV curve. It is estimated that this device

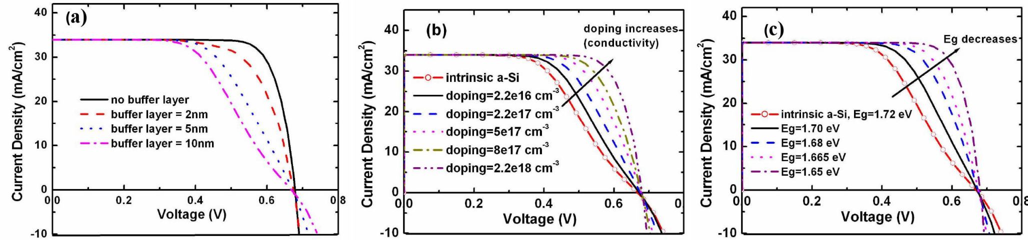

Figure 9.4: The simulated effects of the buffer layer thickness (a), doping (b), and bandgap (c) on the IV curve of IBC-SHJ devices. Taken from [121].

architecture could yield devices with efficiencies around 26%.

Low lifetime thin film IBC's have also been explored through device simulation using Sentuarus Device by Nichiporuk *et al.* [28]. This optmization study was carried out for n and p type 50 μm thick substrates with 200 and 300 μm diffusion lengths. The effect of SRV, substrate doping and emitter doping on device performance was investigated. They found that high performance comes for low substrate doping, high emitter doping and low SRV's. The optimized efficiency was simulated to be 20%.

This review has covered the major IBC type-cell designs and relevant device modeling associated with these structures. In the next sections a device optimization for a screen printing compatible IBC cells is developed and a design path to push cell efficiency towards the Shockley-Queisser limit that could surpass the 25% efficient world-record PERL cell [122] is proposed. These simulations show how the PV industry increase cell efficiency to lower the cost of photovoltaic created electricity through implementation of next generation solar cells.

9.2 Introduction

Low-cost high-efficiency solar cells are the key to grid parity. Among various high-efficiency cell structures, the interdigitated back contact (IBC) solar cell has produced the highest cell efficiencies on large area substrates (24.2 %) [123]. Also Fraunhofer ISE has demonstrated

a small area bi-facial IBC cell with 22.1% and 18.6% front and rear illumination efficiencies respectively [124]. While the IBC cell structure lends itself to high efficiency devices, it also usually requires complex processing steps such as masking, patterning or photolithography. Screen printed IBC devices have reached efficiencies above 19% but still required the use of photolithography for masking diffusions [125]. The recent development of implantation [126], screen printable inks [53] and laser chemical processing [127] in high efficiency solar cells could pave the way for a low-cost screen printed IBC device with no masking steps. The advent of these technologies has created the possibility of low cost manufacturable IBC devices and the need for a device optimization for a screen printable device design. The objective of this paper is to find the design space where high-efficiency screen printed devices can be manufactured.

9.3 *Simulations*

For this work the finite element analysis software Sentaurus Device (formerly DESSIS) was used. Because of the periodicity of the IBC structure it can be simulated with the unit cell shown in figure 9.5. To ensure the accuracy of this work we used Fermi-Dirac statistics

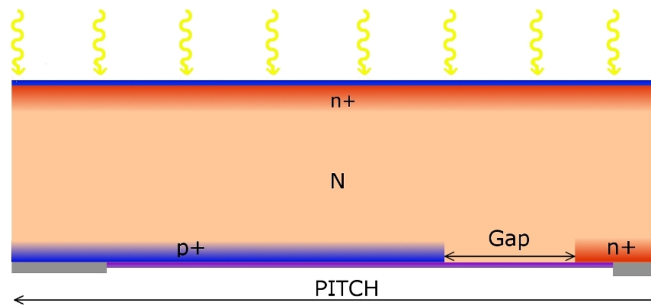

Figure 9.5: Modeled unit cell

and the following models: Auger recombination, Shockley Reid Hall recombination, Phillips mobility model and the Schenck band gap narrowing model. The fixed cell parameters are shown in table 9.1.

We chose the width of the back surface field to be 300 μm (150μm half width) and the gap to be 75μm to ensure the simulation's compatibility with screen printing technology. The width of the emitter was chosen to give a large emitter to pitch ratio of 77.5%, which

Table 9.1: Modeled Cell Parameters

Substrate Thickness (μm)	200
Pitch (μm)	1000
p^+ emitter half width (μm)	775
n^+ BSF half width (μm)	150
Gap (μm)	75
BSF contact half width (μm)	60
Emitter contact half width (μm)	150
Substrate Doping (P) (Ω-cm)	2
Bulk lifetime (μs)	1500
FSF profile	varied
FSRV (cm/s)	determined by profile
BSF profile	varied
SRV on BSF (cm/s)	determined by profile
Emitter profile	varied
SRV on Emitter (cm/s)	determined by profile
SRV on Gap (cm/s)	determined by substrate doping
SRV on Contacts (cm/s)	$1.56 \text{x} 10^7$

allows the device to perform better even in the lower lifetime material[128]. In the final section of this paper the pitch and emitter structure will be optimized for a screen printable device as well. For these simulations we varied the surface recombination velocity with the doping profile according to equation 9.1 .

$$S_o = S_{o1}\left(\frac{N_{dop}}{N_1}\right)^{\gamma_1} + S_{o2}\left(\frac{N_{dop}}{N_2}\right)^{\gamma_2} \quad (9.1)$$

In the above relation N_1,N_2,γ_1 and γ_2 are fitting parameters. This equation was used to fit a variety surface recombination velocities for different doping levels with different passivation schemes and surfaces by Altermatt et. al [35]. For this work we chose to use parameters that were used to fit data for an oxidized textured surface to try to set realistic limits on cell performance.

9.4 Results

9.4.1 FSF Profile

The first profile we optimized for the IBC device design was the n^+ front surface field. The gaussian profile was varied over a range of depths and doping levels that can be seen in table 9.2 and results of the simulations can be seen in figure 9.6. Simulations with low peak doping density front surface fields ($< 4.2\text{x}10^{19}$) had the best efficiencies due to lower auger recombination and low surface recombination. Therefore, for the rest of the simulations we chose $3.47\text{x}10^{18}/\text{cm}^3$ as the peak FSF doping and 0.4 μm as the FSF profile depth.

Table 9.2: Profiles Simulated

$N_d(\#/\text{cm}^3)$	Depths (μ m)	S.R.V. (cm/s)
$1.0\text{x}10^{18}$	0.2-0.8	$7.52\text{x}10^2$
$3.47\text{x}10^{18}$	0.2-0.8	$1.12\text{x}10^3$
$1.20\text{x}10^{19}$	0.2-0.8	$2.79\text{x}10^3$
$4.16\text{x}10^{19}$	0.2-0.8	$5.27\text{x}10^4$
$1.44\text{x}10^{20}$	0.2-0.8	$2.09\text{x}10^6$
$5.0\text{x}10^{20}$	0.2-0.8	$5.00\text{x}10^7$

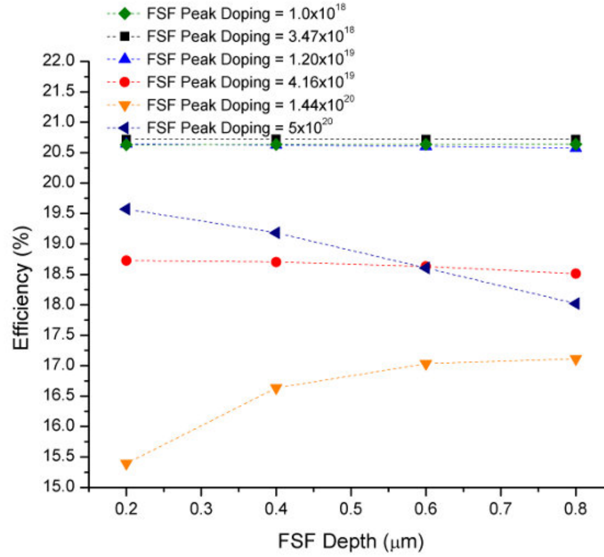

Figure 9.6: cell efficiency for different FSF profiles

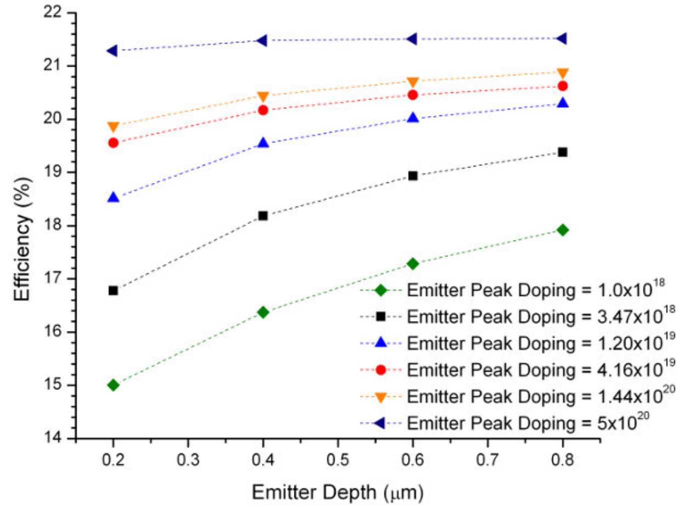

Figure 9.7: cell efficiency for different emitter profiles

9.4.2 Emitter Profile

Next the p^+ emitter profile was varied over the same range as shown in table 9.2. For this work we chose not to use a selective emitter over the contact to simulate a more manufacturable device. Because of this it must have a sufficient doping level to allow for good contact as well as shield the carriers from the high recombination contact region.Figure 9.7 demonstrates that contrary to the FSF, higher doping levels in the emitter give the best results for this structure. Efficiency shows a strong dependency on the doping level for this structure with over a 6 % absolute efficiency drop from very high doping levels to very low doping. Therefore we chose an optimum emitter doping of $5.0\text{x}10^{20}/\text{cm}^3$ with a junction depth of 0.6 μm, which makes it essentially opaque or insensitive to the surface recombination velocity. Shallower and lightly doped emitters are adversely affected by high screen printed contact recombination: Notice that the heavily doped opaque emitter relaxes the requirement for high quality passivation of the doped surface making it more manufacturable.

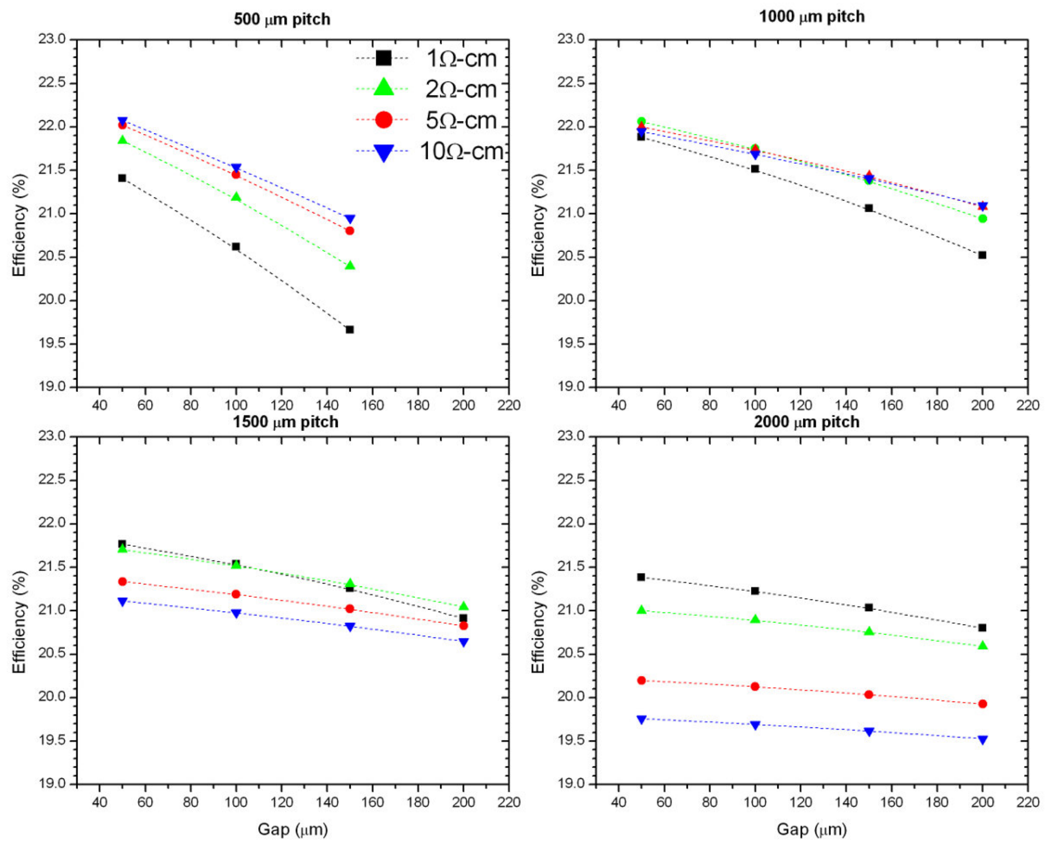

Figure 9.8: cell efficiency for the optimized diffusions for a screen printed IBC as a function of pitch, gap and bulk resistivity

9.4.3 BSF Profile

The results of the simulations demonstrating the effect that the BSF doping profile has on efficiency can be seen in figure 9.9. The BSF profile has similar restraints as the emitter in that it must also have a high enough doping level to be contactable and shield carriers from a wide contact area. The efficiency shows the same trend as it did for the emitter although it is not as sensitive to the BSF peak doping as it was to the emitter. We see the simulated efficiency increases with BSF peak doping and depth. For a BSF peak doping of 5.0x10^{20}/cm^3 these simulations predict an efficiency over 22%.

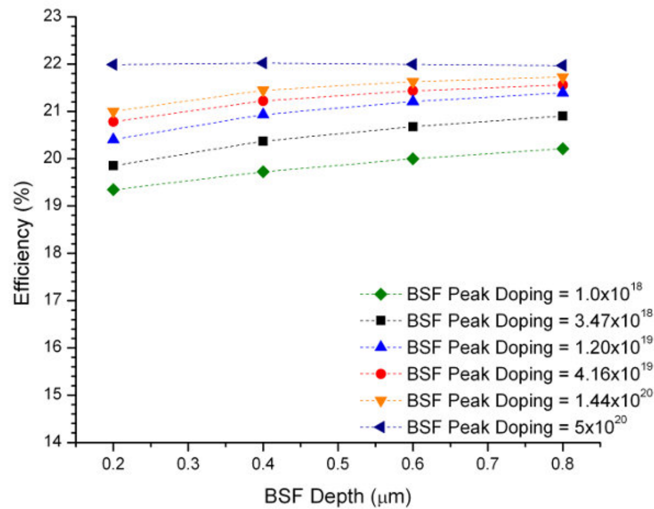

Figure 9.9: cell efficiency for different BSF profiles

9.5 Pitch, Gap Width and Bulk Resistivity

Simulations were performed to optimize a screen printing compatible IBC design using the optimized front surface field, rear surface field and emitter discussed already. To optimize the cell design; the pitch, gap width and bulk resistivity were varied (see table 9.3) while keeping all other parameters constant. Figure 9.8 shows efficiency versus gap width for different pitches, gap widths and base resistivity's. The results show that achieving over 22% is possible for a 500 μm pitch and a 10 Ω-cm resistivity material and a 50 μm gap. It is interesting to note that the best performing devices within each pitch group are of different

resistivity's. For a short 500 μm pitch a high resistivity material performs best due do to the higher current seen in high resistivity materials. However, at this pitch efficiency shows a strong dependence on the gap size because a small change in gap size is a large change in the gap to pitch ratio which is an important parameter for these types of cells [128]. For Larger pitches the high resistivity material begins to perform worse due to fill factor losses from the resistance of the bulk. A pitch of 2000 μm gives the best simulated efficiency of 21.4% for a 1 Ω-cm base resistivity, at this pitch the fill factor varies strongly with base resistivity from over 78 % for 1 Ω-cm to below 70% for 10 Ω-cm. It should be noted that as the pitch increases the dependence of efficiency on the gap is reduced, this could be important for manufacturing actual devices if fabrication is limited by ability of screen printing technology to keep a small gap between the n^+ and p^+ regions of the cell. We predict efficiencies of 20.8% for devices with a 2000 μm pitch and a 200 μm gap which should be compatible with current technologies.

Table 9.3: Values of varied parameters

Gap (μm)	50-200
Pitch(μm)	500-2000
Base Resistivity (Ω-cm)	1-10

9.6 Conclusion

Simulations were performed with the aim of optimizing design for low cost manufacturable IBC solar cells. Our simulations show potential for up to 22% efficiencies,this was done while keeping a large fraction of the rear side of the cell poorly passivated. We found that very heavy doping levels in the emitter and BSF lead to the highest performance for this structure. It was shown the the best efficiencies (over 22%) are on high resistivity material with a small contact pitch and to relax the need for a small gap a low resistivity base still gives 20.8% with a large gap of 200 μm. The device dimensions used in these simulations should be compatible with screen printing technologies available today and the doping levels are well above what is required for a good contact. The IBC device structure has the potential to produce high efficiencies on devices with screen printed metallization.

CHAPTER X

DEVELOPMENT OF A STRATEGY TO APPROACH THE SCHOCKLEY-QUEISSER LIMIT THROUGH NUMERICAL SIMULATIONS

10.1 The Shockley-Queisser Limit

In their 1961 seminal work Shockley and Queisser introduced the so called detailed balance limit to solar cell efficiency [129], this limit is often called the Shockley-Queisser limit. The detailed balance approach is easy to understand and does not delve into device specifics, it calculates the maximum theoretical efficiency in a manner similar to the way the second law of thermodynamics limits the theoretical efficiency of a steam power plant. In their work they calculate the number of photons (assuming AM0 spectrum) incident on a solar cell made of a semiconductor with bandgap E_G at room temperature. They assume that every photon with energy greater than E_G is absorbed and creates a single electron-hole pair and that at thermal equilibrium every electron-hole pair that is created must recombine to balance that generation. The only recombination mechanism they account for is radiative recombination. They found that for E_G of 1.09 eV (very close to Si's E_G of 1.12 eV) that this recombination amounts to 0.27 fA/cm^2. This recombination current is actually the upper bound of the J_0 for the device and limits the open circuit voltage to about 0.845 V [130]. Shockley and Queisser found that the detailed balance limit efficiency for a single junction solar cell is 30%. In 1984 Tiedje *et al.* revisited the Shockley-Queisser limit for Si using the AM1.5G spectrum that is found at the earth's surface and found that the limit efficiency improves to 32.9%, however with the inclusion of Auger recombination the limit efficiency goes back down to 29.8% [131]. This limit is still considered the theoretical maximum for Si solar cells, however it has been shown that a one-sun efficiency of 43.6% is possible for semiconductors that exhibit avalanche generation (multiple electron hole pairs generated for photons with energy much larger than E_G) [132].

10.2 Using recent PV technologies to approach the Shockley-Queisser limit

As previously discussed, the IBC concept is very advantageous for high efficiency device design due to it's lack of shading and minimal series resistance. Additionally, the size of the diffused regions and therefore the auger recombination of these devices can be minimized. In order for a solar cell to approach the Schockley-Queisser limit all recombination mechanisms must be minimized, these include recombination through traps, auger, surface recombination at Si/dielectric interfaces and recombination at Si/contact interfaces. Radiative recombination is also present in C-Si but it is a small fraction of the total recombination in most devices because of silicon's indirect band gap. Recombination through traps can be minimized by using high lifetime n type substrate. And the PCSC design is uniquely suited to minimize auger recombination because the diffused regions where auger recombination dominates are limited to small points on the rear side. Surface recombination at the Si/dielectric interfaces and Si/contact interfaces are what remain as a major barrier to approaching the Schockley-Queisser limit. In this section an optimization of the IBC device structure will be presented to address these remaining two challenges by including Al_2O_3 surface passivation and passivated contacts. This optimization will include the cell thickness, base resistivity, the effect of passivating the emitter contact, the effect of passivating the BSF contact, the effect of an induced junction by Al_2O_3 surface passivation to enlarge the emitter fraction and additionally the effect of an induced floating junction for front surface passivation. The simulation results show that through the implementation of this device design a new world record can be achieved. Further, it is shown that if lambertian light scattering can be achieved an efficiency greater than 27% can be achieved. In figure 10.1 the cell parameters which are varied are highlighted on an IBC diagram.

Recently the negatively charged dielectric Al_2O_3 has been shown to passivate both p and n type substrates by field effect passivation [46]. This passivation has been shown to be superior to passivation by amorphous Si and by thermal SiO_2 and has been shown to give a J_{0e} on p^+ diffused surfaces on below 10 fA/cm^2. Another innovation to reduce recombination in solar cells is the concept of the passivated contact. Passivated contacts can

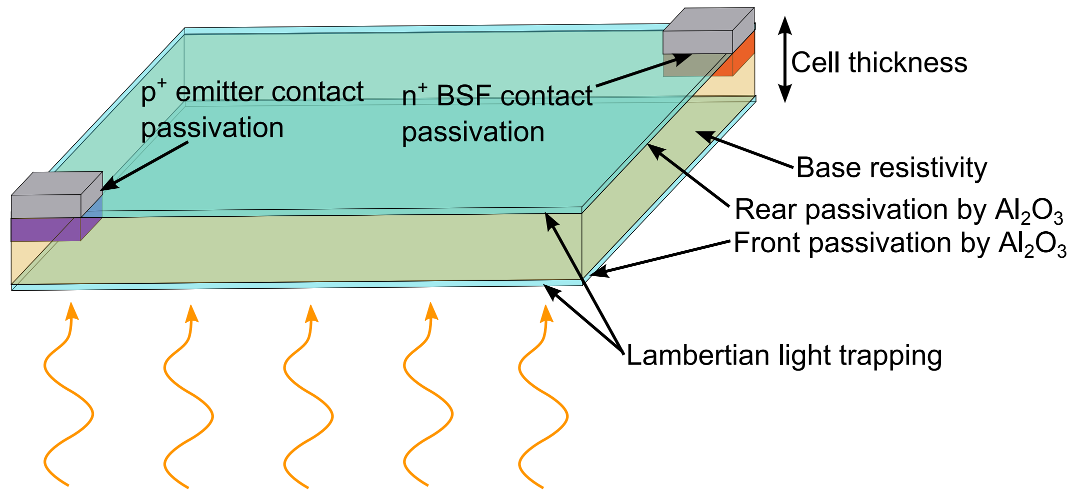

Figure 10.1: Schematic of an IBC showing the device regions optimized in this study.

be achieved by the use of heterojunctions, for example the Sanyo HIT cell [133], or by the use of a thin passivating dielectric which can passivate the surface but is thin enough to tunnel through [134]. The goal of all the approaches to the passivated contact is to either only allow minority carriers in the base to pass into the emitter, a so-called passivated emitter, or to only allow the majority carriers in the emitter or BSF to pass into the contact. Reflecting the majority carriers reduces the recombination because all recombination mechanisms depend on the np product. There are several ways to achieve a passivated contact or passivated emitter, some band diagrams showing different ways to achieve a passivated contact or emitter are shown in figure 10.2. The first method shown on the left is a passivated emitter

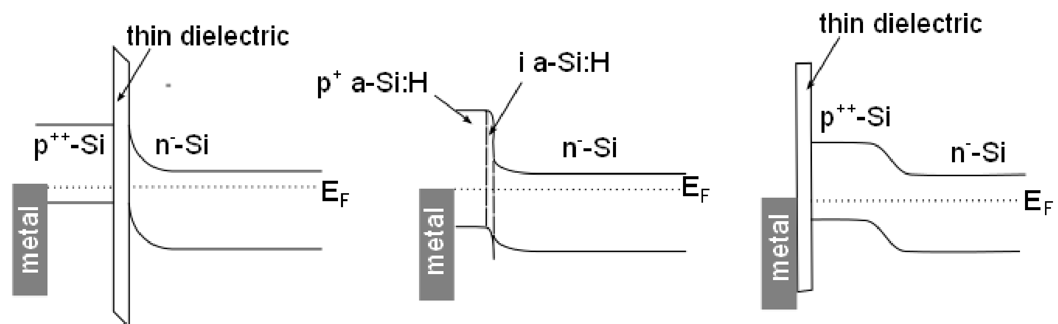

Figure 10.2: Three concepts for a passivated contact(left)doped poly-Si on top of a lowly doped substrate with a thin oxide in between (center) the HIT concept, amorphous-Si junction with a thin intrinsic layer at the interface (right) diffused p^{++} emitter with a thin interfacial oxide between emitter and contact.

achieved by growing a very thin dielectric between the n base substrate and p^{++} doped poly-Si. The middle diagram shows the heterojunction with intrisic thin layer concept, this features a p^{+} doped a-Si emitter which has a wider band gap than C-Si. The wider bandgap creates a large potential barrier for base majority carriers to flow into the emitter. The thin intrinsic layer is grown at the interface to reduce surface recombination at the C-Si/a-Si interface. The diagram on the right shows a passivated contact on a p^{++} emitter, this is achieved by growing a thin dielectric on in between the emitter and the contact. This dielectric must be thin enough to allow tunneling of the emitter majority carriers into the metal contact. For the purposes of this work, the passivated concept simulated is most similar to the far right figure. The contacts in the simulation are "passivated" by assigning an SRV the Si/contact interface.

In the chapter the properties of passivated contacts and surface passivation by Al_2O_3 are demonstrated seperately, then an optimization of an IBC device is carried using these parameters and it is shown that this device is capable of world record efficiencies.

10.3 Quantifying the benefit of passivated contacts through numerical simulation

In this work the effect of the passivated contact will be taken into account by adjusting the SRV at the Si/contact interface. These results will give insight into the SRV required to achieve extremely low J_0 for the diffused regions. The effect of the SRV on J_0 can be found through numerical simulation in the following way. J_0 can be defined as the majority carrier saturation current flowing from the emitter to the base [135]. For example, for an type diffusion on a p type substrate, J_0 can be expressed as is shown in equation 10.1

$$J_{0e} \equiv \frac{-J_p(x'_e)}{n(x'_e)p(x'_e) - n_0(x'_e)p_0(x'_e)} n_0(x'_e)p_0(x'_e) \tag{10.1}$$

where x'_e is the edge of the depletion region on the emitter side, n_0 and p_0 are the equilibrium electron and hole concentrations, finally n, p and J_p are electron and hole concentrations and hole current respectively at a given bias. Therefore values of J_{0e} can be obtained through numerical simulation for a given diffusion profile and SRV value.

The simulation domain is a simple n^{+} p junction (or p^{+} n to explore boron diffused

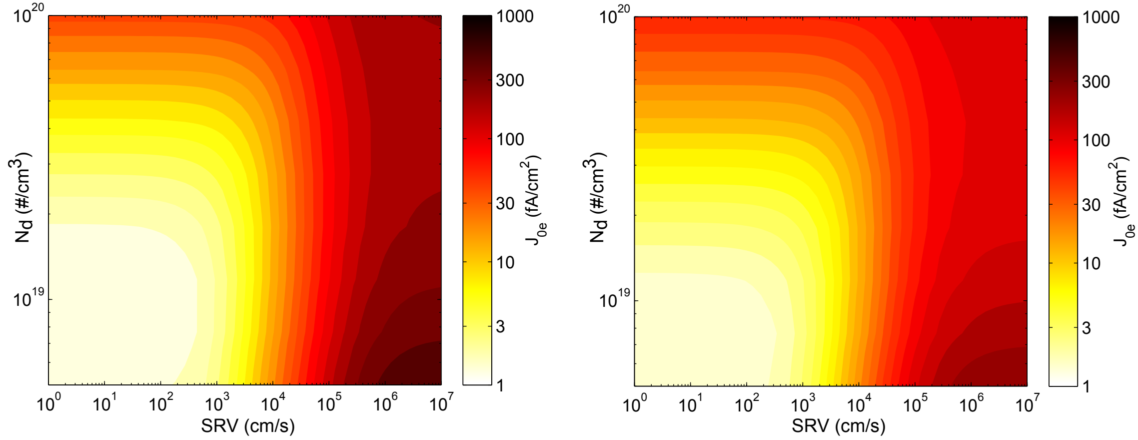

Figure 10.3: Effect of SRV and peak doping level on J_{0e} for 0.5 (left) and 1.0 (right) micron gaussian phosphorus diffusions

regions) with a very small contact on the n^+ emitter and a contact on the base side. The device is simulated under equilibrium to find the junction edge location and the equilibrium electron and hole concentrations. After this the device is simulated under a forward bias of 0.77 V. The electron and hole concentrations as well as the hole current are probed at the junction edge again and a J_0 value is calculated. Using this method, contour plots of J_{0e} versus peak doping and SRV for 0.5 and 1 micron phosphorus and boron doped emitters. Figures 10.3 and 10.4 are the contour plots of the phosphorus and boron emitters. For both n^+ and p^+ diffused regions an SRV of less than 1000 cmm/s is required to obtain low J_{0e} below 5 fA/cm^2 which should be a goal for approaching the theoretical limit. For both phosphorus and boron diffused surfaces the one micron deep junction gives a higher J_{0e} for a given doping level and SRV compared the the 0.5 micron deep junction. Lower doped diffusion achiever lower J_{0e}'s because of less Auger recombination, however, in practice a compromise must be struck between good contact properties and minimized recombination.

10.4 Quantifying the benefit of aluminum oxide surface passivation through numerical simulation

The effectiveness of field effect passivation by the high negative charge in aluminum oxide was investigated by numerically obtaining J_{0e} for a undiffused n-type surface passivated by a dielectric with a surface charge density of $1\text{x}10^{13}/cm^3$ and an SRV of 20 cm/s. The

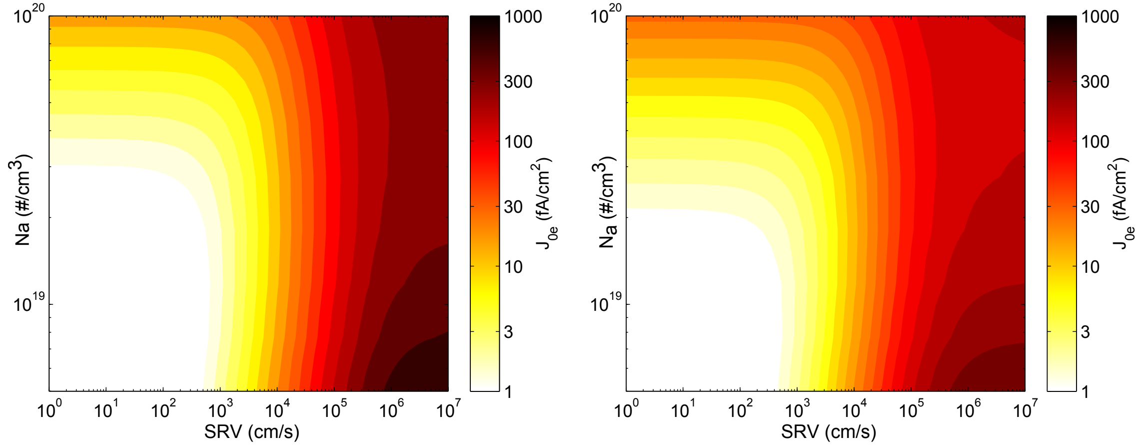

Figure 10.4: Effect of SRV and peak doping level on J_{0e} for 0.5 (left) and 1.0 (right)micron gaussian boron diffusions

simulations reveal an induced junction with an exponential profile with a shallow junction depth of 0.13 microns and a sheet resistance of 1459 $\Omega/\square$. The induced hole density and band bending provided by the high negative charge in the dielectric is shown in figure 10.5. The upward band bending at the surface rejects electrons and minimizes recombination. The numerically determined J_{0e} of the induced junction was found to be 4.6 fA/cm^2

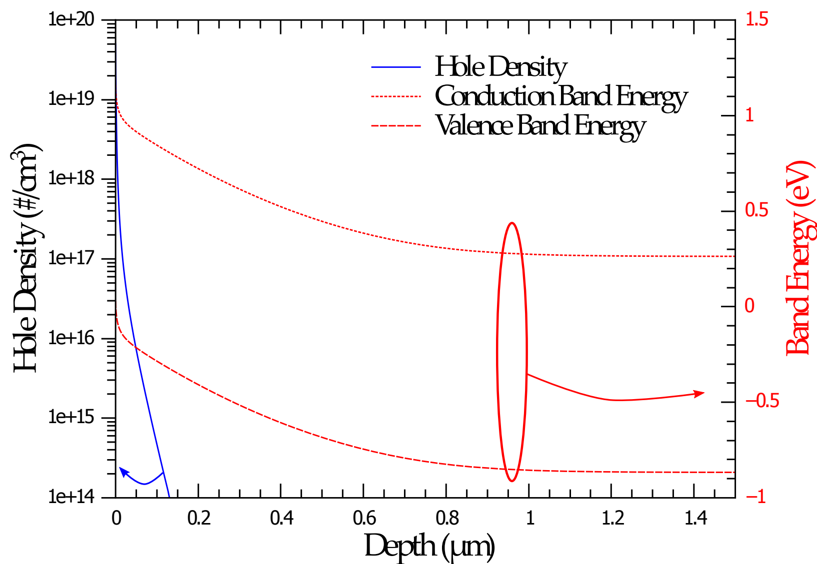

Figure 10.5: Hole density and band bending induced by high negative charge in Al_2O_3.

10.5 *Exploring the practical limit of silicon solar cells*

In this section the IBC device architecture will be optimized for maximum performance without passivated contacts and without Al_2O_3 surface passivation. The benefit of passivated contacts and induced junction by Al_2O_3 will be quantified and the practical limit on solar cell efficiency is found to be 27.15% using these new PV technologies. The physical models used in these simulations are identical to those described in chapter 3. The unit cell simulated and mesh generated for these simulations is shown in figure 10.6 and the parameters for device simulation are shown in table 10.1. In figure 10.6, the device is shown from the rear side of the device. The mesh on the emitter and BSF regions is smaller because of the higher current and carrier densities. Additionally, the mesh near the front and rear surfaces is very fine in the direction parallel to the surface to accurately account for the induced charge when a charged dielectric is used in the simulations.

Figure 10.6: Bottom view of unit cell and mesh used in simulations, blue indicates boron doping and red indicates phosphorus doping. Left half of figure from [116].

For simulations which include Al_2O_3 rear side passivation the induced junction is adjacent to the n^+ BSF which raises concerns over possible shunts between the BSF and the induced emitter. In the simulation results no evidence of shunting was found. To understand the lack of shunt behavior, the simulation results were explored in the region near the edge of the BSF (seen in figure 10.7). It was found that a depletion region separates the n^+ and p^+ regions preventing the shunt.

Table 10.1: Initial Modeled Cell Parameters

Thickness (μm)	180
Unit Cell Width (μm)	100
Bulk Lifetime (μs)	2000
Emitter Contact Width(μm)	20
BSF Contact Width(μm)	10
Emitter Depth (μm)	1
BSF Depth(μm)	1
SRV (cm/s)	10
Passivated Contacts	No
external r_s (Ω-cm^2)	0.2

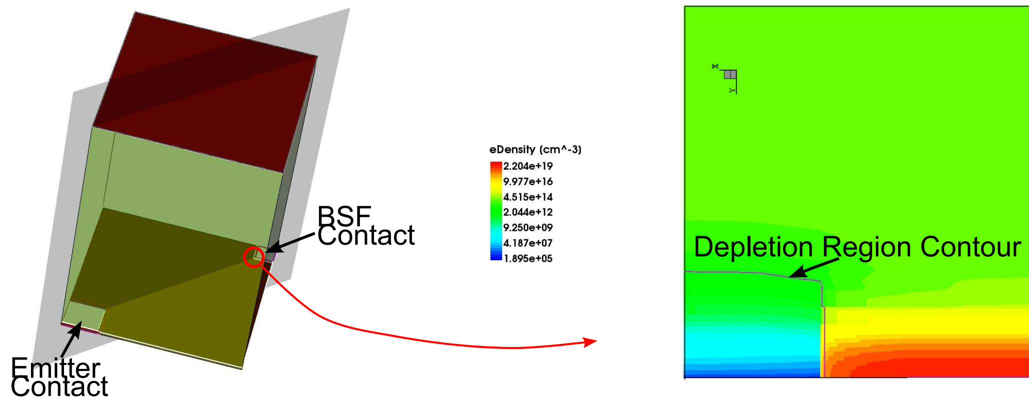

Figure 10.7: (left) Unit cell simulated showing 2d slice taken to explore shunt behavior (right) zoomed in view of highlighted portion of the unit cell showing the depletion region between the n^+ and p^+ regions .

10.5.1 Cell Thickness and Resistivity

The first device parameters explored in this study are the device thickness and resistivity. As expected, as the device thickness increases the J_{sc} increases due to the increased absorption. The V_{oc} decreases with increasing thickness because the total amount of recombination in the base, J_{0b}, increases with increasing thickness. High resistivity substrates showed a trend of decreasing fill factor with increasing thickness while lower resistivity devices fill factors were less sensitive to the device thickness. This trend is typical of rear junction devices where carriers must diffuse through the bulk to be collected at the rear. The maximum efficiency achievable turns out to be independent of the substrate resistivity, higher resistivity devices have higher J_{sc} but lower FF compared to lower resistivity devices, in the end the effects offset each other, which is convenient from a manufacturing point of view because the process is robust to substrates with different doping levels. Based on these results, further device optimization will be performed on 140 μm thick devices with $1x10^{14}$ P atoms/cm^3 which give an efficiency of 22.4%.

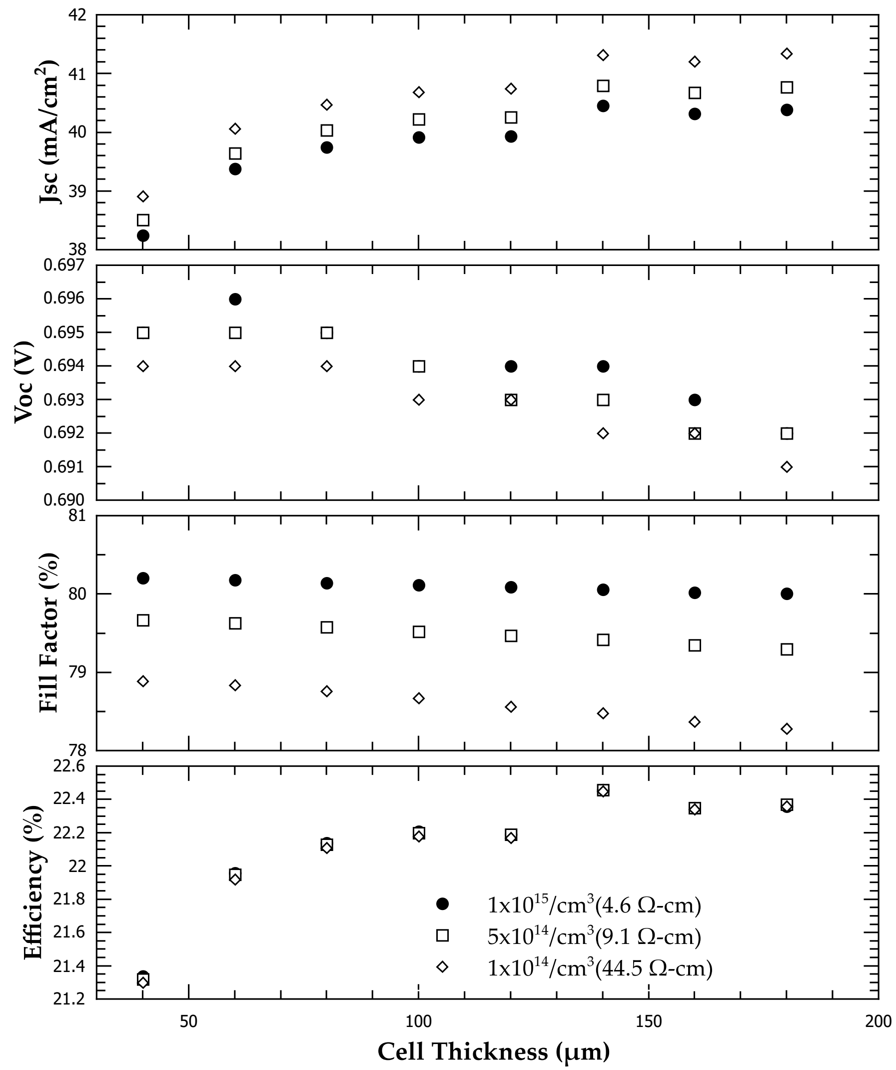

Figure 10.8: Effect of device thickness and base resistivity on cell parameters.

10.5.2 Passivated Emitter Contact

In section 10.3 the effect of the SRV on the J_0 for B diffused regions. Here this is extended to show the benefit of a passivated B emitter contact on device performance for a broad range of peak doping levels and SRV values. The doping profiles used in these simulations were gaussian in shape and 1 μm deep. The results of these simulations will give a guideline of the contact passivation levels required to improve efficiency. The SRV values are varied from near perfect passivation (10 cm/s) up the SRV values common to metal/Si interfaces ($1x10^7$ cm/s). The results of the simulations are shown in figure 10.9. The results show that more lightly doped emitters are more sensitive to the SRV of the contact. This is because for higher doping levels Auger recombination is dominant over surface recombination, so more highly doped surfaces are less sensitive to the contact SRV. The results show that a contact SRV of 1000 cm/s should be the target for development in practice because a further reduction in SRV has virtually no benefit. Alone, the addition of a passivated emitter contact boosts the device efficiency from 22.4% to 22.8%. For further optimization the passivated emitter contact parameters will be set to an SRV of 1000 cm/s and a peak doping of $2.2x10^{19}$ B atoms/cm^3.

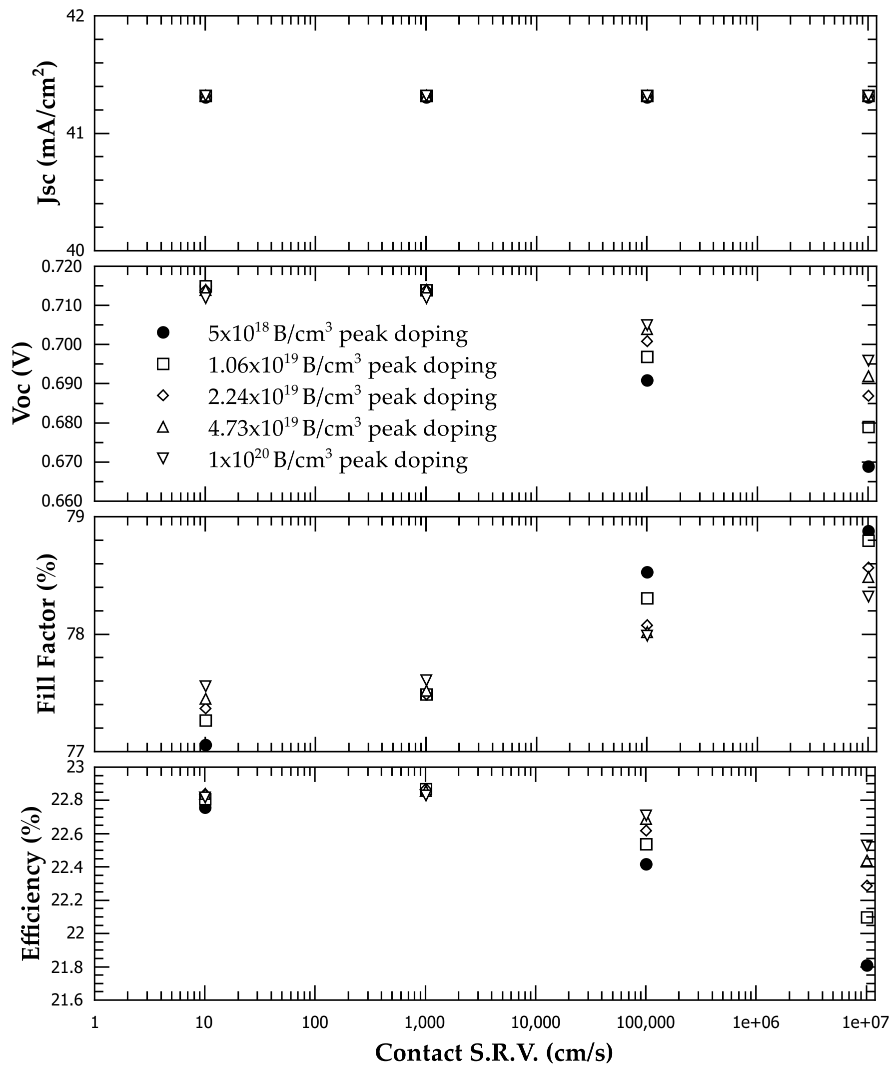

Figure 10.9: Effect of SRV of emitter contact.

10.5.3 Passivated BSF Contact

Using the optimized device thickness, substrate doping and emitter passivation, the next device aspect optimized is the properties of the P doped BSF contact. The BSF doping profiles and contact SRV's were varied identically to the method used to change the emitter profiles in section 10.5.2. The results of the optimization study can be seen in figure 10.10. The $J_{sc}$is independent of the BSF doping and the V_{oc} is sensitive to the SRV especially for low doping, similar to the results for the emitter contact. However, it is interesting to note that for low SRV values a more highly doped BSF provides a superior FF to a lowly doped BSF. To understand this effect, contour plots of the hole density for simulations with high and low BSF doping with an BSF contact SRV of 10 cm/s near the maximum power point are shown in figure 10.11. When the BSF contact has a low SRV and low doping then both surface recombination and Auger recombination are minimized which improves the V_{oc} however as you can it creates a large carrier density gradient around the contacts which has been shown to result in lower terminal voltages and high average carrier densities [136]. These higher carrier densities are the reason for higher SRH recombination which has a quadratic dependence on carrier density. Similar to the passivated emitter contact, we find that a peak doping around $2.2\text{x}10^{19}/cm^3$ with an S of 1000 cm/s is all that is required for best results. With an optimized emitter and BSF contact we find that an efficiency of 23% is achievable.

10.5.4 Front and Rear surface passivation by Al_2O_3

The benefits of surface passivation by the highly negatively charged dielectric Al_2O_3 are discussed in section 10.4, here the application of this dielectric for front and rear surface passivation of the optimized IBC structure is reviewed. The improvements on device performance by front and rear passivation are taken into account separately and are quantified in table 10.5.4. The addition of Al_2O_3 for rear surface passivation comes from the induced emitter on the back side, the addition of the induced emitter increases the emitter fraction from 1% to 99% which has been shown to be an important parameter for IBC cells [128]. The induced emitter created by Al_2O_3 surface passivation increases the Jsc, Voc and FF.

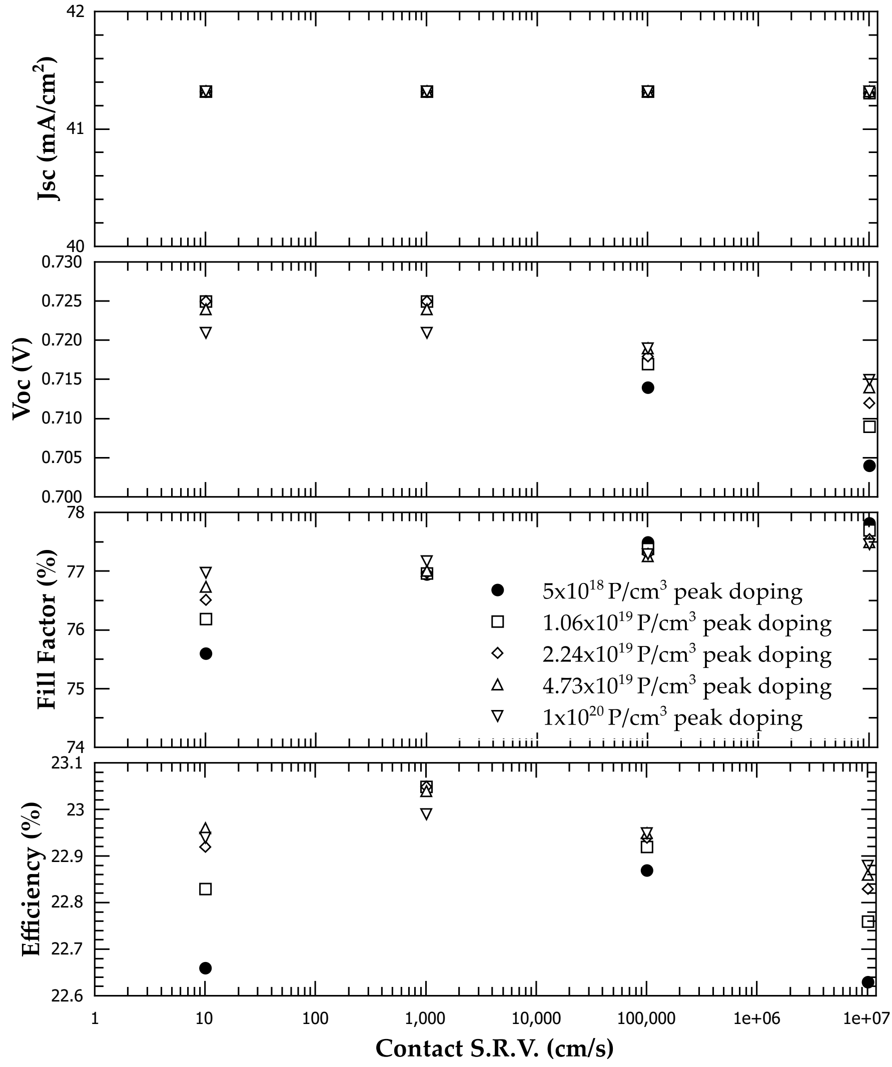

Figure 10.10: Effect of SRV of BSF contact.

Surface Charge (rear, front)	V_{oc}(mV)	J_{sc}(mA/cm^2)	F.F. (%)	Efficiency (%)
0,0	724.7	41.32	76.98	23.05
-1x10^{13} ,0	730.6	41.95	78.75	24.14
0,-1x10^{13}	731.5	41.73	79.13	24.16
-1x10^{13} ,-1x10^{13}	737.5	42.15	82.43	25.62

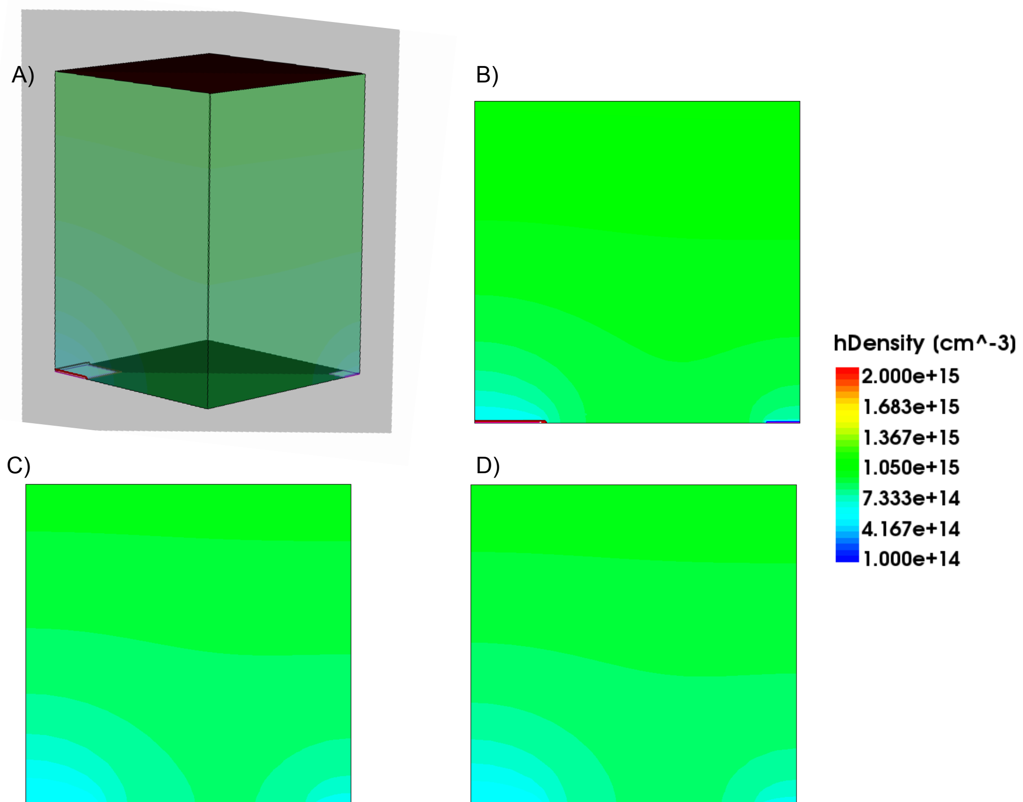

Figure 10.11: A) Figure showing the 3D unit cell and the region from which a 2D slice is taken. B,C and D are contour plots of the hole density within the device for simulations with low BSF doping, low BSF SRV (B) low BSF doping, high BSF SRV (C) and high BSF doping, low BSF SRV (D).

The Jsc is improved by shortening the distance carriers must travel to be collected and thereby reducing the chance of recombination in the bulk. The FF gain is because carriers can travel through a lower resistance path in the induced emitter compared to the bulk. This effect is shown in figure 10.12, where the hole current path is traced from the surface of the device to the emitter contact for simulations with and without Al_2O_3 passivation. Additionally, a small V_{oc} gain is acheived through the field effect passivation, a

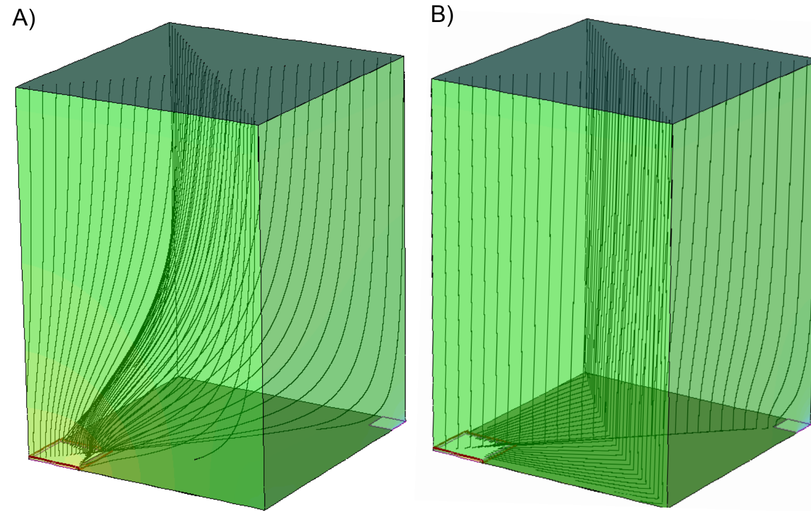

Figure 10.12: Streamlines showing hole current path from the front of the device for A) no induced rear emitter and B) with induced rear emitter.

larger enhancement would be seen if the interface SRV were higher than 10 cm/s.

The addition of the Al_2O_3 passivation of the front surface also introduces similar gains in Jsc, Voc and FF. The combination of front and rear passivation by Al_2O_3 is a dramatic increase over just a well passivated surface with no charge. The end result is an efficiency increase in cell efficiency of over 1.5% absolute to 25.62%.

10.5.5 Lambertian light trapping

Lambertian scattering is achieved when the intensity of light scattered off of a surface is isotropic. Lambertian scattering is considered to be an ideal case for the back surface reflector of a solar cell. In a 1982 seminal work yablanovitch *et al.* showed that for a solar cell with a lambertian rear reflector that maximum path length for a photon of a given wavelength to travel within a solar cell of thickness d is $4n^2d$ [137], where n is the index of

refraction of the solar cell at that wavelength. Although it has recently been shown that there are techniques to surpass the Yablonovitch limit [138], for the purposes of this study it will be taken as an upper bound to the amount of current that can be absorbed. To explore the upper limits of solar cell efficiency simulations were carried on the optimized device design discussed previously. The absorbed current at each wavelength was scaled to the yablonovitch limit and the device thickness was reoptimized for this regime. The results of these simulations are shown in figure 10.13. The trends in the cell parameters are as expected, J_{sc} increases with device thickness because of increased pathlength, while FF and V_{oc} decrease with increasing device thickness due to increased resistance and bulk recombination respectively. The net result is an optimum thickness of 100 μm where an efficiency of 27.15% is possible.

10.5.6 Roadmap

In conclusion, implementation and further development of existing photovoltaic technologies can lead toward record device efficiency using the design shown in this thesis. A roadmap showing the efficiency enhancements for implementation of these technologies is shown in figure 10.14. Currently here at Georgia Tech we can fabricate solar cells of around 20.5% with our "Delta Star" architecture. The improvements from here come through; switching to a point contact cell (~2%), the addition of passivated contacts (~0.5%) and the introduction of front and rear passivation by Al_2O_3 (~1.5%). These improvements would yield a cell with world record efficiency of 25.62%, readers should note that device models and parameters have been chosen to be realistic and achievable. Further improvements for an ideal case from there come through perfect light trapping (27.15%) and elimination of series resistance (27.47%). This work shows the path towards record efficiency through achievable cell improvements and realistic cell design parameters.

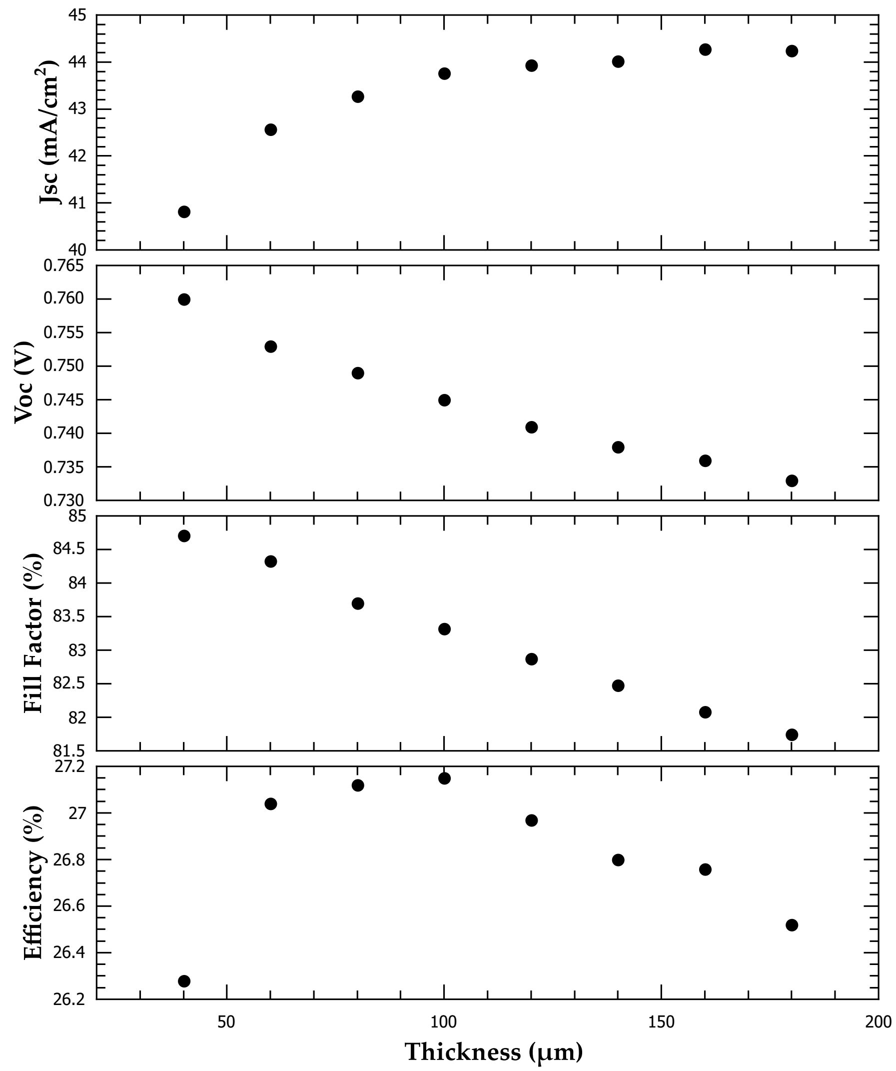

Figure 10.13: Effect of cell thickness of optimized device with Lambertian light trapping.

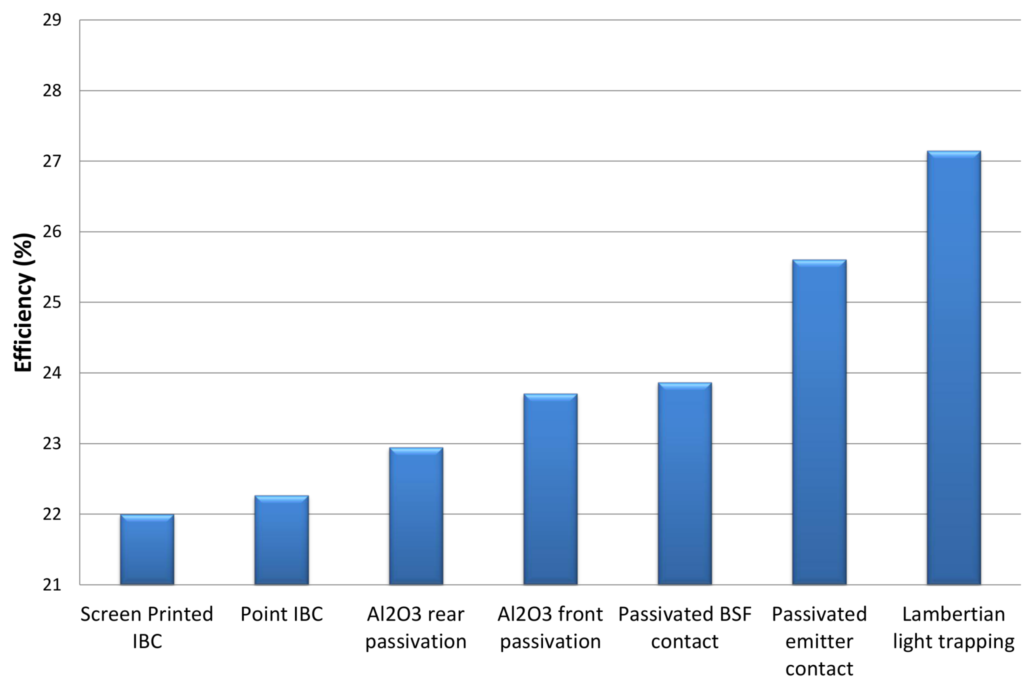

Figure 10.14: The path to over 27% through technology innovations and device optimization.

CHAPTER XI

CONCLUSIONS AND FUTURE WORK

This chapter highlights the scientific contributions made through the course of the research. These contributions are first highlighted here and then discussed more in depth in the following paragraphs. Following this summary is suggestions for future work. The first contribution made in this thesis involves the demonstration through 2D modeling of the advantage of selective emitter solar cells over homogeneous emitter solar cells. This modeling was made possible through the application of a Schottky barrier contact resistance model to screen printed Ag contacts whose contact mechanism is still not completely understood. It is shown, however, that despite the variety of contact mechanisms, the collective sum of all the parts can be described using a Schotty barrier model. Secondly, a process to implement selective emitter technology using a UV laser was developed. UV laser doping is found to create highly doped layers compatible with low ohmic contacts when P-glass formed as a byproduct of $POCl_3$ diffusion is used as the dopant source. However, the selectively UV laser doped regions have lower spectral response when compared to the field region due to heavy doping effects which leads to a lower J_{sc}. This problem is solved through the introduction of a novel new device design with a segmented selective emitter. UV laser doped solar cells with the segmented selective emitter cell design exhibit cell efficiency greater than 19%. In addition, this process is also shown to be compatible with an emitter etch-back process without the need of a masking step. This etch-back process also yields device efficiencies of 19%. Looking now towards future trends in photovoltaics, 3D numerical modeling is performed to show the practical limit of solar cells is 27% if passivated contacts and superior surface passivation is achieved along with improved light trapping. Finally, design guidelines are developed through 2D device modeling for a screen printed IBC cells which is shown to be capable of efficiencies greater than 22%.

11.1 Accurate modeling of screen printed contacts and the benefit of selective emitter solar cells

A model for doping dependent contact resistance for screen printed silicon solar cells is required for accurate device modeling. This is a challenge because, unlike evaporated contacts, carrier transport mechanisms through screen printed contacts are not well defined or understood. This deficiency has limited the accuracy of device optimization attempts because contact resistance severely limits device performance in the low doping regime. In this thesis it is shown for the first time that despite the complex nature and variety of transport mechanisms of silver screen printed pastes, the behavior can be described as Schottky-like with an effective barrier height dictated by paste constituents and firing conditions. A combination of theoretical modeling and experimental data was used to extract barrier heights associated with different screen printed pastes. It was found that most screen printed pastes have an effective barrier heigh between 2 and 3 eV. This model was applied to show the benefit of a selective emitter over a homogeneous emitter for various effective barrier heights. The modeling predicts greater than 0.4% efficiency benefit for selective emitter solar cells compared to a homogeneous emitter solar cells with Al BSF.

11.2 Investigation and optimization of ultraviolet laser doping on Si

After establishing the efficiency entitlement of screen printed selective emitter solar cells, UV laser doping for the formation of selective emitters in crystalline silicon solar cells is explored. Most studies in the past have focused on laser doping with a green laser (λ=532nm) but few studies using UV laser doping in C-Si solar exist. Various doping sources are explored for laser doping including spin on B and P dopants as well as P-glass formed afer $POCl_3$ diffusion as a source. It is shown that UV laser doping with spin on dopants is not well suited for creating heavily doped regions, however, it is found that UV laser doping is quite effective at creating heavily doped regions with minimal surface damage using P-glass as the dopant source when the low laser pulse powers are used ($>$ 100 khz, $<$ 100 μJ/pulse). The resulting doped layers provided an order of magnitude improvement in contact resistance when compared to screen printed contacts on high sheet resistance emitters ($>$ 100 $\Omega/\square$),

enabling the fabrication of high efficiency selective emitter cells in this research.

11.3 Application of UV laser doping in crystalline Si solar cells

It is shown that for the first time that a selective emitter by UV laser irradiation is capable of increasing device efficiencies above 19%. The UV laser doping process is optimized and roughly 30 μJ/pulse is found to be the optimum power to create a highly doped selective emitter without damaging the substrate. The UV laser doped selective emitter cells show improvement in V_{oc} and FF compared to reference cells without a selective emitter. However, it was found that the high doping and defects created in the laser doped region lowered the J_{sc} compared to the reference. The low J_{sc} problem is solved in this research through the creation of a novel cell design, the segmented selective emitter solar cell. In this device design, the continuous selective emitter region is replaced by segments of high and low doped regions to reduce the heavy doping effects. The result of this development is an industry ready solar cell which has a demonstrated cell efficiency achieving above 19%. Additionally, UV laser doping with a segmented selective emitter is applied with an emitter etchback technology. In this process the highly doped surface region of the cell is etched away which is shown to reduce the J_{0e} of the emitter. The etchback process is demonstrated to be compatable with UV laser doped selective emitters without the need of a masking step. This process is also shown to give 19% efficiency.

11.4 2D and 3D modeling of back contact solar cells to determine the practical efficiency limit and optimize a screen printed IBC cell

The world's best Si solar cell is 25% today but the theoretical efficiency limit established by Schockley and Queisser is 29.3%. In this thesis an attempt is made to provide a roadmap to a 27% efficienct cell through modeling and design of a point contact solar cell. A practically achievable path towards a world record solar cell has been developed in this thesis. Extensive device modeling in this work has shown that through implementation and further development of passivated contacts and surface passivation by aluminum oxide cell efficiency's greater than 25.5% are achievable. Further, the addition of improved light trapping can push the cell efficiency above 27%. Additionally, a back contacted device for which

design guidelines are given in this thesis is an IBC with screen printed contacts. These simulations incorporated doping profiles and dimensions which are fully contactable and able to be aligned with current screen printing technology. These two groups of simulations represent a low cost manufacturable path to greater than 22% efficient screen printed IBC cell as well as guidelines to achieve world record laboratory cell efficiencies of 27% through the implemenation of Al_2O_3 and passivated contacts using an IBC device design.

11.5 Suggested future work

Future work related to this thesis involves further development of passivated contacts for n and p type surfaces and well as light trapping techniques, so that the predicted maximum practical efficiency around 27% can be achieved. One promising technology for improved light trapping is black silicon, which has very good antireflection properties without an antireflection coating, however surface passivation is a challenge in this case. More work especially needs to be done in the development of passivated contacts for B diffused surfaces. For P diffused surface passivated contacts have been demonstrated however, this technology is still in it's infancy and needs further deveopment. The development of passivated contacts enables cell V_{oc}'s above 700 mV. For smaller incremental gains in cell efficiency the UV laser doping process should be adopted to a cell structure with a passivated rear as opposed to an Al BSF. The difference in these two cell structures is shown in figure 11.1. These solar

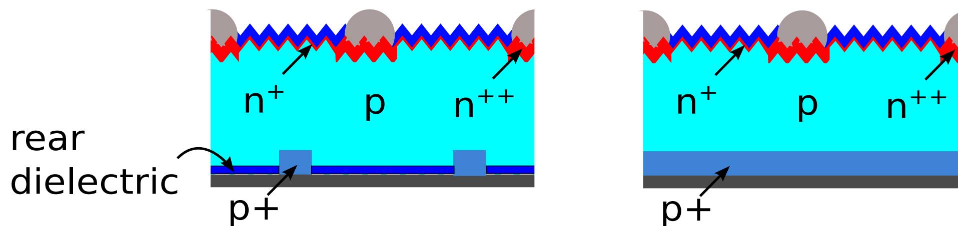

Figure 11.1: Selective emitter solar cell with (left) and without (right) a passivated rear for improved passivation and relfectance.

cells have a much higher V_{oc} compared to Al BSF solar cells as well as an improved J_{sc} due to the improved reflectance of the Si/SiN_x interface compared to the Si/Al paste interface. The development of this process will require the development of a method for a single sided $POCl_3$ diffusion, which has so far proven difficult but should be possible. The development

of this cell structure should push cell efficiency near 21%. Finally the screen printed IBC device designed in this thesis should be fabricated, the simplest approach for the would be through using patterned implantation as a means for creating the alternating P and B diffused regions on the rear side of the device. This device should allow device efficiencies above 22%.

APPENDIX A

INPUT FILES FOR SENTAURUS WORKBENCH FOR SOLAR CELL SIMULATION

Sentaurus Device Editor code to create a typical crystalline Si solar cell.

```
;;Solar Cell Model
;; John Renshaw
;; 11/2/2012

(sde:clear)

;;;;Definitions placed here;;;;;;;;;;;;;;;;;;;;;;;;;;;;;;;;;
(display "...defining commonly used parameters...")(newline)
;;material properties
(define cellWidth @width@)  ;microns
(define cellDepth @siThick@)  ;microns
(define sinThick @sinThick@)  ;microns
;;doping properties
(define substrateDoping @subDoping@) ;/cm^3
(define pDopingPeak @emitterDop@) ; #/cm^3
(define junctionDepth @emitterDep@)  ;microns
(define bsfDoping @bsfDop@) ; #/cm^3
(define bsfThick @bsfDep@) ;microns
;;contact properies
(define frontContactHalfWidth @contWidth@) ;microns
;;refinement properties
```

```
(define opticalDepth @optDepth@) ;microns



;; Build cell components here;;;;;;;;;;;;;;;;;;;;;;;;;;;;;;;

(display "...build structures...")(newline)


;;Silicon substrate

(sdegeo:create-rectangle

(position 0.0 0.0 0.0)

(position cellWidth cellDepth 0)

"Silicon" "R.Substrate")


;;SiN AR coating

(sdegeo:create-rectangle

(position frontContactHalfWidth 0.0 0.0)

(position cellWidth (- sinThick) 0)

"Si3N4" "R.Nitride")


;;;; Add dopings here;;;;;;;;;;;;;;;;;;;;;;;;;;;;;;;;;;;;;;

(display "...defining doping...")(newline)

;;Constant substrate doping;;;;;;;;;;;;;;;;;;


(sdedr:define-refinement-window

"Win.substrateDoping"

"Rectangle"

(position 0 0 0)

(position cellWidth cellDepth 0)

)
```

```
(sdedr:define-constant-profile
"Profile.substrateDoping"
"BoronActiveConcentration"
 substrateDoping)

(sdedr:define-constant-profile-placement
"Place.substrateDoping"
"Profile.substrateDoping"
 "Win.substrateDoping" )

;;Gaussian emitter profile;;;;;;;;;;;;;;;;;;

(sdedr:define-refinement-window
"Win.gaussEmitterDoping"
"Line"
(position 0 0 0)
(position cellWidth 0 0)
)

(sdedr:define-gaussian-profile
"gaussEmitterDoping"
"PhosphorusActiveConcentration"
"PeakPos" 0
"PeakVal" pDopingPeak
"ValueAtDepth" substrateDoping
"Depth" junctionDepth
"Gauss"  "Factor" 0
)
```

```
(sdedr:define-analytical-profile-placement
"Place.gaussEmitterDoping"
 "gaussEmitterDoping"
 "Win.gaussEmitterDoping"
"Positive"
"noReplace"
"Eval"
)



;;Constant BSF doping;;;;;;;;;;;;;;;;;;;;;;


(sdedr:define-refinement-window
"Win.bsfDoping"
"Rectangle"
(position 0 cellDepth 0)
(position cellWidth (- cellDepth bsfThick) 0)
)


(sdedr:define-constant-profile
"Profile.bsfDoping"
"BoronActiveConcentration"
 bsfDoping)


(sdedr:define-constant-profile-placement
"Place.bsfDoping"
"Profile.bsfDoping"
 "Win.bsfDoping" )
;;;;;;;;;;;Add contacts here;;;;;;;;;;;;;;;;;;;;;;;
```

```
(display "...adding contacts...")(newline)
(sdegeo:insert-vertex (position frontContactHalfWidth 0 0.0))

(sdegeo:define-contact-set "nContact" 4 (color:rgb 1 0 0 ))
(sdegeo:define-contact-set "pContact" 4 (color:rgb 0 0 1))

(sdegeo:define-2d-contact (find-edge-id
(position (/ frontContactHalfWidth 2) 0 0))  "nContact" )
(sdegeo:define-2d-contact (find-edge-id
(position (/ cellWidth 2) cellDepth 0))  "pContact" )

(sde:refresh)
;;;;;;;;;;;Add optical generation here;;;;;;;;;;;;;;;;;;;;;;;;;;
(display "...adding optical generation...")(newline)

(sdedr:define-refinement-window "Win.opticalGen" "Line"
(position frontContactHalfWidth 0 0)
(position cellWidth 0 0)
)

(sdedr:define-1d-external-profile
"Profile.opticalGen"
"opticalGen.plx"
 "Scale" 1.0
 "Erf"
 "Factor" 0.0)

(sdedr:define-analytical-profile-placement
 "Place.opticalGen"
```

```
 "Profile.opticalGen"
 "Win.opticalGen"
"Positive"
"NoReplace"
"Eval"
)


;;;;;;;;;;Add mesh refinements here;;;;;;;;;;;;;;;;;;;;;;;;;;;;;;;;;
(display "...adding refinements...")(newline)
;;;;global refinenment;;;;;;;;;;;;;;;

(sdedr:define-refinement-size "Ref.global" 30 10 0 10 5 0)
(sdedr:define-refinement-window "Win.global" "Rectangle"
(position 0 0 0)
(position cellWidth cellDepth 0) )

(sdedr:define-refinement-placement
"Place.global"
"Ref.global"
 "Win.global" )


;;;;front contact refinenment;;;;;;;;;;;;;;;

(sdedr:define-refinement-size "Ref.contact" .5 .1 0 1 .01 0)
(sdedr:define-refinement-window "Win.contact" "Rectangle"
(position (- frontContactHalfWidth 3) 0 0)
(position (+ frontContactHalfWidth 3) 0.1 0) )
```

```
(sdedr:define-refinement-placement
"Place.contact"
 "Ref.contact"
 "Win.contact" )

;;;;optical refienment;;;;;;;;;;;;;;

(sdedr:define-refinement-window "Win.optical" "Rectangle"
(position 0 0 0)
(position cellWidth opticalDepth 0) )
(sdedr:define-multibox-size "Ref.optical" 10 1 5 .001  0 1.3 )
(sdedr:define-multibox-placement
"Place.optical"
"Ref.optical"
 "Win.optical")

;;;;BSF refinement;;;;;;;;;;;;;;

(sdedr:define-refinement-window "Win.bsfRef" "Rectangle"
(position 0 cellDepth 0)
(position cellWidth (- cellDepth (+ bsfThick 3)) 0)
)
(sdedr:define-multibox-size "Ref.bsfRef"  10 1 5 .01 0 -1.2 )
(sdedr:define-multibox-placement
"Place.bsfRef"
"Ref.bsfRef"
"Win.bsfRef")
```

```
;;;;;build mesh;;;;;;;;;;;;;;;;;;;;;;;;;;;;;;;;;;;;;;;;;;;;;;
(display "...building mesh...")(newline)
(sde:save-model (string-append "n" "@node@" "_msh"))
(display "...building mesh...")(newline)
(sdeio:save-dfise-bnd "all" (string-append "n" "@node@" "_msh.bnd") )
(display "...building mesh...")(newline)
(sde:build-mesh "snmesh" "-discontinuousData -F tdr"
(string-append "n" "@node@" "_msh"))
```

The following is the sentaurus device code to choose models and methods for solving the coupled Poisson and electron and hole continuity equations

```
##SDevice Solar Cell simulation File
##John Renshaw 11/2/2012

#setdep @node|sde@

File {
* input files:
Grid = "n@node|sde@_msh.tdr"
* output files:
Plot = "n@node@_des.tdr"
Current = "n@node@_des.plt"
Output = "n@node@_des.log"
OpticalGenerationInput =   "n@node|sde@_msh.tdr"
parameter="@parameter@"

}

Electrode {
{ Name="nContact" Voltage=0.0 DistResist=SchottkyResist }
{ Name="pContact" Voltage=0.0 }
}

Physics {
Area = @<1e11/1047.5>@ #normalize area to 1 cm^2
   Temperature=300

Mobility (PhuMob(Klaassen))
```

```
EffectiveIntrinsicDensity (TableBGN) #looks up tabulated values of Schenk BGN model
Recombination(
Auger
SRH(DopingDependence)
)
* Use fermi statistics
Fermi(-WithJoyceDixon)

Optics(
OpticalGeneration(
ReadFromFile(Scaling=@<1-busShadingFrac>@)
)
)

}

Physics (MaterialInterface="Silicon/Si3N4"){
Recombination(SurfaceSRH)
}



Plot {
eDensity hDensity eCurrent hCurrent
Potential SpaceCharge ElectricField
eMobility hMobility eVelocity hVelocity
Doping DonorConcentration AcceptorConcentration
SRH Auger OpticalGeneration
```

```
}

Math {
Extrapolate
Derivatives
Iterations=50
Notdamped=20
RelErrControl
  ErReff(electron)=1.e3
   ErReff(hole)=1.e3
  Digits=5
method=Pardiso
-MetalConductivity
BreakCriteria { Current (Contact = "pContact" maxval = 1e-10)}
}

Solve{
Poisson
coupled { poisson electron hole }

Quasistationary( InitialStep=0.1 MaxStep=0.08 Minstep=1e-6
DoZero
Goal{name="pContact" voltage=0.45} )
{ coupled { poisson electron hole } }

Quasistationary( InitialStep=0.03 MaxStep=0.03 Minstep=1e-6
Goal{name="pContact" voltage=0.75} )
{ coupled { poisson electron hole } }
```

```
}
```

This is a parameter file which includes the models used in the simulations and their parameters

```
Electrode = "nContact" {
SchottkyResistance {
Rinf = 2.4000e-09 , 5.2000e-09 # [Ohm*cm^2]
PhiB = 1.80 , 0.51 # [eV]
mt = 0.19 , 0.16 # [1]
}
}

Material = "Silicon" {

Epsilon
{ *  Ratio of the permittivities of material and vacuum

  * epsilon() = epsilon
epsilon = 11.9 # [1] modified from 11.7 to 11.9 to match with PC1D by Kim
}

Bandgap {
    Eg0 = +1.1752165e+00  # n_i = 9.65e9 at 300 K (Altermatt PVSC Sapporo 1999)
    alpha = +4.73e-04
    beta = +6.36e+02
}

eDOSMass {
```

```
    Formula = 1
    a = +1.905e-01
    ml = +9.163e-01
}

ConstantMobility:
{ * mu_const = mumax (T/T0)^(-Exponent)
mumax = 1.4170e+03 ,4.7050e+02 # [cm^2/(Vs)] default is 1.4170e+03 ,4.7050e+02
Exponent = 2.5 ,2.2 # [1] [cm^2/(Vs)] default is 2.5 ,2.2
}

Scharfetter {
  * tau = taumin + ( taumax - taumin ) / ( 1 + ( N/Nref )^gamma)
  * tau(T) = tau * ( (T/300)^Talpha )          (TempDep)
 * tau(T) = tau * exp( Tcoeff * ((T/300)-1) ) (ExpTempDep)
taumin = 0,0 # [s]
  taumax = 500e-6 ,5000e-6  # [s]
  Nref = 1.0000e+16 ,1.0000e+16 # [cm^(-3)]
gamma = 1 ,1 # [1] changed to 1 from 1.739 jr
Talpha = -1.5 ,-1.5 # [1]
Tcoeff = 2.55 ,2.55 # [1]
Etrap = 0.0000e+00 # [eV]
}
```

```
* Tabulated Values from Schenk model
TableBGN {
Acceptor  +1.0000000e+10  +000000000e+00
Acceptor  +1.0000000e+15  +1.4051583e-03
Acceptor  +1.1748976e+15  +1.5206727e-03
Acceptor  +1.3803843e+15  +1.6454732e-03
Acceptor  +1.6218101e+15  +1.7802713e-03
Acceptor  +1.9054607e+15  +1.9258276e-03
Acceptor  +2.2387211e+15  +2.0829536e-03
Acceptor  +2.6302680e+15  +2.2525147e-03
Acceptor  +3.0902954e+15  +2.4354322e-03
Acceptor  +3.6307805e+15  +2.6326857e-03
Acceptor  +4.2657952e+15  +2.8453154e-03
Acceptor  +5.0118723e+15  +3.0744238e-03
Acceptor  +5.8884366e+15  +3.3211775e-03
Acceptor  +6.9183097e+15  +3.5868093e-03
Acceptor  +8.1283052e+15  +3.8726185e-03
Acceptor  +9.5499259e+15  +4.1799729e-03
Acceptor  +1.1220185e+16  +4.5103084e-03
Acceptor  +1.3182567e+16  +4.8651296e-03
Acceptor  +1.5488166e+16  +5.2460092e-03
Acceptor  +1.8197009e+16  +5.6545873e-03
Acceptor  +2.1379621e+16  +6.0925695e-03
Acceptor  +2.5118864e+16  +6.5617248e-03
Acceptor  +2.9512092e+16  +7.0638822e-03
Acceptor  +3.4673685e+16  +7.6009265e-03
Acceptor  +4.0738028e+16  +8.1747919e-03
Acceptor  +4.7863009e+16  +8.7874538e-03
```

```
Acceptor  +5.6234133e+16  +9.4409168e-03
Acceptor  +6.6069345e+16  +1.0137196e-02
Acceptor  +7.7624712e+16  +1.0878292e-02
Acceptor  +9.1201084e+16  +1.1666151e-02
Acceptor  +1.0715193e+17  +1.2502602e-02
Acceptor  +1.2589254e+17  +1.3389274e-02
Acceptor  +1.4791084e+17  +1.4327467e-02
Acceptor  +1.7378008e+17  +1.5317973e-02
Acceptor  +2.0417379e+17  +1.6360844e-02
Acceptor  +2.3988329e+17  +1.7455116e-02
Acceptor  +2.8183829e+17  +1.8598517e-02
Acceptor  +3.3113112e+17  +1.9787260e-02
Acceptor  +3.8904514e+17  +2.1016072e-02
Acceptor  +4.5708819e+17  +2.2278648e-02
Acceptor  +5.3703180e+17  +2.3568704e-02
Acceptor  +6.3095734e+17  +2.4881569e-02
Acceptor  +7.4131024e+17  +2.6215946e-02
Acceptor  +8.7096359e+17  +2.7575083e-02
Acceptor  +1.0232930e+18  +2.8966616e-02
Acceptor  +1.2022644e+18  +3.0400895e-02
Acceptor  +1.4125375e+18  +3.1888388e-02
Acceptor  +1.6595869e+18  +3.3437288e-02
Acceptor  +1.9498446e+18  +3.5052217e-02
Acceptor  +2.2908677e+18  +3.6734250e-02
Acceptor  +2.6915348e+18  +3.8481835e-02
Acceptor  +3.1622777e+18  +4.0292000e-02
Acceptor  +3.7153523e+18  +4.2161341e-02
Acceptor  +4.3651583e+18  +4.4086607e-02
Acceptor  +5.1286138e+18  +4.6064873e-02
```

```
Acceptor  +6.0255959e+18  +4.8093417e-02
Acceptor  +7.0794578e+18  +5.0169411e-02
Acceptor  +8.3176377e+18  +5.2289550e-02
Acceptor  +9.7723722e+18  +5.4449713e-02
Acceptor  +1.1481536e+19  +5.6644789e-02
Acceptor  +1.3489629e+19  +5.8868845e-02
Acceptor  +1.5848932e+19  +6.1115840e-02
Acceptor  +1.8620871e+19  +6.3381069e-02
Acceptor  +2.1877616e+19  +6.5663281e-02
Acceptor  +2.5703958e+19  +6.7967054e-02
Acceptor  +3.0199517e+19  +7.0304467e-02
Acceptor  +3.5481339e+19  +7.2695032e-02
Acceptor  +4.1686938e+19  +7.5163362e-02
Acceptor  +4.8977882e+19  +7.7735212e-02
Acceptor  +5.7543994e+19  +8.0433422e-02
Acceptor  +6.7608298e+19  +8.3275258e-02
Acceptor  +7.9432823e+19  +8.6271728e-02
Acceptor  +9.3325430e+19  +8.9428500e-02
Acceptor  +1.0964782e+20  +9.2747564e-02
Acceptor  +1.2882496e+20  +9.6228912e-02
Acceptor  +1.5135612e+20  +9.9871838e-02
Acceptor  +1.7782794e+20  +1.0367577e-01
Acceptor  +2.0892961e+20  +1.0764072e-01
Acceptor  +2.4547089e+20  +1.1176740e-01
Acceptor  +2.8840315e+20  +1.1605729e-01
Acceptor  +3.3884416e+20  +1.2051250e-01
Acceptor  +3.9810717e+20  +1.2513568e-01
Acceptor  +4.6773514e+20  +1.2992990e-01
Acceptor  +5.4954087e+20  +1.3489856e-01
```

Acceptor	+6.4565423e+20	+1.4004528e-01
Acceptor	+7.5857758e+20	+1.4537385e-01
Acceptor	+8.9125094e+20	+1.5088819e-01
Acceptor	+1.0471285e+21	+1.5659232e-01
Acceptor	+1.2302688e+21	+1.6249042e-01
Acceptor	+1.4454398e+21	+1.6858680e-01
Acceptor	+1.6982437e+21	+1.7488602e-01
Acceptor	+1.9952623e+21	+1.8139296e-01
Acceptor	+2.3442288e+21	+1.8811299e-01
Acceptor	+2.7542287e+21	+1.9505213e-01
Acceptor	+3.2359366e+21	+2.0221722e-01
Acceptor	+3.8018940e+21	+2.0961622e-01
Acceptor	+4.4668359e+21	+2.1725839e-01
Acceptor	+5.2480746e+21	+2.2515463e-01
Acceptor	+6.1659500e+21	+2.3331769e-01
Acceptor	+7.2443596e+21	+2.4176248e-01
Acceptor	+8.5113804e+21	+2.5050626e-01
Acceptor	+1.0000000e+22	+2.5956885e-01
Donor	+1.0000000e+10	+000000000e+00
Donor	+1.0000000e+15	+1.4062347e-03
Donor	+1.1748976e+15	+1.5219386e-03
Donor	+1.3803843e+15	+1.6469623e-03
Donor	+1.6218101e+15	+1.7820231e-03
Donor	+1.9054607e+15	+1.9278886e-03
Donor	+2.2387211e+15	+2.0853788e-03
Donor	+2.6302680e+15	+2.2553687e-03
Donor	+3.0902954e+15	+2.4387915e-03
Donor	+3.6307805e+15	+2.6366404e-03
Donor	+4.2657952e+15	+2.8499720e-03

```
Donor     +5.0118723e+15  +3.0799081e-03
Donor     +5.8884366e+15  +3.3276384e-03
Donor     +6.9183097e+15  +3.5944230e-03
Donor     +8.1283052e+15  +3.8815942e-03
Donor     +9.5499259e+15  +4.1905585e-03
Donor     +1.1220185e+16  +4.5227991e-03
Donor     +1.3182567e+16  +4.8798772e-03
Donor     +1.5488166e+16  +5.2634341e-03
Donor     +1.8197009e+16  +5.6751936e-03
Donor     +2.1379621e+16  +6.1169637e-03
Donor     +2.5118864e+16  +6.5906400e-03
Donor     +2.9512092e+16  +7.0982093e-03
Donor     +3.4673685e+16  +7.6417546e-03
Donor     +4.0738028e+16  +8.2234619e-03
Donor     +4.7863009e+16  +8.8456296e-03
Donor     +5.6234133e+16  +9.5106804e-03
Donor     +6.6069345e+16  +1.0221177e-02
Donor     +7.7624712e+16  +1.0979842e-02
Donor     +9.1201084e+16  +1.1789578e-02
Donor     +1.0715193e+17  +1.2653491e-02
Donor     +1.2589254e+17  +1.3574911e-02
Donor     +1.4791084e+17  +1.4557386e-02
Donor     +1.7378008e+17  +1.5604661e-02
Donor     +2.0417379e+17  +1.6720575e-02
Donor     +2.3988329e+17  +1.7908875e-02
Donor     +2.8183829e+17  +1.9172870e-02
Donor     +3.3113112e+17  +2.0514899e-02
Donor     +3.8904514e+17  +2.1935611e-02
Donor     +4.5708819e+17  +2.3433144e-02
```

Donor	+5.3703180e+17	+2.5002439e-02
Donor	+6.3095734e+17	+2.6635059e-02
Donor	+7.4131024e+17	+2.8319882e-02
Donor	+8.7096359e+17	+3.0044811e-02
Donor	+1.0232930e+18	+3.1799142e-02
Donor	+1.2022644e+18	+3.3575801e-02
Donor	+1.4125375e+18	+3.5372605e-02
Donor	+1.6595869e+18	+3.7192170e-02
Donor	+1.9498446e+18	+3.9040695e-02
Donor	+2.2908677e+18	+4.0926272e-02
Donor	+2.6915348e+18	+4.2857330e-02
Donor	+3.1622777e+18	+4.4841561e-02
Donor	+3.7153523e+18	+4.6885363e-02
Donor	+4.3651583e+18	+4.8993682e-02
Donor	+5.1286138e+18	+5.1170056e-02
Donor	+6.0255959e+18	+5.3416736e-02
Donor	+7.0794578e+18	+5.5734777e-02
Donor	+8.3176377e+18	+5.8124085e-02
Donor	+9.7723722e+18	+6.0583432e-02
Donor	+1.1481536e+19	+6.3110525e-02
Donor	+1.3489629e+19	+6.5702249e-02
Donor	+1.5848932e+19	+6.8355268e-02
Donor	+1.8620871e+19	+7.1067129e-02
Donor	+2.1877616e+19	+7.3837903e-02
Donor	+2.5703958e+19	+7.6672069e-02
Donor	+3.0199517e+19	+7.9579985e-02
Donor	+3.5481339e+19	+8.2578090e-02
Donor	+4.1686938e+19	+8.5687344e-02
Donor	+4.8977882e+19	+8.8930252e-02

Donor	+5.7543994e+19	+9.2327600e-02
Donor	+6.7608298e+19	+9.5896151e-02
Donor	+7.9432823e+19	+9.9647875e-02
Donor	+9.3325430e+19	+1.0359053e-01
Donor	+1.0964782e+20	+1.0772892e-01
Donor	+1.2882496e+20	+1.1206626e-01
Donor	+1.5135612e+20	+1.1660522e-01
Donor	+1.7782794e+20	+1.2134866e-01
Donor	+2.0892961e+20	+1.2630001e-01
Donor	+2.4547089e+20	+1.3146340e-01
Donor	+2.8840315e+20	+1.3684371e-01
Donor	+3.3884416e+20	+1.4244647e-01
Donor	+3.9810717e+20	+1.4827781e-01
Donor	+4.6773514e+20	+1.5434434e-01
Donor	+5.4954087e+20	+1.6065310e-01
Donor	+6.4565423e+20	+1.6721147e-01
Donor	+7.5857758e+20	+1.7402714e-01
Donor	+8.9125094e+20	+1.8110807e-01
Donor	+1.0471285e+21	+1.8846250e-01
Donor	+1.2302688e+21	+1.9609897e-01
Donor	+1.4454398e+21	+2.0402636e-01
Donor	+1.6982437e+21	+2.1225397e-01
Donor	+1.9952623e+21	+2.2079164e-01
Donor	+2.3442288e+21	+2.2964992e-01
Donor	+2.7542287e+21	+2.3884018e-01
Donor	+3.2359366e+21	+2.4837493e-01
Donor	+3.8018940e+21	+2.5826799e-01
Donor	+4.4668359e+21	+2.6853482e-01
Donor	+5.2480746e+21	+2.7919283e-01

```
Donor     +6.1659500e+21  +2.9026166e-01
Donor     +7.2443596e+21  +3.0176349e-01
Donor     +8.5113804e+21  +3.1372335e-01
Donor     +1.0000000e+22  +3.2616938e-01
}



##from Aletermatt models for numerical device simulations of crystall....
Auger {
 * R_Auger = ( C_n n + C_p p ) ( n p - ni_eff^2)
 * with C_n,p = (A + B (T/T0) + C (T/T0)^2) (1 + H exp(-{n,p}/N0))
A = 2.8e-31 ,7.91e-32 # [cm^6/s]
B = 0,-1.239e-32 # [cm^6/s]
C = 0 ,3.231e-32 # [cm^6/s]
H = 8 ,8 # [1]
N0 = 2.5e+17 ,2.5e+17 # [cm^(-3)]
}

}



MaterialInterface = "Silicon/Si3N4" {
  SurfaceRecombination {
  S0 =1000,1000 * [cm/s]
  Sref = .001 * [1]

  }
}
```

The following tool is for the inspect tool, this code is used to extract the solar cell Jsc, Voc, FF and Eff.

```
#setdep @node|sdevice@
proj_load /nethome/jrenshaw3/Solar_Cell/n@node|sdevice@_des.plt data
#--- Load J(V)----------------------------------------------------------
cv_createDS J {data pContact OuterVoltage} {data nContact TotalCurrent} y
cv_create V {data pContact OuterVoltage} {data pContact OuterVoltage} y
#--- Calculate P(V)-----------------------------------------------------
cv_createWithFormula P "<V>*<J>" A A
cv_display P y
#--- Calculate Pmax(V),Jsc,Voc,FF and Eff-------------------------------
set MaxPP [cv_compute "vecmax(<P>)/1000" A A A A ]
set Jsc [cv_compute "vecvaly(<J>,0)" A A A A ]
set Voc [expr [cv_compute "veczero(<J>)" A A A A]]
set FF [expr $MaxPP*100000/($Jsc*$Voc)]
set Eff [expr $FF*$Jsc*$Voc/100 ]
puts [format "%s %s %.4f %s" Voc = $Voc V]
puts [format "%s %s %.1f %s" Jsc = $Jsc mA/cm^2]
puts [format "%s %s %.1f %s" FF = $FF %]
puts [format "%s %s %.1f %s" Eff = $Eff %]
puts "Saving J(V) and P(V)"
cv_write plt n@node|sdevice@_iv.plt "J P"
puts "finished"
ft_scalar JSC [format %.2f $Jsc]
ft_scalar VOC [format %.4f $Voc]
ft_scalar FF [format %.2f $FF]
ft_scalar EFF [format %.2f $Eff]
```

APPENDIX B

DEVELOPMENT OF LOW-COST PLATED CONTACT SOLAR CELLS USING A SCREEN PRINTED DIELECTRIC ETCHING PASTE

B.1 Introduction

The aim of this work is to develop a low cost high efficiency solar cell fabrication process that utilizes plated Ni/Ag front side metallization without the aid of photolithography. Plated contacts have several advantages over screen printed contacts. Screen printed contacts can exhibit high contact resistance because the current must flow through Ag crystallites formed during firing then tunnel through an insulating glass layer to reach the metal finger bulk [139].With plated contacts the current transfer is through a Ni silicide layer directly to the metal finger bulk. Even though Ni silicide forms a Schottky contact with n-type silicon with a barrier height of 0.66 eV [140], it is still suitable for a low resistance contact as long as the emitter doping is above $10^19/cm^3$ [141] so that the barrier is thin enough for electrons to easily tunnel through. Another advantage of plated contacts is that the finger bulk has a lower resistivity than screen printed contacts because it is a more pure Ag deposit, thus less Ag is required. Because of these advantages, several high efficiency devices have been fabricated using plated contacts. For example, UNSWs PERL cell achieved a world record efficiency for a crystalline silicon solar cell of 24.7% using an evaporated seed layer and plating [142], [102]. E.J. Lee *et al.* Have demonstrated PERC cell efficiencies of 20.2 % using plated Ni/Cu front contacts [143]. Plated Ni/Cu contacts have also been used to acheive 18.1% on large area multicrystalline substrates using a single sided buried contact design [144]. Our fabrication process utilizes a screen printed dielectric etching paste (Merck SolarEtch) that is used to selectively remove the Silicon Nitride antireflection coating for the fingers and busbars instead of photolithography. This dielectric layer patterning method involves fewer steps than photolithography and utilizes tools that can be found in industry

today.All of the metallization steps are self-aligned. Using this process we have achieved efficiencies greater than 18 % and fill factors in excess of 0.79 on a 1.3 Ω-cm p type substrate on an emitter with low surface concentration.

B.2 Experiment

For this work 1.3 Ω-cm, p type float zone wafers were employed. The waferswere textured in a heated potassium hydroxide and isopropyl alcohol solution to produce random pyramids on the surface to reduce the surface reflectance. After texturing the waferswere cleaned by an RCA process.The waferswere diffused in a tube furnace, using phosphorus oxychloride ($POCl_3$) as the phosphorus source. Because Ni is a fast diffuser in silicon [145], the doping profile is critical to cell performance. If the emitter is too shallow the cell will be shunted by Ni, but if the emitter has a high doping concentration then the open circuit voltage and short circuit current of the cell will be poor because of Auger recombination. The emitter designed for plated contact solar cells (PCSC) has a low surface concentration and a deep junction. Figure B.1 demonstrates the difference in a standard 45 Ω/□ profile spreading resistance profile and the PCSC emitter profile.

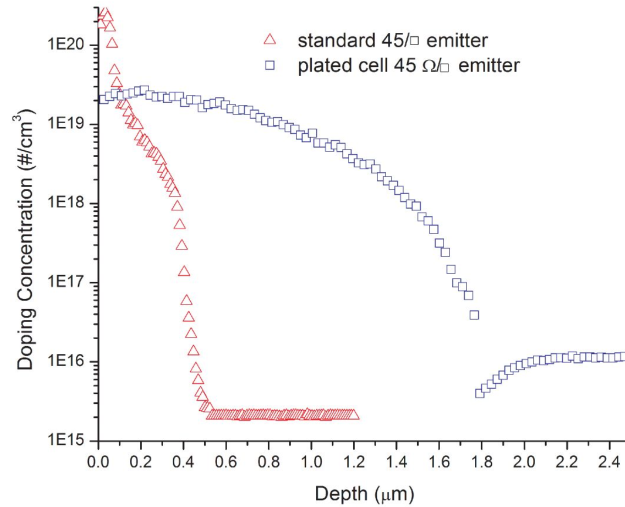

Figure B.1: Plated cell emitter profile vs standard type emitter.

To examine the potential electrical characteristics of such a doping profile, photoconductance of high resistivityn type wafers with the same diffusion shown above was measured

using QSSPCD (figure B.2). The results show that the emitter engineered for this cell has a low emitter saturation current, J_{0e}, of 40 femptoamps/cm^2 at an injection level of 1 x 10^15 carriers/cm^3 . For a short circuit current of 38 mA/cm^2 at 300 K, the upper bound for the open circuit voltage is found to be 717 mV using the relation below and assuming that the short circuit current is the same as the light generated current and that j_{0b} is negligible [6].

$$V_{oc} = \frac{kT}{q} ln(\frac{J_{sc}}{J_0} - 1) \tag{B.1}$$

Following P diffusion, 750 Åof PECVD SiNx was deposited on the wafer as an antireflection

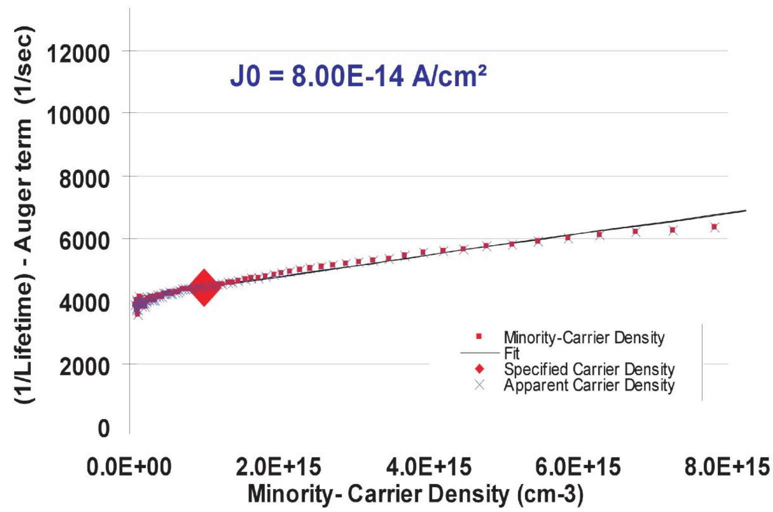

Figure B.2: Quasi-steady-state photoconductance decay curve and J_{0e} fit .

(AR) coating and front passivation later after diffusion. Following AR coating, windows for the front contacts were etched out of the nitride layer using Merck SolarEtch BES in a simple three step process.First, the etching paste is screen printed. Next, the wafer is immediately placed on a hot plate at 340 ^oC for ninety seconds. Finally, the etching paste residue is removed in a 0.1% KOH solution at 40 ^oC in an ultrasonic bath for 90 seconds. A commercial aluminum paste was screen printed on the wafer and fired in a belt furnace for form a back surface field and rear contact simultaneously. Front side cell metallization was realized through electroless Ni plating and light induced Ag plating. The plated Ni layer was annealed at 400° C in a tube furnace to form a silicide layer before Ag plating. The final step in the fabrication procedure was to isolate the 4 cm^2 cells on the wafer with

a dicing saw. To compare how plated contacts and screen printed contacts perform on this type of emitter, screen print contacted solar cells were made on wafers that were processed the same way up to Si_3N_4 deposition. A flow chart of the fabrication procedure is shown in figure B.3.

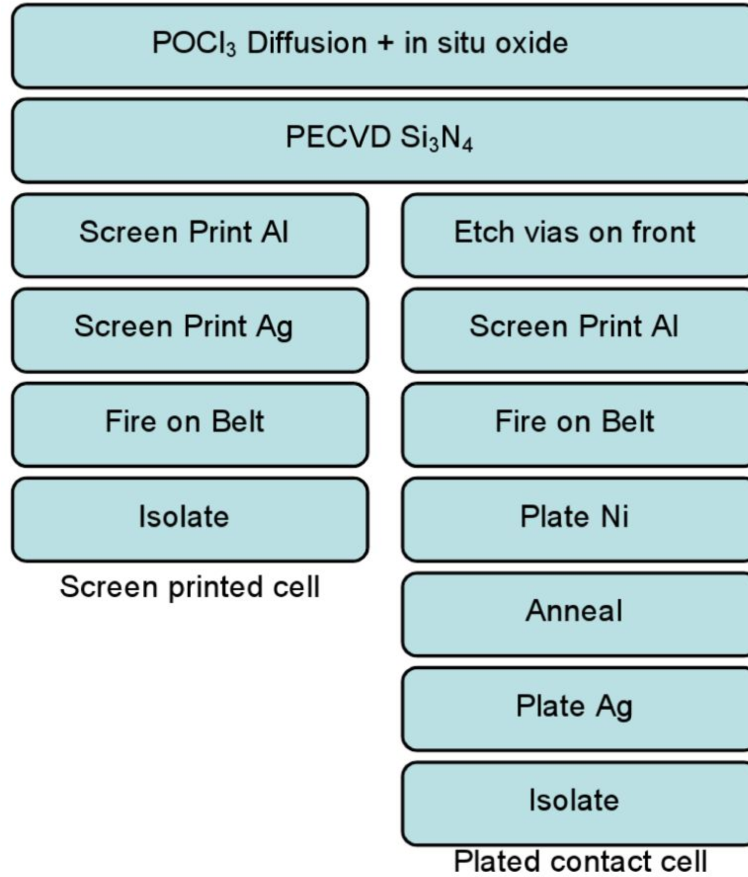

Figure B.3: Cell fabrication process for plated and screen printed cells in this work.

B.3 Solar Cell Performance

B.3.1 Cell Data

The cell results measured at Georgia Tech for our 4 cm^2 cells are shown in table B.1. Efficiencies of 18.4 and 17.9 % have been achieved using plated contacts and screen printed contacts respectively.The low resistivity Ni silicide contact and the low finger resistance due to the pure metal front side contacts give the best plated cell on the wafer a low series resistance of 0.4 Ω-cm^2. The series resistance was consistently low across all the cells on

the wafer, showing that this technology could be scalable. The screen printed cells did not perform as well as the plated cells because their series resistance is twice as high on average. The higher series resistance is the cause of the lower fill factors seen in the screen printed cells.

Table B.1: IV parameters of identically processed cells with screen printed vs plated metallization

	V_{oc}(mV)	J_{sc}(mA/cm^2)	F.F. (%)	Efficiency (%)	n-factor	R_s(Ω-cm^2)	R_{sh}(Ω-cm^2)
			Plated Wafer				
Best	633	36.5	79.8	18.4	1.1	0.4	2556
Average	629	35.8	78.5	17.6	1.2	0.6	84058
			Screen Printed Wafer				
Best	640	36.5	76.9	17.9	1.2	0.9	82980
Average	634	36.2	75.5	17.3	1.1	1.2	345848

The reflectance and spectral response were measured on the best plated and screen printed cells to determine their internal quantum efficiency(IQE). The reflectance and IQE curves are shown in figure B.4. The plated cells lower reflectance is because the silicon nitride was brought closer to the optimal thickness when it was treated in hydrofluoric acid to prepare the surface for Ni plating.

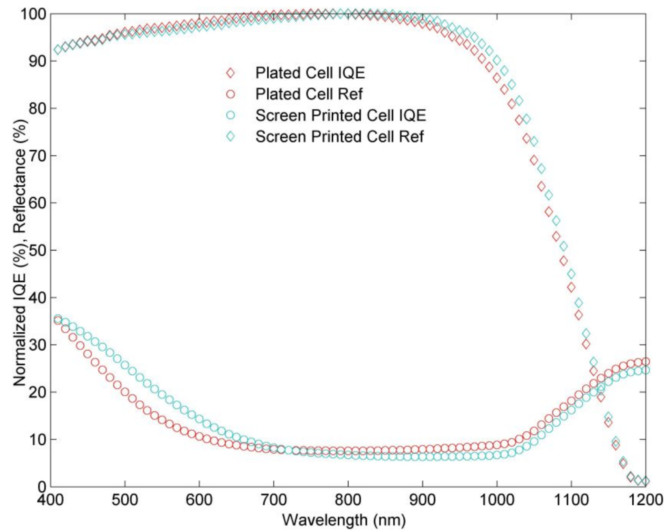

Figure B.4: Reflectance and normalized internal quantum efficiency of the highest efficiency screen printed solar cells compared with plated contact solar cells.

B.3.2 Contact

The contact resistance was measured using the TLM method. This method allows the contact resistance (R_c) and emitter sheet resistance ($R_s h$) to be determined simultaneously. The transmission line consists of a set of metal contacts in a line, each contact pad has the same width and the pads are set apart at increasing length intervals.The resistance between each contact pad is measured (R_T) and then R_c and $R_s h$ can be extrapolated the following relation [146].

$$R_T = R_{sh} * d/w + 2R_c \quad \text{(B.2)}$$

Where d is the spacing between the pads and w is the width of the contact pads. The measured contact e stance from the TLM pattern of a plated cell and a screen printed cell are shown in figure B.5. The measured specific contact resistivity, ρc, for the plated and

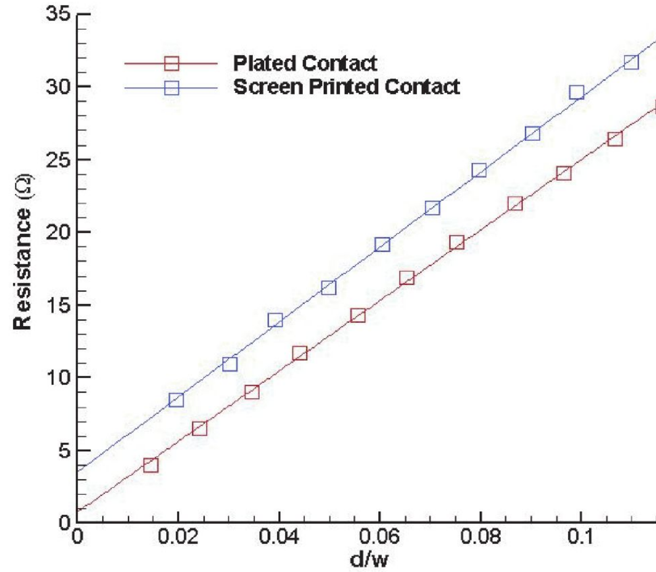

Figure B.5: Comparison of contact resistance measurements made from TLM pads made on screen printed vs plated contacts.

screen printed TLM pads are 120 and 2300 $\mu\Omega$-cm^2 respectively.A contact resistivity of below 1000 $\mu\Omega$-cm^2 is required for sufficiently low power loss at one sun applications [147]. Our results show that plated contacts are more suitable for lightly doped emitters than screen printed contacts.

Figure B.6 show scanning electron microscope images taken from a finished plated contact solar cell ,PCSC, that has been cleaved so that a cross section bay be examined.

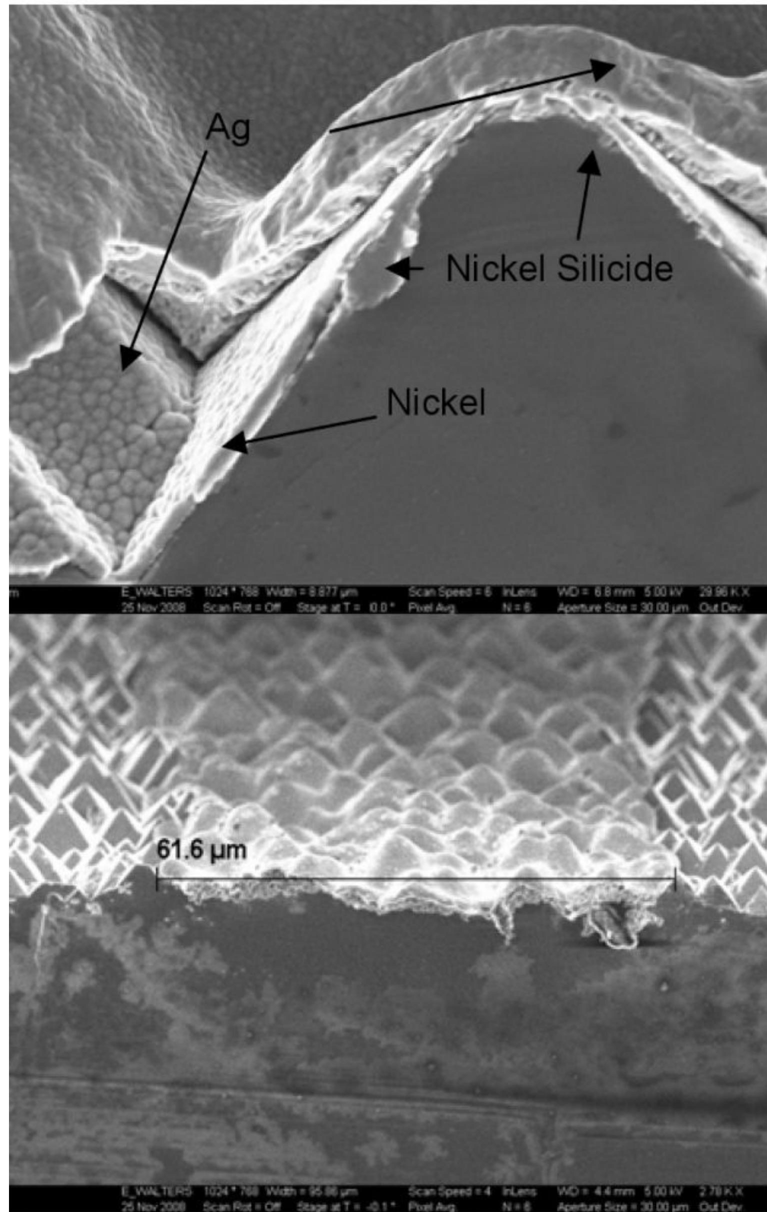

Figure B.6: SEM images of fingers on a finished plated cell

Figure B.6 5 confirms the existence of a non-uniform silicide layer between the plated metal layers and the emitter. The non-uniformity of the silicide layer could be due to the short anneal time that is used to avoid shunting the junction. Despite the non-homogeneous nature of the silicide, low resistance contacts have been formed as shown in figure 5. This

could be due to very good contact at the local silicide points or it could be due in part to current traveling through silicon directly into Ni. We have shown in previous work that it is possible to contact silicon with plated Ni/Ag contacts with no Ni anneal [147], however the adhesion was poor and the contacts were not stable over long periods of time without the anneal. Figure 5 demonstrates that finger widths as low as 60 microns can be achieved using this fabrication method and that silicon nitride is a suitable mask for electroless Ni plating. Secondary ion mass spectroscopy 10 minute tube anneal at 400 ^{o} C is roughly 0.3 μm which is far less than the junction depth of about 1.8 μm.

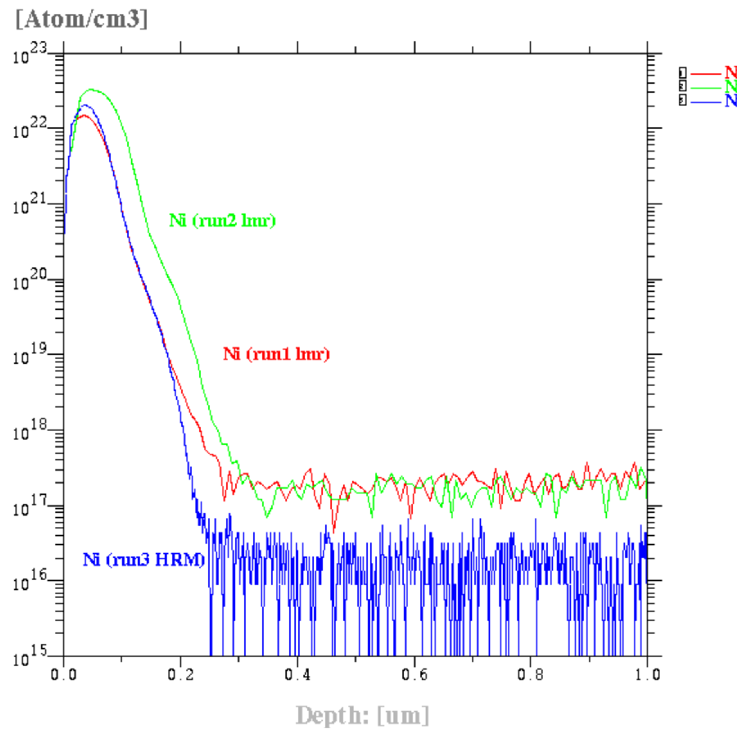

Figure B.7: SIMS profile for Ni on a Si wafer that has been through a tube anneal.

B.4 Conclusion

We have demonstrated high solar cell efficiencies using a screen printed dielectric etching paste to form vias in silicon nitride so that it maybe used as a mask for electroless Ni and light induced Ag plating. With better surface passivation to obtain higher open circuit voltages efficiencies in excess of 19% are possible. Our metallization process allows for good ohmic contact (ρ_c of 120 $\mu\Omega$-cm^2) to emitters with low surface doping concentration

compared with screen printed contacts. Future work will be focused on fabricating solar cells with better surface passivation and higher open circuit voltage to push the efficiency beyond 19%.

REFERENCES

[1] "U.S. Energy Information Administration,AEO2012 Early Release Overview,January 23, 2012,", http://www.eia.gov/forecasts/aeo/er/early_fuel.cfm.

[2] "U.S. Energy Information Administration, Renewable Energy Consumption and Electrictiy Preliminary Statistics, June 28, 2011,", http://www.eia.gov/renewable/annual/preliminary/.

[3] "Average price of photovoltaic cells and modules, 2001-2010,", http://www.eia.gov/renewable/annual/solar_photo/.

[4] "U.S. Energy Information Administration, Today in Energy, November 9, 2011,", http://www.eia.gov/todayinenergy/detail.cfm?id=3850.

[5] J. Nelson, *The physics of solar cells*volume 57 (Imperial College Press London, 2003).

[6] M. A. Green, *Solar cells: Operating principles, technology, and system applications* (Englewood Cliffs, NJ, Prentice-Hall, Inc., 1982.˜288 p., 1982).

[7] "Standard Solar Spectra,", http://pveducation.org/pvcdrom/appendicies/standard-solar-spectra.

[8] "Reference Solar Spectral Irradiance: Air Mass 1.5,", http://rredc.nrel.gov/solar/spectra/am1.5/.

[9] "Global Horizontal Radiation,", http://eosweb.larc.nasa.gov/cgi-bin/sse/global.cgi?

[10] "International Energy Statistics,", http://www.eia.gov/cfapps/ipdbproject/iedindex3.cfm?tid=2&pid=2&aid=2&cid=regions,&syid=2006&eyid=2010&unit=BKWH.

[11] "U.S. Energy Information Association, International Energy Statistics,", http://www.eia.gov/cfapps/ipdbproject/IEDIndex3.cfm?tid=2&pid=2&aid=2.

[12] K. R. Mcintosh, *Lumps, Humps and Bumps: Three Detrimental E ects in the CurrentVoltage Curve of Silicon Solar Cells*, PhD thesis UNSW 2001.

[13] A. Luque and S. Hegedus, *Handbook of Photovoltaic Science and Engineering* (Wiley, 2010).

[14] R. Eisberg and R. Resnick, *Quantum physics of atoms, molecules, solids, nuclei, and particles* (Wiley, 1985).

[15] A. Schenk, "Finite-temperature full random-phase approximation model of band gap narrowing for silicon device simulation," *Journal of Applied Physics* **84**, 3684 (1998).

[16] D. Roulston, N. Arora, S. Chamberlain, and S. Diodes, "Modeling and measurement of minority-carrier lifetime versus doping in diffused layers of n+-p silicon diodes," *IEEE transactions on electron devices* , 284 (1982).

[17] Synopsys, "Sentaurus,".

[18] D. Klaassen, "A unified mobility model for device simulationI. Model equations and concentration dependence," *Solid-State Electronics* **35** (1992).

[19] C. W. Gwyn, D. L. Scharfetter, and J. L. Wirth, "The analysis of radiation effects in semiconductor junction devices," *IEEE TRANSACTIONS ON NUCLEAR SCIENCE* , 153 (1967).

[20] J. Fossum, "Computer-aided numerical analysis of silicon solar cells," *Solid-State Electronics* **19**, 269 (1976).

[21] J. Gray, R. Schwartz, and R. Nasby, "Two dimensional effects in conventional solar cells operated at high intensities," in *IEEE Electron Devices Meeting* pp. 510–513 1982.

[22] D. Rover, P. Basore, and G. Thorson, "Solar Cell Modeling on Personal Computers," in *Conference Record of the 18th IEEE Photovoltaic Specialists Conference* pp. 703–709 IEEE 1985.

[23] K. Rapolu, P. Singh, and S. P. S. Shea, "TWO DIMENSIONAL NUMERICAL MODELING OF A SILICO N SOLAR CELL WITH SELECTIVE EMITTER CONFIGURATION," in *Photovoltaic Specialists Conference (PVSC), 2010 35th IEEE* pp. 2227–2232 Honolulu 2010 IEEE.

[24] R. Brendel, "Modeling solar cells with the dopant-diffused layers treated as conductive boundaries," *Progress in Photovoltaics: Research and Applications* , 31 (2012).

[25] P. P. Altermatt, S. Steingrube, Y. Yang, C. Sprodowski, T. Dezhdar, S. Koc, B. Veith, S. Herrman, R. Bock, K. Bothe, J. Schmidt, and R. Brendel, "HIGLY PREDICTIVE MODELLING OF ENTIRE SI SOLAR CELLS FOR INDUSTRIAL APPLICATIONS," in *24th European Photovoltaic Solar Energy Conference* No. September pp. 901–905 Hamburg 2009.

[26] P. P. Altermatt, G. Heiser, A. G. A. Aberle, A. Wang, J. Zhao, S. J. Robinson, S. Bowden, and M. A. Green, "Spatially resolved analysis and minimization of resistive losses in highefficiency Si solar cells," *Progress in Photovoltaics: Research and Applications* **4**, 399 (1996).

[27] F. Kiefer and C. Ulzhoÿfer, "High Efficiency N-Type Emitter-Wrap-Through Silicon Solar Cells," *IEEE journal of Photovoltaics* **1**, 49 (2011).

[28] O. Nichiporuk, a. Kaminski, M. Lemiti, a. Fave, and V. Skryshevsky, "Optimisation of interdigitated back contacts solar cells by two-dimensional numerical simulation," *Solar Energy Materials and Solar Cells* **86**, 517 (2005).

[29] A. Kanevce and W. K. Metzger, "The role of amorphous silicon and tunneling in heterojunction with intrinsic thin layer (HIT) solar cells," *Journal of Applied Physics* **105**, 094507 (2009).

[30] R. Bank, D. Rose, and W. Fichtner, "Numerical methods for semiconductor device simulation," *IEEE transactions on electron devices* , 1031 (1983).

[31] G. R. Liu and S. S. Quek, *The finite element method [electronic resource] : a practical course / G.R. Liu, S.S. Quek.* (Oxford ; Boston : Butterworth-Heinemann, 2003., 2003).

[32] M. N. O. Sadiku, *Numerical Techniques in Electromagnetics, Second Edition*, 2 ed. (CRC Press, 2000).

[33] J. O. Schumacher, *Numerical simulation of silicon solar cells with novel cell structures*, PhD thesis University of Konstanz 2000.

[34] P. P. Altermatt, "Models for numerical device simulations of crystalline silicon solar cellsa review," *Journal of Computational Electronics* **10**, 314 (2011).

[35] P. P. Altermatt, J. O. J. O. Schumacher, A. Cuevas, M. J. Kerr, S. W. Glunz, R. R. King, G. Heiser, and A. Schenk, "Numerical modeling of highly doped Si:P emitters based on FermiDirac statistics and self-consistent material parameters," *Journal of Applied Physics* **92**, 3187 (2002).

[36] J. O. Schumacher, P. P. Altermatt, G. Heiser, and A. G. Aberle, "Application of an improved band-gap narrowing model to the numerical simulation of recombination properties of phosphorus-doped silicon emitters," *Solar Energy Materials and Solar Cells* **65**, 95 (2001).

[37] J. Slotboom and H. D. Graaff, "Measurements of bandgap narrowing in Si bipolar transistors," *Solid-State Electronics* **19**, 857 (1976).

[38] J. D. Alamo, S. Swirhun, and R. Swanson, "Simultaneous measurement of hole lifetime, hole mobility and bandgap narrowing in heavily doped n-type silicon," in *Electron Devices Meeting, 1985 International* pp. 290–293 1985.

[39] J. Schmidt and K. Bothe, "Structure and transformation of the metastable boron- and oxygen-related defect center in crystalline silicon," *Physical Review B* **69**, 024107 (2004).

[40] K. Bothe, R. Sinton, and J. Schmidt, "Fundamental boron-oxygen-related carrier lifetime limit in mono- and multicrystalline silicon," *Progress in Photovoltaics: Research and Applications* **13**, 287 (2005).

[41] T. Hallberg, J. L. Lindström, L. Murin, and V. Markevich, "The Oxygen Dimer in Silicon: Some Experimental Observations," *Materials Science Forum* **258-263**, 361 (1997).

[42] J. Dziewior and W. Schmid, "Auger coefficients for highly doped and highly excited silicon," *Applied Physics Letters* **31**, 346 (1977).

[43] J. Schmidt, M. Kerr, and P. P. Altermatt, "Coulomb-enhanced Auger recombination in crystalline silicon at intermediate and high injection densities," *Journal of Applied Physics* **88**, 1494 (2000).

[44] a. Richter, F. Werner, a. Cuevas, J. Schmidt, and S. Glunz, "Improved Parameterization of Auger Recombination in Silicon," *Energy Procedia* **27**, 88 (2012).

[45] P. Altermatt, H. Plagwitz, R. Bock, J. Schmidt, R. Brendel, M. J. Kerr, and A. Cuevas, "The surface recombination velocity at boron-doped emitters: comparison between various passivation techniques," *21st European Photovoltaic Solar Energy Conference* , 647 (2006).

[46] B. Hoex, J. Schmidt, R. Bock, P. P. Altermatt, M. C. M. van de Sanden, and W. M. M. Kessels, "Excellent passivation of highly doped p-type Si surfaces by the negative-charge-dielectric Al2O3," *Applied Physics Letters* **91**, 112107 (2007).

[47] Report No., , 2009 (unpublished).

[48] B. Phong, "Illumination for computer generated pictures," *Communications of the ACM* **18**, 311 (1975).

[49] S. Duttagupta, F. Ma, B. Hoex, T. Mueller, and A. G. Aberle, "Optimised Antireflection Coatings using Silicon Nitride on Textured Silicon Surfaces based on Measurements and Multidimensional Modelling," *Energy Procedia* **15**, 78 (2012).

[50] M. A. Green and M. J. Keevers, "Optical properties of intrinsic silicon at 300 K," *Progress in Photovoltaics: Research and Applications* **3**, 189 (1995).

[51] M. Kang and A. Rohatgi, "Development and use of a simple numerical model to quantify the impact of key photovoltaics system parameters on the levelized cost of electricity," in *Photovoltaic Specialists Conference (PVSC), 2012 38th IEEE* pp. 2932–2937 Austin, TX 2012 IEEE.

[52] T. C. Röder, S. J. Eisele, P. Grabitz, C. Wagner, G. Kulushich, J. R. Köhler, and J. H. Werner, "Add-on laser tailored selective emitter solar cells," *Progress in Photovoltaics: Research and Applications* **18**, 505 (2010).

[53] H. Antoniadis, F. Jiang, W. Shan, and Y. Liu, "All screen printed mass produced silicon ink selective emitter solar cells," *Photovoltaic Specialists Conference (PVSC), 2010 35th IEEE* , 1193 (2010).

[54] I. Cooper, K. Tate, A. Carroll, K. Mikeska, R. Reedy, and A. Rohatgi, "Low resistance screen-printed Ag contacts to POCl3 emitters with low saturation current density for high efficiency Si solar cells," in *Photovoltaic Specialists Conference, 2012. 38th IEEE* Austin, TX 2012.

[55] M. Zanuccoli, P. F. P. Bresciani, M. Frei, H.-W. Guo, H. Fang, M. Agrawal, C. Fiegna, and E. Sangiorgi, "2-D Numerical Simulation and Modeling of Monocrystalline Selective Emitter Solar Cells," in *Photovoltaic Specialists Conference (PVSC), 2012 38th IEEE* No. 1 pp. 2262–2265 Honolulu 2010 IEEE.

[56] R. DeRose, M. Zanuccoli, P. Magnone, D. Tonini, M. Galiazzo, G. Cellere, M. Frei, H.-W. Guo, C. Fiegna, and E. Sangiorgi, "2-D NUMERICAL ANALYSIS OF THE IMPACT OF THE HIGHLY-DOPED PROFILE ON SELECTIVE EMITTER SOLAR CELL PERFORMANCE," in *Photovoltaic Specialists Conference (PVSC), 2010 35th IEEE* No. 1 pp. 2556–2559 Honolulu 2011 IEEE.

[57] J. Greulich, U. Jager, S. Rein, R. Preu, and J. Ulrich, "A Review and Comparison of One- and Two-Dimensional Simulations of Solar Cells Featuring Selective Emitters," *IEEE journal of Photovoltaics* **2**, 1 (2012).

[58] W. Schottky, "Semiconductor Theory of the Blocking Layer (German)," *Naturwissenschaften* **26**, 843 (1938).

[59] K. Varahramyan and E. Verret, "A model for specific contact resistance applicable for titanium silicide-silicon contacts," *Solid-State Electronics* **39**, 1601 (1996).

[60] C. Ballif, D. M. Huljic, G. Willeke, and a. Hessler-Wyser, "Silver thick-film contacts on highly doped n-type silicon emitters: Structural and electronic properties of the interface," *Applied Physics Letters* **82**, 1878 (2003).

[61] E. Cabrera, S. Olibet, J. Glatz-Reichenbach, R. Kopecek, D. Reinke, and G. Schubert, "Current transport in thick film Ag metallization: Direct contacts at Silicon pyramid tips?," *Energy Procedia* **8**, 540 (2011).

[62] M. Hilali, M. Al-jassim, M. M, B. To, H. Moutinho, A. Rohatgi, and S. Asher, "Understanding the Formation and Temperature Dependence of Thick-Film Ag Contacts on High-Sheet-Resistance Si Emitters for Solar Cells," *Journal of The Electrochemical Society* **152**, 742 (2005).

[63] M. Horteis, D. Grote, S. Binder, a. Filipovic, D. Schmidt, and S. W. Glunz, "Fine line printed and plated contacts on high ohmic emitters enabling 20% cell efficiency," *2009 34th IEEE Photovoltaic Specialists Conference (PVSC)* , 000060 (2009).

[64] G. Schubert, *Thick Film Metallisation of Crystalline Silicon Solar Cells*, PhD thesis University of Konstanz 2006.

[65] J. Fairfield and G. Schwuttke, "Silicon diodes made by laser irradiation," *Solid State Electronics* **11**, 1175 (1968).

[66] R. T. Young and R. F. Wood, "Laser processing of semiconductor materials," *Annual Review of Materials Science* **12**, 323 (1982).

[67] E. I. Shtyrkov, I. B. Khaibullin, M. M. Zaripov, M. F. Galyatudinov, and R. M. Bayazitov, "Local laser annealing of implantation doped semiconductor layers," *Soviet Physics-Semiconductors* **9**, 1309 (1975).

[68] G. A. Kachurin, E. V. Nidaev, A. V. Khodyachikh, and L. A. Kovaleva, "ANNEALING OF IMPLANTED LAYERS BY A SCANNING LASER BEAM.," *Sov. Phys. Semicond* **10**, 1128 (1976).

[69] A. G. Klimenko, E. A. Klimenko, and V. I. Donin, "Restoration by an argon laser beam of the single-crystal structure of a silicon surface amorphized by ion implantation," *Soviet Journal of Quantum Electronics* **2**, 2356 (1975).

[70] M. Thompson, J. Mayer, and A. Cullis, "Silicon melt, regrowth, and amorphization velocities during pulsed laser irradiation," *Physical Review Letters* **50**, 896 (1983).

[71] R. Hull, *Properties of crystalline silicon* (INSPEC, 1999).

[72] F. Trumbore, "Solid Solubilities of Impurity Elements in Germanium and Silicon," *Bell System Technical Journal* **39**, 205 (1960).

[73] T. F. Deutsch, D. Ehrlich, D. Rathman, D. Silvesmith, and R. Osgood, "Electrical properties of laser chemically doped silicon," *Applied Physics Letters* **39**, 825 (1981).

[74] A. Slaoui, F. Foulon, and P. Siffert, "Excimer laser induced doping of phosphorus into silicon," *Journal of Applied Physics* **67**, 6197 (1990).

[75] S. D. Unamuno and E. Fogarassy, "A thermal description of the melting of c-and a-silicon under pulsed excimer lasers," *Applied Surface Science* **36**, 1 (1989).

[76] T. Sameshima and S. Usui, "The Dopamt Diffusion Mechanism in Eicimer Laser Induced Molten Silicon," in *MRS Proceedings* volume 101 pp. 491–494 1987.

[77] X. Zhang, J. Ho, and C. Grigoropoulos, "Ultra-shallow p+-junction formation in silicon by excimer laser doping: a heat and mass transfer perspective," *International journal of heat and mass transfer* **39**, 3835 (1996).

[78] U. Besi-vetrella, E. Salza, L. Pirozzi, S. Noel, A. Slaoui, and J. C. Muller, "Selective doping of silicon by rapid thermal and laser assisted processes," *Materials Science in Semiconductor Processing* **1**, 325 (1999).

[79] M. Birnbaum, "Semiconductor Surface Damage Produced by Ruby Lasers," *Journal of Applied Physics* **36**, 3688 (1965).

[80] Y. Matsuoka, "Laser-induced damage in semiconductors," *Journal of Physics: D* **9**, 215 (1978).

[81] P. M. Mooney, R. T. Young, J. Karins, Y. H. Lee, and J. W. Corbett, "Defects in Laser Damaged Silicon Observed by DLTS," *physica status solidi (a)* **31**, 22 (1978).

[82] A. Barhdadi, B. Hartiti, and J.-c. C. Muller, "Active Defects Generated in Silicon by Laser Doping Process," *The African Review of Physics* **6**, 229 (2011).

[83] T. F. Deutsch, "Efficient Si solar cells by laser photochemical doping," *Applied Physics Letters* **38**, 144 (1981).

[84] S. Wenham, *Laser grooved silicon solar cells*, PhD thesis UNSW 1986.

[85] S. Braun, A. Zuschlag, B. Raabe, and G. Hahn, "The Origin of Background Plating," *Energy Procedia* **8**, 565 (2011).

[86] M. Green, C. Chong, F. Zhang, A. Sproul, J. Zolper, and S. R. Wenham, "20% efficient laser grooved, buried contact silicon solar cells," in *Photovoltaic Specialists Conference (PVSC), 1988 20th IEEE* pp. 411–414 1988.

[87] a.U. Ebong, S. Lee, C. Honsberg, and S. Wenham, "Optimization of boron groove diffusion for double sided buried contact silicon solar cells," *Conference Record of the Twenty Fifth IEEE Photovoltaic Specialists Conference - 1996* , 513 (1996).

[88] J. Guo, B. Tjahjono, and J. Cotter, "19.2% efficiency n-type laser-grooved silicon solar cells," in *Photovoltaic Specialists Conference (PVSC), 31st IEEE* pp. 983–986 2005.

[89] B. Tjahjono, M. Yang, C. Lan, and J. Ting, "18.9% efficient laser doped selective emitter solar cell on industrial grade p-type Czochralski wafer," in *25th European Photovoltaic Solar Energy Conference and Exhibition* No. September pp. 1396–1400 2010.

[90] Z. Shi, S. Wenham, and J. Ji, "Mass production of the innovative PLUTO solar cell technology," in *2009 34th IEEE Photovoltaic Specialists Conference (PVSC)* pp. 001922–001926 Ieee 2009.

[91] D. Kray, M. Aleman, A. Fell, S. Hopman, K. Mayer, M. Mesec, R. Muller, G. Willeke, S. W. Glunz, B. Bitnar, D.-H. Neuhaus, R. Ludeman, T. Schlenker, D. Manz, A. Bentzen, E. Sauar, A. Pauchard, and B. Richerzhagen, "Laser-doped Silicon Solar Cells by Laser Chemical Processing (LCP) exceeding 20% Efficiency," in *Photovoltaic Specialists Conference (PVSC), 33th IEEE* 2008.

[92] M. Sierra Trillo, M. Glatthaar, S. Hopman, and I. Krossing, "Impact of the solvent properties on the morphology of the silicon surface generated by laser ablation under a solvent film," in *27th European Photovoltaic Solar Energy Conference* pp. 1978–1981 2012.

[93] E. Hoffmann, T. Roder, and J. Kohler, "Self-doping laser transferred contacts for c-Si solar cells," *Photovoltaic Specialists Conference (PVSC), 2012 38th IEEE* , 1059 (2012).

[94] R. Ferré, R. Gogolin, J. Müller, N.-P. Harder, and R. Brendel, "Laser transfer doping for contacting n-type crystalline Si solar cells," *Physica Status Solidi (a)* **208**, 1964 (2011).

[95] L. L. Q. L. Zhu, J. Gong, J. Huang, P. She, M. L. M. Zeng, L. Li, M. Z. Dai, and Q. Wan, "Improving the efficiency of crystalline silicon solar cells by an intersected selective laser doping," *Solar Energy Materials and Solar Cells* **95**, 3347 (2011).

[96] U. JÃger, B. Thaidigsmann, M. Okanovic, R. Preu, U. Jäger, and U. JÃger, "Quantum Efficiency Analysis of Highly Doped Areas for Selective Emitter Solar Cells," *Energy Procedia* **8**, 193 (2011).

[97] K. Tu, "Selective growth of metal rich silicide of near noble metals," *Applied Physics Letters* **27**, 221 (1975).

[98] Coherent, *AVIA 355-10 Specification Sheet* (Coherent, 2007).

[99] B. Hallam, S. Wenham, A. Sugianto, L. Mai, C. Chong, M. Edwards, D. Jordan, and P. Fath, "Record Large-Area p-Type CZ Production Cell Efficiency of 19 . 3 % Based on LDSE Technology," **1**, 43 (2011).

[100] S. Proctor, L. Linholm, and J. Mazer, "Direct Measurements of Interfacial Contact Resistance, End Contact Resistance, and Interfacial Contact Layer Uniformity," *IEEE transactions on electron devices* **30**, 1535 (1983).

[101] R. Sinton, A. Cuevas, and M. Stuckings, "Quasi-steady-state photoconductance, a new method for solar cell material and device characterization," in *Photovoltaic Specialists Conference (PVSC), 1996 25th IEEE* 1996.

[102] J. Zhao, A. Wang, P. Altermatt, S. R. Wenham, and M. Green, "24% efficient PERL silicon solar cell: recent improvements in high efficiency silicon cell research," *Solar energy materials ...* **42**, 87 (1996).

[103] A. Esturo-breton, F. Binaie, M. Breselge, T. Frieß, M. Geiger, E. Holbig, S. Keller, T. Kühn, J. Maier, A. Münzer, R. Schlosser, A. Schmid, C. Voyer, P. Winter, K. Bayer, J. Krümberg, S. Henze, I. Melnyk, M. Schmidt, S. Klingbeil, F. Walter, R. Kopecek, K. Peter, and P. Fath, "CRYSTALLINE SI SOLAR CELLS WITH SELECTIVE EMITTER FOR INDUSTRIAL MASS PRODUCTION," in *24th European Photovoltaic Solar Energy Conference* No. September pp. 1068–1071 2009.

[104] M. Nejati, W. Zhang, and L. Huang, "Etching paste for innovative solar cell applications," in *Photovoltaic Specialists Conference (PVSC), 2012 38th IEEE* 2012.

[105] R. Low, A. Gupta, N. Bateman, D. Ramappa, P. Sullivan, W. Skinner, J. Mullin, S. Peters, and H. Weiss-Wallrath, "High efficiency selective emitter enabled through patterned ion implantation," *2010 35th IEEE Photovoltaic Specialists Conference* , 001440 (2010).

[106] M. Kerr, J. Schmidt, A. Cuevas, and J. Bultman, "recombination velocity of phosphorus-diffused silicon solar cell emitters passivated with plasma enhanced chemical vapor deposited silicon nitride and thermal silicon," *Journal of Applied Physics* **89**, 3821 (2001).

[107] H. Haverkamp, A. Dastgheib-Shirazi, B. Raabe, F. Book, G. Hahn, and A. Shirazi, "Minimizing the electrical losses on the front side: development of a selective emitter process from a single diffusion," in *Photovoltaic Specialists Conference (PVSC), 2008 33th IEEE* No. September pp. 1–4 IEEE 2008.

[108] R. Utama, A. Lennon, M. Lenio, N. Borojevic, A. Karpour, A. Ho-Baillie, and S. Wenham, "Inkjet printing for high efficiency selective emitter silicon solar cell," in *23rd European Photovoltaic Solar Energy Conference* pp. 1687–1690 2008.

[109] C. E. Dubé, B. Tsefrekas, D. Buzby, R. Tavares, W. Zhang, A. Gupta, R. J. Low, W. Skinner, and J. Mullin, "High efficiency selective emitter cells using patterned ion implantation," *Energy Procedia* **8**, 706 (2011).

[110] M. a. Green, "Self-consistent optical parameters of intrinsic silicon at 300K including temperature coefficients," *Solar Energy Materials and Solar Cells* **92**, 1305 (2008).

[111] H. Kodera, "Diffusion Coefficienct of Impurites in Silicon Melt.pdf," *Japanese Journal of Applied Physics* **2**, 212 (1963).

[112] A. Y. C. Yu, "Electron tunneling and contact resistance of metal-silicon contact barriers," *Solid-State Electronics* **13**, 239 (1970).

[113] K. H. Yang, "An Etch for Delineation of Defects in Silicon," *Journal of The Electrochemical Society* **131**, 1140 (1984).

[114] R. R. King, R. Sinton, and R. Swanson, "Studies of Diffused Phosphorus Emitters : Saturation Quantum Efficiency," *IEEE transactions on electron devices* **37**, 365 (1990).

[115] M. Lammert and R. Schwartz, "The Interdigitated Back Contact Solar Cell: for Use in Concentrated Sunlight," *IEEE transactions on electron devices* **24**, 337 (1977).

[116] R. M. Swanson, "POINT-CONTACT S O L A R CELLS : MODELING AND EXPERIMENT," *Solar Cells* **7**, 85 (1986).

[117] H. Ohtsuka, Y. Ohkura, T. Uematsu, and T. Warabisako, "Three-dimensional numerical analysis of contact geometry in back-contact solar cells," *Progress in Photovoltaics: Research and Applications* **2**, 275 (1994).

[118] M. Lu, S. Bowden, U. Das, and R. Birkmire, "Interdigitated back contact silicon heterojunction solar cell and the effect of front surface passivation," *Applied Physics Letters* **91**, 063507 (2007).

[119] M. Taguchi, A. Terakawa, E. Maruyama, and M. Tanaka, "Obtaining a higher Voc in HIT cells," *Progress in Photovoltaics: Research and Applications* **13**, 481 (2005).

[120] M. Tanaka and M. Taguchi, "Development of new a-Si/c-Si heterojunction solar cells: ACJ-HIT (artificially constructed junction-heterojunction with intrinsic thin-layer)," *Japanese journal of ...* **31**, 3518 (1992).

[121] M. Lu, U. Das, S. Bowden, S. Hegedus, and R. Birkmire, "Optimization of interdigitated back contact silicon heterojunction solar cells by two-dimensional numerical simulation," *2009 34th IEEE Photovoltaic Specialists Conference (PVSC)* , 001475 (2009).

[122] J. Zhao, A. Wang, and M. Green, "High-efficiency PERL and PERT silicon solar cells on FZ and MCZ substrates," *Solar energy materials and solar cells* **65**, 429 (2001).

[123] P. J. Cousins, D. D. Smith, H.-C. Luan, J. Manning, T. D. Dennis, A. Waldhauer, K. E. Wilson, G. Harley, and W. P. Mulligan, "Generation 3: Improved performance at lower cost," in *Photovoltaic Specialists Conference (PVSC), 2010 35th IEEE* pp. 275–278 2010.

[124] J. Dicker, J. O. Schumacher, W. Warta, and S. W. Glunz, "Analysis of one-sun monocrystalline rear-contacted silicon solar cells with efficiencies of 22.1%," *Journal of Applied Physics* **91**, 4335 (2002).

[125] K. Nakamura, T. Isaka, Y. Funakoshi, Y. Tonomura, T. Machida, and K. Okamoto, "High Efficiency Back Contact Si Solar Cells Based on Industrial Technology," in *15th International Photovoltaic Science and Engineering Conference* pp. 869–872 2005.

[126] A. Rohatgi and D. Meier, "Developing low-cost, high-throughput processing techniques for 20%-efficient monocrystalline cells," *Photovoltaics International,Technical Papers* (2010).

[127] D. Kray, M. Aleman, A. Fell, S. Hopman, K. Mayer, M. Mesec, R. Muller, G. P. Willeke, S. W. Glunz, B. Bitnar, D.-H. Neuhaus, R. Ludemann, T. Schlenker, D. Manz, A. Bentzen, E. Sauar, A. Pauchard, and B. Richerzhagen, "Laser-doped silicon solar cells by Laser Chemical Processing (LCP) exceeding 20% efficiency," in *Photovoltaic Specialists Conference, 2008. PVSC '08. 33rd IEEE* pp. 1–3 2008.

[128] D. S. Kim, V. Meemongkolkiat, A. Ebong, B. Rounsaville, V. Upadhyaya, A. Das, and A. Rohatgi, "2D-Modeling and Development of Interdigitated Back Contact Solar Cells on Low-Cost Substrates," in *Photovoltaic Energy Conversion, Conference Record of the 2006 IEEE 4th World Conference on* volume 2 pp. 1417–1420 2006.

[129] W. Shockley and H. J. Queisser, "Detailed Balance Limit of Efficiency of p-n Junction Solar Cells," *Journal of Applied Physics* **32**, 510 (1961).

[130] R. Swanson, "Approaching the 29% limit efficiency of silicon solar cells," in *Photovoltaic Specialists Conference, 2005. ...* pp. 0–5 2005.

[131] T. Tiedje and E. Yablonovitch, "Limiting efficiency of silicon solar cells," *IEEE transactions on electron devices* **31**, 711 (1984).

[132] J. Werner, R. Brendel, and H. J. Queisser, "New upper efficiency limits for semiconductor solar cells," *...Energy Conversion, 1994., ...* , 1742 (1994).

[133] M. Taguchi, K. Kawamoto, S. Tsuge, T. Baba, and H. Sakata, "HIT Cells-High-Efficiency Crystalline Si Cells with Novel Structure," *Progress in Photovoltaics: Research and Applications* **8**, 503 (2000).

[134] D. Zielke, J. H. Petermann, F. Werner, B. Veith, R. Brendel, and J. Schmidt, "Contact passivation in silicon solar cells using atomic-layer-deposited aluminum oxide layers," *physica status solidi (RRL) - Rapid Research Letters* **5**, 298 (2011).

[135] H. Mäckel and K. Varner, "On the determination of the emitter saturation current density from lifetime measurements of silicon devices," *Progress in Photovoltaics: Research and Applications* (2012).

[136] R. Sinton and R. Swanson, "Design criteria for Si point-contact concentrator solar cells," *IEEE transactions on electron devices* **34**, 2116 (1987).

[137] E. L. I. Yablonovitch and G. D. Cody, "Intensity Enhancement in Textured Optical Sheets for Solar Cells," *IEEE transactions on electron devices* **29**, 300 (1982).

[138] T. Markvart, "Beyond the Yablonovitch limit: Trapping light by frequency shift," *Applied Physics Letters* **98**, 071107 (2011).

[139] G. Schubert, F. Huster, and P. Fath, "Physical understanding of printed thick-film front contacts of crystalline Si solar cellsâReview of existing models and recent developments," *Solar Energy Materials and Solar Cells* **90**, 3399 (2006).

[140] K. Maex and M. Rossum, *Properties of metal silicides* (Stevenage: INSPEC, 1995).

[141] R. Pierret, *Semiconductor Device Fundamentals* (Addison-Wesley Publishing Company, Inc, 1996).

[142] M. A. Green, K. Emery, Y. Hishikawa, and W. Warta, "Solar Cell Efficiency Tables (Version 32)," *Progress in Photovoltaics: Research and Applications* **16**, 435 (2008).

[143] E. Lee, D. Kim, and S. Lee, "Ni/Cu metallization for low-cost high-efficiency PERC cells," *Solar Energy Materials and Solar Cells* **74**, 65 (2002).

[144] M. M. Cann, B. Raabe, W. Jooss, R. Kopecek, and P. Fath, “18 . 1 % EFFICIENCY FOR A LARGE AREA , MULTI-CRYSTALLINE SILICON SOLAR CELL,” in *4th World Conference on Photovoltaic energy conversion* pp. 894–899 2006.

[145] M. Lee and P. Bennett, “Bulk versus surface transport of nickel and cobalt on silicon,” *Physical review letters* **75**, 4460 (1995).

[146] G. Reeves and H. Harrison, “Obtaining the specific contact resistance from transmission line model measurements,” *Electron Device Letters, IEEE* , 111 (1982).

[147] D. Schroder and D. Meier, “Solar cell contact resistancea review,” *IEEE transactions on electron devices* , 637 (1984).

PUBLICATIONS

[1] **J. S. Renshaw**, I. B. Cooper, and A. Rohatgi. Quantitative understanding of the benefit of selective emitters on screen printed si solar cells as a function of improved paste contact properties. *Applied Physics Letters*, 102(1):013502, 2013.

[2] **J. S. Renshaw**, A. Upadhyaya, V Upadhyaya, .I.B. Cooper, and A. Rohatgi. Optimization of ultraviolet laser doping for crystalline silicon solar cells with a novel segmented selective emitter design. *Progress in Photovoltaics*, 2012.

[3] I.B. Cooper, A. Ebong, **J. S. Renshaw**, R. Reedy, M. Al-Jassim, and A. Rohatgi. Understanding and use of ir belt furnace for rapid thermal firing of screen-printed contacts to si solar cells. *Electron Device Letters, IEEE*, 31(5):461 –463, may 2010.

[4] C.W. Chen, A. Ebong, **J. S. Renshaw**, K. Tate, F. Zimbardi, A. Rohatgi, and M. Finot. Development and understanding of high-efficiency screen-printed concentrator silicon solar cells. *IEEE Journal of Photovoltaics*, (99):1–5, 2011.

[5] **J. S. Renshaw**, A. Upadhyaya, V. Upadhyaya, and A. Rohatgi. Crystalline silicon solar cells with segmented selective emitter by ultraviolet laser doping. In *38th IEEE Photovoltaic Specialists Conference (PVSC)*, 2012.

[6] **J. S. Renshaw** and A. Rohatgi. Device optimization for screen printed interdigitated back contact solar cells. In *37th IEEE Photovoltaic Specialists Conference (PVSC)*, pages 002924–002927, 2011.

[7] A. Ebong, **J. S. Renshaw**, B. Rounsaville, I.B. Cooper, K. Tate, A. Rohatgi, S.W. Glunz, M. Hrteis, A. Mette, M. Gundermann, M. Dovrat, E. Kritchman, D. Brusilovsky, and A. Benichou. Ink jetted seed and plated grid solar cells with homogeneous high sheet resistance emitters. In *25th European Photovoltaic Solar Energy Conference and Exhibition / 5th World Conference on Photovoltaic Energy Conversion, 6-10 September 2010, Valencia, Spain*, pages 2390–2394, 2010.

[8] A. Ebong, **J. S. Renshaw**, I. Cooper, B. Rounsaville, K. Tate, and A. Rohatgi. Understanding and implementing high quality contacts to advanced emitters for high efficiency solar cells. In *2nd Workshop on Metallization of Crystalline Silicon Solar Cells, 2010.*, 2010.

[9] I.B. Cooper, A. Ebong, **J. S. Renshaw**, B. Rounsaville, R. Reedy, M. Al-Jassim, and A. Rohatgi. High throughput rapid thermal firing of screen-printed contacts to si solar cells on low quality materials. In *25th European Photovoltaic Solar Energy Conference and Exhibition / 5th World Conference on Photovoltaic Energy Conversion, 6-10 September 2010, Valencia, Spain*, 2010.

[10] **J. S. Renshaw**, A. Ebong, S. Ramanathan, I.B. Cooper, K. Tate, A. Rohatgi, and I. Koehler. Development of low-cost plated contact solar cells using a screen printed dielectric etching paste. In *24th European Photovoltaic Solar Energy Conference, 21-25 September 2009, Hamburg, Germany*, 2009.

[11] **J. S. Renshaw**, MH Kang, V. Meemongkolkiat, A. Rohatgi, D. Carlson, and M. Bennett. 3d-modeling of a back point contact solar cell structure with a selective emitter. In *34th IEEE Photovoltaic Specialists Conference (PVSC)*, pages 000375–000379. IEEE, 2009.

[12] **J. S. Renshaw**, A. Ebong, and A. Rohatgi. Development of low cost plated contact solar cells on high sheet resistance emitters. In *18th Workshop on Crystalline Silicon Solar Cells and Modules: Materials and Processes*, 2008.

VITA

John Renshaw was born in Seattle, Washington in 1982. He received his Bachelor of Science degree in Physics from Washington State University in Spring 2006 and began work on his PhD in Physics in Fall 2006 at Georgia Institute of Technology where he joined the University Center of Excellence for Photovoltaics. His research interests are in crystalline silicon photovoltaics and include laser doped selective emitter solar cells and 2D and 3D modeling of advanced solar cell structures as well as next generation photovoltaic materials.